Karlsruher Institut für Technologie

Schriftenreihe
Kontinuumsmechanik im Maschinenbau

32

Tobias Karl

Micromechanical Modeling of Short-Fiber Orientation Dynamics

KIT Scientific Publishing

Tobias Karl

Micromechanical Modeling of Short-Fiber Orientation Dynamics

Schriftenreihe
Kontinuumsmechanik im Maschinenbau
Band 32

Karlsruher Institut für Technologie (KIT)
Institut für Technische Mechanik
Bereich Kontinuumsmechanik

Hrsg. Prof. Dr.-Ing. habil. Thomas Böhlke

Eine Übersicht aller bisher in dieser Schriftenreihe erschienenen Bände finden Sie am Ende des Buchs.

Micromechanical Modeling of Short-Fiber Orientation Dynamics

by
Tobias Karl

KIT Scientific Publishing

Karlsruher Institut für Technologie
Institut für Technische Mechanik
Bereich Kontinuumsmechanik

Micromechanical Modeling of Short-Fiber Orientation Dynamics

Zur Erlangung des akademischen Grades eines Doktors der Ingenieurwissenschaften (Dr.-Ing.) von der KIT-Fakultät für Maschinenbau des Karlsruher Instituts für Technologie (KIT) genehmigte Dissertation

von Tobias Karl, M.Sc.

Tag der mündlichen Prüfung: 20. Januar 2025
Hauptreferent: Prof. Dr.-Ing. Thomas Böhlke
Korreferentin: Prof. Dr.-Ing. Bettina Frohnapfel
Korreferentin: Prof. Dr. rer. nat. Christina Papenfuß

Impressum

Scientific Publishing

Karlsruher Institut für Technologie (KIT)
KIT Scientific Publishing
Straße am Forum 2
D-76131 Karlsruhe

www.bibliothek.kit.edu/ksp.php | E-Mail: info@ksp.kit.edu | Shop: www.ksp.kit.edu

Print on Demand 2025 – Gedruckt auf FSC-zertifiziertem Papier

ISSN 2192-693X
ISBN 978-3-7315-1431-2
DOI 10.5445/KSP/1000180614

Danksagung

Diese Dissertation entstand während meiner wissenschaftlichen Tätigkeit am Karlsruher Institut für Technologie (KIT). Mein besonderer Dank gilt Prof. Dr.-Ing. Thomas Böhlke vom Institut für Technische Mechanik und Prof. Dr.-Ing. Bettina Frohnapfel vom Institut für Strömungsmechanik für ihre intensive und engagierte Betreuung. Die gewährten Freiheiten in der institutsübergreifenden Zusammenarbeit haben mir wertvolle Möglichkeiten zur fachlichen und persönlichen Weiterentwicklung geboten. Ich durfte von ihrem umfangreichen Erfahrungsschatz profitieren und konnte mich stets auf wertvolle Impulse sowie konstruktive Rückmeldungen verlassen. Ihre Begeisterung, Wertschätzung und ihr Interesse an meiner Arbeit haben mich jederzeit motiviert.

Mein Dank gilt zudem Prof. Dr. rer. nat. Christina Papenfuß für die Anfertigung des Drittgutachtens, ihr tiefgehendes Interesse und die angenehme Zusammenarbeit. Für den Prüfungsvorsitz danke ich Prof. Dr.-Ing. Martin Heilmaier.

Der Friedrich und Elisabeth Boysen-Stiftung danke ich für die finanzielle Förderung (BOY-163) und dem Land Baden-Württemberg für die Unterstützung durch das bwHPC. Dem KIT danke ich für die kostenfreie Nutzung verschiedener Software und für die finanzielle Unterstützung meiner Open Access Publikationen.

Ich danke Dr.-Ing. Davide Gatti für die vielen fachlichen Diskussionen und die Unterstützung. Bereits während der Betreuung meiner Masterarbeit hat er meine Arbeitsweise geprägt und mich insbesondere in der Anfangszeit meiner Promotion intensiv begleitet. Für die tolle Zusammenarbeit danke ich Prof. Dr. rer. nat. Matti Schneider. Seine

umfassenden und konstruktiven Rückmeldungen haben wesentlich zur Weiterentwicklung meiner Arbeit beigetragen. Jan Zartmann und Simon Dalpke danke ich für die angenehme und verlässliche Zusammenarbeit im Rahmen einer Publikation.

Ein großes Dankeschön geht an Sabine Bernecker-Dennig, Helga Betsarkis, Ute Schlumberger-Maas und Ariane van Elst sowie an Karin Fritsch-Kirchner und Sibela Hasecic für die Unterstützung in allen organisatorischen Angelegenheiten. Dr.-Ing. Tom-Alexander Langhoff danke ich für die Organisation der Lehre sowie für seine Unterstützung bei der Beschaffung technischer Ausstattung.

Allen Kolleginnen und Kollegen danke ich für das herzliche und produktive Miteinander. Der persönliche und fachliche Austausch mit euch war fantastisch und immer eine große Hilfe. Die gemeinsam verbrachte Zeit auf Konferenzen, bei Sportevents und beim Angeln wird mir in bester Erinnerung bleiben. Besonders dankbar bin ich für die hier entstandenen Freundschaften. Meiner Zimmerkollegin Dr.-Ing. Loredana Kehrer danke ich für die tolle Zeit und für ihre Unterstützung in allen Belangen.

Mein besonderer Dank gilt Ramona A., Lara B., Daniel B., Dominik G., Michael G., Vivien und Johannes N., Thomas N., Alea R. und Dr. phil. Steffen S. für die langjährige Freundschaft. Die gemeinsame Zeit beim Wandern, Kochen, Grillen, bei Spieleabenden und im zurückliegenden Studium bedeutet mir sehr viel.

Meinem Onkel Bernd danke ich für die gemeinsamen Wanderungen, die vielen Gespräche und dafür, dass er immer an mich glaubt.

Mein größter Dank gilt meinen Eltern und meiner Schwester, die mir mit ihrem Vertrauen, ihrem Rückhalt und ihrer Verlässlichkeit beim Bewältigen vieler Herausforderungen stets eine große Stütze sind. Liebe Mama, lieber Papa und liebe Julia, euch widme ich diese Arbeit. Danke, dass ihr immer für mich da seid.

Karlsruhe, im August 2025 Tobias Karl

Publications and citation

This thesis represents a publication-based doctoral thesis. It is partly based on the following peer-reviewed journal articles, as indicated in the respective sections. All journal articles are published under the terms of the Creative Commons license CC BY 4.0, and links to these publications are given below along with the bibliographic details: [1]

1. Karl, T., Gatti, D., Frohnapfel, B., Böhlke, T., 2021b. Asymptotic fiber orientation states of the quadratically closed Folgar-Tucker equation and a subsequent closure improvement. Journal of Rheology 65 (5), 999–1022. URL: https://doi.org/10.1122/8.0000245.
2. Karl, T., Böhlke, T., 2022. Unified mean-field modeling of viscous short-fiber suspensions and solid short-fiber reinforced composites. Archive of Applied Mechanics 92 (12), 3695–3727. URL: https://doi.org/10.1007/s00419-022-02257-4.
3. Karl, T., Schneider, M., Böhlke, T., 2023a. On fully symmetric implicit closure approximations for fiber orientation tensors. Journal of Non-Newtonian Fluid Mechanics 318, Article 105049. URL: https://doi.org/10.1016/j.jnnfm.2023.105049.

[1] https://creativecommons.org/licenses/by/4.0/, all articles are reproduced with permission from the Society of Rheology: https://pubs.aip.org/sor/jor/pages/permissions, from Springer: https://www.springer.com/gp/rights-permissions/obtaining-permissions/882, and from Elsevier: https://www.elsevier.com/about/policies-and-standards/copyright/permissions, all links retrieved on April 30, 2024.

4. Karl, T., Zartmann, J., Dalpke, S., Gatti, D., Frohnapfel, B., Böhlke, T., 2023b. Influence of flow-fiber coupling during mold-filling on the stress field in short-fiber reinforced composites. Computational Mechanics 71 (5), 991–1013. URL: https://doi.org/10.1007/s00466-023-02277-z.
5. Karl, T., Böhlke, T., 2024. Generalized micromechanical formulation of fiber orientation tensor evolution equations. International Journal of Mechanical Sciences 263, Article 108771. URL: https://doi.org/10.1016/j.ijmecsci.2023.108771.

Citation of text passages

The following part addresses the citation of sections that consist either partially or entirely of the publications listed before. In this thesis, a distinction between the following two cases is made:

1. If a section of this thesis consists only of text passages from one of the publications above, the citation is done via a footnote at the respective section heading. In this first case, the following formulation is used: *This section is directly taken from [reference].*
2. If a section of this thesis consists of text passages from the publications above and additionally contains newly written content, then the citation is also done via a footnote at the respective section heading. In this second case, the following formulation is used: *This section consists of parts from [reference(s)]. Additional text passages have been added.*

The monographic style of this thesis requires an editorial revision of the parts taken from the journal articles, which underlies both cases described above. The numbering of sections, equations, figures, and tables is adapted. Symbols, terms, abbreviations, and parameters are

unified to ensure consistency. The numerical citation style of the underlying publications is changed to Harvard style in the present thesis. In addition, references to books and doctoral theses are extended by providing the respective page or section numbers. Where necessary, section titles are adapted and sections are reformatted. Minor linguistic changes are made. Grammar, tenses, and punctuation are revised. This linguistic and grammatical revision of the text is based on DeepL® Write [2] as an artificial intelligence tool. Cross-references to other sections are added. Parts taken from the underlying publications are shortened where necessary to avoid redundancy.

Citation of figures and tables

If a figure or a table is taken from one of the underlying journal articles listed before, this is indicated in the respective caption. Since all figures or tables are modified at least in size and font style, they are cited as follows: *[...], adapted from [reference]*. The captions are revised where necessary.

All figures are created using either PGFPlots, Inkscape®, or TikZ, both data generation and preparation is based on MATLAB®, and regarding chapter 3, data generation is also based on OpenFOAM® and Abaqus®. [3] Except for MATLAB® and Abaqus®, whose licenses were provided by the Karlsruhe Institute of Technology (KIT), all software tools used refer to the GNU General Public License (GPL). [4]

[2] `https://www.deepl.com/de/write`, retrieved on August 24, 2024.

[3] PGFPlots: `https://github.com/pgf-tikz/pgfplots`, Inkscape®: `https://inkscape.org`, TikZ: `https://tikz.org`, MATLAB®: `https://www.mathworks.com/products/matlab.html`, OpenFOAM®: `https://www.openfoam.com`, Abaqus®: `https://www.3ds.com/products/simulia/abaqus`, all links retrieved on August 24, 2024.

[4] `https://www.gnu.org/licenses/quick-guide-gplv3.html`, retrieved on August 24, 2024.

Zusammenfassung

Kurzfaserverstärkte Polymere werden beispielsweise im Leichtbau eingesetzt und zeichnen sich durch eine anisotrope Mikrostruktur aus. Die Herstellung durch das Spritzgussverfahren erlaubt die Realisierung großer Stückzahlen und die Erzeugung komplexer Bauteilgeometrien. Die vorherrschende Strömung beim Einspritzvorgang der Fasersuspension beeinflusst das Orientierungsverhalten der Kurzfasern und damit die sich einstellende Mikrostruktur des Bauteils. Die präzise Vorhersage der damit verbundenen makroskopischen Eigenschaften ist von großer industrieller Bedeutung. Diese Arbeit befasst sich mit der mikromechanischen Modellierung der Entwicklung der Faserorientierung während der Formfüllung kurzfaserverstärkter Polymere. Diese wird aus drei Teilen bestehend interpretiert. Der erste Teil umfasst die Untersuchung der Orientierungsentwicklung unter Berücksichtigung der anisotropen Viskosität der Fasersuspension, genannt Flow-Fiber Coupling. Durch die Verwendung von Orientierungstensoren sind Schließungen notwendig, die den zweiten Teil der Arbeit bilden und insbesondere im mikromechanischen Kontext zur Abschätzung effektiver mechanischer Eigenschaften untersucht werden. Die Formulierung der Entwicklungsgleichungen der Orientierungstensoren basierend auf mikromechanischen Ansätzen wird im dritten Teil behandelt. Hinsichtlich des Flow-Fiber Couplings während der Formfüllung werden die Auswirkungen auf das Spannungsfeld im belasteten Festkörper untersucht und in diesem Kontext die Rolle des Viskositätsmodells der Matrix analysiert. Ausgewählte Verfahren zur numerischen Stabilisierung werden diskutiert und die räumliche Beschränkung der Kopplung vorgeschlagen. Die aus der Literatur be-

kannte quadratische Schließung wird durch Symmetrisierung in eine neue Form überführt, die aus zwei Varianten besteht. Des Weiteren wird das Konzept der impliziten Schließungen eingeführt und untersucht. Basierend auf einem Mean-Field Ansatz erfolgt die Formulierung der Entwicklungsgleichung des Orientierungstensors beliebiger Stufe. Die allgemeine Formulierung erlaubt die Verwendung beliebiger Modelle durch Einsetzen der entsprechenden Lokalisierungsrelationen und damit die Berücksichtigung der anisotropen Mikrostruktur der Fasersuspension in der Entwicklungsgleichung. Insbesondere ermöglicht die freie Modellwahl die Betrachtung der Faserverteilung.

Das Flow-Fiber Coupling führt durch die Beeinflussung der Orientierung zu Unterschieden im Spannungsfeld des belasteten Festkörpers im Bereich von über $\pm 10\,\%$ relativ zum entkoppelten Vorgehen. Verglichen mit der Verwendung konstanter Viskosität führt die Berücksichtigung von scherverdünnendem Verhalten der Matrix zu Spannungsunterschieden von ca. $\pm 5\,\%$. Verglichen mit der quadratischen Schließung führt die vorgeschlagene symmetrische quadratische Schließung zu einer genaueren Abschätzung effektiver mechanischer Eigenschaften und zu einer verbesserten Vorhersage der Orientierungsentwicklung. Die quadratische und hybride Form des impliziten Schließungsansatzes können in ein 1D Problem überführt werden und stellen eine effiziente Approximation der Maximum-Entropie Methode dar. Beide impliziten Schließungen sind der symmetrischen quadratischen Schließung in der Abschätzung effektiver mechanischer Eigenschaften überlegen, sie führen allerdings zu Oszillationen in der Orientierungsentwicklung. Die Ergebnisse der formulierten Entwicklungsgleichungen für die Orientierung zeigen das bekannte periodische Verhalten in einer Scherströmung, während der Einfluss der Volumenfraktion und der Effekt der räumlichen Faserverteilung prägnant ist. Das Schließungsproblem hängt vom gewählten Mean-Field Modell ab, ebenso der Berechnungsaufwand bedingt durch die etwaige Integration über die Einheitskugel.

Summary

Short-fiber reinforced polymers are used, for example, in lightweight design and are characterized by an anisotropic microstructure. Production by injection molding allows the realization of large quantities and the creation of complex part geometries. The predominant flow during the injection process of the viscous fiber suspension influences the orientation behavior of the short fibers and thus the resulting microstructure of the manufactured part. The precise prediction of the associated macroscopic mechanical properties is of great industrial importance. This thesis deals with the micromechanical modeling of the fiber orientation evolution during mold-filling of short-fiber reinforced polymers. This is interpreted as consisting of three parts. The first part includes the investigation of the orientation evolution considering the anisotropic viscosity of the fiber suspension, which is called flow-fiber coupling throughout this thesis. The use of orientation tensors requires closures, which form the second part of this thesis and are investigated in particular in a micromechanical context for the estimation of effective mechanical properties. The formulation of the evolution equations of the orientation tensors based on micromechanical approaches is addressed in the third part of the present work. Regarding the flow-fiber coupling during mold-filling, the effects on the stress field in the loaded solid composite are investigated and the role of the viscosity model of the matrix is analyzed. Selected methods for numerical stabilization are discussed and the spatial restriction of the coupling is proposed. The common quadratic closure known from the literature is transformed by symmetrization into a new form consisting of two variants. Furthermore,

the concept of implicit closures is introduced and investigated. Based on a mean-field approach, the evolution equation of the orientation tensor of arbitrary order is formulated. The general formulation allows the use of arbitrary mean-field models by inserting the respective localization relations and thus the consideration of the anisotropic microstructure of the fiber suspension in the evolution equation. In particular, the spatial distribution of the fibers can be considered by a proper choice of the mean-field model.

The results show that flow-fiber coupling leads to differences in the stress field of the loaded solid in the range of more than $\pm 10\,\%$ relative to the decoupled procedure by influencing the orientation field during mold-filling. Compared to the use of constant viscosity, the consideration of shear-thinning behavior of the matrix leads to stress differences of approximately $\pm 5\,\%$. Compared to the quadratic closure, the proposed symmetric quadratic closure leads to a more accurate estimation of the effective mechanical properties and to an improved prediction of the orientation evolution. The quadratic and hybrid formulation of the proposed implicit closure approach can be transformed into a 1D problem and represent an efficient approximation of the maximum-entropy method. Both considered implicit closures are superior to the symmetric quadratic closure in the estimation of effective mechanical properties, however, they lead to oscillations in the evolution of fiber orientation. The results of the formulated evolution equations for the fiber orientation tensor show the well-known periodic behavior in a simple shear flow, while the influence of the fiber volume fraction and the effect of the spatial fiber distribution are distinct. The closure problem depends on the chosen mean-field model, as well as the computational effort due to the possible numerical integration over the unit sphere.

Contents

Chapter 1

Introduction

Contents overview. This chapter provides an introduction to this thesis, with particular emphasis on the complexity and diversity of fiber suspension modeling as a specialized engineering field. In addition, an overview of selected publications in the field is given. With regard to the originality of this thesis, the central research questions and contributions to the state of the art are discussed. This chapter concludes with describing the notation and nomenclature.

1.1 Motivation [1]

The class of composite materials is diverse, and as described by, e.g., Henning and Moeller (2011) (pp. 339–341), a matrix is combined with reinforcing elements to produce a material whose properties differ from those of the constituents used. With the task of embedding the reinforcing elements and defining the shape of the part, various materials can be used as matrix material, such as polymers, metals, and ceramics (Henning and Moeller, 2011) (p. 341). The present work focuses on polymer matrix materials with fibers as reinforcing elements. Typically, reinforcing fibers are classified according to their length in the manufactured part, as described by Schürmann (2007) (p. 138): Short fibers refer

[1] This section consists of parts from Karl et al. (2021b), Karl and Böhlke (2022), Karl et al. (2023b), and Karl and Böhlke (2024). Additional text passages have been added.

to a fiber length in the range $0.1\,\mathrm{mm}$ to $1\,\mathrm{mm}$, the class of long fibers covers $1\,\mathrm{mm}$ to $50\,\mathrm{mm}$, and continuous fibers range from $50\,\mathrm{mm}$ up to an infinite aspect ratio, which refers to the fiber length divided by the fiber diameter.[2] Analogous to the matrix material, the reinforcing fibers can be manufactured from a variety of materials such as glass, carbon, and aramid. For a comprehensive description of these materials including the relevant mechanical properties, see, e.g., Schürmann (2007) (pp. 21–81). In addition to the restriction to polymer matrices, this study focuses on short glass fibers. The diameter of these fibers ranges from $5\,\mu\mathrm{m}$ to $24\,\mu\mathrm{m}$ according to Schürmann (2007) (p. 28) and, therefore, the aspect ratio α as a non-dimensional representation of the fiber geometry varies roughly in the range of 4 to 200.

Short-fiber reinforced polymers are commonly used in lightweight design. The case of adding fibers into a polymer matrix allows the mass-production of lightweight components with complex shapes while retaining the desired stiffness and strength. These beneficial properties as described by, e.g., Böhlke et al. (2019) (pp. 1–2) and Tucker III (2022a) (p. 1), are crucial for the use in many applications since the 1960s, such as civil and aircraft engineering (Chawla, 2019) (pp. 3–4). From the application point of view, fiber-reinforced polymer composites enhance the mechanical properties of conventional materials (Ashby, 2006) (p. 30) in order to reduce the mass of components – a point which is also addressed by Chawla (2019) (p. 4) referring to an illustration of Deutsch (1978). It is shown that, in direct comparison with steel and aluminum, composite materials are superior in terms of various mechanical properties. In this context, Fig. 1.1, which Ashby (2006) calls a materials property chart, serves as an additional graphical illustration.

[2] The terms short or long used to describe the fiber geometry do not necessarily refer to the dimensions of the manufactured part or cavity, as may be the case for thin-walled parts. During mold-filling of fiber suspensions, this can lead to restrictions in the orientation behavior of the fibers. In this context, reference is made to Secs. 3.1.3 and 3.4.

The stiffness represented by Young's modulus E and the mass density ρ is shown for different material classes, such as foams, polymers, composites, metals, and ceramics. The diagram inspired by Ashby (2006) demonstrates, that composite materials, e.g., fiber reinforced polymers, show an increased stiffness compared to pure polymers with only a slight increase in mass density.

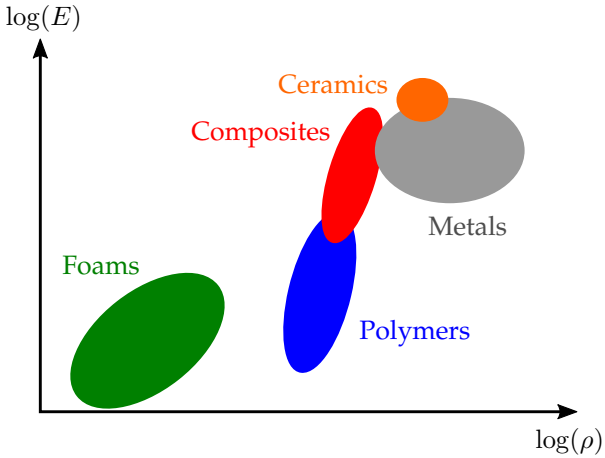

Figure 1.1: A so-called materials property chart according to Ashby (2006) showing Young's modulus E and mass density ρ for various material classes, own representation based on Ashby (2006) (p. 48, Fig. 4.2).

Short-fiber reinforced polymers, a special case of the so-called discontinuous fiber reinforced composites (Tucker III, 2022a) (pp. 1–2), are manufactured by injection molding. In this process, granulate of the composite material is brought to a viscous state and then injected into the cavity (Tucker III, 2022a) (p. 1). A comprehensive introduction to injection molding can be found in, e.g., Zheng et al. (2011). From an engineering point of view, the modeling of injection molding processes of short-fiber suspensions is a challenging task, which can be attributed to the following points. The list of these exemplary points is based

on selected core topics of injection molding processes as addressed in Zheng et al. (2011), extended by aspects relevant to this thesis:

- In general, the rheological behavior of the polymer melt depends on the shear rate. A list of common so-called non-Newtonian viscosity models can be found in Zheng et al. (2011) (pp. 18–19), including the model of Cross (1965) used in the present thesis.
- Changes in temperature during the mold-filling process affects the viscous behavior of the polymer melt with a phase transition from fluid to solid being present as described by, e.g., Zheng et al. (2011) (pp. 8–9, 28–31, 47–64) and Oumer and Mamat (2012). Therefore, modeling the mold-filling process is a multi-physical task.
- The mold-filling process itself can be modeled as a decoupled process, i.e. the fiber-induced anisotropic viscosity is neglected. This is in contrast to the coupled approach, where the fiber suspension is modeled with anisotropic viscosity, leading to an influence of the fiber orientation evolution on the flow field and vice versa, see, e.g., Advani and Tucker III (1987). The latter modeling approach is called flow-fiber coupling throughout the present thesis.[3] The differences between the coupled and the decoupled approach are addressed in various works contributing to the field of fiber suspension modeling, a selection of which is addressed in Sec. 1.2.1. Considering the anisotropic viscosity of fiber suspensions in the context of the flow-fiber coupled approach is accompanied by difficult numerical handling as addressed by, e.g., Verleye and Dupret (1993), VerWeyst and Tucker III (2002), Favaloro et al. (2018), and Tseng and Favaloro (2019). The topic of

[3] The term flow-fiber coupling is oriented to, e.g., Krochak et al. (2009), Li and Luyé (2018), and Mezi et al. (2019a). Many other formulations exist in the literature, e.g., anisotropic flow used by Altan et al. (1992), fiber-flow interaction in the study of Dupret and Verleye (1999), flow/orientation coupling used by VerWeyst and Tucker III (2002), and anisotropic rheology used by Lee et al. (2022).

flow-fiber coupling with the underlying publication Karl et al. (2023b) is discussed in chapter 3 of the present thesis.

- In the context of flow-fiber coupling, the selection of a suitable modeling of the effective anisotropic viscosity is extremely important, since it is hard to be determined experimentally, as described by Schneider (2016) and Bertóti (2021) (p. 18). On one hand, reorientation takes place instantaneously during the experiments, and on the other hand, many independent parameters have to be determined depending on the present material symmetry, as discussed by Schneider (2016) and Bertóti (2021) (p. 18). In this context, homogenization techniques can be used to estimate the effective anisotropic linear viscous behavior of fiber suspensions (Schneider, 2016; Bertóti and Böhlke, 2017; Bertóti, 2021; Bertóti et al., 2021) in the context of multi-scale modeling of injection molding processes. As a part of the fundamentals in chapter 2, mean-field modeling of anisotropic viscosity is addressed referring to the underlying publication Karl and Böhlke (2022).
- A sufficient mathematical description of the fiber orientation state that describes the anisotropy of the short-fiber suspension must be chosen. The averaging concept of fiber orientation tensors, introduced in the fundamental works of Kanatani (1984) and Advani and Tucker III (1987), is useful for engineering practice, as described by, e.g., Tucker III (2022a) (p. 119). In this context, additional complexity arises due to the closure problem as described by, e.g., Advani and Tucker III (1987) and Advani and Tucker III (1990). An introduction to the description of fiber orientation states and to the closure problem is given in chapter 2 as a part of the fundamentals. Chapters 4 and 5 with the underlying publications Karl et al. (2021b) and Karl et al. (2023a) contribute to the field by proposing two different closure methods.
- Predicting the evolution of fiber orientation during mold-filling is crucial for estimating the anisotropic properties of short-fiber suspensions and short-fiber reinforced composites as described by Tucker

III (2022a) (p. 4). As part of a simulative approach to lightweight design, models for a reliable orientation prediction are needed to implement a virtual process chain (Böhlke et al., 2019; Görthofer et al., 2019; Meyer et al., 2023) in engineering practice. As described by Verleye and Dupret (1993), difficulties arise when formulating models for the orientation dynamics due to a variety of physical influences, which all have to be identified and considered. A brief introduction to the modeling of short-fiber orientation dynamics is provided in chapter 2. Chapter 6 contributes to the modeling of short-fiber orientation dynamics in the context of a micromechanical approach with its underlying publication Karl and Böhlke (2024).

In the context of the complexity of the fiber suspension mold-filling process addressed before, this thesis deals with the micromechanical modeling of short-fiber orientation dynamics. First, this micromechanical modeling requires consideration of the microstructure during mold-filling in the presence of anisotropic and heterogeneous viscosity. Secondly, the proposed closure approximations are examined and evaluated based on the quality of the prediction of anisotropic viscous and elastic properties in order to sufficiently represent the microstructure in terms of micromechanical mean-field modeling. Thirdly, the orientation dynamics, which refer to the evolution of the fiber orientation, are modeled on a micromechanical basis. In this sense, the anisotropic microstructure is considered in the mathematical formulation of the governing differential equation for the fiber orientation tensor of arbitrary order to describe the orientation dynamics in general. The following overview of selected literature is based on these three topics.

1.2 State of the art

1.2.1 Flow-fiber coupling [4]

Regarding the modeling of mold-filling processes, both a decoupled and a flow-fiber coupled approach are possible. In this respect, reference is made to, e.g., VerWeyst and Tucker III (2002) and the literature review therein. Three main points can be identified in this context: The effect of the flow-fiber coupling on the flow field, the influenced fiber orientation evolution due to the changed flow conditions, and finally the change of the mechanical properties of the composite, which depend on the local fiber orientation. Regarding these three points, an overview of selected publications is provided in the following. A discussion of earlier works contributing to the field of flow-fiber coupling can be found in, e.g., VerWeyst and Tucker III (2002). The study of VerWeyst and Tucker III (2002) itself extends earlier works by a 3D modeling in the context of flow-fiber coupling. In addition, a correction scheme for non-physical components of the fiber orientation tensor is described. Their results show that the impact of flow-fiber coupling varies with the considered flow case and that the weakest effects can be observed in a center-gated disk flow compared to a contraction and an expansion flow.

The fiber-induced anisotropic viscosity in the flow-fiber coupled approach causes changes of the velocity field during mold-filling. Latz et al. (2010) investigated the flow-fiber coupling from a fluid mechanics perspective in a channel flow, a flow around a cylinder, and in a contraction flow. Different coupling intensities were considered with the result, that the coupling effects are significant in the channel and in the contraction flow. It is shown that, e.g. for the channel flow, the stronger the coupling, the flatter the velocity profile. This flattening was already reported in

[4] This section consists of parts from Karl et al. (2023b). Additional text passages have been added.

the early studies of Altan et al. (1992) and Tang and Altan (1995). The importance of accounting for flow-fiber coupling in mold-filling simulations is demonstrated in a low Reynolds number flow through a tapered channel by Krochak et al. (2009). Both isotropic and aligned orientation states were applied at the inlet, showing that the flow changes towards a plug flow because of flow-fiber coupling. Their research, based on an orientation distribution function (ODF) approach, shows that for both inlet conditions the changes in the velocity field due to flow-fiber coupling are evident. Flow-fiber coupled mold-filling simulation based on the ODF was carried out by Mezi et al. (2019a) in 2D geometries and by Férec et al. (2020) in 3D for axisymmetric geometries. The results of Mezi et al. (2019a) illustrate the already addressed flattening of the velocity profile caused by flow-fiber coupling, whereas it is shown by Férec et al. (2020) that the die swell ratio differs between the coupled and decoupled approach. In addition, the difference between Newtonian and non-Newtonian matrix fluid is addressed by Mezi et al. (2019a). Mezi et al. (2019b) observed a flattening of the velocity profile in the context of flow-fiber coupling for die swell flows. Their results show that the swell ratio of the flow is affected by flow-fiber coupling. By using a scalar rheological model, Li and Luyé (2019) studied the flow-fiber coupling effects based on mold-filling simulations of a rectangular plate. In addition, three different orientation evolution models were used in their study. They observed, that the coupling effects strongly depend on the chosen orientation evolution model. In this context, the classical Folgar-Tucker model, referring to Folgar and Tucker III (1984) and Advani and Tucker III (1987), shows less coupling effects than the reduced-strain closure model (RSC) proposed by Wang et al. (2008). The aforementioned flattening of the velocity profile also occurs. In addition, the study of Li and Luyé (2018) shows that results based on flow-fiber coupling improve parameter optimization of fiber orientation models in the core region of the flow. For their optimization procedure, the RSC model depending on two parameters and the center-gated disk flow problem

were chosen. The results show that consideration of anisotropic viscosity combined with the effect of an inhomogeneous fiber volume fraction can minimize the error of the RSC model with respect to experimentally measured fiber orientation and compared to the decoupled approach. The center region between the walls can be seen as crucial for minimizing the error under flow-fiber coupling. However, close to the walls, the results of the optimization procedure are almost the same for both the decoupled and the coupled approach. According to Li and Luyé (2018), the significance of flow-fiber coupling is underlined by their findings. Tseng and Favaloro (2019) introduced the informed isotropic viscosity model in order to improve convergence compared to the classic models of, e.g., Dinh and Armstrong (1984) and Lipscomb II et al. (1988). It is shown, that for simple and complex geometries the proposed model is capable of reproducing experimental findings and that the coupling effects on the flow field are not negligible. The informed isotropic viscosity model was used by Huang and Lai (2020) to show that flow-fiber coupling influences the melt front behavior and that the coupling effects are locally different. Lee et al. (2022) also used the informed isotropic viscosity model and studied the compression molding process of composite material. Sommer et al. (2018) investigated the flow-fiber coupling effects in a squeeze flow. Their results show that only a flow-fiber coupled analysis is capable of predicting the physically correct anisotropic behavior of the suspension. Based on a two-phase flow, Wittemann et al. (2019) implemented the flow-fiber coupling approach with a non-Newtonian, temperature-, and curing-dependent viscosity model for fiber-laden thermosets. The coupled simulation shows a better agreement of the pressure field with experimental measurements than the decoupled approach. Subsequently, Wittemann et al. (2022) incorporated the effect of fiber breakage into a flow-fiber coupled simulation with the result that both the experimentally determined pressure and fiber length distribution can be predicted more accurately compared to the approach that neglects fiber breakage. The effects of flow-fiber

coupling in the context of additive manufacturing were studied by Wang and Smith (2019), Wang and Smith (2021b), and Wang and Smith (2021a). That considering flow-fiber coupling has a clear impact on the spatial evolution of the free surface of the fiber suspension is shown by Wang and Smith (2019; 2021b). Difference fields of both velocity components in 2D between the coupled and the decoupled approach are given in Wang and Smith (2021b). It is shown that flow-fiber coupling leads to a velocity difference of $13.8\,\%$ relative to the so-called deposition rate of the process. Both Wang and Smith (2019) and Wang and Smith (2021b) describe the effect of the coupling on the velocity field as remarkable. Wang and Smith (2021a) also provide a detailed analysis of the velocity field for the investigated additive manufacturing process. Their results show maximum differences in the velocity components between the coupled and decoupled approach of $27\,\%$ and $50\,\%$, depending on the considered velocity component in 2D. Regarding the stationary value at the outlet, a difference of $13\,\%$ between the coupled and decoupled generated suspension velocity occurs.

The flow-fiber coupling effects on the velocity field addressed before have a direct influence on the fiber orientation evolution. Chung and Kwon (2002a;c) studied the flow-fiber coupling effects on the fiber orientation field. Their results show that flow-fiber coupling clearly influences the fiber orientation prediction. The results refer to a center-gated disk flow in which a spatially inhomogeneous coupling effect can be identified. Near the gate, the flow-fiber coupling effect is more pronounced than in regions further away from the gate, which is directly related to the spatially varying flattening of the velocity profile, as illustrated by Chung and Kwon (2002c). In Chung and Kwon (2002a;c), a further point is highlighted, namely the differences between modeling using the so-called Hele-Shaw approximation and mold-filling

simulation based on so-called fountain flow modeling.[5] Their results show that flow-fiber coupling effects on the orientation field are more pronounced under fountain flow conditions compared to the Hele-Shaw model. Backed up by experimental data, the fountain flow modeling led to precise results. In contrast, the center-gated disk simulation of VerWeyst and Tucker III (2002) was performed without modeling the fountain flow. Although the region close to the gate was also identified as the most interesting in terms of flow-fiber coupling, a decoupled approach is suggested by VerWeyst and Tucker III (2002) for practice. A center-gated disk geometry is also included in the study of Favaloro et al. (2018). The flow-fiber coupling was realized by the proposed informed isotropic viscosity model. The results show that the proposed model causes the well-known and often discussed flattening and a broad region where the orientation tensor components are almost constant over the thickness. As already addressed, Krochak et al. (2009) considered two different inlet conditions, namely an aligned and a random or isotropic orientation state. Their results also show that, in contrast to the aligned inlet condition, the flow-fiber coupling under an isotropic inflow orientation state clearly affects the reorientation behavior of the embedded fibers. Latz et al. (2010) found that the stronger the coupling, the larger the region of isotropic orientation in the channel center region. They conclude that the impact of flow-fiber coupling on the reorientation

[5] The term fountain flow refers to Rose (1961) who describes this phenomenon as the fountain effect. Following Zheng et al. (2011) (pp. 122–124) and the references therein, fountain flow effects occur at moving phase fronts: The velocity of the fluid particles in the center of the channel decreases when they are close to the phase front and a deflection perpendicular to the main flow direction occurs, causing the fluid particles to move towards the wall region. The Hele-Shaw model represents an approximation for flows through thin gaps as addressed by, e.g., Altan et al. (1990) and Tucker III (1991). It should be noted that the first flow regime of Tucker III (1991) refers to the Hele-Shaw model where a decoupled approach may be used for simplicity, which is also described by, e.g., VerWeyst and Tucker III (2002). As described by Zheng et al. (2011) (p. 123), the Hele-Shaw approach is not capable of modeling the aforementioned fountain flow effect at a curved phase front.

behavior of the fibers is distinct. Li and Luyé (2019) observed that the fiber orientation evolution is clearly influenced by the changed flow kinematics for the studied mold-filling process of a rectangular plate. It is shown that the orientation results based on the RSC model can be improved by up to $8\,\%$ in terms of a relative error measure when flow-fiber coupling is considered compared to the decoupled approach. Wang and Smith (2019; 2021b) investigated flow-fiber coupling regarding an additive manufacturing process. The fiber orientation evolution referred to the orthotropically closed Folgar-Tucker model and the coupling was realized based on the fourth-order fiber orientation tensor. Significant differences in the fiber orientation tensor were observed due to flow-fiber coupling. The results of Wang and Smith (2019) show an increased alignment in the main flow direction predicted by the coupled approach compared to the decoupled simulation. Difference fields between the coupled and decoupled computed components of the fiber orientation tensor are provided in the study of Wang and Smith (2021b). It is shown that flow-fiber coupling causes differences in the intervals -0.1 to 0.1, -0.2 to 0.2, and -0.5 to 0.5, depending on the respective component of the fiber orientation tensor. In contrast, Mezi et al. (2019a;b) and Férec et al. (2020) did not observe significant differences regarding the fiber orientation state between the decoupled and the coupled approach in their simulation setups. That the effects of flow-fiber coupling vary locally is emphasized by the study of Huang and Lai (2020). They considered a plate with three specimens placed in such a way that different filling states are present. A comparison with experimentally determined fiber orientations at various points inside the specimens shows that a coupled simulation approach gives more precise results than a decoupled approach over all points. However, the results of Huang and Lai (2020) also indicate that the coupling effects inside the specimens vary in terms of intensity with the considered locations. The same plate and specimen configuration was used in the recent work of Huang et al. (2023). They investigated the shrinkage

behavior and observed both a higher pressure at the gate and a different phase front geometry due to flow-fiber coupling compared to the decoupled approach. In addition, Huang et al. (2023) provide a tabular summary of selected studies in the context of flow-fiber coupling which includes information about the geometry, materials, modeling, and the main findings. Recently, Tseng (2024) improved the informed isotropic viscosity model of Favaloro et al. (2018) and Tseng and Favaloro (2019) by a parameter which depends on the fiber aspect ratio and the fiber volume fraction. The mold-filling process of a flat plate was conducted using both a decoupled and coupled approach. The results show, in comparison with measured fiber orientation profiles across the thickness of the plate, that the orientation in the center region for high fiber volume fractions is only sufficiently predicted by a coupled approach. In addition, the anisotropic behavior of the free surface, the so-called ear flow front, is only present when flow-fiber coupling is considered.

Selected studies on the last aspect of flow-fiber coupling, the effects on elastic properties, are discussed in the following. The impact of flow-fiber coupling on Young's modulus in the main flow direction is shown in Li and Luyé (2019). They used the model of Tandon and Weng (1984) to estimate the five elastic constants describing the transversely isotropic material symmetry. This transversely isotropic stiffness tensor was used as an input for the orientation averaging procedure of Advani and Tucker III (1987). The results of Li and Luyé (2019) indicate that the prediction of Young's modulus based on the coupled approach is closer to the experimental measurements than the Young's modulus based on decoupled modeling. In the context of an outlook, Li and Luyé (2019) address the need for investigating flow-fiber coupling effects during mold-filling with regard to the impact on the stress field under load of the composite part. Karl et al. (2021a) studied the effect of flow-fiber coupling on both velocity and fiber orientation. A simple channel flow and a flow over

a backward-facing step was considered with a detailed analysis of the aforementioned velocity flattening. Consistent with the studies already addressed, distinct differences in fiber orientation are shown. Based on polar plots of the direction-dependent Young's modulus referring to Böhlke and Brüggemann (2001) computed with the model of Mori and Tanaka (1973) based on the representation given in, e.g., Brylka (2017) (p. 38) or Benveniste (1987), the flow-fiber coupling effects on the local elastic anisotropy are shown. In this context, the results of Wang and Smith (2019; 2021b) demonstrate significant differences due to flow-fiber coupling in the engineering constants describing the effective elastic anisotropy. Wang and Smith (2019) used the model of Tandon and Weng (1984) combined with the orientation averaging scheme of Advani and Tucker III (1987) to estimate the anisotropic stiffness tensor. The results show that, e.g., for the Young's modulus in main flow direction, a relative difference of almost $16\,\%$ occurs between the coupled approach and the decoupled approach, whose fiber orientation fields are used to estimate the elastic constants. In this context, the study of Wang and Smith (2021b) indicates that the value of the fiber-fiber interaction parameter of the Folgar-Tucker model can significantly influence the estimate of the anisotropic elastic properties. Regarding selected engineering constants, relative differences up to approximately $23\,\%$ arise when changing the interaction constant from 0.001 to 0.01. Wang and Smith (2021a) present a finite element procedure regarding flow-fiber coupling with the result that the differences caused by flow-fiber coupling can be significant. Differences up to $27\,\%$ to $50\,\%$ in the velocity field and differences up to approximately $8\,\%$ in the tensile modulus were observed, depending on which velocity component or which of the nine elastic constants are considered. These quantitative statements of Wang and Smith (2021a) are preceded by a change in fiber orientation due to the flow-fiber coupling, which can be quantified with up to $17\,\%$ in main flow direction. Wang (2022) improved the algorithm of Wang and Smith (2021a) by optimizing the scalar viscosity in order to consider higher fiber aspect ratios with

less numerical difficulties. Different fiber aspect ratios were considered and the difficulty of generating a mesh which can be applied to all aspect ratios is addressed. For fiber aspect ratios beyond 25, Wang (2022) suggests using additional methods to improve the convergence of flow-fiber coupled simulations.

1.2.2 Closure approximations [6]

As already addressed in Sec. 1.1, the use of fiber orientation tensors is associated with a closure problem. Modeling the orientation dynamics of the second-order fiber orientation tensor, a selection of various models is provided in the following Sec. 1.2.3, include the fourth-order fiber orientation tensor. Since the fourth-order orientation tensor is unknown, this inherently defines a closure problem as described by, e.g., Advani and Tucker III (1987), which extends to arbitrary tensor orders. [7] Therefore, when integrating evolution equations for the second-order orientation tensor, a proper approximation of the fourth-order orientation tensor in terms of the second-order orientation tensor is needed (Advani and Tucker III, 1987). Another important application of closures is the method of orientation averaging depending on both the second- and fourth-order orientation tensor in order to estimate effective properties of anisotropic materials (Advani and Tucker III, 1987). A comprehensive listing of various closure approximations is given in Breuer et al. (2019) and in the recent publication of Al-Qudsi et al. (2022). In the following, details on selected closures are discussed in order to make the present thesis self-contained.

[6] This section consists of parts from Karl et al. (2023a). Additional text passages have been added.

[7] As an example, the evolution equation of the fourth-order fiber orientation tensor depends on the sixth-order fiber orientation tensor as shown in, e.g., Advani and Tucker III (1987), Altan et al. (1990), and Altan et al. (1992). Regarding closures for the sixth-order fiber orientation tensor, the reader is referred to, e.g., Advani and Tucker III (1987) and Jack and Smith (2005; 2006).

From the perspective of algebraic simplicity, the quadratic closure (QC) approximates the fourth-order orientation tensor by a dyadic product of the respective second-order tensor. The origin of QC lies in the orientation modeling of so-called rodlike polymers with reference made to the works of, e.g., Doi (1981) and Marrucci and Grizzuti (1984). The concept of QC was later taken up in the context of fiber suspensions and fiber reinforced composites by, e.g., Advani and Tucker III (1987) and Advani and Tucker III (1990). Leading to the exact fourth-order orientation tensor for the unidirectional (UD) orientation state, the QC shows a lack of full index symmetry as described by, e.g., Advani and Tucker III (1987). Their results show that the QC tends to overestimate the alignment in a simple shear flow compared to the ODF-based solution for orientation states with a distinct degree of isotropy. Kröger et al. (2008) propose a quadratic closure scheme, formulated in terms of so-called alignment tensors, to approximate the unknown higher-order alignment tensor while maintaining the required full index symmetry and the exactness for both UD and isotropic orientation states. Please note that alignment tensors are the third-kind orientation tensors described by Kanatani (1984), which are symmetric and traceless. The results of Kröger et al. (2008) show that the proposed closure improves the approximation compared to other non-fitted closures and that the investigated error almost coincides with that of the Bingham distribution (Bingham, 1974). Furthermore, Kim et al. (2015) proposed a symmetric QC consisting of constant, linear, and quadratic terms with one single coefficient depending on the invariants of the second-order orientation tensor.

The linear closure (LIN) was introduced by Hand (1962) and refers to a fully symmetric approximation of the fourth-order orientation tensor. Leading to the requested fourth-order fiber orientation tensor for the isotropic orientation state as described by, e.g., Advani and Tucker III (1987), their results and additionally the results of, e.g., Verleye and

Dupret (1993) show that the orientation dynamics referring to LIN tend to oscillate when a distinct degree of alignment is present.

The convex combination of LIN and QC is called hybrid closure (HYB) and was proposed by Advani and Tucker III (1987) with the idea of designing a simply structured closure leading to exact results for both the UD and the isotropic orientation state. The results of Advani and Tucker III (1987) regarding orientation evolution in a simple shear flow show that HYB leads to more reliable predictions compared to the results of QC and LIN. Han and Im (1999) developed an improved HYB. In addition, Petty et al. (1999) proposed a generalized HYB approach in order to address the lack of full index symmetry of the common HYB.

The natural closure (NAT) proposed by Verleye and Dupret (1993), which is also addressed in, e.g., Dupret and Verleye (1999), Chung and Kwon (2002b), and Montgomery-Smith et al. (2011a), is based on the assumption of an interaction-free fiber suspension. NAT is formulated via general fully symmetric basis tensors depending on the second-order identity tensor and the second-order fiber orientation tensor. The coefficients of these basis tensors depend on the invariants of the second-order fiber orientation tensor with an explicit formulation only possible in 2D as described by Verleye and Dupret (1993) and Dupret and Verleye (1999). For interaction-free fiber suspensions, the evolution of the ODF can be expressed analytically referring to Dinh and Armstrong (1984) and Lipscomb II et al. (1988). This analytical formulation is called canonical distribution function and is used for approximating the coefficients of the 3D version of NAT (Dupret and Verleye, 1999).

Similar to NAT, the fast exact closure (FEC) proposed by Montgomery-Smith et al. (2011a) assumes an interaction-free fiber suspension. As already discussed in the context of NAT, an analytical expression describing the reorientation behavior exists called canonical distribution function. It is shown by Montgomery-Smith et al. (2011a) that the exact

fourth-order orientation tensor can be expressed via elliptic integrals [8] referring to the eigensystem defined by the positive definite tensor included in the canonical distribution function. Following Montgomery-Smith et al. (2011a), the computation of the elliptic integrals can be avoided, but FEC requires the integration of an additional tensorial evolution equation and the computation of eigenvalues and transformations between coordinate systems. According to Montgomery-Smith et al. (2011a), the computational effort can be compared to the orthotropic closure which is addressed next. The subsequent work of Montgomery-Smith et al. (2011b) addresses the formulation of FEC for fiber orientation evolution equations considering fiber-fiber interaction, such as the Folgar-Tucker model and the anisotropic rotary diffusion model addressed in the next section, which are not accounted for in Montgomery-Smith et al. (2011a).

The concept of an orthotropic closure (ORT) was proposed by Cintra and Tucker III (1995). This approach is based on coinciding eigensystems of the second- and fourth-order orientation tensor with the full index symmetry being fulfilled by definition. Three unknown components of the fourth-order orientation tensor can be identified in the eigensystem for which polynomials in two eigenvalues of the second-order orientation tensors are postulated. The coefficients of these polynomials are fitted to ODF-based solutions. The results of Cintra and Tucker III (1995) show that ORT can be seen as a sufficient approach leading to reliable orientation prediction in different flows. However, there is a shortcoming, namely that ORT leads to oscillations in a simple shear flow for weak fiber-fiber interaction of the Folgar-Tucker model. In this context, Chung and Kwon (2001) developed a revised ORT based on different polynomials to get rid of the oscillations in a simple shear

[8] For further information on elliptic integrals and related approximation methods, the reader is referred to, e.g., Carlson and Notis (1981), Carlson (1995), and Ospald (2019) (pp. 35–61).

flow in order to model the reorientation behavior under weak fiber-fiber interaction. Chung and Kwon (2002b) used higher-order polynomials in order to further increase the accuracy of predicting the fiber orientation evolution. In their study, ORT is called eigenvalue-based optimal fitting closure (EBOF). Kuzmin (2018) investigated the orientation prediction of various ORT models in different homogeneous flows. In addition to the so-called smooth and fitted models of Cintra and Tucker III (1995), Kuzmin (2018) studied a linear, quadratic, and a mixed ORT model along with two proposed models based on NAT in 2D. A novel orthotropic fitted closure was proposed by Al-Qudsi et al. (2022) and different well known closure approximations were compared with each other in terms of Young's moduli and experimental investigations.

The invariant-based optimal fitting closure (IBOF) was proposed by Chung and Kwon (2002b) and aims to generate an optimum from NAT and EBOF and get rid of the shortcomings of both. As described by Chung and Kwon (2002b), EBOF leads to well predicted orientation states and the underlying polynomial fit is able to account for different fiber-fiber interaction strengths in the context of the Folgar-Tucker equation, but, in contrast, the eigensystem of the second-order orientation tensor that is the basis of EBOF leads to an intensive computational effort. Furthermore, as described by Dupret and Verleye (1999) and Chung and Kwon (2002b), the 3D version of NAT contains singular expressions that should be avoided from a numerical perspective. In addition, since NAT is based on the assumption of an interaction-free fiber suspension, the behavior of real fiber suspensions is not completely modeled and therefore generality cannot be ensured (Dupret and Verleye, 1999). However, following Chung and Kwon (2002b), the formulation of NAT in terms of the invariants of the second-order fiber orientation tensor is computationally favorable compared to EBOF, because there is no need to compute eigenvalues and perform transformations between different coordinate systems. The IBOF closure uses the fully symmetric

basis tensors of NAT with the coefficients modeled as polynomials in the invariants of the second-order fiber orientation tensor. The coefficients of the polynomials are in turn determined based on the ODF solution for different flows and different fiber interaction parameters. The results of Chung and Kwon (2002b) show that the reorientation behavior predicted by IBOF is sufficiently consistent with EBOF, but with a $60\,\%$ to $70\,\%$ saving in computation time by using IBOF instead of EBOF.

A neural network approach was used by ul Qadir and Jack (2009) in the context of a trained ORT closure. Their results show that the so-called neural network-based orthotropic closure leads to better results compared to ORT while maintaining the computational effort. Jack et al. (2010) also used an artificial neural network approach and proposed a fitted closure with a strongly reduced computational effort compared to ORT. Recently, Ogierman (2022) proposed a genetic closure approximation based on an optimization procedure. This closure led to precise results and offered the distribution of the elastic constants, but appeared to be rather inefficient compared to more common closures.

As discussed by Tucker III (2022b), a closure function with the second-order fiber orientation tensor as an input leads to an orthotropic fourth-order fiber orientation tensor. In this context, Tucker III (2022b) refers to the studies of Cintra and Tucker III (1995) and Jack and Smith (2007). For the special case of planar fiber orientation states, Tucker III (2022b) advanced to the field of non-orthotropic closure functions for the fourth-order fiber orientation tensor. Such a closure function requires an additional objective dependency, with the strain-rate tensor being an obvious choice, as described by Cintra and Tucker III (1995) and Tucker III (2022b). Tucker III (2022b) proposed that non-orthotropic closures for the special case of planar orientation states depend on a scalar measure: The angle between the eigenvectors of the strain-rate tensor and the second-order fiber orientation tensor, where both eigenvectors refer to the respective maximum eigenvalue. Referring to the recent

works Bauer and Böhlke (2022a), Bauer and Böhlke (2022b), and Bauer and Böhlke (2023), it is known that three parameters describe a planar fourth-order orientation tensor, with one being the known largest eigenvalue of the second-order fiber orientation tensor. Tucker III (2022b) proposed that the remaining two parameters depend on both the known largest eigenvalue of the second-order fiber orientation tensor and on the angular measure between the eigenvectors already discussed. An ODF-based fitting procedure for various fiber interaction parameters and flows was performed to determine the unknown two parameters. The results of Tucker III (2022b) show that the reorientation prediction of the second-order fiber orientation tensor using the non-orthotropic closure almost coincide with the ODF-based reorientation prediction, which is seen as the exact solution.

In contrast to the previously discussed closure approaches aimed at approximating the fourth-order fiber orientation tensor, the entire closure term contained in each tensorial evolution equation, a selection of which is addressed in Sec. 1.2.3, can be approximated. This closure term is formulated as a linear mapping of the strain-rate tensor over the fourth-order orientation tensor and thus represents an unknown second-order tensor depending on the flow kinematics as given in, e.g., Advani and Tucker III (1987). In this context, Hinch and Leal (1976) derived closure formulations for the aforementioned second-order closure term with two different situations being considered, namely weak flow and strong flow. In the context of the Folgar-Tucker model, weak flow refers to intense fiber interaction and strong flow refers to small fiber interaction parameters, respectively (Advani and Tucker III, 1990). In addition, so-called composite closures were derived by Hinch and Leal (1976) by mixing the approaches of both weak and strong flow. As reported by, e.g., Chung and Kwon (2002b), the proposed closures can lead to oscillatory behavior and cannot be applied to general flows. Extending the work of Hinch and Leal (1976), Advani and Tucker III

(1990) derived corresponding approximations of the fourth-order fiber orientation tensor without the need to consider the strain-rate tensor in the respective formulation.

Closure approximations can also be formulated based on the definition of fiber orientation tensors. As discussed in Sec. 2.4.1, this definition involves an integral over the unit sphere, which can be computed numerically to obtain the tensorial information about the fiber orientation as described by, e.g, Advani and Tucker III (1987). Various integration schemes have been proposed for this numerical procedure with a special distribution of integration points on the unit sphere including their weights. [9] Since the complete ODF is usually unknown due to the high computational effort discussed at the beginning of Sec. 1.2.3, so-called reconstruction methods for the ODF with respect to a finite number of known fiber orientation tensors are applied, as described by, e.g., Breuer et al. (2019), Tucker III (2022b), and Tucker III (2022a) (pp. 34–39). The resulting ODF estimate can be used to numerically compute fiber orientation tensors of arbitrary order. It is possible to obtain an approximated ODF based on its series expansion as addressed in Kanatani (1984), Advani and Tucker III (1987), and Onat and Leckie (1988). When orientation tensors of different orders are known, the third-kind formulation of them can be computed following Kanatani (1984) and the series depending on the known orientation tensors can be truncated as illustrated in, e.g., Kanatani (1984) and Advani and Tucker III (1987). Another procedure is given by assuming an interaction-free fiber suspension in the context of the NAT closure with the underlying

[9] For further information the reader is referred to, e.g., Stroud (1971) (Secs. 2.7 and 8.6), Atkinson (1982), and Bažant and Oh (1986). Integration schemes of various orders were proposed by Lebedev (1977), Lebedev and Skorokhodov (1992), Lebedev (1995), and Lebedev and Laikov (1999), which are used throughout this thesis based on the implementation of Parrish (2021). More recently, Goldberg et al. (2017) proposed a numerical integration technique over the unit sphere with the distribution of integration points depending on the ODF.

and so-called canonical distribution function (Verleye and Dupret, 1993; Dupret and Verleye, 1999) as the postulated ODF which corresponds to the angular central Gaussian distribution (ACG) described by Tyler (1987). For the functional form of ACG representing the exact solution for the special case of absent fiber interaction, see also Dinh and Armstrong (1984), Lipscomb II et al. (1988), and Montgomery-Smith et al. (2011a). It should be noted that ACG is also called Jeffery distribution according to Tucker III (2022a) (pp. 36–37) and Tucker III (2022b), where an overview of the relevant literature in this context can also be found. Similarly, the Bingham distribution (Bingham, 1974) can be chosen as an approximate ODF, which is directly related to the maximum entropy method (MEM) of Jaynes (1957), see also Chaubal and Leal (1998), van Gurp (1998), Tucker III (2022b), and Papenfuß (2022). Nabergoj et al. (2022) used an ellipsoid function in view of a function-based reconstruction method for the ODF only dependent on the second-order fiber orientation tensor. The reader is referred to, e.g., Breuer et al. (2019), Tucker III (2022b), and Nabergoj et al. (2022) for a comparison of different methods and for further details. Analytical expressions for ODFs with respect to various material symmetries can be found in Moakher and Basser (2015), which can be used directly to compute the corresponding fiber orientation tensor of arbitrary order.

1.2.3 Short-fiber orientation dynamics [10]

According to Advani and Tucker III (1987), the ODF allows an extensive representation of both the fiber orientation state and the corresponding orientation evolution in flows of short-fiber suspensions. The evolution of the ODF is subject to the Fokker-Planck equation (Fokker, 1914; Planck, 1917) as discussed by, e.g., Akbar and Altan (1992), Férec et al. (2008),

[10] This section consists of parts from Karl et al. (2023a) and Karl and Böhlke (2024). Additional text passages have been added.

Montgomery-Smith et al. (2011a;b), and Lohmann (2016). Together with the studies of, e.g., Mezi et al. (2019a) and Férec et al. (2020), the computationally expensive character of this approach becomes apparent, since in addition to the temporal and spatial discretization, the orientation space represented by the surface of the unit sphere must also be discretized with sufficient accuracy.

The orientation evolution of a single rigid fiber embedded in a Newtonian fluid can be traced back to Jeffery (1922). Regarding a more recent derivation of Jeffery's equation, the reader is referred to Junk and Illner (2007). One of the characteristics of the motion of a single fiber is its periodic behavior, called Jeffery orbits, as described by, e.g., Ingber and Mondy (1994). In the context of Jeffery's equation, Bretherton (1962) and Giesekus (1962) describe the reorientation behavior in view of a geometric generalization. Beyond these studies, several reconsiderations of Jeffery's equation were made incorporating narrow gaps, e.g., Perez et al. (2016) and Scheuer et al. (2016), inertia effects, e.g., Einarsson et al. (2014), Einarsson et al. (2015), and Scheuer et al. (2020), non-Newtonian fluids or second-order fluids, e.g., Férec et al. (2017b) referring to, e.g., Leal (1975) and Brunn (1977) in the sense of a generalized formulation, Férec et al. (2017a), Abtahi and Elfring (2019), Férec et al. (2021), and Borzacchiello et al. (2016) or special particle geometries, e.g., Ishimoto (2020a) and Ishimoto (2020b).

Considering the second-order fabric tensor of the first kind proposed by Kanatani (1984), known as the second-order fiber orientation tensor of Advani and Tucker III (1987), the Folgar-Tucker equation, referring to the works of Folgar and Tucker III (1984) and Advani and Tucker III (1987), models the orientation evolution based on Jeffery's model and a diffusion-based phenomenological extension accounting for fiber-fiber interaction. A so-called fiber interaction parameter was introduced to model the strength of fiber-fiber interaction. This parameter is typically selected accounting for the fiber aspect ratio and the fiber volume

fraction as addressed in Bay (1991) (pp. 117–120) and Phan-Thien et al. (2002). Using a potential-based modeling, Latz et al. (2010) derived an evolution equation for the second-order fiber orientation tensor containing a so-called collision tensor. It should be noted that the collision tensor consists of two opposing mechanisms: Diffusion as a driving force towards an isotropic state and the nematic part forcing an alignment. The diffusion part of Latz' model refers to the interaction term of the Folgar-Tucker equation.

As described by Wang et al. (2008), the rate of reorientation of real fiber suspensions is overestimated by Jeffery's model. Following a phenomenological approach of slowing down the evolution of the eigenvalues of the orientation tensor by an additional scalar parameter, the reduced-strain closure model (RSC) was derived by Wang et al. (2008). This model refers to a modified Folgar-Tucker equation accounting for the so-called slow orientation kinetics. In addition, Wang et al. (2008) derived a corresponding evolution equation at the level of the Fokker-Planck equation to describe the slowed-down evolution of the ODF.

Phelps and Tucker III (2009) introduced the anisotropic rotary diffusion model both without (ARD) and with (ARD-RSC) consideration of slow orientation kinetics in the context of Wang et al. (2008). Based on the fact that long fibers interact differently with each other compared to short fibers, Phelps and Tucker III (2009) modeled the so-called anisotropic interaction based on a phenomenological approach depending on the second-order fiber orientation tensor, the strain-rate tensor, and fitted scalar parameters. In order to contribute to a more general application of the ARD model combined with slow orientation kinetics, Tseng et al. (2013) proposed a combination of an improved anisotropic rotary diffusion model (iARD) with a retardant principal rate model (RPR), both depending on two parameters to be fitted. This model is abbreviated with iARD-RPR. The algebraic complexity of the ARD model of Phelps

and Tucker III (2009) was reduced, but at the cost of violating the principle of material objectivity. Regarding the principle of material objectivity, reference is made to, e.g., Truesdell and Noll (1965) (pp. 41–47). As described by Tseng et al. (2013), the proposed iARD-RPR model is capable of predicting the so-called core-shell structure for a center-gated disk flow with respect to experimental data. Tseng et al. (2016) derived an objective correction of the iARD model (o-iARD) also leading to the well-known core-shell structure observed in measurements. A further development based on the work of Phelps and Tucker III (2009) can be found in the study of Tseng et al. (2018) proposing the principle anisotropic rotary diffusion model (pARD). The idea behind is to model the anisotropic interaction based on a second-order tensor sharing the eigensystem with the second-order orientation tensor. The results show that measured orientation states can be well predicted based on a combination with the RPR model, which is called pARD-RPR model.

Kugler et al. (2020a) used the pARD-RPR model and proposed a flow-dependent evolution equation for the second-order fiber orientation tensor. Their model is based on an interpolation between the model optimized for a shear flow and the model optimized for an elongational flow. In this context, the importance of flow-type-dependent orientation models for the prediction of fiber orientation evolution in injection molding, which is characterized by complex flow kinematics, is also addressed by Chen et al. (2019a;b). The study of Favaloro and Tucker III (2019) compares several ARD models, including those previously described. Parameter maps are provided regarding the asymptotic orientation state of the second-order fiber orientation tensor evolving in a simple shear flow.

Kugler et al. (2020b) provide an overview of models for the description of the evolution of the second-order fiber orientation tensor. In view of predicting the orientation behavior of single fibers, the numerical method of smooth particle hydrodynamics is also addressed by Kugler

et al. (2020b). [11] This method serves as a way to calibrate the parameters of phenomenological orientation models, as is done by, e.g., Meyer et al. (2020).

In light of single fiber considerations, Férec et al. (2009) studied the orientation evolution at the averaged level of the second-order orientation tensor depending on both hydrodynamic and direct interaction of the embedded single fibers. In this context, so-called interaction tensors of second and fourth order were derived and both a linear and quadratic closure approach were used for the fourth-order interaction tensor. The work of Férec et al. (2014) builds on Férec et al. (2009) and proposed an orthotropic fitted closure for the fourth-order interaction tensor. Also Wittemann et al. (2021) used the averaged orientation tensor description for modeling the orientation evolution and considered hydrodynamic and direct interaction of the embedded fibers, namely the effects of drag, lift, friction, and lubrication.

Gilormini and Chinesta (2019) studied anisotropy effects on the evolution behavior of rod-like particles. They developed a dumbbell model for slender fibers embedded in an anisotropic suspension. This anisotropy represents the hydrodynamic interaction between the fibers arising with an increasing fiber volume fraction. In their approach they used the viscous drag force in an incompressible suspension with fiber-induced orthotropic material symmetry for modeling the hydrodynamic interaction. The micromechanical model of Mori and Tanaka (Mori and Tanaka, 1973; Benveniste, 1987) and the IBOF closure developed by Chung and Kwon (2002b) was used. The results of Gilormini and Chinesta show distinct differences between the classical Jeffery model (Jeffery, 1922; Junk and Illner, 2007) and the proposed anisotropic orientation model. The latter causes a stronger alignment with an increasing fiber volume

[11] Introduced by Gingold and Monaghan (1977) and Lucy (1977), smooth particle hydrodynamics represents a mesh-free Lagrangian approach for the simulation of continuum mechanical problems.

fraction (moderate) and an increasing fiber aspect ratio (distinct) in the shear direction compared to the Jeffery model. In addition, the 2D case is briefly addressed referring to the work of Fletcher (2009) with the result, that in 2D the anisotropy of the surrounding fluid does not affect the spin of the embedded fiber.

Favaloro (2020), on the other hand, used the mean-field approaches of Reuss (1929) and of Mori and Tanaka (Mori and Tanaka, 1973; Benveniste, 1987) to describe the motion of a single fiber embedded in an anisotropic fiber suspension. Based on this single-fiber consideration, the corresponding evolution equation for the second-order orientation tensor was derived by means of upscaling. Favaloro found that, in contrast to the Reuss model depending on the particle number, the Mori-Tanaka model leads to an additional term that scales with the fiber volume fraction and is in this sense consistent with the interaction models of Férec et al. (2009) and Férec et al. (2014). The results for a shear flow show the same behavior as the model of Gilormini and Chinesta (2019), namely that the consideration of the fiber volume fraction leads to a more pronounced alignment. In addition, it is shown by Favaloro (2020) that the derived orientation evolution equations can be easily modified by an additional parameter similar to the RSC model of Wang et al. (2008) to account for slower orientation dynamics.

The study of Favaloro (2020) is mainly based on the work of Wetzel and Tucker III (2001) with the underlying PhD thesis of Wetzel (1999). Wetzel and Tucker III (2001) studied the deformation of an ellipsoidal Newtonian droplet embedded in a Newtonian matrix fluid for the first time in 3D. They used the compact localization tensor notation which is related to the basis of mean-field homogenization: Eshelby's single inclusion problem (Eshelby, 1957; 1959). It should be noted that the approach of Wetzel and Tucker covers arbitrary flow conditions and fluid viscosities under Stokes flow conditions and neglects interfacial tension of the considered ellipsoidal droplet. In earlier works, e.g., Bilby

et al. (1975), Howard and Brierley (1976), and Bilby and Kolbuszewski (1977) the results of Eshelby were applied for special flows and under geometric restrictions of the droplet. A remarkable finding of Wetzel and Tucker is the mean-field based derivation of Jeffery's equation (Jeffery, 1922; Junk and Illner, 2007) assuming a rigid spheroidal particle and the localization tensor of the dilute distribution, which is given in, e.g., Tucker III and Liang (1999).

The publication of Ponte Castañeda (2021) generalizes, e.g., the work of Avazmohammadi and Ponte Castañeda (2015) in the context of the Hashin-Shtrikman-Willis approach referring to Hashin and Shtrikman (1963) and Willis (1977), which was formulated by Ponte Castañeda and Willis (1995), in order to describe the orientation and shape evolution of deformable ellipsoidal particles with different distributions and geometries. The embedded particles are considered viscoelastic or elasto-viscoplastic, whereas the fluid can show Newtonian or viscoplastic behavior. Since this thesis is not focused on deformable particles, the reader is referred to the literature survey of Ponte Castañeda (2021) for more details on this subject. As stated by Ponte Castañeda (2021), the Jeffery equation follows as a special case for rigid particles in a Newtonian matrix fluid, provided a dilute distribution is assumed, as it was done by Wetzel and Tucker III (2001).

The study of Kailasam and Ponte Castañeda (1998) should also be discussed in this context, which contributes to the constitutive modeling of linear viscous composites subjected to finite deformation. It is stated by Kailasam and Ponte Castañeda (1998) that finite deformation can cause a pronounced evolution of the anisotropic microstructure and that comprehensive modeling at the macroscale involves modeling both the effective anisotropic behavior and the orientation dynamics of the microstructure, the latter being defined by both the distribution and orientation of inclusions or pores. Similar to Ponte Castañeda (2021), the approach is based on deformable inclusions and both their orientation

and distribution are free to evolve. In addition, the presented model is able to account for the evolution of the volume fractions of the phases. The results of Kailasam and Ponte Castañeda (1998) are of particular interest for the present thesis, since they consider the special case of a two-phase linear viscous composite with rigid inclusions and an incompressible matrix fluid. It is shown for the dilute regime and for shear deformation that the inclusion geometry is crucial for the evolution of the orientation angle and that the latter increases periodically for finite particle aspect ratios, which is consistent with, e.g., Ingber and Mondy (1994) referring to Jeffery (1922).

1.3 Contributions and research questions

The following contributions to the three main topics of flow-fiber coupling, closure approximations, and fiber orientation dynamics will be realized and discussed separately in this thesis in order to make the respective effects accessible individually. In other words, the simultaneous consideration of flow-fiber coupling, novel closure approximations, and a proposed fiber orientation evolution model is not part of this thesis, as the goal is to investigate the individual effects in a fundamental way.

1.3.1 Flow-fiber coupling [12]

Since the fiber orientation dynamics depend on the flow field, flow-fiber coupling plays a crucial role in the context of the anisotropic viscosity of fiber suspensions. The prediction of fiber orientation dynamics during mold-filling requires a comprehensive understanding of the flow-fiber coupling effects. In the context of the state of the art in this field, which is

[12] This section consists of parts from Karl et al. (2023b). Additional text passages have been added.

addressed in Sec. 1.2.1, the following research questions are formulated:

- It is not fully understood how flow-fiber coupling in mold-filling simulation affects the stress field in the solid composite under load based on the final elastic properties after fluid-solid transition. With this in mind, what is the role of the rheological model for the matrix fluid in a quantifiable context?
- How can the coupled flow-fiber simulation be stabilized to account for the full viscous anisotropy of the fiber suspension and relevant fiber volume fractions and aspect ratios?

The applied procedure corresponds to that of a virtual process chain, such as that used by, e.g., Buck et al. (2015), Zaidani et al. (2015), Görthofer et al. (2019), Gajek et al. (2021), and Meyer et al. (2023). Such a procedure consists of, i.a., a mold-filling or process simulation of the viscous fiber suspension and the use of the generated orientation data for modeling the anisotropic elastic behavior in a solid composite simulation. From a methodological point of view, the mold-filling simulation in the present thesis refers to an isothermal, two-phase finite volume approach without modeling the phase transition from fluid to solid in order to focus purely on the effects of anisotropic viscosity. Furthermore, the effects of Newtonian and non-Newtonian polymer matrix behavior are investigated and compared. For the solid composite simulation, the finite element method is chosen and the entire process is modeled micromechanically unified based on mean-field homogenization, both for the fiber suspension and for the solid composite. In addition, a detailed analysis of the two-phase mold-filling simulation effects on the local fiber orientation with respect to the alternative steady-state approach is provided. Besides well-known methods to handle numerical instabilities, such as implicit discretization and under-relaxation, the method of spatially restricting the flow-fiber coupling is proposed.

Based on a detailed quantifying analysis of the results, which is based on the mold-filling simulation of a generic rib geometry, the distinct effects of flow-fiber coupling and the modeling of the matrix fluid on the stress field in the solid composite under load become apparent. These effects are caused by the deviations in the fiber orientation field, which also strongly depend on the modeling approach and justify the necessity of simulating the actual mold-filling.

1.3.2 Closure approximations [13]

The present thesis is focused on the averaging concept of fiber orientation tensors referring to Kanatani (1984) and Advani and Tucker III (1987) for describing the anisotropic microstructure of viscous short-fiber suspensions and solid short-fiber reinforced composites. As stated in Sec. 1.2.2, a proper closure method has to be used in order to approximate the fourth-order orientation tensor with the known second-order orientation tensor. In the context of the state of the art in the field of closure approximations discussed in Sec. 1.2.2, the following research questions are formulated:

- How can the simple concept of the quadratic closure be maintained and its drawbacks overcome to obtain more reliable predictions of orientation evolution and estimates of effective anisotropic properties?
- Since the tensorial closures all depend explicitly on the known second-order orientation tensor, the question is how to propose an alternative concept based on the necessary properties and relations between the second- and fourth-order fiber orientation tensor?

[13] This section consists of parts from Karl et al. (2021b) and Karl et al. (2023a). Additional text passages have been added.

From a methodological point of view, symmetrization is used to formulate two versions of a novel normalized fully symmetric quadratic closure. The first version improves the reconstruction of orientation data and the estimation of the effective viscous and elastic properties. The second version is formulated in terms of a process-dependent closure function approach to be used in the Folgar-Tucker equation describing the orientation evolution of the second-order fiber orientation tensor. The first version thus refers to the classical closures, while the second version refers to an approximation of the entire second-order closure term arising in the evolution equation of the second-order fiber orientation tensor similar to the approach of Hinch and Leal (1976). In this context, additional reference is made to Advani and Tucker III (1990). The previous works by Doi (1981), Marrucci and Grizzuti (1984), Kröger et al. (2008), and Kim et al. (2015) are joined by the first version of the proposed fully symmetric quadratic closure. In addition, a novel closure approximation method for fiber orientation tensors is proposed, namely the fully symmetric implicit closure. The implicit nature of this closure is due to the use of an unknown closure tensor which has to be determined with the known second-order orientation tensor. The core of the new implicit closure concept is the contraction condition (Advani and Tucker III, 1987) and since the novel approach is formulated in a fully symmetric way, all necessary algebraic properties are fulfilled. Both the quadratic and the hybrid formulation of the novel closure approach can be reduced to a 1D non-linear equation, whose unique solution is simple to determine. Besides both the quadratic and hybrid formulation of the novel closure method, any fully symmetric implicit extensions are possible in the proposed closure approach. It is shown that both considered fully symmetric implicit closures share the property of induced oscillations in a simple shear flow. This behavior is no coincidence, as both implicit closures may be rigorously shown to approximate the MEM. The second version of the symmetric quadratic closure, on the other hand, shows no oscillations in a simple shear

flow and improves the orientation prediction compared to the common quadratic closure. For an infinite aspect ratio, the respective orientation prediction is almost identical to the IBOF-related results. The estimation of anisotropic properties shows that both considered examples of implicit closures are superior to the first version of the novel symmetric quadratic closure. Due to the well-converging 1D formulation of both implicit closures, the computational effort of the implicit closures is in the order of magnitude of the IBOF closure, while here the symmetric quadratic closure is superior to the IBOF closure by an order of magnitude.

1.3.3 Short-fiber orientation dynamics [14]

The present work aims at a micromechanically consistent approach for anisotropic fiber suspensions. This includes the consideration of anisotropy in the evolution equation of fiber orientation tensors and builds on the flow-fiber coupling and the inherent closure problem of the tensorial approach. In the context of the state of the art in the field of fiber orientation dynamics discussed in Sec. 1.2.3, the following research questions are formulated:

- It is an open question how to account for the anisotropic microstructure of fiber suspensions in general in the evolution equation of fiber orientation tensors. In this context, what is the formulation for the general even-order tensor to describe the evolution of higher statistical moments of the orientation distribution function?
- What is the effect of different mean-field models that are used to take microstructure information into account in the evolution equation for the fiber orientation tensor and which models are suitable for use in engineering practice?

[14] This section consists of parts from Karl and Böhlke (2024). Additional text passages have been added.

- How can the spatial distribution of the fibers be taken into account in the evolution equation of the fiber orientation tensor and how does this affect the prediction of the orientation evolution?

Based on a linear homogenization approach, the evolution equation of the fiber orientation tensor is formulated taking into account the anisotropic viscosity in such a way that variable mean-field models are applicable for the localization relations. From the point of view of a single fiber, this corresponds to a hydrodynamic interaction between the fiber and its environment, referring to an anisotropic suspension. The derived interaction term, representing the anisotropic environment of a single fiber, is discussed as a micromechanical convergence criterion of the underlying integral operator. In this context, the works of Wetzel (1999), Wetzel and Tucker III (2001), Gilormini and Chinesta (2019), and Favaloro (2020) are generalized. Specifically, the orientation evolution equations for four different mean-field models are specified and compared for a simple shear flow. The fiber orientation tensor evolution equation is formulated for arbitrary even order, which is an additional algebraic generalization. The studies of Hill (1999), Böhlke (2006), and Papenfuß (2019) are put into a new context in the sense of considering the anisotropic viscosity of the fiber suspension in this equation of arbitrary even order. In particular, it is shown how Jeffery's equation (Jeffery, 1922; Junk and Illner, 2007) and the Folgar-Tucker equation (Folgar and Tucker III, 1984; Advani and Tucker III, 1987) for the orientation tensor of arbitrary even order follow from the general mean-field approach by proving the equivalence with the single fiber formulation of Wetzel (1999) and Wetzel and Tucker III (2001). Based on the micromechanical model proposed by Ponte Castañeda and Willis (1995), an equation is presented to describe the evolution of the fiber orientation tensor depending on the spatial distribution of the fibers. In the context of the homogenization approach proposed by Ponte

Castañeda and Willis (1995), the present thesis is related to Kailasam and Ponte Castañeda (1998) and Ponte Castañeda (2021) addressing the effective viscosity including microstructure evolution of composite materials. As one of several selected models, the present thesis also uses the approach of Ponte Castañeda and Willis (1995) to describe the microstructure evolution, but in the sense of a generalized approach modeling the fiber orientation tensor dynamics of arbitrary order for fiber suspensions, taking into account the anisotropy of the fiber suspension. The consideration of the spatial fiber distribution is clearly evident in the reorientation behavior, and the influence of both the mean-field model and the fiber volume fraction is noticeable. It can be seen that the micromechanically derived interaction term cannot suppress the periodic orientation dynamics. Furthermore, the computational effort differs significantly depending on the chosen mean-field model, which is due to the fact that a formulation without numerical integration over the unit sphere is generally not ensured. Depending on the chosen mean-field model, the closure problem requires either a reconstruction of the orientation distribution function or the use of common approaches to approximate the unknown higher-order fiber orientation tensor.

1.4 Notation and nomenclature

Frequently used acronyms, symbols, and operators are listed below. Multiple meanings are separated by semicolons. In the present thesis, a symbolic tensor notation is mainly used and the index notation, if used, refers to a Cartesian coordinate system.

Symbolic tensor notation

$a, b, A, B, \ldots$	Latin scalars
$\alpha, \beta, \gamma, \ldots$	Greek scalars

$\boldsymbol{a}, \boldsymbol{b}, \boldsymbol{c}, \ldots$	Vectors
$\boldsymbol{A}, \boldsymbol{B}, \boldsymbol{C}, \ldots$	Latin second-order tensors
$\boldsymbol{\sigma}, \boldsymbol{\varepsilon}, \boldsymbol{\Omega}, \ldots$	Greek second-order tensors
$\mathbb{A}, \mathbb{B}, \mathbb{C}, \ldots$	Fourth-order tensors
$\mathbb{A}_{\langle n \rangle}, \mathbb{B}_{\langle n \rangle}, \ldots$	Tensors of arbitrary order n

Acronyms

ACG	Angular central Gaussian distribution
ARD	Anisotropic rotary diffusion model
Ca	Capillary number
Co	Courant number
DD	Dilute distribution model
DS	Differential scheme
EBOF	Eigenvalue-based optimal fitting closure
EM	Effective medium method
FEC	Fast exact closure
HYB	Hybrid closure
iARD	Improved ARD
IBOF	Invariant-based optimal fitting closure
ISO	Isotropic orientation state
JE	Jeffery model
LIN	Linear closure
MEM	Maximum entropy method
MT	Mori-Tanaka model
NAT	Natural closure
o-iARD	Objective iARD
ODF	Orientation distribution function
ORT	Orthotropic closure
pARD	Principle ARD
PCW	Ponte Castañeda-Willis model
PI	Planar isotropic orientation state

QC	Quadratic closure
Re	Reynolds number
RPR	Retardant principal rate model
RSC	Reduced-strain closure model
SC	Self-consistent model
SIHYB	Symmetric implicit hybrid closure
SIP	Single inclusion problem
SIQ	Symmetric implicit quadratic closure
SQC	Symmetric quadratic closure
TPCP	Three-phase contact point
UD	Unidirectional orientation state
VOF	Volume of fluid method
WLF	Williams-Landel-Ferry model

Sub- and superscripts

$(\cdot)^{A}$	Skew-symmetric part
$(\cdot)_{aniso}$	Anisotropic part
$(\cdot)_{c}$	Computational
$(\cdot)_{d}$	Distribution
$(\cdot)^{*}$	Non-dimensional field or operator
$(\cdot)_{expl}$	Explicit discretization
$(\cdot)_{F}$	Fiber
$(\cdot)_{i}$	Inclusion
$(\cdot)_{impl}$	Implicit discretization
$(\cdot)_{M}$	Matrix
$(\cdot)_{p}$	Pressure
$(\cdot)_{ref}$	Reference value
$(\cdot)_{0}$	Reference placement or value; initial value
$(\cdot)_{rel}$	Relative value
$(\cdot)_{sr}$	Spatially restricted
$(\cdot)_{susp}$	Suspension

$(\cdot)^{\mathsf{S}}$	Symmetric part
$(\cdot)_{\mathsf{trans}}$	Transition
$(\cdot)^{\mathsf{ur}}$	Under-relaxed
$(\cdot)_{\mathsf{v}}$	Viscous

Latin letters

a	Abbreviation in 1D SIHYB; periodic function
A	Scalar factor in derivation of SQC
A_1, A_2	Parameters WLF model
b	Abbreviation in 1D SIHYB; periodic function
b_i	Coefficients orientation average
c	Volume fraction
C_{I}	Fiber interaction coefficient
d	Distance; spatial dimension
D	Diffusion on unit sphere
D_1, D_2	Parameters WLF model
e	Specific internal energy; error measures
E	Young's modulus
f	ODF; function implicit closures
g	Function boundary condition; function 1D SIHYB
G	Shear modulus
h	Channel height; function polarization tensor
$J_{\mathcal{S}}$	Jacobian determinant reorientation
k	Parameter hybrid closure
K	Bulk modulus
m	Parameter Cross model
n	Tensor order; number of phases; Parameter Cross model; time index; iteration index
N_{p}	Particle number
p	Pressure
p_η	Specific entropy production

P_i	Abbreviations components polarization tensor
r	Relaxation factor
s	Abbreviation in implicit closures
t	Time
T	Period length Jeffery model
v_{b}	Bulk velocity
w	Specific internal heat source
W	Dissipation
W^*	Complementary dissipation
$\boldsymbol{b}$	Specific body force
$\boldsymbol{c}$	Abbreviation in angular momentum
$\boldsymbol{d}$	Tensile direction; shear direction
$\boldsymbol{e}_i$	Cartesian basis vectors
$\boldsymbol{f}$	Flow-fiber coupling term
$\boldsymbol{g}$	Green's function
$\boldsymbol{n}$	Normal vector; normal direction on unit sphere
$\boldsymbol{p}$	Shear plane normal; direction on unit sphere
$\boldsymbol{q}$	Heat flux
$\boldsymbol{r}$	Reference vector in angular momentum
$\boldsymbol{r}_i$	Right eigenvectors
$\boldsymbol{t}$	Stress vector
$\boldsymbol{u}$	Displacement field
$\boldsymbol{v}$	Velocity field
$\boldsymbol{x}$	Actual placement
$\boldsymbol{X}$	Reference placement
$\boldsymbol{A}$	Arbitrary microstructure tensor
$\boldsymbol{B}$	Implicit closure tensor
$\boldsymbol{B}_i$	Basis tensors normalized Voigt notation
$\boldsymbol{C}$	General sym. pos. semi-def. tensor
$\boldsymbol{D}$	Strain-rate tensor
$\boldsymbol{E}$	Green strain tensor
$\boldsymbol{F}$	Deformation gradient; function implicit closures

$\boldsymbol{F}_{\mathcal{S}}$	Reorientation gradient on unit sphere
$\boldsymbol{G}$	Green's function; general function; closure tensor of ACG and MEM
$\boldsymbol{H}$	Displacement gradient
$\boldsymbol{I}$	Second-order identity tensor
$\boldsymbol{I}_{(2)}$	Second-order identity tensor in 2D
$\boldsymbol{K}$	Abbreviation in polarization tensor
$\boldsymbol{L}$	Velocity gradient
$\boldsymbol{N}$	Second-order fiber orientation tensor
$\boldsymbol{Q}$	Orthogonal tensor
$\boldsymbol{R}$	Right-hand side Folgar-Tucker equation
$\boldsymbol{S}$	Symmetric tensor; abbreviation in IBOF closure
$\boldsymbol{W}$	Spin tensor
$\boldsymbol{Z}$	Shape tensor of inclusion
$\mathbb{A}$	Strain-rate concentration or localization tensor
$\mathbb{B}$	Viscous stress concentration or localization tensor
$\mathbb{B}_{ij}$	Basis tensors normalized Voigt notation
$\mathbb{C}$	Stiffness tensor
$\delta\mathbb{C}$	Stiffness tensor difference
$\mathbb{E}$	Eshelby tensor
$\mathbb{H}$	Abbreviation in polarization tensor
$\mathbb{F}$	Fluidity tensor; closure function
$\mathbb{G}$	General function
$\mathbb{I}$	Fourth-order identity tensor
$\mathbb{I}^{\mathsf{S}}$	Identity on symmetric second-order tensors
$\mathbb{I}^{\mathsf{A}}$	Identity on skew-sym. second-order tensors
$\mathbb{J}_{\mathsf{F}}$	Jeffery tensor
$\mathbb{N}$	Fourth-order fiber orientation tensor
$\mathbb{P}_1$	Identity on spherical second-order tensors
$\mathbb{P}_2$	Identity on deviatoric second-order tensors
$\mathbb{P}_0, \mathbb{P}_{\mathsf{i}}$	Polarization tensor of inclusion
$\mathbb{P}_{\mathsf{d}}$	Polarization tensor of distribution

$\mathbb{R}$	Abbreviation in MT; reduction tensor
$\mathbb{T}$	General transversely isotropic tensor
$\mathbb{V}$	Viscosity tensor
$\delta\mathbb{V}$	Viscosity tensor difference
$\mathbb{D}_{\langle n \rangle}$	Diffusion tensor of order n on unit sphere
$\mathbb{N}_{\langle n \rangle}$	Fiber orientation tensor of order n

Greek letters

α	Fiber aspect ratio
β_i	Coefficients IBOF closure
$\dot{\gamma}$	Shear rate
δ	Parameter flow regime
δ_{ij}	Kronecker delta or components of $\boldsymbol{I}$
ϵ	Parameter flow regime
η	Specific entropy; information theoretic entropy
η_0, η_2, η_3	Coefficients MEM approximation
θ	Temperature
ϑ	Angle
κ	Curvature; parameter SQC; parameter RSC
κ_i	Non-negative real numbers
λ_i	Eigenvalues of $\boldsymbol{N}$
μ_{v}	Volume or bulk viscosity
μ_{s}, μ	Shear viscosity
μ_0	Newtonian viscosity Cross model
μ_i	Eigenvalues of $\boldsymbol{B}$
ν	Poisson's ratio; kinematic viscosity
ν_0	Kinematic viscosity Cross model
ξ	Shape factor Folgar-Tucker equation
ρ	Mass density
σ	Surface tension
τ^*	Parameter Cross model

φ	Angle
ψ	Helmholtz free energy; phase parameter VOF
$\boldsymbol{\chi}$	Motion
$\boldsymbol{\chi}_{\mathcal{S}}$	Motion on unit sphere
$\boldsymbol{\varepsilon}$	Infinitesimal strain tensor
$\boldsymbol{\sigma}$	Cauchy stress tensor
$\boldsymbol{\sigma}_{\mathsf{v}}$	Viscous stress tensor
$\boldsymbol{\tau}$	Viscous stress polarization
$\boldsymbol{\Omega}$	Additional spin tensor
$\mathbb{\Gamma}$	Integral operator
$\boldsymbol{\Delta}_{\langle 8\rangle}$	Identity on irreducible fourth-order tensors

Operators, integration areas, and sets

$\boldsymbol{A}\boldsymbol{b}$	Linear mapping: $A_{ij}b_j = c_i$
$\boldsymbol{A}\boldsymbol{B}$	Linear mapping: $A_{ik}B_{kj} = C_{ij}$
$\mathbb{C}[\boldsymbol{B}]$	Linear mapping: $C_{ijkl}B_{kl} = A_{ij}$
$\mathbb{A}\mathbb{B}$	Linear mapping: $A_{ijmn}B_{mnkl} = C_{ijkl}$
$\boldsymbol{a} \times \boldsymbol{b}$	Cross product
$\boldsymbol{A} \cdot \boldsymbol{B}$	Scalar product: $A_{ij}B_{ij} = c$
$\boldsymbol{A} \otimes \boldsymbol{B}$	Dyadic product: $A_{ij}B_{kl} = C_{ijkl}$
$\boldsymbol{A} \square \boldsymbol{B}$	Box product: $A_{ik}B_{lj} = C_{ijkl}$
$\boldsymbol{A} \boxtimes \boldsymbol{B}$	Box-times product: $A_{im}B_{mj} + A_{jm}B_{im} = C_{ij}$
$\boldsymbol{Q} \star \boldsymbol{A}$	Rayleigh product: $A_{ij}(\boldsymbol{Q}\boldsymbol{e}_i) \otimes (\boldsymbol{Q}\boldsymbol{e}_j) = \boldsymbol{B}$
$\det(\cdot)$	Determinant
$\operatorname{div}(\cdot)$	Divergence
$\operatorname{div}_{\mathcal{S}}(\cdot)$	Divergence on unit sphere
$\operatorname{grad}(\cdot)$	Gradient
$\Delta(\cdot)$	Laplacian
$\Delta_{\mathcal{S}}(\cdot)$	Laplacian on unit sphere
$\operatorname{rot}(\cdot)$	Rotation
$\operatorname{skw}(\cdot)$	Skew-symmetric part

$\mathrm{sym}(\cdot)$	Symmetric part
$\mathrm{tr}(\cdot)$	Trace
$(\cdot)^{\circ}$	Spherical part
$(\cdot)'$	Deviatoric or irreducible part
$\dot{(\cdot)}, (\cdot)^{\cdot}$	Material time derivative
$(\cdot)^{\mathsf{T}}$	Transposition
$(\cdot)^{\mathsf{T}_{\mathsf{R}}}$	Transposition of right index pair
$(\cdot)^{\otimes n}$	Dyadic product with result of order n
$\langle\cdot\rangle$	Volume average
$\langle\cdot\rangle_{\mathsf{F}}$	Orientation average
$\bar{(\cdot)}$	Effective field
$\hat{(\cdot)}$	Fluctuation field
$[\![\cdot]\!]$	Jump over singular surfaces
$\|\cdot\|$	Frobenius norm
$\triangle(\cdot)$	Difference field; increment
$v(t)$	Material volume in actual placement
$\partial v(t)$	Boundary of $v(t)$
$\mathrm{d}v$	Volume element of $v(t)$
$\mathrm{d}a$	Surface element of $\partial v(t)$
V	Fixed representative volume element
∂V	Boundary of V
Γ	Singular surface embedded in V
$\mathrm{d}V$	Volume element of V
$\mathrm{d}A$	Surface element of ∂V or Γ
$\mathcal{S}$	Unit sphere
$\mathrm{d}S$	Surface element of $\mathcal{S}$
Inv^{+}	Set of invertible tensors with $\det(\cdot) > 0$
Orth^{+}	Set of orthogonal tensors with $\det(\cdot) = 1$
$\mathbb{R}^d$	d-dimensional real space
SO3	Set of orthogonal tensors
SymDev	Set of symmetric deviatoric tensors

Chapter 2

Fundamentals

Contents overview. As a basis for the following parts of this thesis, the present chapter deals with fundamental kinematic relations and balance equations used in continuum mechanics. In addition, the constitutive modeling of linear viscous fluids and linear elastic solids is presented. The fundamentals of fiber orientation description, fiber orientation dynamics, and the closure problem are also discussed. In particular, the assumptions and fundamental relations of mean-field homogenization limited to short-fiber suspensions are presented.

2.1 Kinematics [1]

The motion of all material points which are related to a considered material volume is described by the function $\boldsymbol{\chi}$. The reference placement of these points at the initial time $t = 0$ is denoted by $\boldsymbol{X}$ and the actual placement refers to $\boldsymbol{x}$, both of which can be computed for a known motion at a given time t as follows

$$\boldsymbol{x} = \boldsymbol{\chi}(\boldsymbol{X}, t), \qquad \boldsymbol{X} = \boldsymbol{\chi}^{-1}(\boldsymbol{x}, t). \tag{2.1}$$

[1] For the fundamental relations presented in this section, reference is made to Gurtin et al. (2010) (Secs. 5, 6, 9, 11, 52.1) , Liu (2002) (Sec. 1), and Haupt (2002) (Sec. 1).

Based on these two formulations, the displacement field $\boldsymbol{u}$ can be defined with respect to the reference and the actual placement, which are also referred to as the Lagrangian and Eulerian parametrization

$$\boldsymbol{u}(\boldsymbol{X},t) = \boldsymbol{\chi}(\boldsymbol{X},t) - \boldsymbol{X}, \qquad \boldsymbol{u}(\boldsymbol{x},t) = \boldsymbol{x} - \boldsymbol{\chi}^{-1}(\boldsymbol{x},t). \tag{2.2}$$

The displacement gradient $\boldsymbol{H}$ is typically computed in the reference placement as follows

$$\boldsymbol{H} = \frac{\partial \boldsymbol{u}(\boldsymbol{X},t)}{\partial \boldsymbol{X}}, \tag{2.3}$$

which is related to the deformation gradient $\boldsymbol{F}$ via

$$\boldsymbol{F} = \frac{\partial \boldsymbol{\chi}(\boldsymbol{X},t)}{\partial \boldsymbol{X}} = \boldsymbol{H} + \boldsymbol{I}, \quad \det(\boldsymbol{F}) > 0. \tag{2.4}$$

The second-order identity tensor is given by $\boldsymbol{I}$ and $\det(\cdot)$ refers to the determinant. With the deformation gradient at hand, the Green strain tensor $\boldsymbol{E}$ can be defined as follows

$$\boldsymbol{E} = \frac{1}{2}(\boldsymbol{F}^{\mathsf{T}}\boldsymbol{F} - \boldsymbol{I}), \tag{2.5}$$

with the alternative formulation based on the displacement gradient by using Eq. (2.4)

$$\boldsymbol{E} = \frac{1}{2}(\boldsymbol{H} + \boldsymbol{H}^{\mathsf{T}} + \boldsymbol{H}^{\mathsf{T}}\boldsymbol{H}). \tag{2.6}$$

The restriction to so-called small deformations is commonly used in continuum mechanics based on the assumption $\|\boldsymbol{H}\| = \sqrt{\boldsymbol{H} \cdot \boldsymbol{H}} \ll 1$, with $\|\cdot\|$ denoting the Frobenius norm. In this context, the Green strain tensor can be approximated properly by $\boldsymbol{E} \approx \boldsymbol{\varepsilon}$ with the so-called infinitesimal strain tensor $\boldsymbol{\varepsilon}$ defined as the symmetric part of the displacement gradient

$$\boldsymbol{\varepsilon} = \operatorname{sym}(\boldsymbol{H}) = \frac{1}{2}(\boldsymbol{H} + \boldsymbol{H}^{\mathsf{T}}). \tag{2.7}$$

Based on the function $\boldsymbol{\chi}$, the velocity field $\boldsymbol{v}$ can be computed as follows with respect to the reference and the actual placement

$$\boldsymbol{v}(\boldsymbol{X},t) = \frac{\partial \boldsymbol{\chi}(\boldsymbol{X},t)}{\partial t}, \qquad \boldsymbol{v}(\boldsymbol{x},t) = \left.\frac{\partial \boldsymbol{\chi}(\boldsymbol{X},t)}{\partial t}\right|_{\boldsymbol{\chi}^{-1}}, \tag{2.8}$$

with $|_{\boldsymbol{\chi}^{-1}}$ indicating the transformation $\boldsymbol{X} = \boldsymbol{\chi}^{-1}(\boldsymbol{x},t)$. The velocity gradient $\boldsymbol{L}$ refers to the actual placement and can be calculated either from the velocity field or from the deformation gradient as follows

$$\boldsymbol{L} = \frac{\partial \boldsymbol{v}(\boldsymbol{x},t)}{\partial \boldsymbol{x}}, \qquad \boldsymbol{L} = \dot{\boldsymbol{F}}\boldsymbol{F}^{-1}. \tag{2.9}$$

In Eq. (2.9), $\dot{\boldsymbol{F}}$ refers to the the material time derivative of the deformation gradient. The velocity gradient can be decomposed into the symmetric strain-rate tensor $\boldsymbol{D} = \mathrm{sym}(\boldsymbol{L})$ and into the skew-symmetric spin tensor $\boldsymbol{W} = \mathrm{skw}(\boldsymbol{L})$ as follows

$$\boldsymbol{D} = \frac{1}{2}(\boldsymbol{L} + \boldsymbol{L}^{\mathsf{T}}), \qquad \boldsymbol{W} = \frac{1}{2}(\boldsymbol{L} - \boldsymbol{L}^{\mathsf{T}}). \tag{2.10}$$

The gradient operator in the actual placement $\partial(\cdot)/\partial\boldsymbol{x}$ is denoted by $\mathrm{grad}(\cdot)$ in the following. Unless otherwise stated, from now on all field quantities refer to the actual placement.

2.2 Balance equations [2]

The following part represents a brief discussion of the standard balance equations used in continuum mechanics. For each balance equation, both the integral formulation and the local form are given. For the sake of brevity, the discussion of singular surfaces is omitted. Further details

[2] For the fundamental relations presented in this section, reference is made to Gurtin et al. (2010) (Secs. 18, 19, 26, 27), Liu (2002) (Secs. 2, 5), and to Haupt (2002) (Secs. 2, 3).

on singular surfaces can be found in, e.g., Liu (2002) (Secs. 2, 5), Haupt (2002) (Secs. 2, 3), and in Gurtin et al. (2010) (Secs. 32, 33).

With respect to the material volume $v(t)$ in the actual placement, the integral form of the mass balance reads as follows with ρ denoting the mass density and with the volume element $\mathrm{d}v$ in the actual placement

$$\frac{\mathrm{d}}{\mathrm{d}t}\int_{v(t)} \rho \,\mathrm{d}v = 0. \tag{2.11}$$

The corresponding local form[3] of the mass balance reads with $\mathrm{div}(\cdot)$ denoting the divergence

$$\dot{\rho} + \rho \,\mathrm{div}(\boldsymbol{v}) = 0 \tag{2.12}$$

and the material time derivative of the mass density is given by

$$\dot{\rho} = \frac{\partial \rho}{\partial t} + \mathrm{grad}(\rho) \cdot \boldsymbol{v}, \tag{2.13}$$

which is computed similarly for all other scalar fields. The integral form of the linear momentum balance reads as follows

$$\frac{\mathrm{d}}{\mathrm{d}t}\int_{v(t)} \rho\boldsymbol{v} \,\mathrm{d}v = \int_{v(t)} \rho\boldsymbol{b} \,\mathrm{d}v + \int_{\partial v(t)} \boldsymbol{\sigma}\boldsymbol{n} \,\mathrm{d}a. \tag{2.14}$$

In the integral equation above, $\boldsymbol{b}$ refers to the specific body force, $\boldsymbol{\sigma}$ represents the Cauchy stress tensor, the outward normal vector on the boundary $\partial v(t)$ is given by $\boldsymbol{n}$, and $\mathrm{d}a$ denotes the surface element of the boundary $\partial v(t)$ in the actual placement. After applying the mass

[3] The derivation of the local form from the integral formulation generally involves three steps. First, the Reynolds transport theorem is used to reformulate the material time derivative of the integral. Second, the divergence theorem is used to transform surface integrals into volume integrals. Third, localization is used to extract the local form of each balance equation from its volume integral formulation. In this context, reference is made to, e.g., Gurtin et al. (2010) (Secs. 4.1, 15.3, 16).

balance, the local form of the balance of linear momentum reads

$$\rho \dot{\boldsymbol{v}} = \rho \boldsymbol{b} + \operatorname{div}(\boldsymbol{\sigma}), \tag{2.15}$$

with the material time derivative of the velocity

$$\dot{\boldsymbol{v}} = \frac{\partial \boldsymbol{v}}{\partial t} + \operatorname{grad}(\boldsymbol{v})\boldsymbol{v}. \tag{2.16}$$

The integral formulation of the angular momentum balance, using the abbreviation $\boldsymbol{c} = \boldsymbol{x} - \boldsymbol{r}$, is as follows, assuming non-polar materials

$$\frac{\mathrm{d}}{\mathrm{d}t} \int_{v(t)} \boldsymbol{c} \times (\rho \boldsymbol{v}) \, \mathrm{d}v = \int_{v(t)} \boldsymbol{c} \times (\rho \boldsymbol{b}) \, \mathrm{d}v + \int_{\partial v(t)} \boldsymbol{c} \times (\boldsymbol{\sigma} \boldsymbol{n}) \, \mathrm{d}a, \tag{2.17}$$

with $\boldsymbol{r}$ representing an arbitrary reference point. The local form of the angular momentum balance reduces to the symmetry of the Cauchy stress tensor when both the mass balance and the linear momentum balance are incorporated

$$\boldsymbol{\sigma} = \boldsymbol{\sigma}^{\mathsf{T}}. \tag{2.18}$$

The integral form of the total energy balance is formulated as follows

$$\begin{aligned} \frac{\mathrm{d}}{\mathrm{d}t} \int_{v(t)} \rho(e + \frac{1}{2} \boldsymbol{v} \cdot \boldsymbol{v}) \, \mathrm{d}v = & \int_{v(t)} \rho w \, \mathrm{d}v + \int_{v(t)} \rho \boldsymbol{b} \cdot \boldsymbol{v} \, \mathrm{d}v \\ & + \int_{\partial v(t)} (\boldsymbol{\sigma} \boldsymbol{n}) \cdot \boldsymbol{v} \, \mathrm{d}a - \int_{\partial v(t)} \boldsymbol{q} \cdot \boldsymbol{n} \, \mathrm{d}a, \end{aligned} \tag{2.19}$$

with the corresponding local form of the total energy balance

$$\rho \dot{e} + \frac{1}{2} \rho (\boldsymbol{v} \cdot \boldsymbol{v})^{\cdot} = \rho w - \operatorname{div}(\boldsymbol{q}) + \rho \boldsymbol{b} \cdot \boldsymbol{v} + \operatorname{div}(\boldsymbol{\sigma}^{\mathsf{T}} \boldsymbol{v}). \tag{2.20}$$

The specific internal energy is represented by e, w refers to specific internal sources of heat, and the heat flux is given by $\boldsymbol{q}$. The balance of internal energy represents one part of the total energy balance above

and its integral formulation reads

$$\frac{\mathrm{d}}{\mathrm{d}t}\int_{v(t)} \rho e \,\mathrm{d}v = \int_{v(t)} \rho w \,\mathrm{d}v - \int_{\partial v(t)} \boldsymbol{q}\cdot\boldsymbol{n}\,\mathrm{d}a + \int_{v(t)} \boldsymbol{\sigma}\cdot\boldsymbol{D}\,\mathrm{d}v. \tag{2.21}$$

The local form of the balance of internal energy reads as follows

$$\rho\dot{e} = \rho w - \mathrm{div}(\boldsymbol{q}) + \boldsymbol{\sigma}\cdot\boldsymbol{D}. \tag{2.22}$$

For the sake of brevity, the kinetic energy balance is omitted since it follows directly by subtracting the internal energy balance from the total energy balance. To close this section, the entropy balance is addressed with its integral formulation

$$\frac{\mathrm{d}}{\mathrm{d}t}\int_{v(t)} \rho\eta \,\mathrm{d}v = \int_{v(t)} \frac{\rho w}{\theta} \,\mathrm{d}v - \int_{\partial v(t)} \frac{\boldsymbol{q}\cdot\boldsymbol{n}}{\theta}\,\mathrm{d}a + \int_{v(t)} \rho p_\eta \,\mathrm{d}v. \tag{2.23}$$

In the equation above, the specific entropy is given by η, the temperature is denoted by θ and the specific entropy production is represented by p_η. It is assumed that the specific entropy supply reads w/θ and that the entropy flux is represented by $\boldsymbol{q}/\theta$. The respective local form of the entropy balance reads as follows

$$\rho\dot{\eta} = \frac{\rho w}{\theta} - \mathrm{div}\Big(\frac{\boldsymbol{q}}{\theta}\Big) + \rho p_\eta. \tag{2.24}$$

The second law of thermodynamics $p_\eta \geq 0$ is commonly considered in the form of the Clausius-Duhem inequality in order to ensure thermodynamically consistent constitutive modeling as proposed by Coleman and Noll (1963). Using both the specific Helmholtz free energy $\psi = e - \eta\theta$ and the internal energy balance, the Clausius-Duhem inequality can be formulated as follows

$$\boldsymbol{\sigma}\cdot\boldsymbol{D} - \rho\dot{\psi} - \rho\dot{\theta}\eta - \frac{1}{\theta}\boldsymbol{q}\cdot\mathrm{grad}(\theta) \geq 0. \tag{2.25}$$

It should be noted that from now on, the modeling is limited to isothermal processes. The total energy balance, the internal energy balance, and the entropy balance are addressed for the sake of completeness.

2.3 Constitutive modeling of fluids and solids

This section presents the basic constitutive equations for linear viscous fluids and linear elastic solids. These constitutive models are applied in this thesis in the context of modeling anisotropic material behavior based on mean-field homogenization. The remainder of this thesis focuses on short-fiber suspensions with fiber-induced anisotropic viscous behavior. A detailed discussion of the modeling of the anisotropic stiffness of short-fiber reinforced composites is not part of this thesis.

2.3.1 Linear viscous fluids [4]

The Cauchy stress tensor of a linear viscous fluid is given by the relation

$$\boldsymbol{\sigma} = -p\boldsymbol{I} + \mathbb{V}[\boldsymbol{D}], \tag{2.26}$$

with the pressure p and the fourth-order viscosity tensor $\mathbb{V}$. The viscosity tensor of a pure fluid can be expressed in terms of the volume or bulk viscosity μ_v and the shear viscosity μ_s as follows

$$\mathbb{V} = 3\mu_\mathrm{v}\mathbb{P}_1 + 2\mu_\mathrm{s}\mathbb{P}_2, \tag{2.27}$$

which is a constant tensor and refers to a so-called Newtonian fluid. The tensor $\mathbb{P}_1$ refers to the identity on spherical second-order tensors and $\mathbb{P}_2$

[4] For the fundamental relations of linear viscous fluids, reference is made to Gurtin et al. (2010) (Secs. 45, 46), Liu (2002) (Sec. 4.2.2), Haupt (2002) (Sec. 5.3), and to Zheng et al. (2011) (Secs. 2.2.1, 2.2.2).

represents the identity on deviatoric second-order tensors. Both tensors are defined as follows with $(\cdot)^{\mathsf{T_R}}$ denoting the transposition $A^{\mathsf{T_R}}_{ijkl} = A_{ijlk}$

$$\mathbb{P}_1 = \frac{1}{3}\boldsymbol{I}\otimes\boldsymbol{I}, \qquad \mathbb{P}_2 = \frac{1}{2}\big(\boldsymbol{I}\square\boldsymbol{I} + (\boldsymbol{I}\square\boldsymbol{I})^{\mathsf{T_R}}\big) - \frac{1}{3}\boldsymbol{I}\otimes\boldsymbol{I}. \tag{2.28}$$

Note that the identity on symmetric second-order tensors $\mathbb{I}^{\mathsf{S}}$

$$\mathbb{I}^{\mathsf{S}} = \frac{1}{2}\big(\boldsymbol{I}\square\boldsymbol{I} + (\boldsymbol{I}\square\boldsymbol{I})^{\mathsf{T_R}}\big) \tag{2.29}$$

is related to $\mathbb{P}_1$ and $\mathbb{P}_2$ via $\mathbb{I}^{\mathsf{S}} = \mathbb{P}_1 + \mathbb{P}_2$. For the special case of incompressibility, the mass balance reduces to the following kinematic constraint for the velocity field

$$\operatorname{div}(\boldsymbol{v}) = 0, \tag{2.30}$$

which is equal to a vanishing trace of the strain-rate tensor $\operatorname{tr}(\boldsymbol{D}) = 0$. As a consequence, the viscous stress tensor $\boldsymbol{\sigma}_{\mathsf{v}}$ given by

$$\begin{aligned}\boldsymbol{\sigma}_{\mathsf{v}} &= \mathbb{V}[\boldsymbol{D}] \\ &= 3\mu_{\mathsf{v}}\mathbb{P}_1[\boldsymbol{D}] + 2\mu_{\mathsf{s}}\mathbb{P}_2[\boldsymbol{D}] \\ &= 3\mu_{\mathsf{v}}\boldsymbol{D}^{\circ} + 2\mu_{\mathsf{s}}\boldsymbol{D}',\end{aligned} \tag{2.31}$$

with the spherical part $\boldsymbol{D}^{\circ}$ and the deviatoric part $\boldsymbol{D}'$ of the strain-rate tensor, simplifies to

$$\boldsymbol{\sigma}_{\mathsf{v}} = 2\mu_{\mathsf{s}}\boldsymbol{D}'. \tag{2.32}$$

Implied by the equation above and the equality $\boldsymbol{D} = \boldsymbol{D}'$, the following reduced viscosity tensor is used for the special case of incompressibility

$$\mathbb{V} = 2\mu_{\mathsf{s}}\mathbb{P}_2. \tag{2.33}$$

From now on, the shear viscosity μ_{s} is denoted by μ. In order to take the so-called non-Newtonian behavior into account, the model of a

generalized Newtonian fluid can be used. This approach is based on the linear structure of the viscous stress tensor, whose shear viscosity is modeled as a function of the shear rate $\dot{\gamma}$

$$\mathbb{V} = 2\mu(\dot{\gamma})\mathbb{P}_2. \tag{2.34}$$

2.3.2 Linear elastic solids [5]

The Cauchy stress tensor of a linear elastic solid is given by the following relation representing Hooke's law in 3D

$$\boldsymbol{\sigma} = \mathbb{C}[\boldsymbol{\varepsilon}], \tag{2.35}$$

with the fourth-order stiffness tensor $\mathbb{C}$. The special case of an isotropic stiffness is uniquely described by two elastic constants as follows

$$\mathbb{C} = 3K\mathbb{P}_1 + 2G\mathbb{P}_2, \tag{2.36}$$

with the compression or bulk modulus K and the shear modulus G. Alternatively, Young's modulus E and Poisson's ratio ν can be used by inserting the following relations in the equation above for the isotropic stiffness tensor

$$K = \frac{E}{3(1-2\nu)}, \qquad G = \frac{E}{2(1+\nu)}. \tag{2.37}$$

Hooke's law for the Cauchy stress tensor restricted to the special case of isotropic elastic behavior reads as follows

$$\boldsymbol{\sigma} = \frac{1}{3}(3K - 2G)\,\mathrm{tr}(\boldsymbol{\varepsilon})\boldsymbol{I} + 2G\boldsymbol{\varepsilon}. \tag{2.38}$$

[5] For the fundamental relations of linear elastic solids, reference is made to Gurtin et al. (2010) (Sec. 52), Liu (2002) (Sec. 4.2.1), and to Haupt (2002) (Sec. 5.4).

2.4 Short-fiber orientation states

This section covers the fundamentals of the mathematical description of fiber orientation as applied in this work. In addition, the associated evolution equation for the fiber orientation state is introduced.

2.4.1 Description of the microstructure [6]

The fiber orientation of a given microstructure is most comprehensively described by the ODF f, which is a probability density function with the following properties according to Advani and Tucker III (1987) and Moakher and Basser (2015)

$$f(\boldsymbol{n}) \geq 0, \qquad \int_{\mathcal{S}} f(\boldsymbol{n}) \, \mathrm{d}S(\boldsymbol{n}) = 1, \qquad f(\boldsymbol{n}) = f(-\boldsymbol{n}). \tag{2.39}$$

The vector $\boldsymbol{n}$ refers to an arbitrary normal direction on the unit sphere $\mathcal{S}$ with the surface element $\mathrm{d}S(\boldsymbol{n})$. It should be noted that the notation $\mathrm{d}S(\boldsymbol{n})$ indicates that $\boldsymbol{n}$ represents the integration variable. As time-varying and inhomogeneous microstructures are considered throughout this work, the function f also depends on the time t and the spatial coordinate $\boldsymbol{x}$, which is not indicated in Eq. (2.39) for clarity. As described by, e.g., Böhlke et al. (2010), Müller and Böhlke (2016), and Bauer and Böhlke (2022b), the function f refers to the infinitesimal volume fraction $\mathrm{d}v/v$ of fibers aligned in the direction $\boldsymbol{n}$

$$\frac{\mathrm{d}v}{v}(\boldsymbol{n}) = f(\boldsymbol{n}) \mathrm{d}S(\boldsymbol{n}). \tag{2.40}$$

In engineering practice, fiber orientation tensors following Kanatani (1984) and Advani and Tucker III (1987) are used to represent moments

[6] This section consists of parts from Karl and Böhlke (2024). Additional text passages have been added.

of the ODF f and refer to a coarse-grained representation of the microstructure. The orientation tensor of the first kind and of arbitrary even order n reads as follows based on Kanatani (1984) and Advani and Tucker III (1987)

$$\mathbb{N}_{\langle n \rangle}(\boldsymbol{x}, t) = \int_{\mathcal{S}} f(\boldsymbol{x}, t, \boldsymbol{n}) \boldsymbol{n}^{\otimes n} \, \mathrm{d}S(\boldsymbol{n}). \tag{2.41}$$

The generalized notation $\boldsymbol{n}^{\otimes n}$ used in Eq. (2.41) represents the dyadic product of the integration variable $\boldsymbol{n}$ which results in a n-th order tensor and is oriented to, e.g., Dupret and Verleye (1999) and Moakher and Basser (2015). A restriction to the second- and fourth-order orientation tensors $\boldsymbol{N}$ and $\mathbb{N}$ in order to reduce the computational effort in engineering practice leads to a loss of microstructure information, since the ODF f is approximated by a truncated series as given in Kanatani (1984) and Advani and Tucker III (1987). This series representation typically refers to the orientation tensors of the third kind for which reference is made to Kanatani (1984). Besides the full index symmetry, the following properties hold for the tensors $\boldsymbol{N}$ and $\mathbb{N}$ as described by Advani and Tucker III (1987)

$$\mathrm{tr}(\boldsymbol{N}) = 1, \qquad \mathbb{N}[\boldsymbol{I}] = \boldsymbol{N}. \tag{2.42}$$

The property $\mathbb{N}[\boldsymbol{I}] = \boldsymbol{N}$ is called the contraction condition and it states that an orientation tensor of arbitrary even order contains the orientation tensor of the next lower even order (Kanatani, 1984). It should be noted that the contraction condition plays an important role in chapter 5 for defining the novel implicit closure approach. As can be seen in the detailed explanations of the properties of orientation tensors provided by Tucker III (2022a) (pp. 22–34), the range of eigenvalues $\lambda_i \in [0, 1]$ of the tensor $\boldsymbol{N}$ defines its positive semi-definiteness which can be transferred to the tensor $\mathbb{N}$.

To close this section, reference is made to the recent publication of Bauer and Böhlke (2022b) for a general parametrization of second- and fourth-order orientation tensors. Both tensors are split up into an isotropic and an anisotropic part. The latter depends on a different number of parameters depending on the given material symmetry. The respective and so-called admissible parameter ranges are analyzed by Bauer and Böhlke (2022b) based on the required algebraic property of positive semi-definiteness. In this context, the special case of planar orientation states is addressed in Bauer and Böhlke (2023) and Bauer and Böhlke (2022a) study the effective anisotropic stiffness of composites based on different planar fiber orientation states compatible with the so-called admissible parameter range.

2.4.2 Short-fiber orientation dynamics [7]

For the sake of brevity, the focus of this section is limited to the evolution of the second-order fiber orientation tensor. Regarding the evolution of the ODF, reference is made to chapter 5 and the orientation dynamics of single fibers are discussed in chapter 6 in the context of a generalized description of the orientation dynamics in view of fiber orientation tensors of arbitrary order.

Throughout the chapters 3 to 5, the orientation evolution is subject to the Folgar-Tucker equation following Folgar and Tucker III (1984) and Advani and Tucker III (1987)

$$\dot{\boldsymbol{N}} = \boldsymbol{W}\boldsymbol{N} - \boldsymbol{N}\boldsymbol{W} + \xi\big(\boldsymbol{D}\boldsymbol{N} + \boldsymbol{N}\boldsymbol{D} - 2\mathbb{F}[\boldsymbol{D}]\big) + 2C_\mathrm{I}\dot{\gamma}(\boldsymbol{I} - 3\boldsymbol{N}). \quad (2.43)$$

In Eq. (2.43), the shape parameter ξ depends on the constant fiber aspect ratio α via $\xi = (\alpha^2 - 1)/(\alpha^2 + 1)$. The intensity of fiber-fiber interaction

[7] This section consists of parts from Karl et al. (2021b), Karl et al. (2023a), and Karl et al. (2023b). Additional text passages have been added.

is represented by the fiber interaction parameter C_I, which is also called interaction coefficient or Folgar-Tucker diffusivity, and $\dot{\gamma} = \sqrt{2\boldsymbol{D} \cdot \boldsymbol{D}}$ refers to the equivalent shear rate. The material time derivative of the second-order fiber orientation tensor reads

$$\dot{\boldsymbol{N}} = \frac{\partial \boldsymbol{N}}{\partial t} + \mathrm{grad}(\boldsymbol{N})\boldsymbol{v}. \tag{2.44}$$

As already discussed in Sec. 1.2.2, the Folgar-Tucker equation is not closed. With respect to the classic closure approach, the closure function $\mathbb{F}$ refers to $\mathbb{F}(\boldsymbol{N})$ in Eq. (2.43), which is addressed in the upcoming Sec. 2.5 in the context of the general closure problem. The general representation of a closure via a function $\mathbb{F}$ is oriented to, e.g., Jack and Smith (2005). It should be noted that in the context of Eq. (2.43), neutrally buoyant, isotropically interacting rigid short fibers are considered embedded in an incompressible matrix fluid without body forces referring to Jeffery (1922), Folgar and Tucker III (1984), and Altan and Tang (1993). In addition, Jeffery (1922) assumed a homogeneous creeping flow of a Newtonian matrix fluid and neglected Brownian motion as addressed in, e.g., Ingber and Mondy (1994).

The material time derivative on the left-hand side of Eq. (2.43) together with the first two terms on the right-hand side constitute an objective rate of the orientation tensor $\boldsymbol{N}$, namely the Jaumann rate. This has already been stated by Petty et al. (1999) referencing Bird et al. (1987). Furthermore, Eq. (2.43) gives the Jaumann rate of the orientation tensor $\boldsymbol{N}$ as an isotropic function of the argument list $\mathcal{L} = \{\boldsymbol{D}, \boldsymbol{N}, \mathbb{N}\}$. Further information on isotropic functions can be found in, e.g., Gurtin et al. (2010) (Sec. 113). The Folgar-Tucker equation (2.43) can be rewritten in the following general form with the function of the right-hand side $\boldsymbol{R}(\mathcal{L})$ and the Jaumann rate of $\boldsymbol{N}$ on the left-hand side

$$\dot{\boldsymbol{N}} - \boldsymbol{W}\boldsymbol{N} + \boldsymbol{N}\boldsymbol{W} = \boldsymbol{R}(\mathcal{L}). \tag{2.45}$$

The aforementioned isotropic specification follows directly $\forall \boldsymbol{Q} \in \mathrm{Orth}^{+}$,

$$\boldsymbol{Q}\star(\dot{\boldsymbol{N}} - \boldsymbol{W}\boldsymbol{N} + \boldsymbol{N}\boldsymbol{W}) = \boldsymbol{R}(\boldsymbol{Q}\star\mathcal{L}), \tag{2.46}$$

which means that actively rotated input arguments $\mathcal{L}$ result in an active rotation of the Jaumann rate of $\boldsymbol{N}$. Regarding this objective rotational rate, reference is made to Zaremba (1903) and Jaumann (1911).

To conclude this section, it should be noted that Hand (1962) derived an evolution equation for a symmetric microstructure tensor whose algebraic formulation is similar to Eq. (2.43) derived by Advani and Tucker III (1987). In contrast to Eq. (2.43), Hand's equation only accounts for the shape parameter $\xi = 1$ and the diffusion term is related to a rotational diffusion coefficient instead of using a proportionality to an interaction parameter and the shear rate as proposed by Folgar and Tucker III (1984). In addition, the trace-preserving property of the derived evolution equation for the tensorial orientation state is addressed by Hand (1962) and compactly reads $\mathrm{tr}(\dot{\boldsymbol{N}}) = 0$.

2.5 Closure problem [8]

As a complement to Sec. 1.2.2, which deals with the state of the art of closure approximations, this section discusses the properties that a closure must fulfill. In addition, the complexity of finding a proper closure is addressed.

Closure approximations seek to approximate the fourth-order fiber orientation tensor $\mathbb{N}$ as a function $\mathbb{F}$ of the second-order fiber orientation tensor $\boldsymbol{N}$

$$\mathbb{N} \approx \mathbb{F}(\boldsymbol{N}). \tag{2.47}$$

[8] This section consists of parts from Karl et al. (2021b) and Karl et al. (2023a). Additional text passages have been added.

Due to the relation $\mathbb{N}[\boldsymbol{I}] = \boldsymbol{N}$ as given in Advani and Tucker III (1987), the second-order fiber orientation tensor may be extracted from the fourth-order fiber orientation tensor. The inverse operation is not well-posed. In particular, there are different second-order fiber orientation tensors realizing one and the same fourth-order fiber orientation tensor. It is noted that a closure is realizable if the value $\mathbb{F}(\boldsymbol{N})$ arises as the fourth moment of an ODF. Different ODFs may lead to an identical $\boldsymbol{N}$ and $\mathbb{N}$, also with a distinct sixth-order orientation tensor $\mathbb{N}_{\langle 6 \rangle}$. This fact is addressed by Tucker III (2022a) (p. 20) stating that every ODF correlates with exactly one second-order fiber orientation tensor and that different ODFs can result in exactly the same second-order fiber orientation tensor. In particular, different ODFs can be based on an indistinguishable second-order fiber orientation tensor (Tucker III, 2022a) (p. 34). The recent study of Bauer et al. (2023) addresses the central question of the realizability of fourth-order orientation tensors. It is shown that for a fully symmetric fourth-order tensor, positive semi-definiteness and the trace condition, which is related to the sum over the eigenvalues, qualify this tensor to be a realizable fourth-order orientation tensor. It should be noted that the result of Bauer et al. (2023) is limited to 2D and 3D and cannot be transferred to higher dimensions. In addition, realizable orientation states in the context of a closure approximation are also addressed by Petty et al. (1999). Following Bauer et al. (2023), the proposed closures in the chapters 4 and 5 are shown to approximate a realizable fourth-order orientation tensor.

In the following, it is discussed which properties of a closure are implied if only full index symmetry and the contraction condition are assumed. According to Advani and Tucker III (1987) a closure function $\mathbb{F}(\boldsymbol{N})$ is needed, which both generates a fully symmetric orientation tensor $\mathbb{N}$ and fulfills the contraction condition $\mathbb{N}[\boldsymbol{I}] = \boldsymbol{N}$. It should be noted that $\boldsymbol{N}$ is seen as the exact second-order orientation tensor fulfilling all necessary algebraic properties, e.g., the trace condition, the symmetry

condition and positive semi-definiteness. The trace condition of the fourth-order orientation tensor $\mathrm{tr}(\mathbb{N}) = \mathbb{N} \cdot (\boldsymbol{I} \square \boldsymbol{I}) = 1$, which refers to a special case of the general expression given in Moakher and Basser (2015), is a direct consequence of both algebraic properties needed for the function $\mathbb{F}(\boldsymbol{N})$. It is clarified that for exact tensors $\boldsymbol{N}$ and $\mathbb{N}$, the trace conditions $\mathrm{tr}(\mathbb{N}) = 1$ and $\mathrm{tr}(\boldsymbol{N}) = 1$ are connected as follows by using the complete index symmetry of $\mathbb{N}$ and the property $\mathbb{N}[\boldsymbol{I}] = \boldsymbol{N}$

$$\begin{aligned} \mathrm{tr}(\mathbb{N}) = \mathbb{N} \cdot \mathbb{I} = N_{ijkl}\delta_{ik}\delta_{lj} = N_{ijij} = N_{iijj} = \boldsymbol{I} \cdot \mathbb{N}[\boldsymbol{I}] \\ = \boldsymbol{I} \cdot \boldsymbol{N} = \mathrm{tr}(\boldsymbol{N}) = 1. \end{aligned} \tag{2.48}$$

In the equation above, the fourth-order identity tensor $\mathbb{I} = \boldsymbol{I} \square \boldsymbol{I}$ is used and δ_{ij} refers to the components of the identity tensor $\boldsymbol{I}$ with $\delta_{ij} = 1$ for $i = j$ and $\delta_{ij} = 0$ for $i \neq j$. In addition, the consistency with the flow $\mathrm{tr}(\mathbb{N}[\boldsymbol{D}]) = \boldsymbol{N} \cdot \boldsymbol{D}$ in the context of the Folgar-Tucker equation (Folgar and Tucker III, 1984; Advani and Tucker III, 1987), which is addressed by Petty et al. (1999), is also fulfilled by imposing $\mathbb{N}[\boldsymbol{I}] = \boldsymbol{N}$ and the full index symmetry

$$\mathrm{tr}(\mathbb{N}[\boldsymbol{D}]) = N_{iikl}D_{kl} = \mathbb{N}[\boldsymbol{I}] \cdot \boldsymbol{D} = \boldsymbol{N} \cdot \boldsymbol{D}. \tag{2.49}$$

It should be noted that the consistency with the flow given in Eq. (2.49) is also addressed by Hinch and Leal (1976) and Linn (2005) and it ensures that the Folgar-Tucker equation preserves the trace of the second-order fiber orientation tensor. As outlined by Advani and Tucker III (1987), if the algebraic properties of different closures match, their individual accuracy remains crucial. This implies that defining a closure that is in line with all essential algebraic properties does not necessarily lead to a sufficient prediction of the orientation evolution or to a sufficient estimation of the anisotropic properties.

To close this section it is noted that regarding the admissible parameter space, Bauer and Böhlke (2022b) investigated LIN proposed by Hand

(1962), ORT referring to Cintra and Tucker III (1995), and the IBOF closure proposed by Chung and Kwon (2002b). In addition, the division of closure approximations into three groups is addressed, namely closures with algebraic assumptions as a background, closures based on material symmetry assumptions, and closures with an assumed ODF.

2.6 Micromechanical modeling of short-fiber suspensions [9]

This section discusses the fundamentals of mean-field homogenization of viscous fiber suspensions, both in terms of the assumptions made and the basic equations. Thus, this section forms the basis for the following chapters, in which the flow-fiber coupling is investigated on a micromechanical basis, novel closure approximations are compared in view of their prediction accuracy with respect to viscous and elastic anisotropy, and a contribution is made to the micromechanical modeling of the reorientation behavior of short fibers. The fundamental relations in Sec. 2.6 refer to previous studies, e.g., Thevenin and Perreux (1996), Kailasam and Ponte Castañeda (1998), Bertóti and Böhlke (2017), Bertóti (2021) (pp. 15–16, 31–33), Ponte Castañeda (2021), and Kammer and Ponte Castañeda (2022). To make this thesis self-contained, an overview of selected literature on mean-field homogenization to predict the anisotropic viscosity of short-fiber suspensions is provided in App. A. In particular, selected literature in the field of solid composites is discussed in App. A, since the various mean-field approaches have been developed primarily to estimate the effective anisotropic elastic properties.

[9] This section, including all of its subsections, represents a rewritten summary of relevant content of Karl and Böhlke (2022), extended by additional text passages and discussing further literature.

2.6.1 Assumptions and scale-bridging relations

Before discussing the scale-bridging relations, the following list summarizes the fundamental assumptions of mean-field homogenization that are assumed to be valid throughout this thesis:

- The microstructure of the short-fiber suspension is assumed to be statistically homogeneous as addressed in, e.g., Hashin (1964; 1965), Willis (1977; 1981), Walpole (1981), and Torquato (2002) (pp. 28–30).
- The ergodic hypothesis which is addressed in, e.g., Hashin (1964; 1965), Willis (1981), and Torquato (2002) (pp. 28–30) is assumed to be valid and only representative volume elements according to, e.g., Hill (1963), Hashin (1964; 1965), Willis (1981), and Walpole (1981) are considered.
- Cracks or voids are excluded, which means that the microstructure is assumed to be coherent according to Hill (1963) or, in other words, both the displacement or velocity field and the stress vector are continuous, as addressed by, e.g., Hashin (1964; 1965).
- The Hill-Mandel condition (Hill, 1963; Mandel, 1980) is assumed to be valid for viscous short-fiber suspensions. Additional reference is made to, e.g., Hill (1967), Huet (1990), and to the upcoming Sec. 2.6.2 where the Hill-Mandel condition is reviewed in detail.
- Only two-phase microstructures are considered, with reference to Hill (1963) and to the special case discussed in, e.g., Walpole (1981). Both the fibers and the matrix are assumed to have constant and isotropic mechanical properties (Hill, 1963). In case of viscous short-fiber suspensions, the spheroidal fibers are considered as rigid bodies similar to, e.g., Kailasam and Ponte Castañeda (1998), Schneider (2016), Bertóti and Böhlke (2017), Ponte Castañeda (2021), Bertóti et al. (2021), Bertóti (2021) (pp. 31–33), Kammer et al. (2022), and Kammer and Ponte Castañeda (2022).

- It is assumed that the constitutive law has the same mathematical structure at the microscale and at the macroscale, such as in, e.g., Hill (1963), Hashin (1964; 1965), Walpole (1969; 1981), and Willis (1977; 1981) for the special case of linear elasticity. In the case of the present work, this means that both the matrix fluid and the short-fiber suspension are modeled as linear viscous similar to, e.g., Thevenin and Perreux (1996), Kailasam and Ponte Castañeda (1998), Bertóti and Böhlke (2017), Bertóti (2021) (pp. 15–16, 31–33), and the special case included in the formulation of Ponte Castañeda (2021).
- The considered short-fiber suspension is assumed to undergo a Stokes flow or creeping flow, as described by, e.g., Schneider (2016), Ponte Castañeda (2021), Kammer et al. (2022), and Favaloro (2020).
- Both the matrix fluid and the fiber suspension are assumed to be incompressible similar to, e.g., Kailasam and Ponte Castañeda (1998), Bertóti and Böhlke (2017), Traxl et al. (2020), Ponte Castañeda (2021), Bertóti et al. (2021), Bertóti (2021) (pp. 15–16, 31–33), and Kammer et al. (2022).
- Short-fiber suspension flows are characterized by an evolving fiber orientation that determines the anisotropic viscous response. For each homogenization step, the fiber orientation state, or in other words the microstructure, is considered as steady-state similar to, e.g., Kailasam and Ponte Castañeda (1998) and Ponte Castañeda (2021).

The following constitutive equations are defined at the microscale of the short-fiber suspension similar to Sec. 2.3.1

$$\boldsymbol{\sigma} = -p\boldsymbol{I} + \mathbb{V}[\boldsymbol{D}], \qquad \boldsymbol{D} = \mathbb{F}[\boldsymbol{\sigma}_{\mathrm{v}}], \tag{2.50}$$

with the fluidity tensor $\mathbb{F} = \mathbb{V}^{-1}$ representing the inverse of the viscosity tensor as described by, e.g., Schneider (2016). Similar to Kailasam and Ponte Castañeda (1998) and Ponte Castañeda (2021), the following dissi-

pations are considered at the microscale for viscous fiber suspensions

$$2W = \boldsymbol{D} \cdot \mathbb{V}[\boldsymbol{D}], \qquad 2W^* = \boldsymbol{\sigma}_{\mathsf{v}} \cdot \mathbb{F}[\boldsymbol{\sigma}_{\mathsf{v}}], \tag{2.51}$$

comparable to the elastic energy consideration of anisotropic composites as described by Hashin (1964). Analogously, the constitutive relations at the macroscale read as follows

$$\bar{\boldsymbol{\sigma}} = -\bar{p}\boldsymbol{I} + \bar{\mathbb{V}}[\bar{\boldsymbol{D}}], \qquad \bar{\boldsymbol{D}} = \bar{\mathbb{F}}[\bar{\boldsymbol{\sigma}}_{\mathsf{v}}], \tag{2.52}$$

whereby all occurring quantities $\bar{(\cdot)}$ are referred to as effective quantities with the corresponding dissipations at the macroscale

$$2\bar{W} = \bar{\boldsymbol{D}} \cdot \bar{\mathbb{V}}[\bar{\boldsymbol{D}}], \qquad 2\bar{W}^* = \bar{\boldsymbol{\sigma}}_{\mathsf{v}} \cdot \bar{\mathbb{F}}[\bar{\boldsymbol{\sigma}}_{\mathsf{v}}]. \tag{2.53}$$

Following, e.g., Hill (1963) and Walpole (1969; 1981), the fourth-order localization or concentration tensors $\mathbb{A}$ and $\mathbb{B}$ are used to relate the quantities across the scales and they are applied in the present thesis for the special case of short-fiber suspensions

$$\langle \boldsymbol{D} \rangle_\gamma = \langle \mathbb{A} \rangle_\gamma [\bar{\boldsymbol{D}}], \qquad \langle \boldsymbol{\sigma}_{\mathsf{v}} \rangle_\gamma = \langle \mathbb{B} \rangle_\gamma [\bar{\boldsymbol{\sigma}}_{\mathsf{v}}]. \tag{2.54}$$

The relations in Eq. (2.54) state that the volume-averaged localization tensors $\langle \mathbb{A} \rangle_\gamma$ and $\langle \mathbb{B} \rangle_\gamma$ regarding γ-phase map the effective fields to the local average fields in the γ-phase as given in Hill (1963) and Walpole (1969; 1981). The localization tensors themselves are connected to each other via the effective properties and the properties of the γ-phase

$$\langle \mathbb{A} \rangle_\gamma = \mathbb{F}_\gamma \langle \mathbb{B} \rangle_\gamma \bar{\mathbb{V}}, \qquad \langle \mathbb{B} \rangle_\gamma = \mathbb{V}_\gamma \langle \mathbb{A} \rangle_\gamma \bar{\mathbb{F}}, \tag{2.55}$$

as addressed in, e.g., Hill (1963) and Walpole (1969; 1981) for the case of linear elastic composites.

2.6.2 Hill-Mandel condition [10]

In the following, the Hill-Mandel condition for viscous fiber suspensions is addressed in detail including the consideration of singular surfaces. In this context, reference is made to Hill (1963) and Mandel (1980). For the special case of viscous fiber suspensions, reference is made to, e.g., Traxl et al. (2020) and Bertóti et al. (2021). In particular, the connection to the work of Adams and Field (1991) is emphasized, in which statistically homogeneous and ergodic polycrystals are considered. The dissipation rate formulated in Adams and Field (1991) corresponds to the dissipation $2W$ for fiber suspensions discussed in the present work. The consideration of dissipation is analogous to the consideration of elastic energy, as described by Hashin (1964). The Hill-Mandel condition for viscous suspensions reads

$$2\langle W\rangle = \langle \boldsymbol{\sigma}_{\mathsf{v}} \cdot \boldsymbol{D}\rangle = \langle \boldsymbol{\sigma}_{\mathsf{v}}\rangle \cdot \langle \boldsymbol{D}\rangle, \tag{2.56}$$

or equivalently $\langle \hat{\boldsymbol{\sigma}}_{\mathsf{v}} \cdot \hat{\boldsymbol{D}}\rangle = 0$, with $\hat{(\cdot)}$ denoting fluctuations and $\langle\cdot\rangle$ representing the general volume average. In order to derive Eq. (2.56), the local viscous dissipation $2W$ given in Eq. (2.51) and its volume average $2\langle W\rangle$ are considered

$$2W = \boldsymbol{\sigma}_{\mathsf{v}} \cdot \boldsymbol{D}, \qquad 2\langle W\rangle = \langle \boldsymbol{\sigma}_{\mathsf{v}} \cdot \boldsymbol{D}\rangle. \tag{2.57}$$

The decomposition of the local fields $\boldsymbol{\sigma}_{\mathsf{v}}(\boldsymbol{x}), \boldsymbol{D}(\boldsymbol{x})$ into the volume averages $\langle \boldsymbol{\sigma}_{\mathsf{v}}\rangle, \langle \boldsymbol{D}\rangle$ and the local fluctuations $\hat{\boldsymbol{\sigma}}_{\mathsf{v}}(\boldsymbol{x}), \hat{\boldsymbol{D}}(\boldsymbol{x})$

$$\boldsymbol{\sigma}_{\mathsf{v}} = \langle \boldsymbol{\sigma}_{\mathsf{v}}\rangle + \hat{\boldsymbol{\sigma}}_{\mathsf{v}}, \qquad \boldsymbol{D} = \langle \boldsymbol{D}\rangle + \hat{\boldsymbol{D}}, \tag{2.58}$$

[10] This section consists of parts from Karl and Böhlke (2022). Additional text passages have been added.

leads to the following volume-averaged viscous dissipation by using $\langle \hat{\boldsymbol{\sigma}}_\mathsf{v} \rangle = \mathbf{0}$ and $\langle \hat{\boldsymbol{D}} \rangle = \mathbf{0}$ as a property of a fluctuation field (Hashin, 1964) following from the decomposition given in Eq. (2.58)

$$2\langle W \rangle = \langle \boldsymbol{\sigma}_\mathsf{v} \rangle \cdot \langle \boldsymbol{D} \rangle + \langle \hat{\boldsymbol{\sigma}}_\mathsf{v} \cdot \hat{\boldsymbol{D}} \rangle. \tag{2.59}$$

The volume average of the scalar product of the fluctuation terms $\langle \hat{\boldsymbol{\sigma}}_\mathsf{v} \cdot \hat{\boldsymbol{D}} \rangle$ can be reformulated as follows by applying the product rule, the symmetry of $\hat{\boldsymbol{\sigma}}_\mathsf{v}$ and $\hat{\boldsymbol{D}}$ with the fluctuation of the velocity field $\hat{\boldsymbol{v}}$

$$\begin{aligned} \langle \hat{\boldsymbol{\sigma}}_\mathsf{v} \cdot \hat{\boldsymbol{D}} \rangle &= \langle \hat{\boldsymbol{\sigma}}_\mathsf{v} \cdot \operatorname{grad}(\hat{\boldsymbol{v}}) \rangle \\ &= \langle \operatorname{div}(\hat{\boldsymbol{\sigma}}_\mathsf{v}^\mathsf{T} \hat{\boldsymbol{v}}) \rangle - \langle \hat{\boldsymbol{v}} \cdot \operatorname{div}(\hat{\boldsymbol{\sigma}}_\mathsf{v}) \rangle. \end{aligned} \tag{2.60}$$

To further simplify Eq. (2.60), the balance of linear momentum for viscous suspensions without body forces is considered in the common form without dimensions (Spurk and Aksel, 2020) (p. 110)

$$\frac{\partial \boldsymbol{v}^*}{\partial t^*} + \operatorname{grad}^*(\boldsymbol{v}^*)\boldsymbol{v}^* = -\operatorname{grad}^*(p^*) + \frac{1}{\mathrm{Re}} \operatorname{div}^*(\boldsymbol{\sigma}_\mathsf{v}^*). \tag{2.61}$$

In Eq. (2.61), fields and operations without dimensions are denoted by $(\cdot)^*$, and Re refers to the Reynolds number. Similar to previous studies, e.g., Schneider (2016), Favaloro (2020), Bertóti et al. (2021), and Ponte Castañeda (2021), Stokes flow with $\mathrm{Re} \ll 1$ is considered in the context of this work for which the pressure and the viscous forces are in equilibrium. As a consequence, local accelerations due to changes in time and convective accelerations are neglected. Note that for the latter, also small spatial gradients of the flow are assumed leading to the simplified linear momentum balance with dimensions as given in, e.g., Spurk and Aksel (2020) (p. 112)

$$\operatorname{grad}(p) = \operatorname{div}(\boldsymbol{\sigma}_\mathsf{v}). \tag{2.62}$$

In this context, the parallels of linear elastic solids and linear viscous suspensions are addressed in the literature, e.g., in Kailasam and Ponte Castañeda (1998), Torquato (2002) (pp. 337–338), and Ponte Castañeda (2021), as long as the kinematic constraints are the same for both viscous fiber suspensions and solid composites. Next, the decompositions $p = \langle p \rangle + \hat{p}$ and $\boldsymbol{\sigma}_\mathsf{v} = \langle \boldsymbol{\sigma}_\mathsf{v} \rangle + \hat{\boldsymbol{\sigma}}_\mathsf{v}$ are used in combination with the linearity of $\mathrm{grad}(\cdot)$ and $\mathrm{div}(\cdot)$, leading to the linear momentum balance in terms of averages and fluctuations

$$\mathrm{grad}(\langle p \rangle) + \mathrm{grad}(\hat{p}) = \mathrm{div}(\langle \boldsymbol{\sigma}_\mathsf{v} \rangle) + \mathrm{div}(\hat{\boldsymbol{\sigma}}_\mathsf{v}). \tag{2.63}$$

Since $\langle p \rangle$ and $\langle \boldsymbol{\sigma}_\mathsf{v} \rangle$ are constant, Eq. (2.63) reduces in a trivial way to the linear momentum balance for the fluctuations which has the same form as Eq. (2.62)

$$\mathrm{grad}(\hat{p}) = \mathrm{div}(\hat{\boldsymbol{\sigma}}_\mathsf{v}). \tag{2.64}$$

By inserting Eq. (2.64) into Eq. (2.60) and after applying the product rule again, the volume average of the fluctuation terms reads

$$\begin{aligned} \langle \hat{\boldsymbol{\sigma}}_\mathsf{v} \cdot \hat{\boldsymbol{D}} \rangle &= \langle \mathrm{div}(\hat{\boldsymbol{\sigma}}_\mathsf{v}^\mathsf{T} \hat{\boldsymbol{v}}) \rangle - \langle \hat{\boldsymbol{v}} \cdot \mathrm{grad}(\hat{p}) \rangle \\ &= \langle \mathrm{div}(\hat{\boldsymbol{\sigma}}_\mathsf{v}^\mathsf{T} \hat{\boldsymbol{v}}) \rangle - \langle \mathrm{div}(\hat{\boldsymbol{v}} \hat{p}) \rangle + \langle \hat{p} \, \mathrm{div}(\hat{\boldsymbol{v}}) \rangle. \end{aligned} \tag{2.65}$$

Using the incompressibility condition formulated in terms of velocity fluctuations $\mathrm{div}(\hat{\boldsymbol{v}}) = 0$, Eq. (2.65) can be expressed as follows

$$\begin{aligned} \langle \hat{\boldsymbol{\sigma}}_\mathsf{v} \cdot \hat{\boldsymbol{D}} \rangle &= \langle \mathrm{div}(\hat{\boldsymbol{\sigma}}_\mathsf{v}^\mathsf{T} \hat{\boldsymbol{v}}) \rangle - \langle \mathrm{div}(\hat{\boldsymbol{v}} \hat{p}) \rangle \\ &= \frac{1}{V} \int_V \mathrm{div}(\hat{\boldsymbol{\sigma}}_\mathsf{v}^\mathsf{T} \hat{\boldsymbol{v}}) \, \mathrm{d}V - \frac{1}{V} \int_V \mathrm{div}(\hat{\boldsymbol{v}} \hat{p}) \, \mathrm{d}V. \end{aligned} \tag{2.66}$$

The fixed representative volume element is denoted by V and $\mathrm{d}V$ represents the corresponding integrator. In the next step, the Gaussian integral theorem with the singular surface Γ as given in, e.g., Gurtin et al. (2010) (p. 215) is applied to transform the volume integrals into surface

integrals with the boundary $\partial V \backslash \Gamma$ excluding singular surfaces. The integrator $\mathrm{d}A$ refers to both the singular surface Γ and to the boundary $\partial V \backslash \Gamma$. In the following equation, $[\![\cdot]\!]$ refers to the jump operator defined via $[\![\cdot]\!] = (\cdot)^+ - (\cdot)^-$ as given in, e.g., Gurtin et al. (2010) (p. 209) with $(\cdot)^+$ and $(\cdot)^-$ denoting the volumes separated by the singular surface

$$\begin{aligned}\langle \hat{\boldsymbol{\sigma}}_{\mathsf{v}} \cdot \hat{\boldsymbol{D}} \rangle = \frac{1}{V} \int_{\partial V \backslash \Gamma} (\hat{\boldsymbol{\sigma}}_{\mathsf{v}}^{\mathsf{T}} \hat{\boldsymbol{v}}) \cdot \boldsymbol{n} \, \mathrm{d}A - \frac{1}{V} \int_{\Gamma} [\![\hat{\boldsymbol{\sigma}}_{\mathsf{v}}^{\mathsf{T}} \hat{\boldsymbol{v}}]\!] \cdot \boldsymbol{n} \, \mathrm{d}A \\ - \frac{1}{V} \int_{\partial V \backslash \Gamma} (\hat{\boldsymbol{v}} \hat{p}) \cdot \boldsymbol{n} \, \mathrm{d}A + \frac{1}{V} \int_{\Gamma} [\![\hat{\boldsymbol{v}} \hat{p}]\!] \cdot \boldsymbol{n} \, \mathrm{d}A. \end{aligned} \tag{2.67}$$

To achieve a convenient notation being compatible with the solid mechanics considerations, the stress vectors $\boldsymbol{t}_{\mathsf{v}} = \boldsymbol{\sigma}_{\mathsf{v}} \boldsymbol{n}$ and $\boldsymbol{t}_{\mathsf{p}} = -p\boldsymbol{n}$ representing viscous and pressure forces are introduced leading to

$$\begin{aligned}\langle \hat{\boldsymbol{\sigma}}_{\mathsf{v}} \cdot \hat{\boldsymbol{D}} \rangle &= \frac{1}{V} \int_{\partial V \backslash \Gamma} (\hat{\boldsymbol{t}}_{\mathsf{p}} + \hat{\boldsymbol{t}}_{\mathsf{v}}) \cdot \hat{\boldsymbol{v}} \, \mathrm{d}A - \frac{1}{V} \int_{\Gamma} [\![(\hat{\boldsymbol{t}}_{\mathsf{p}} + \hat{\boldsymbol{t}}_{\mathsf{v}}) \cdot \hat{\boldsymbol{v}}]\!] \, \mathrm{d}A \\ &= \frac{1}{V} \int_{\partial V \backslash \Gamma} \hat{\boldsymbol{t}} \cdot \hat{\boldsymbol{v}} \, \mathrm{d}A - \frac{1}{V} \int_{\Gamma} [\![\hat{\boldsymbol{t}} \cdot \hat{\boldsymbol{v}}]\!] \, \mathrm{d}A. \end{aligned} \tag{2.68}$$

In Eq. (2.68), the addition of the force vectors

$$\boldsymbol{t} = \boldsymbol{\sigma} \boldsymbol{n} = (-p\boldsymbol{I} + \boldsymbol{\sigma}_{\mathsf{v}}) \boldsymbol{n} = \boldsymbol{t}_{\mathsf{p}} + \boldsymbol{t}_{\mathsf{v}} \tag{2.69}$$

is used to obtain a structure like the one commonly used in solid mechanics. The fluctuation term $\langle \hat{\boldsymbol{\sigma}}_{\mathsf{v}} \cdot \hat{\boldsymbol{D}} \rangle$ in Eq. (2.68) depends on the stress vector fluctuations $\hat{\boldsymbol{t}}$ and the velocity fluctuations $\hat{\boldsymbol{v}}$ at the boundary $\partial V \backslash \Gamma$, if cracks and voids are excluded. Therefore, $\boldsymbol{t}$ and $\boldsymbol{v}$ are continuous over Γ leading to a vanishing integral over Γ, since $[\![\boldsymbol{t}]\!] = \boldsymbol{0}$ and $[\![\boldsymbol{v}]\!] = \boldsymbol{0}$ hold. In this context, reference is made to Sec. 2.6.1 where the assumptions of mean-field homogenization are addressed. The remaining integral over

the boundary without singular surfaces $\partial V \backslash \Gamma$

$$\langle \hat{\boldsymbol{\sigma}}_{\mathsf{v}} \cdot \hat{\boldsymbol{D}} \rangle = \frac{1}{V} \int_{\partial V \backslash \Gamma} \hat{\boldsymbol{t}} \cdot \hat{\boldsymbol{v}} \, \mathrm{d}A \tag{2.70}$$

vanishes and consequently Eq. (2.56), which represents the Hill-Mandel condition for viscous suspensions, holds if any of the following four cases hold:

- Homogeneous velocity at the boundary $\partial V \backslash \Gamma$: $\hat{\boldsymbol{v}} = \boldsymbol{0}$ or equivalently $\boldsymbol{v} = \langle \boldsymbol{v} \rangle$ implied by the homogeneous displacement boundary condition described by Hill (1963; 1967) for linear elastic solids.
- Homogeneous stress at the boundary $\partial V \backslash \Gamma$: $\hat{\boldsymbol{t}} = \boldsymbol{0}$ or equivalently $\boldsymbol{t} = \langle \boldsymbol{t} \rangle$ implied by the homogeneous stress boundary condition described by Hill (1963; 1967) for linear elastic solids.
- Periodic boundary conditions as described by, e.g., Suquet (1987) and this implies a periodic field $\hat{\boldsymbol{v}}$ and an anti-periodic field $\hat{\boldsymbol{t}}$ at the boundary.
- Ergodic media in the limit $V \to \infty$: $2\langle W \rangle \to \langle \boldsymbol{\sigma}_{\mathsf{v}} \rangle \cdot \langle \boldsymbol{D} \rangle$ following the argumentation of Hashin (1964) that the contribution of the fluctuations $\langle \hat{\boldsymbol{\sigma}}_{\mathsf{v}} \cdot \hat{\boldsymbol{D}} \rangle$ does not play a role in the context of large representative statistically homogeneous and ergodic volume elements.

Motivated by the Hill-Mandel condition and the accessibility of $\langle \boldsymbol{\sigma}_{\mathsf{v}} \rangle$ and $\langle \boldsymbol{D} \rangle$ over $\partial V \backslash \Gamma$ for the assumptions made, the effective fields are equal to the volume averages as used by, e.g., Kailasam and Ponte Castañeda (1998), Traxl et al. (2020), and Bertóti (2021) (p. 31)

$$\langle \boldsymbol{\sigma}_{\mathsf{v}} \rangle = \bar{\boldsymbol{\sigma}}_{\mathsf{v}}, \qquad \langle \boldsymbol{D} \rangle = \bar{\boldsymbol{D}}, \qquad \langle W \rangle = \bar{W}. \tag{2.71}$$

For polycrystalline materials, Adams and Field (1991) list similar relations as in Eq. (2.71) when appropriate boundary conditions are pre-

scribed. Based on the assumptions made, the equivalence between the volume averages and the effective values of the fields involved for the special case of linear elasticity is also addressed in, e.g., Walpole (1981) and Willis (1981). The derivation of the Hill-Mandel condition does not imply that the viscous stress and the strain rate are constitutively coupled as described by, e.g., Traxl et al. (2020). Equation (2.56) corresponds to the Hill-Mandel condition given in Traxl et al. (2020) and refers to the macroscopic viscous dissipation addressed by Bertóti et al. (2021).

2.6.3 Fundamental mean-field equations

Implied by the equivalence between the volume averages and the effective value of both the viscous stress tensor and the strain-rate tensor given in Eq. (2.71) and by applying the localization relations given in Eq. (2.54), the following expressions

$$\begin{aligned} \langle \boldsymbol{\sigma}_{\mathsf{v}} \rangle &= \langle \mathbb{V}[\boldsymbol{D}] \rangle = \langle \mathbb{V}\mathbb{A} \rangle [\bar{\boldsymbol{D}}] = \bar{\mathbb{V}}[\bar{\boldsymbol{D}}] = \bar{\boldsymbol{\sigma}}_{\mathsf{v}}, \\ \langle \boldsymbol{D} \rangle &= \langle \mathbb{F}[\boldsymbol{\sigma}_{\mathsf{v}}] \rangle = \langle \mathbb{F}\mathbb{B} \rangle [\bar{\boldsymbol{\sigma}}_{\mathsf{v}}] = \bar{\mathbb{F}}[\bar{\boldsymbol{\sigma}}_{\mathsf{v}}] = \bar{\boldsymbol{D}} \end{aligned} \tag{2.72}$$

form the basis for the formulation of the effective viscosity $\bar{\mathbb{V}}$ and the effective fluidity $\bar{\mathbb{F}}$ of an anisotropic short-fiber suspension

$$\bar{\mathbb{V}} = \langle \mathbb{V}\mathbb{A} \rangle = \sum_{\gamma=1}^{n} c_\gamma \mathbb{V}_\gamma \langle \mathbb{A} \rangle_\gamma, \qquad \bar{\mathbb{F}} = \langle \mathbb{F}\mathbb{B} \rangle = \sum_{\gamma=1}^{n} c_\gamma \mathbb{F}_\gamma \langle \mathbb{B} \rangle_\gamma. \tag{2.73}$$

In general, n-phases are considered with the corresponding volume fraction c_γ, the viscosity $\mathbb{V}_\gamma$, and the averaged localization tensor $\langle \mathbb{A} \rangle_\gamma$ of the γ-phase. Equations (2.72) and (2.73) are given analogously for the effective stiffness and compliance of heterogeneous composites in, e.g., Hill (1963) and Walpole (1981) and they are addressed in a similar way for viscous composites or fiber suspensions in, e.g., Kailasam and Ponte Castañeda (1998), Bertóti (2021) (pp. 31–32), and Ponte Castañeda

(2021). Considering only two phases ($n = 2$) and by using the following expressions for the total volume average of the localization tensors $\mathbb{A}$ and $\mathbb{B}$ as given in, e.g., Hill (1963) and Walpole (1969; 1981)

$$\begin{aligned}\langle \mathbb{A} \rangle &= \mathbb{I}^{\mathsf{S}} = c_{\mathsf{M}} \langle \mathbb{A} \rangle_{\mathsf{M}} + c_{\mathsf{F}} \langle \mathbb{A} \rangle_{\mathsf{F}}, \\ \langle \mathbb{B} \rangle &= \mathbb{I}^{\mathsf{S}} = c_{\mathsf{M}} \langle \mathbb{B} \rangle_{\mathsf{M}} + c_{\mathsf{F}} \langle \mathbb{B} \rangle_{\mathsf{F}},\end{aligned} \tag{2.74}$$

the fundamental mean-field equations read as follows

$$\begin{aligned}\bar{\mathbb{V}} &= \mathbb{V}_{\mathsf{M}} + c_{\mathsf{F}} (\mathbb{V}_{\mathsf{F}} - \mathbb{V}_{\mathsf{M}}) \langle \mathbb{A} \rangle_{\mathsf{F}}, \\ \bar{\mathbb{F}} &= \mathbb{F}_{\mathsf{M}} + c_{\mathsf{F}} (\mathbb{F}_{\mathsf{F}} - \mathbb{F}_{\mathsf{M}}) \langle \mathbb{B} \rangle_{\mathsf{F}},\end{aligned} \tag{2.75}$$

with index M indicating the matrix phase and index F indicating the fiber phase. The quantities c_{M} and c_{F} are the volume fractions of the matrix and the fibers, respectively. It should be noted that the relations given in Eq. (2.75) follow the procedure given in, e.g., Kailasam and Ponte Castañeda (1998) and Bertóti (2021) (pp. 31–32) and correspond to the relations for the effective properties of a solid composite given in, e.g., Hill (1963), Willis (1977; 1981), and Walpole (1981). From an algebraic point of view it is appropriate to use the relation for the effective fluidity $\bar{\mathbb{F}}$ given in Eq. (2.75), since the rigid fiber assumption $\mathbb{V}_{\mathsf{F}} \to \infty$ can be applied leading to a vanishing fluidity $\mathbb{F}_{\mathsf{F}}$ of the fiber phase as done by Bertóti (2021) (p. 32–33) and Bertóti et al. (2021)

$$\begin{aligned}\bar{\mathbb{F}} &= \mathbb{F}_{\mathsf{M}} - c_{\mathsf{F}} \mathbb{F}_{\mathsf{M}} \langle \mathbb{B} \rangle_{\mathsf{F}} \\ &= \mathbb{F}_{\mathsf{M}} - c_{\mathsf{F}} \mathbb{F}_{\mathsf{M}} \langle \mathbb{V}\mathbb{A}\bar{\mathbb{F}} \rangle_{\mathsf{F}} \\ &= \mathbb{F}_{\mathsf{M}} - c_{\mathsf{F}} \mathbb{F}_{\mathsf{M}} \mathbb{V}_{\mathsf{F}} \langle \mathbb{A} \rangle_{\mathsf{F}} \bar{\mathbb{F}}.\end{aligned} \tag{2.76}$$

The following explicit expression for the effective fluidity tensor can be derived based on Eq. (2.76)

$$\bar{\mathbb{F}} = \left(\mathbb{I}^{\mathsf{S}} + c_{\mathsf{F}} \mathbb{F}_{\mathsf{M}} \mathbb{V}_{\mathsf{F}} \langle \mathbb{A} \rangle_{\mathsf{F}} \right)^{-1} \mathbb{F}_{\mathsf{M}}, \tag{2.77}$$

which in turn can be converted by inversion into to following expression for the effective viscosity tensor of the short-fiber suspension

$$\bar{\mathbb{V}} = \mathbb{F}_{\mathsf{M}}^{-1}\big(\mathbb{I}^{\mathsf{S}} + c_{\mathsf{F}}\mathbb{F}_{\mathsf{M}}\mathbb{V}_{\mathsf{F}}\langle\mathbb{A}\rangle_{\mathsf{F}}\big). \tag{2.78}$$

After a proper simplification, the following final expression is obtained

$$\bar{\mathbb{V}} = \mathbb{V}_{\mathsf{M}} + c_{\mathsf{F}}\mathbb{V}_{\mathsf{F}}\langle\mathbb{A}\rangle_{\mathsf{F}}, \tag{2.79}$$

which is based on the approximation of the difference $\mathbb{V}_{\mathsf{F}} - \mathbb{V}_{\mathsf{M}} \approx \mathbb{V}_{\mathsf{F}}$ in Eq. (2.75) for the special case of rigid fibers or at least for a high inclusion viscosity compared to the matrix viscosity $\mathbb{V}_{\mathsf{F}} \gg \mathbb{V}_{\mathsf{M}}$.

In the following Sec. 2.6.4, the effective viscosity tensor of the short-fiber suspension given in Eq. (2.79) is specified for selected mean-field models. In this context, the localization relations of the respective references are used and the rigid fiber assumption is applied to further simplify the expressions leading to the provided estimates for the effective anisotropic viscosity tensor of short-fiber suspensions based on mean-field homogenization.

2.6.4 Mean-field models

Before discussing different mean-field models, it is briefly discussed how the anisotropic microstructure can be incorporated into the expression for the effective viscosity tensor given in Eq. (2.79). As already described in, e.g., Walpole (1969), the information about the orientation is represented by the respective average over the inclusion phase in Eq. (2.79). As a consequence, the average over the fiber phase $\langle\cdot\rangle_{\mathsf{F}}$ refers to the so-called orientation average of Advani and Tucker III (1987) for the special case of fiber orientations

$$\langle\mathbb{T}\rangle_{\mathsf{F}} = \int_{\mathcal{S}} \mathbb{T}(\boldsymbol{n}) f(\boldsymbol{n}) \,\mathrm{d}S(\boldsymbol{n}). \tag{2.80}$$

It should be noted that the orientation average over the inclusion phase is often denoted by $\{\cdot\}$ as in, e.g., Walpole (1969), Benveniste (1987), and Ponte Castañeda and Willis (1995). For the special case of a transversely isotropic tensor $\mathbb{T}$, the orientation average given in Eq. (2.80) can be expressed as follows depending on the leading fiber orientation tensors $\boldsymbol{N}$ and $\mathbb{N}$ as described by Advani and Tucker III (1987)

$$\begin{aligned}\langle \mathbb{T} \rangle_{\mathsf{F}} = {} & b_1 \mathbb{N} + b_2 (\boldsymbol{N} \otimes \boldsymbol{I} + \boldsymbol{I} \otimes \boldsymbol{N}) \\ & + b_3 \big(\boldsymbol{N} \square \boldsymbol{I} + (\boldsymbol{N} \square \boldsymbol{I})^{\mathsf{T}_{\mathsf{R}}} + \boldsymbol{I} \square \boldsymbol{N} + (\boldsymbol{I} \square \boldsymbol{N})^{\mathsf{T}_{\mathsf{R}}} \big) \\ & + b_4 \boldsymbol{I} \otimes \boldsymbol{I} + b_5 \mathbb{I}^{\mathsf{S}},\end{aligned} \tag{2.81}$$

with the following relations for the coefficients b_i depending on the components of the tensor $\mathbb{T}$ with respect to $\boldsymbol{e}_1$ as the direction of the symmetry axis

$$\begin{aligned} b_1 &= T_{1111} + T_{2222} - 2T_{1122} - 4T_{1212}, \\ b_2 &= T_{1122} - T_{2233}, \\ b_3 &= T_{1212} + (T_{2233} - T_{2222})/2, \\ b_4 &= T_{2233}, \\ b_5 &= T_{2222} - T_{2233}. \end{aligned} \tag{2.82}$$

The simplified representation (2.81) of Eq. (2.80) cannot be applied in general. Special cases require the ODF instead of using the leading fiber orientation tensors. Such a special case is given for material behavior beyond linear constitutive modeling as described by Tucker III (2022b) with a reference to the works of Pierard et al. (2004) and Doghri and Tinel (2005). As described by Hessman et al. (2021), further special cases arise in the context of orientation averaging when the transversely isotropic material symmetry of the orientation-averaged tensor $\mathbb{T}$ is not given, when multiple materials are involved, or when damage mechanisms of the composite phases are considered.

Various estimating approaches for the effective viscosity $\bar{\mathbb{V}}$ based on selected mean-field models are addressed in the following. These relations can be derived by replacing the stiffness tensor $\mathbb{C}$ by the viscosity tensor $\mathbb{V}$ in the respective localization tensors of the cited works, inserting these localization tensors into the fundamental mean-field equation (2.79), and applying the rigid fiber assumption analogously to, e.g., Bertóti (2021) (p. 32–33) and Bertóti et al. (2021).

The **dilute distribution model (DD)** represents the first mean-field approach addressed here and the corresponding localization tensor given in, e.g., Benveniste et al. (1991) and Tucker III and Liang (1999) reads as follows

$$\mathbb{A}_{\mathsf{SIP}} = \left(\mathbb{I}^{\mathsf{S}} + \mathbb{P}_0^{\mathsf{S}}(\mathbb{V}_{\mathsf{F}} - \mathbb{V}_{\mathsf{M}})\right)^{-1}, \tag{2.83}$$

leading to the related estimation of the effective viscosity tensor

$$\bar{\mathbb{V}} = \mathbb{V}_{\mathsf{M}} + c_{\mathsf{F}}\left\langle \left(\mathbb{P}_0^{\mathsf{S}}\right)^{-1} \right\rangle_{\mathsf{F}}. \tag{2.84}$$

The subscript SIP refers to the single inclusion problem of Eshelby (1957; 1959). The tensor $\mathbb{P}_0^{\mathsf{S}}$ refers to the so-called polarization tensor given in, e.g., Willis (1977; 1981) and Ponte Castañeda and Willis (1995), which depends on the fiber geometry and the matrix properties. The corresponding simplified expressions for the special case of incompressibility are provided in Eqs. (E.19) and (E.20) in App. E.4. Note that the superscript S indicates the symmetric representation of the polarization tensor which is of particular importance in chapter 6.

The **Mori-Tanaka model (MT)** proposed by Mori and Tanaka (1973) uses the following localization tensor given in, e.g., Benveniste (1987) and Tucker III and Liang (1999)

$$\begin{aligned}\langle \mathbb{A}_{\mathsf{MT}} \rangle_{\mathsf{F}} &= \langle \mathbb{A}_{\mathsf{SIP}} \rangle_{\mathsf{F}} \left(c_{\mathsf{M}} \mathbb{I}^{\mathsf{S}} + c_{\mathsf{F}} \langle \mathbb{A}_{\mathsf{SIP}} \rangle_{\mathsf{F}}\right)^{-1} \\ &= \left(c_{\mathsf{F}} \mathbb{I}^{\mathsf{S}} + c_{\mathsf{M}} \langle \mathbb{A}_{\mathsf{SIP}} \rangle_{\mathsf{F}}^{-1}\right)^{-1}\end{aligned} \tag{2.85}$$

and the related estimation of the effective viscosity tensor of the short-fiber suspension reads as follows

$$\bar{\mathbb{V}} = \mathbb{V}_{\mathsf{M}} + \frac{c_{\mathsf{F}}}{c_{\mathsf{M}}} \left\langle \left(\mathbb{P}_0^{\mathsf{S}}\right)^{-1} \right\rangle_{\mathsf{F}}, \tag{2.86}$$

which corresponds to the orientation-averaged expression given in Talbot and Willis (1992) transferred to viscosity, see also Bertóti and Böhlke (2017). The MT model is also used to estimate the effective stiffness of the corresponding solid short-fiber reinforced composite in the following parts of this thesis. Note that in this case the inclusion phase, i.e. the fiber phase, is not modeled rigidly, but as an elastic solid like the matrix phase. All other fundamental assumptions discussed in Sec. 2.6.1 remain valid in the corresponding context of anisotropic elastic solid composites.

The **self-consistent model (SC)** referring to Hill (1965) and Budiansky (1965) is based on the following localization tensor

$$\mathbb{A}_{\mathsf{SC}} = \left(\mathbb{I}^{\mathsf{S}} + \bar{\mathbb{P}}_0^{\mathsf{S}}(\mathbb{V}_{\mathsf{F}} - \bar{\mathbb{V}})\right)^{-1} \tag{2.87}$$

which is also given in, e.g., Walpole (1969) and results in the following relation for the anisotropic viscosity tensor

$$\bar{\mathbb{V}} = \mathbb{V}_{\mathsf{M}} + c_{\mathsf{F}} \left\langle \left(\bar{\mathbb{P}}_0^{\mathsf{S}}\right)^{-1} \right\rangle_{\mathsf{F}}. \tag{2.88}$$

In this case, the notation of the polarization tensor $\bar{\mathbb{P}}_0^{\mathsf{S}}$ indicates that it depends on the effective viscosity tensor characterizing the embedding material. The formulation of the effective viscosity tensor in Eq. (2.88) refers to an implicit definition following Hill (1965) and Budiansky (1965) and the computation involves numerical integration over the unit sphere to compute $\bar{\mathbb{P}}_0^{\mathsf{S}}$ based on Eq. (E.15) in App. E.4.

Following the approach of the **differential scheme (DS)** referring to Roscoe (1973), Boucher (1976), and McLaughlin (1977), which is based on

incrementally combining both DD and SC, the corresponding equation for estimating the effective viscosity tensor reads as follows based on the orientation-averaged formulation given in, e.g., Kanaun and Levin (2008) (pp. 169–170)

$$\frac{\mathrm{d}\bar{\mathbb{V}}}{\mathrm{d}c_{\mathsf{F}}} = \frac{1}{1-c_{\mathsf{F}}}\left\langle \left(\bar{\mathbb{P}}_0^{\mathsf{S}}\right)^{-1}\right\rangle_{\mathsf{F}}. \tag{2.89}$$

In order to consider the distribution of the embedded fibers, the **Ponte Castañeda-Willis model (PCW)** proposed by Ponte Castañeda and Willis (1995) is based on both the polarization tensor $\mathbb{P}_{\mathsf{d}}^{\mathsf{S}}$ describing the ellipsoidal distribution (d) and the polarization tensor $\mathbb{P}_{\mathsf{i}}^{\mathsf{S}} = \mathbb{P}_0^{\mathsf{S}}$ referring to the inclusion (i) geometry. The following strain-rate localization tensor refers to a reformulation of the orientation-averaged localization tensor given in Ponte Castañeda and Willis (1995)

$$\langle \mathbb{A}_{\mathsf{PCW}}\rangle_{\mathsf{F}} = \langle \mathbb{A}_{\mathsf{SIP}}\rangle_{\mathsf{F}}\left(\mathbb{I}^{\mathsf{S}} - c_{\mathsf{F}}\mathbb{P}_{\mathsf{d}}^{\mathsf{S}}\delta\mathbb{V}\langle \mathbb{A}_{\mathsf{SIP}}\rangle_{\mathsf{F}}\right)^{-1}, \tag{2.90}$$

with the localization tensor $\mathbb{A}_{\mathsf{SIP}} = \left(\mathbb{I}^{\mathsf{S}} + \mathbb{P}_{\mathsf{i}}^{\mathsf{S}}\delta\mathbb{V}\right)^{-1}$ as given in Eq. (2.83) depending on $\mathbb{P}_{\mathsf{i}}^{\mathsf{S}}$ and on the viscosity difference $\delta\mathbb{V} = \mathbb{V}_{\mathsf{F}} - \mathbb{V}_{\mathsf{M}}$. As a result, the following expression for estimating the effective viscosity tensor based on the PCW model can be derived as

$$\bar{\mathbb{V}} = \mathbb{V}_{\mathsf{M}} + c_{\mathsf{F}}\left(\left\langle \left(\mathbb{P}_{\mathsf{i}}^{\mathsf{S}}\right)^{-1}\right\rangle_{\mathsf{F}}^{-1} - c_{\mathsf{F}}\mathbb{P}_{\mathsf{d}}^{\mathsf{S}}\right)^{-1}, \tag{2.91}$$

similar to the orientation-averaged effective stiffness with rigid inclusions given in Ponte Castañeda and Willis (1995) and based on the expression given in Kammer and Ponte Castañeda (2022) simplified for rigid fibers. It is noted that the localization tensor given in Eq. (2.90) reduces to DD without distribution effects for a vanishing fiber volume fraction as described by Kailasam and Ponte Castañeda (1998). For a further discussion of the PCW model, reference is made to Sec. 6.1.5.

Chapter 3

Micromechanically consistent flow-fiber coupling

Contents overview. The investigation of the flow-fiber coupling effects with respect to the stress field in the solid composite under load represents the first contribution to the micromechanical modeling of short-fiber orientation dynamics. The present chapter begins with a description of the governing equations on both the fluid and solid sides, continues with a description of the numerical procedure with a special focus on methods for stabilizing the fluid solver, and concludes with a discussion of the results. In the latter part, the effects of both flow-fiber coupling and the rheological matrix model are investigated in terms of the fiber orientation and the stress field.

3.1 Governing equations [1]

For both viscous fiber suspensions and solid fiber reinforced composites, the governing equations, material models, and assumptions are addressed in the following. It should be noted that all governing equations must be interpreted in the context of the finite volume method. Regarding the numerical procedure, the reader is referred to Sec. 3.2.

[1] This section is directly taken from Karl et al. (2023b).

3.1.1 Volume of fluid approach [2]

Throughout this chapter, the fiber orientation is described based on the second-order and fourth-order fiber orientation tensor $\boldsymbol{N}$ and $\mathbb{N}$ of the first kind referring to Kanatani (1984) and Advani and Tucker III (1987)

$$\begin{aligned}\boldsymbol{N}(\boldsymbol{x},t) &= \int_{\mathcal{S}} f(\boldsymbol{x},t,\boldsymbol{n})\boldsymbol{n}\otimes\boldsymbol{n}\,\mathrm{d}S(\boldsymbol{n}),\\ \mathbb{N}(\boldsymbol{x},t) &= \int_{\mathcal{S}} f(\boldsymbol{x},t,\boldsymbol{n})\boldsymbol{n}\otimes\boldsymbol{n}\otimes\boldsymbol{n}\otimes\boldsymbol{n}\,\mathrm{d}S(\boldsymbol{n}).\end{aligned} \tag{3.1}$$

During mold-filling, the fiber orientation evolution is modeled based on the Folgar-Tucker equation (Folgar and Tucker III, 1984; Advani and Tucker III, 1987) formulated as follows with the effective flow field

$$\dot{\boldsymbol{N}} = \bar{\boldsymbol{W}}\boldsymbol{N} - \boldsymbol{N}\bar{\boldsymbol{W}} + \xi\big(\bar{\boldsymbol{D}}\boldsymbol{N} + \boldsymbol{N}\bar{\boldsymbol{D}} - 2\mathbb{N}[\bar{\boldsymbol{D}}]\big) + 2C_{\mathrm{I}}\dot{\bar{\gamma}}(\boldsymbol{I} - 3\boldsymbol{N}). \tag{3.2}$$

Reference is made to Sec. 2.4.2 for a detailed discussion of Eq. (3.2). In this chapter the IBOF closure of Chung and Kwon (2002b) is adopted, whose implementation details are addressed in App. B.2.

In order to realize the flow-fiber coupling, the effective viscosity tensor $\bar{\mathbb{V}}$ of the fiber suspension is formulated in terms of fiber orientation tensors $\boldsymbol{N}$ and $\mathbb{N}$. Throughout this study, the effective Cauchy stress tensor $\bar{\boldsymbol{\sigma}}$ refers to a generalized incompressible Newtonian fluid. Furthermore, the MT model (Mori and Tanaka, 1973), applied by, e.g., Bertóti and Böhlke (2017) and Bertóti et al. (2021), for which reference is made to Sec. 2.6.4, is used reading

$$\bar{\boldsymbol{\sigma}} = -\bar{p}\boldsymbol{I} + \bar{\mathbb{V}}[\bar{\boldsymbol{D}}], \qquad \bar{\mathbb{V}} = \mathbb{V}_{\mathsf{M}} + \frac{c_{\mathsf{F}}}{c_{\mathsf{M}}}\Big\langle \big(\mathbb{P}_0^{\mathsf{S}}\big)^{-1}\Big\rangle_{\mathsf{F}}. \tag{3.3}$$

[2] This section consists of parts from Karl et al. (2023b). Additional text passages have been added.

Note that the inversion $\left(\mathbb{P}_0^{\mathsf{S}}\right)^{-1}$ is defined on the symmetric deviatoric subset (symDev) for the considered case of incompressible suspensions with $\left(\mathbb{P}_0^{\mathsf{S}}\right)^{-1}\mathbb{P}_0^{\mathsf{S}} = \mathbb{P}_2$ representing the identity on symDev for second-order tensors. As already discussed in Sec. 2.6.4, the operator $\langle\cdot\rangle_{\mathsf{F}}$ denotes the orientation averaging procedure of Advani and Tucker III (1987) leading to the following expression

$$\bar{\mathbb{V}}[\bar{\boldsymbol{D}}] = \mathbb{V}_{\mathsf{M}}[\bar{\boldsymbol{D}}] + \frac{c_{\mathsf{F}}}{c_{\mathsf{M}}}\left\langle \left(\mathbb{P}_0^{\mathsf{S}}\right)^{-1}\right\rangle_{\mathsf{F}}[\bar{\boldsymbol{D}}], \tag{3.4}$$

with the orientation-averaged part of the viscous stress tensor simplified for the special case of incompressibility

$$\left\langle \left(\mathbb{P}_0^{\mathsf{S}}\right)^{-1}\right\rangle_{\mathsf{F}}[\bar{\boldsymbol{D}}] = b_1\mathbb{N}[\bar{\boldsymbol{D}}] + b_2(\boldsymbol{N}\cdot\bar{\boldsymbol{D}})\boldsymbol{I} + 2b_3(\boldsymbol{N}\bar{\boldsymbol{D}} + \bar{\boldsymbol{D}}\boldsymbol{N}) + b_5\bar{\boldsymbol{D}}. \tag{3.5}$$

The coefficients b_1 to b_5 depend on the orientation-averaged tensor $(\mathbb{P}_0^{\mathsf{S}})^{-1}$ as given in Eq. (2.82) following Advani and Tucker III (1987). As discussed by Karl et al. (2021a), the formulation of the fiber-induced viscous stress based on Eqs. (3.3) and (3.4) in general is not traceless for anisotropic fiber orientation, even for traceless $\bar{\boldsymbol{D}}$ in the incompressible case. In the context of the decoupled approach ($c_{\mathsf{F}} = 0$), only $\bar{\mathbb{V}} = \mathbb{V}_{\mathsf{M}}$ is used and, therefore, the flow field is not influenced by the evolution of the fiber orientation state.

The mold-filling process is based on the volume of fluid method (VOF) covering the two-phase flow of fiber suspension and air. Details about this established method are not given here, but reference is made to the two fundamental works in this field Noh and Woodward (1976) and Hirt and Nichols (1981). Both phases are considered immiscible, isothermal, incompressible, without phase transition, and without body forces. The location of both phases is described by the scalar phase parameter ψ with the value $\psi = 1$ indicating the fiber-laden melt and $\psi = 0$ indicating the air phase. In addition to Eq. (3.2) describing the evolution of the anisotropic microstructure, the following system of equations (3.6) is

solved for the phase parameter ψ, the effective velocity field $\bar{\boldsymbol{v}}$ and for the effective pressure field $\bar{p}$

$$\begin{aligned}
\frac{\partial \psi}{\partial t} + \operatorname{grad}(\psi) \cdot \bar{\boldsymbol{v}} &= 0, \\
\operatorname{div}(\bar{\boldsymbol{v}}) &= 0, \\
\frac{\partial \bar{\rho}\bar{\boldsymbol{v}}}{\partial t} + \operatorname{grad}(\bar{\rho}\bar{\boldsymbol{v}})\bar{\boldsymbol{v}} &= -\operatorname{grad}(\bar{p}) + \operatorname{div}(2\mu\bar{\boldsymbol{D}}) + \sigma\kappa \operatorname{grad}(\psi) + \boldsymbol{f}, \qquad (3.6)
\end{aligned}$$

with the additional force vector $\boldsymbol{f}$ being present only in the fiber-laden melt or suspension (susp) for the flow-fiber coupled approach

$$\boldsymbol{f} = \begin{cases} \operatorname{div}\Big(\dfrac{c_{\mathsf{F}}}{c_{\mathsf{M}}} \Big\langle \big(\mathbb{P}_0^{\mathsf{S}}\big)^{-1} \Big\rangle_{\mathsf{F}} [\bar{\boldsymbol{D}}] \Big), & \boldsymbol{x} \in V_{\mathsf{susp}} \\ \boldsymbol{0}, & \boldsymbol{x} \in V_{\mathsf{air}} \end{cases}. \qquad (3.7)$$

Details about the implementation are given in Sec. 3.2. The surface tension term in Eq. (3.6) of the fiber suspension refers to Brackbill et al. (1992) and σ denotes the surface tension. The curvature κ is defined as follows (Brackbill et al., 1992)

$$\kappa = -\operatorname{div}\left(\frac{\operatorname{grad}(\psi)}{\|\operatorname{grad}(\psi)\|} \right). \qquad (3.8)$$

Furthermore, the effective mass density $\bar{\rho}$ and the shear viscosity μ are defined by the following adapted mixture rules representing phase-dependent fields

$$\begin{aligned}
\bar{\rho} &= \psi \rho_{\mathsf{susp}} + (1-\psi)\rho_{\mathsf{air}} \\
&= \psi(c_{\mathsf{M}}\rho_{\mathsf{M}} + c_{\mathsf{F}}\rho_{\mathsf{F}}) + (1-\psi)\rho_{\mathsf{air}}, \\
\mu &= \psi \mu_{\mathsf{M}} + (1-\psi)\mu_{\mathsf{air}}. \qquad (3.9)
\end{aligned}$$

It should be noted that the fibers are considered in the computation of $\bar{\rho}$ but not in the computation of μ and that $\rho_{\mathsf{susp}} = c_{\mathsf{M}}\rho_{\mathsf{M}} + c_{\mathsf{F}}\rho_{\mathsf{F}}$ corre-

sponds to Voigt's average (Hill, 1963) leading to the exact suspension's density (Schürmann, 2007) (p. 165).

In Eq. (3.3), the matrix viscosity $\mathbb{V}_{\mathsf{M}}$ is considered both Newtonian and non-Newtonian in the context of a generalized Newtonian fluid, see Eq. (2.34). In this chapter, the shear-thinning model proposed by Cross (1965) for the polymer matrix viscosity μ is implemented as follows to be compared with the Newtonian behavior (Thevenin and Perreux, 1996; Karl and Böhlke, 2022)

$$\mu = \frac{\mu_0}{1 + (m\dot{\bar{\gamma}}_{\mathsf{M}})^n}, \qquad \dot{\bar{\gamma}}_{\mathsf{M}} = \sqrt{\frac{\langle \boldsymbol{D} \rangle_{\mathsf{M}} \cdot \langle \boldsymbol{D} \rangle_{\mathsf{M}}}{2}} = \sqrt{\frac{\bar{\boldsymbol{D}} \cdot \bar{\boldsymbol{D}}}{2(1 - c_{\mathsf{F}})^2}}. \tag{3.10}$$

The Newtonian shear viscosity is denoted by μ_0 and both m and n represent model parameters. It should be noted that the air phase is always modeled as a Newtonian fluid. In Eq. (3.10), the assumption of rigid fibers $\langle \boldsymbol{D} \rangle_{\mathsf{F}} = \boldsymbol{0}$ is used in order to express the effective shear rate of the matrix $\dot{\bar{\gamma}}_{\mathsf{M}}$ with respect to the effective strain-rate tensor $\bar{\boldsymbol{D}}$ and the fiber volume fraction c_{F} using $\bar{\boldsymbol{D}} = (1 - c_{\mathsf{F}}) \langle \boldsymbol{D} \rangle_{\mathsf{M}}$.[3] Since the flow-fiber coupling affects the constitutive behavior, the effective shear rate of the matrix $\dot{\bar{\gamma}}_{\mathsf{M}}$ is used instead of the shear rate $\dot{\bar{\gamma}}$ introduced in the context of the Folgar-Tucker equation (3.2). It should be noted that the fiber orientation evolution given in Eq. (3.2) is considered only dependent on the macroscopic strain-rate tensor $\bar{\boldsymbol{D}}$, macroscopic spin tensor $\bar{\boldsymbol{W}}$, and the macroscopic shear rate $\dot{\bar{\gamma}}$. As a consequence, the coupling effects on the fiber orientation evolution are only present due to changes in the flow field compared to the decoupled approach. This procedure ensures a comparable fiber orientation evolution in order to study the coupling effects purely due to viscous anisotropy.

[3] The derivation of this expression uses the implication of the Hill-Mandel condition $\bar{\boldsymbol{D}} = \langle \boldsymbol{D} \rangle$ given in Eq. (2.71) and that the total volume average reads $\langle \boldsymbol{D} \rangle = (1 - c_{\mathsf{F}}) \langle \boldsymbol{D} \rangle_{\mathsf{M}} + c_{\mathsf{F}} \langle \boldsymbol{D} \rangle_{\mathsf{F}}$ similar to Eqs. (2.73) and (2.74), see also Karl and Böhlke (2022).

3.1.2 Solid short-fiber reinforced composites [4]

After fluid-solid transition, effective linear elastic behavior $\bar{\boldsymbol{\sigma}} = \bar{\mathbb{C}}[\bar{\boldsymbol{\varepsilon}}]$ is assumed for the solid fiber reinforced composite, with $\bar{\boldsymbol{\varepsilon}}$ denoting the effective strain and $\bar{\mathbb{C}}$ representing the effective stiffness tensor. It is assumed that the geometry and the fiber orientation field do not change during the fluid-solid transition. For clarity, the fundamentals regarding mean-field modeling are omitted here and reference is made to Sec. 2.6 including App. A. Based on the MT model (Mori and Tanaka, 1973), the effective stiffness tensor reads $\bar{\mathbb{C}} = \mathbb{C}_{\mathsf{M}} + \bar{\mathbb{R}}$ with the abbreviation $\bar{\mathbb{R}}$ defined as follows based on the formulation given in, e.g., Benveniste (1987), Brylka (2017) (p. 38), Hessman et al. (2021), and Karl and Böhlke (2022)

$$\bar{\mathbb{R}} = c_{\mathsf{F}} \Big(c_{\mathsf{F}} \delta\mathbb{C}^{-1} + c_{\mathsf{M}} \Big\langle \big(\delta\mathbb{C}^{-1} + \mathbb{P}_0^{\mathsf{S}} \big)^{-1} \Big\rangle_{\mathsf{F}}^{-1} \Big)^{-1} . \tag{3.11}$$

It should be noted that only homogeneous and isotropic phases are considered as described in Sec. 2.6. In Eq. (3.11), the abbreviation $\delta\mathbb{C}$ refers to $\mathbb{C}_{\mathsf{F}} - \mathbb{C}_{\mathsf{M}}$ with the stiffness of the fiber material $\mathbb{C}_{\mathsf{F}}$ and of the matrix material $\mathbb{C}_{\mathsf{M}}$. In the section at hand, the polarization tensor $\mathbb{P}_0^{\mathsf{S}}$ refers to stiffness computations can be computed analytically based on the expressions given in Ponte Castañeda and Willis (1995). Analogously, $\langle\cdot\rangle_{\mathsf{F}}$ denotes the orientation averaging procedure given in Eq. (2.81) referring to Advani and Tucker III (1987).

The stationary balance of linear momentum without specific body forces $\mathbf{0} = \operatorname{div}(\bar{\boldsymbol{\sigma}})$ is used as the governing equation for the effective displacement field $\bar{\boldsymbol{u}}$

$$\mathbf{0} = (K_{\mathsf{M}} + \frac{1}{3} G_{\mathsf{M}}) \operatorname{grad}\operatorname{div}(\bar{\boldsymbol{u}}) + G_{\mathsf{M}} \Delta\bar{\boldsymbol{u}} + \operatorname{div}\big(\bar{\mathbb{R}}[\operatorname{grad}(\bar{\boldsymbol{u}})]\big), \tag{3.12}$$

[4] This section consists of parts from Karl et al. (2023b). Additional text passages have been added.

with $\Delta(\cdot)$ denoting the Laplacian $\operatorname{div}\operatorname{grad}(\cdot)$. The bulk modulus is represented by K and the shear modulus by G. Based on the right minor symmetry of $\bar{\mathbb{R}}$, the mapping $\bar{\mathbb{R}}[\operatorname{grad}(\bar{\boldsymbol{u}})]$ inherently uses only the symmetric part of $\operatorname{grad}(\bar{\boldsymbol{u}})$, which refers to the effective strain tensor $\bar{\boldsymbol{\varepsilon}}$. The tensor $\bar{\mathbb{R}}$ contains the information about the local fiber orientation state based on orientation averaging. After solving Eq. (3.12) for $\bar{\boldsymbol{u}}$, the effective strain is computed directly by using the kinematic relation $\bar{\boldsymbol{\varepsilon}} = \operatorname{sym}\operatorname{grad}(\bar{\boldsymbol{u}})$ and the effective stress follows from $\bar{\boldsymbol{\sigma}} = \bar{\mathbb{C}}[\bar{\boldsymbol{\varepsilon}}]$.

3.1.3 Scale separation and fundamental assumptions [5]

Fiber orientation tensors inherently represent the averaged orientation state, e.g., on each numerical grid cell in the context of coarse graining, or in other words, representing the so-called sample mean in view of the embedded fibers following Kanatani (1984). Therefore, labeling $\boldsymbol{N}$ and $\mathbb{N}$ as effective fields by $\bar{(\cdot)}$ is omitted throughout this thesis. All other fields are labeled as effective fields to emphasize that they represent averages regarding the scale on which the orientation tensor description is valid. In this context, every grid cell used for numerical computation is seen as a statistically representative volume element across which the described mean-field homogenization is performed. Regarding the assumptions of mean-field modeling, reference is made to Sec. 2.6 and to the references therein. In addition, it is assumed that the fibers can move freely as specified by the kinematics of the flow without geometric restrictions, which is not always guaranteed, especially in thin-walled components. In this context, the reader is referred to the end of Sec. 3.4 and to the references discussed there about so-called confined flow conditions in narrow gaps.

[5] This section consists of parts from Karl et al. (2023b). Additional text passages have been added.

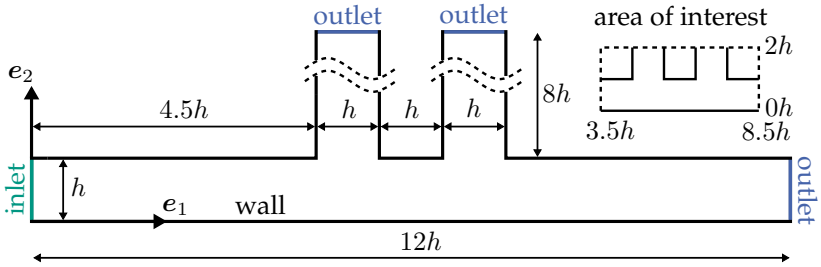

Figure 3.1: Geometry considered for both the mold-filling simulation and for the solid composite simulation with the definition of the area of interest being the basis for the results in Sec. 3.3, adapted from Karl et al. (2023b).

3.2 Numerical procedure

3.2.1 Mold-filling simulation [6]

For both fluid and solid simulations the 2D rib geometry shown in Fig. 3.1 is used. This generic geometry is inspired by the bifurcation flow of Haagh and van de Vosse (1998) and represents a classic thin-walled component. The length h is $2.5 \cdot 10^{-3}\,\mathrm{m}$. The geometry is chosen such that the two ribs experience different flow states towards the end of the mold-filling process, which is discussed in detail in Sec. 3.3.1. It is shown that the two-phase simulation considering the actual mold-filling is necessary in order to predict the fiber orientation state correctly.

The implemented VOF solver is based on the interIsoFoam solver of OpenFOAM® (version 2106) for the isothermal mold-filling of two immiscible and incompressible fluids with Newtonian or non-Newtonian viscosity as described in OpenFOAM® (2021). All of the following basic numerical schemes, standard boundary conditions, and solver descriptions refer to the OpenFOAM® (2021) documentation. The inter-

[6] This section consists of parts from Karl et al. (2023b). Additional text passages have been added.

IsoFoam solver in use differs from the interFoam solver by using the isoAdvector scheme improving the advection towards a sharp interface according to Roenby et al. (2016), Scheufler and Roenby (2019), Gamet et al. (2020), and Larsen et al. (2019). In the fluid solver, body forces due to gravity are neglected in the balance of linear momentum analogous to the solid solver. The implemented methods of stabilizing the mold-filling simulations are addressed in Sec. 3.2.3. Regarding time discretization, the second-order implicit backward scheme is used with the time step $\triangle t$ determined by the maximum Courant number $\max(\mathrm{Co}) = 0.02$, see Eq. (3.24) for further details. This value corresponds to the order of magnitude of the value 0.05 proposed by Larsen et al. (2019) for the related interFoam solver. To ensure sufficient accuracy, $\triangle t$ is limited by the maximum value $10^{-3}\,\mathrm{s}$. All simulations are stopped at the filling level of $99.999\,\%$. In addition, only second-order spatial discretization schemes are used. For solving the system of equations, the multigrid solver GAMG is chosen with GaussSeidel as the smoothing method. In addition, $\bar{p}$ and $\bar{\boldsymbol{v}}$ are computed based on the PISO algorithm proposed by Issa (1986) with 10 corrector steps and no momentum predictor step. As a result of a grid study, 80 orthogonal and uniformly distributed cells per h are set to resolve the fields with sufficient accuracy.

Throughout this study, polypropylene (PP) is considered as the thermoplastic polymer matrix with the melt density $\rho_{\mathsf{M}} = 728\,\mathrm{kg/m^3}$ referring to ≈ 0.8 of the solid density (Harper, 2000) (pp. 5.14–5.15) of $910\,\mathrm{kg/m^3}$ (Schürmann, 2007) (p. 132). The Newtonian kinematic viscosity is set to $\nu_{\mathsf{M}} = 0.779\,\mathrm{m^2/s}$ which corresponds to ν_0 in the shear-thinning Cross model given in Eq. (3.10) as implemented in OpenFOAM® (2021) with the parameter values $n = 0.749$ and $m = 17.366 \cdot 10^{-3}\,\mathrm{s}$ (Osswald and Rudolph, 2015), for details see App. B.1. Please note that the kinematic viscosity ν and the density ρ are used as input in OpenFOAM® instead of the dynamic viscosity $\mu_0 = \nu_0 \rho_{\mathsf{M}}$ which is previously referred to as shear viscosity. The surface tension is set to $\sigma = 0.028\,\mathrm{N/m}$ following Osswald

et al. (2006) (p. 125), for details see App. B.1. For the air phase the default solver parameters $\nu_{\mathsf{air}} = 1.48 \cdot 10^{-5}\,\mathrm{m}^2/\mathrm{s}$ and $\rho_{\mathsf{air}} = 1\,\mathrm{kg}/\mathrm{m}^3$ are used. In this study glass fibers are considered with the density $\rho_{\mathsf{F}} = 2540\,\mathrm{kg}/\mathrm{m}^3$ as given in Schürmann (2007) (p. 30). By defining $h, \bar{v}_{\mathsf{b}}, \nu_{\mathsf{M}}, \rho_{\mathsf{M}}$, and σ as the characteristic quantities, the Reynolds number (Re) and the capillary number (Ca) describing the problem have the following values

$$\mathrm{Re} = \frac{\bar{v}_{\mathsf{b}} h}{\nu_{\mathsf{M}}} \approx 3 \cdot 10^{-4}, \qquad \mathrm{Ca} = \frac{\rho_{\mathsf{M}} \nu_{\mathsf{M}} \bar{v}_{\mathsf{b}}}{\sigma} \approx 2025. \tag{3.13}$$

In this equation, $\bar{v}_{\mathsf{b}}$ refers to the bulk velocity. Based on the value of Re, the mold-filling process approximately corresponds to creeping flow conditions based on Eq. (2.61) and Ca shows that viscous forces dominate surface tension forces.[7] The fixed aspect ratio of the short glass fibers equals $\alpha = 20$ with $C_{\mathsf{I}} = 0.005$ as the fiber-fiber interaction parameter affecting the orientation tensor evolution given in Eq. (3.2). The fibers are considered with a volume fraction of $c_{\mathsf{F}} = 0.2$ which corresponds to $41.1\,\mathrm{wt.\%}$ based on the solid densities. Analogous to Karl et al. (2021a), the thermodynamic consistency is checked during mold-filling based on the isothermal dissipation inequality $\bar{\boldsymbol{D}} \cdot \bar{\mathbb{V}}[\bar{\boldsymbol{D}}] \geq 0$. In this context, additional reference is made to Munganga et al. (2000) and to Eq. (2.25) representing the general form of the so-called Clausius-Duhem inequality.

The initial and boundary conditions for every field are summarized in Tab. 3.1 with the boundaries wall, inlet, and outlet sketched in Fig. 3.1. The zeroGradient condition refers to a vanishing gradient normal to the respective boundary. The zeroGradient condition for ψ corresponds to a contact angle of 90° at the wall, chosen for simplicity. The bound-

[7] Regarding different definitions of Ca, reference is made to, e.g., Guo et al. (2022) and it is noted that Ca defined in Eq. (3.13) refers to the common formulation according to Guo et al. (2022). The interpretation of Ca as the ratio of viscous forces to surface tension forces is also given in, e.g., Gupta et al. (2010).

ary condition fixedFluxPressure adjusts the pressure gradient in order to get a flux on the boundary which is consistent with the velocity boundary condition (OpenFOAM®, 2021). At the inlet, a parabolic velocity profile is set with the bulk velocity $\bar{v}_\mathrm{b} = 0.1\,\mathrm{m/s}$ based on the characteristic velocity given in Haagh and van de Vosse (1998). By choosing the standard interIsoFoam solver, pinning of the contact line is observed. However, the experiments of, e.g., Farotti and Natalini (2018) and Wang et al. (2022) with comparable settings show that form-filling flows are realized with the selected process data described in the section at hand. The observed contact line pinning is most likely related to the high capillary number given in Eq. (3.13). Under high Ca number conditions it is known that a large deformation of the free surface area can occur before the occurrence of a moving contact line.[8] As a result, the advancing contact angle, which is related to Ca through the Cox-Voinov law (Voinov, 1976; Cox, 1986), basically decouples from the static contact angle, with Wörner et al. (2018) as an additional reference. This physical process cannot be captured by the employed VOF formulation in which only the static contact angle is prescribed. In order to enable the corresponding simulations at high Ca with a moving contact line in the standard interIsoFoam solver, a novel boundary

[8] That high Ca numbers are typical for injection molding and that surface tension forces therefore play a minor role is described by, e.g., Haagh and van de Vosse (1998). In the context of the classical no-slip boundary condition, the observed contact line pinning is also addressed by Haagh and van de Vosse (1998) and that an air cushion can form between the suspension and the wall. Haagh and van de Vosse (1998) solve the problem of contact line pinning by introducing a so-called free-slip condition, which locally replaces the no-slip condition around the contact point. Borzenko and Shrager (2015) also address both the occurrence of a so-called gas layer near the wall and the remedy by introducing a local slip condition. The so-called dynamic contact angle, measured starting at the wall and through the suspension to the free surface, evolves to π for small surface tension forces and high viscosity of the suspension (leading to high Ca) as described by Borzenko and Shrager (2015). In the case of contact line pinning, this is consistent with the gas layer and consistent with the interpretation of Ca as the ratio of viscous forces to surface tension forces (Gupta et al., 2010; Guo et al., 2022), that therefore the deformation of the free surface occurs preferentially and not the opposite effect driven by the surface tension force.

	initial	wall	inlet	outlet
ψ	zero	zeroGradient	fixedValue 1	zeroGradient
$\bar{p}$	zero	fixedFluxPressure	zeroGradient	mixedPressureOut
$\bar{\boldsymbol{v}}$	zero	localAirVent	parabolic	airVentBC
$\boldsymbol{N}$	isotropic	zeroGradient	isotropic	zeroGradient
$\boldsymbol{f}$	zero	zeroGradient	zeroGradient	zeroGradient

Table 3.1: Initial and boundary conditions for the extended interIsoFoam solver, adapted from Karl et al. (2023b).

condition, referred to as localAirVent, is implemented. The localAirVent boundary condition, which is inspired by a freely escaping air phase in the previous mold-filling simulations of Hétu et al. (1998), Chang and Yang (2001), and Ospald (2014), enables an outflow of air in an area around the contact point. The boundary condition airVentBC allows the air phase to leave the domain through the outlet until the boundary cells are almost filled with polymer. Then, the condition switches linearly from zeroGradient to the standard no-slip condition and prevents the suspension from flowing out. Both localAirVent and airVentBC are based on the following equation with the implemented blending function $g(\psi)$ and the outward pointing unit normal vector $\boldsymbol{n}$ at each boundary

$$g(\psi)\bar{\boldsymbol{v}} + (1 - g(\psi))\,\mathrm{grad}(\bar{\boldsymbol{v}})\boldsymbol{n} = \boldsymbol{0}. \tag{3.14}$$

The formulation above refers to the mixed boundary condition of OpenFOAM® (2021) modified by the blending function $g(\psi)$, which allows the air phase to leave the domain through the cavity walls or through the outlet boundary until the outer cells are completely filled with the fiber suspension.

The mixedPressureOut boundary condition used by, e.g., Ospald (2014) refers to a constant reference pressure if the boundary cells are completely filled with air ($\psi = 0$). If the boundary cells are completely filled with suspension ($\psi = 1$), the zeroGradient condition is applied.

In between, a mixed boundary condition is applied until the cells are completely filled with the fiber suspension following the condition

$$(1-\psi)\bar{p}+\psi\,\mathrm{grad}(\bar{p})\cdot\boldsymbol{n}=(1-\psi)\bar{p}_{\mathsf{ref}}, \tag{3.15}$$

with the reference pressure chosen as $p_{\mathsf{ref}}=0$. All other boundary conditions listed in Tab. 3.1 are self-explaining and OpenFOAM® standard. The 2D flow is achieved by assigning the empty boundary condition to the front and back faces of the rib geometry.

3.2.2 Solid composite simulation [9]

Regarding the solid composite simulations, the Young's modulus of $1.6\,\mathrm{GPa}$ is used for PP and $73\,\mathrm{GPa}$ for the glass fibers (Schürmann, 2007) (pp. 30, 132). The Poisson's ratio of PP equals 0.4 and 0.22 for the glass fibers (Schürmann, 2007) (pp. 30, 132). With these parameter values, Eqs. (3.11) and (3.12) are uniquely determined. The inlet is clamped with suppressed displacement and rotation. The displacement $\bar{u}_1=1.5\cdot10^{-4}\,\mathrm{m}$ is applied at the two outlets of the ribs, which results in a bending of the whole structure. All details about the boundaries are illustrated in Fig. 3.1. It should be noted that the fluid-solid transition during and after the mold-filling process is assumed to occur instantly without modification of the fiber orientation.

The solid composite simulations throughout this chapter are carried out with the commercial finite element software Abaqus® CAE Standard/Explicit (version 2020). For the following description and further information, reference is made to the Dassault Systèmes® (2020) user manual. The anisotropic stiffness corresponds to the algorithmic tangent in a user-material (UMAT) subroutine implemented in Fortran 90. The

[9] This section consists of parts from Karl et al. (2023b). Additional text passages have been added.

fiber orientation data corresponds to a predefined field as an additional input of the UMAT. Based on the 2D load case, the 4-node bi-linear plane strain element CPE4 is used for meshing the geometry shown in Fig. 3.1. As a result of a grid study, 80 orthogonal and uniformly distributed cells per h are used to sufficiently resolve the stress field. Moreover, the mapping of the orientation data from the fluid to the solid mesh is done based on the nearest-neighbor procedure used by Gajek et al. (2021) extended by the trace-preserving correction scheme of Kuzmin (2018). It should be noted that the orientation data is mapped from the cell centers of the OpenFOAM® mesh to the nodes of the Abaqus® mesh. Since the UMAT is used at the element integration points, the nodal orientation values are interpolated by Abaqus®. It is observed that elements with quadratic trial functions lead to negative eigenvalues of the system matrix. Therefore, using elements with linear trial functions is suggested.

In the context of the recent work of Krauß et al. (2024), it should be emphasized that in the present chapter the closure scheme for computing the fourth-order orientation tensor was applied after mapping the second-order orientation tensor from the fluid to the solid mesh. Regarding the mapping of tensors, or in other words the interpolation of tensors between two different meshes, see also Krauß and Kärger (2022). The study of Krauß et al. (2024) deals with the question whether the order of mapping and closure is important in the context of a so-called virtual process chain. Based on the study of transversely isotropic and planar isotropic fiber orientation states, it is suggested to perform the closure before mapping the orientation data from the fluid to the solid mesh. The list of previous studies provided in Krauß et al. (2024) shows that it is common to perform the closure after mapping, and therefore the numerical approach described in this chapter with its underlying publication Karl et al. (2023b) is consistent with this common procedure.

3.2.3 Fluid solver stabilization methods [10]

In the following subsections, methods for stabilizing the two-phase fluid solver for the computation of the flow-fiber coupled mold-filling process are addressed in detail. The discussion of these methods is adapted to the use of OpenFOAM® and is intended to support engineering practice implementing flow-fiber coupled computations. All of the discussed methods are implemented to enable parallel computations.

Implicit-explicit splitting of the coupling term [11]

In order to improve the stability, as many terms of $\boldsymbol{f}$ given in Eq. (3.7) as possible should be discretized implicitly regarding the primary field $\bar{\boldsymbol{v}}$. It turns out to be numerically unfavorable that gradients can only be discretized explicitly in OpenFOAM® and that the coupling term is dominated by velocity gradients (Ospald, 2014). The coupling term $\boldsymbol{f}$ given in Eq. (3.7) can be rewritten as follows

$$\begin{aligned}\boldsymbol{f} = \operatorname{div}\Big(\frac{c_\mathsf{F}}{c_\mathsf{M}}\big(b_1\mathbb{N}[\bar{\boldsymbol{D}}] + b_2(\boldsymbol{N}\cdot\bar{\boldsymbol{D}})\boldsymbol{I} + 2b_3(\boldsymbol{N}\bar{\boldsymbol{D}} + \bar{\boldsymbol{D}}\boldsymbol{N})\big)\Big) \\ + \operatorname{div}\Big(\frac{c_\mathsf{F} b_5}{c_\mathsf{M}}\bar{\boldsymbol{D}}\Big).\end{aligned} \tag{3.16}$$

Only one part of the second term on the right-hand side of Eq. (3.16) can be discretized implicitly by using the product rule and the incompressibility condition leading to

$$\operatorname{div}\Big(\frac{c_\mathsf{F} b_5}{c_\mathsf{M}}\bar{\boldsymbol{D}}\Big) = \bar{\boldsymbol{D}}\operatorname{grad}\Big(\frac{c_\mathsf{F} b_5}{c_\mathsf{M}}\Big) + \frac{c_\mathsf{F} b_5}{2c_\mathsf{M}}\Delta\bar{\boldsymbol{v}}. \tag{3.17}$$

[10] This section is directly taken from Karl et al. (2023b).
[11] This section is directly taken from Karl et al. (2023b).

By using Eq. (3.17) and Eq. (3.16), the implemented splitting of $\boldsymbol{f}$ reads

$$\begin{aligned}\boldsymbol{f}_{\mathsf{expl}} &= \operatorname{div}\Big(\frac{c_{\mathsf{F}}}{c_{\mathsf{M}}}\big(b_1\mathbb{N}[\bar{\boldsymbol{D}}] + b_2(\boldsymbol{N}\cdot\bar{\boldsymbol{D}})\boldsymbol{I} + 2b_3(\boldsymbol{N}\bar{\boldsymbol{D}} + \bar{\boldsymbol{D}}\boldsymbol{N})\big)\Big) \\ &\quad + \bar{\boldsymbol{D}}\operatorname{grad}\Big(\frac{c_{\mathsf{F}}b_5}{c_{\mathsf{M}}}\Big), \\ \boldsymbol{f}_{\mathsf{impl}} &= \frac{c_{\mathsf{F}}b_5}{2c_{\mathsf{M}}}\Delta\bar{\boldsymbol{v}}. \end{aligned} \tag{3.18}$$

The implicit-explicit splitting of all other terms in the system of governing equations (3.6) for computing ψ, $\bar{p}$, and $\bar{\boldsymbol{v}}$ is not changed and corresponds to the implementation of the basic solver interIsoFoam described in Sec. 3.2.1.

Treatment of the viscous stress [12]

As already discussed by Karl et al. (2021a), the fiber-related part of the viscous stress

$$\bar{\boldsymbol{\sigma}}_{\mathsf{v,F}} = \frac{c_{\mathsf{F}}}{c_{\mathsf{M}}}\Big\langle\big(\mathbb{P}_0^{\mathsf{S}}\big)^{-1}\Big\rangle_{\mathsf{F}}[\bar{\boldsymbol{D}}] \tag{3.19}$$

is not traceless in the case of anisotropic fiber orientation, even for traceless $\bar{\boldsymbol{D}}$. As a consequence, additional contributions to the spherical stress $-p\boldsymbol{I}$ are present, which can be spatially strongly inhomogeneous with negative effects on the pressure solver convergence. Since the pressure acts as a Lagrange multiplier for satisfying the incompressibility constraint as described by, e.g., Ponte Castañeda (2021), without loss of generality, the following expression can be used for the fiber-related viscous stress

$$\bar{\boldsymbol{\sigma}}_{\mathsf{v,F}} = \frac{c_{\mathsf{F}}}{c_{\mathsf{M}}}\mathbb{P}_2\Big\langle\big(\mathbb{P}_0^{\mathsf{S}}\big)^{-1}\Big\rangle_{\mathsf{F}}[\bar{\boldsymbol{D}}]. \tag{3.20}$$

Since the mass balance $\operatorname{div}(\bar{\boldsymbol{v}}) = 0$ is fulfilled in terms of fluxes over the cell faces, the cell-centered $\bar{\boldsymbol{D}}$ is not necessarily traceless due to

[12] This section consists of parts from Karl et al. (2023b). Additional text passages have been added.

interpolation errors. Simulation results show that this error might be large close to the interface with the error decreasing to tolerable values as the distance from the interface increases. In order to ensure that only traceless $\bar{\boldsymbol{D}}$ is used in the viscous stress tensor, the following final expression

$$\bar{\boldsymbol{\sigma}}_{\mathsf{v,F}} = \frac{c_{\mathsf{F}}}{c_{\mathsf{M}}} \mathbb{P}_2 \left\langle \left(\mathbb{P}_0^{\mathsf{S}} \right)^{-1} \right\rangle_{\mathsf{F}} \mathbb{P}_2[\bar{\boldsymbol{D}}] \tag{3.21}$$

is implemented similar to the formulation used by, e.g., Bertóti et al. (2021).

Spatial restriction of the coupling term [13]

In the following, the spatial restriction of $\boldsymbol{f}$ given in Eq. (3.7) is described in detail. As discussed in the literature, e.g., Haagh and van de Vosse (1998), Huilgol and You (2006), Lee and Liao (2008), and Borzenko and Shrager (2015), the three-phase contact point (TPCP) shown in Fig. 3.2 is critical in view of stress singularities. Furthermore, the high material contrast of the air and melt phases combined with the coupling in the area of the phase front has an unfavorable effect. In order to obtain convergence, the coupling is switched on successively with increasing distance from the phase front. Therefore, anisotropic viscosity effects directly at the phase front cannot be taken into account with this procedure. However, this is not critical since the analyzed orientation tensor further downstream is not significantly influenced by this gradual introduction of the flow-fiber coupling behind the phase front.

In order to circumvent interface-induced coupling instabilities, the following procedure is implemented with all areas shown in Fig. 3.2. The area V_{susp} occupied by the fiber suspension is divided into three sub-areas. In the area $V_{\mathsf{decoupled}}$ close to the interface, no flow-fiber coupling is present avoiding large explicit coupling terms. Next, in the transition

[13] This section is directly taken from Karl et al. (2023b).

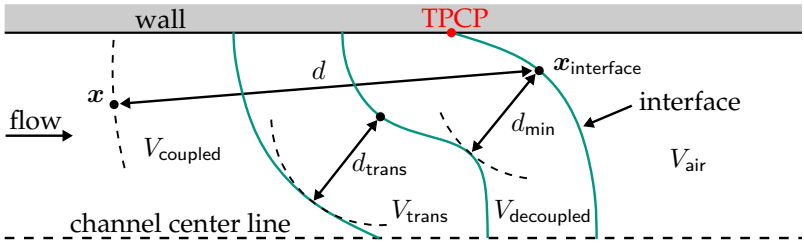

Figure 3.2: Graphical representation of the areas regarding the spatial restriction of the coupling term $\boldsymbol{f}$ with the area totally occupied by the suspension $V_{\text{susp}} = V_{\text{decoupled}} + V_{\text{trans}} + V_{\text{coupled}}$, adapted from Karl et al. (2023b).

zone V_{trans} the coupling strength is increased linearly with increasing distance from the interface. The full flow-fiber coupling is present in V_{coupled}. As an input, d_{min} is set as the minimum distance between the phase front (interface) and the beginning of flow-fiber coupling. In addition, d_{trans} is set as an input representing the width of the transition area. In every time step, the positions of the interface grid cells $\boldsymbol{x}_{\text{interface}}$ are detected by $\|\text{grad}(\psi)\| > 5000\,\text{m}^{-1}$, which turns out to be sufficiently high for the used mesh. Then, for every point $\boldsymbol{x} \in V_{\text{susp}}$ the spatially restricted (sr) coupling term $\boldsymbol{f}_{\text{sr}}$ is clearly determined as follows based on the distance $d = \|\boldsymbol{x} - \boldsymbol{x}_{\text{interface}}\|$

$$\boldsymbol{f}_{\text{sr}} = \begin{cases} \boldsymbol{0}, & d < d_{\text{min}} \\ \dfrac{d - d_{\text{min}}}{d_{\text{trans}}} \boldsymbol{f}, & d_{\text{min}} \leq d < d_{\text{min}} + d_{\text{trans}} \\ \boldsymbol{f}, & d \geq d_{\text{min}} + d_{\text{trans}} \end{cases} . \tag{3.22}$$

It should be noted that Eq. (3.22) refers to both the implicit and the explicit part of the coupling term. In this study, the distances are set to $d_{\text{min}} = d_{\text{trans}} = h/10$.

Under-relaxation of the explicit coupling term [14]

Under-relaxation is a common method in computational fluid dynamics improving numerical convergence (Ferziger et al., 2020) (pp. 140–141). Throughout this chapter, the explicit part of the coupling term is under-relaxed (ur) as follows

$$\boldsymbol{f}_{\mathsf{expl}}^{\mathsf{ur}} = \boldsymbol{f}_{\mathsf{expl}}^{n} + r(\boldsymbol{f}_{\mathsf{expl}}^{n+1} - \boldsymbol{f}_{\mathsf{expl}}^{n}), \tag{3.23}$$

with the relaxation factor $0 < r < 1$, the coupling term of the previous time step $\boldsymbol{f}_{\mathsf{expl}}^{n}$, and $\boldsymbol{f}_{\mathsf{expl}}^{n+1}$ referring to the explicit coupling term depending on the updated fiber orientation tensor and flow kinematics. As a result of under-relaxation, the explicit coupling term is not used entirely updated in the linear momentum balance. As described by, e.g., Ferziger et al. (2020) (pp. 140–141), the relaxation parameter r depends on the flow problem and, therefore, cannot be chosen a priori. In this study it is observed that strong under-relaxation is necessary for strong flow-fiber coupling, e.g., $c_{\mathsf{F}} > 0.1$ and $\alpha > 10$, even for kinematically simple channel flows. Throughout this study, $r = 0.05$ is fixed for the simulation setup. There are no negative effects on the convergence due to this small value of r since both the fiber orientation and the flow field quickly reach stationary values. The simulation results show that the difference $\boldsymbol{f}_{\mathsf{expl}}^{n+1} - \boldsymbol{f}_{\mathsf{expl}}^{n}$ is only present around the transition region, see Fig. 3.2, in which the coupling is not considered fully present anyway.

Remarks on the mesh and time discretization [15]

In this study, it is observed that homogeneous and orthogonal mesh cells are the most suitable for the two-phase mold-filling simulations in terms

[14] This section is directly taken from Karl et al. (2023b).
[15] This section consists of parts from Karl et al. (2023b). Additional text passages have been added.

of computation time. This is due to the fact that non-orthogonal cells require a smaller time step to obtain the same Courant number for similar mesh fineness. As described by, e.g., Ferziger et al. (2020) (pp. 168–169), the Courant number for convective problems is defined as

$$\mathrm{Co} = \frac{v \triangle t}{\triangle x}, \tag{3.24}$$

referring to the original work of Courant et al. (1928) with the time step size $\triangle t$ and $\triangle x / v$ representing the time scale of convection. The length scale $\triangle x$ characterizes the mesh size and the limitation of Co to achieve convergence may result in impractically small time steps for fine meshes and explicit integration schemes (Ferziger et al., 2020) (pp. 171–172). Furthermore, with respect to the coupling term, coarse grids lead to stable solution behavior for spatially strongly inhomogeneous fields. This is due to the fact that gradients are smoothed in this way and thus numerically unfavorable local peaks in the coupling term are avoided. Despite the stability, coarse meshes are not recommended to improve stability due to spatial inaccuracy.

As already described in Sec. 3.2.1, the second-order implicit backward scheme is used for the time discretization. Although this is an unbounded scheme (OpenFOAM®, 2021; Seng et al., 2017), no instabilities related to the time discretization are observed in this study. In case of stability problems, the bounded implicit Euler scheme (OpenFOAM®, 2021) can be used to stabilize the time integration. For progressive waves, the numerical damping of the Euler scheme is addressed by Larsen et al. (2019). It should be noted that this first-order accurate method can only be used if sufficient temporal resolution is ensured or if the integration leads to a stationary solution.

3.3 Results and discussion

3.3.1 Coupling effects on the fiber orientation [16]

In Fig. 3.3, the fiber orientation field $\boldsymbol{N}$ is shown in the area of interest defined in Fig. 3.1. For simplicity, only the results regarding the non-Newtonian case are shown with the decoupled approach in the left column and the coupled approach in the right column, respectively. The plots in Fig. 3.3 serve to clarify the orientation state as a basis for the solid composite simulations discussed in Sec. 3.3.2, which are based on the fiber-induced anisotropic stiffness. This is important because the coupling effects are analyzed only in terms of difference fields. Comparing both columns in Fig. 3.3, it can be observed that the coupling effects, see Sec. 1.2.1, are reproduced, e.g., the distinct isotropic orientation in the horizontal channel center region caused by the flattening of the velocity profile. In the considered 2D flow, mainly N_{11} and N_{22} are influenced by the kinematics, whereas N_{33} evolves due to trace preservation of $\boldsymbol{N}$. The component N_{12} provides information about the eigensystem of $\boldsymbol{N}$ with $N_{12} = 0$ referring to an eigensystem coinciding with the spatial axes. Regarding the 2D flow consideration, $N_{13} = N_{23} = 0$ holds. The area of interest shown in Fig. 3.3 can be divided into two main parts, the lower horizontal area and the vertical ribs. Both parts can be simplified as a simple channel flow, in which the fibers align in the main shear direction. For the horizontal part, this direction is $\boldsymbol{e}_1$ represented by high values of N_{11}. For the vertical ribs, this direction is $\boldsymbol{e}_2$ leading to high values of N_{22}.

By comparing the final fiber orientation states below and inside both ribs at the filling level of $99.999\,\%$, the influence of the different filling behavior is clearly visible: The left rib is completely filled first, while

[16] This section consists of parts from Karl et al. (2023b). Additional text passages have been added.

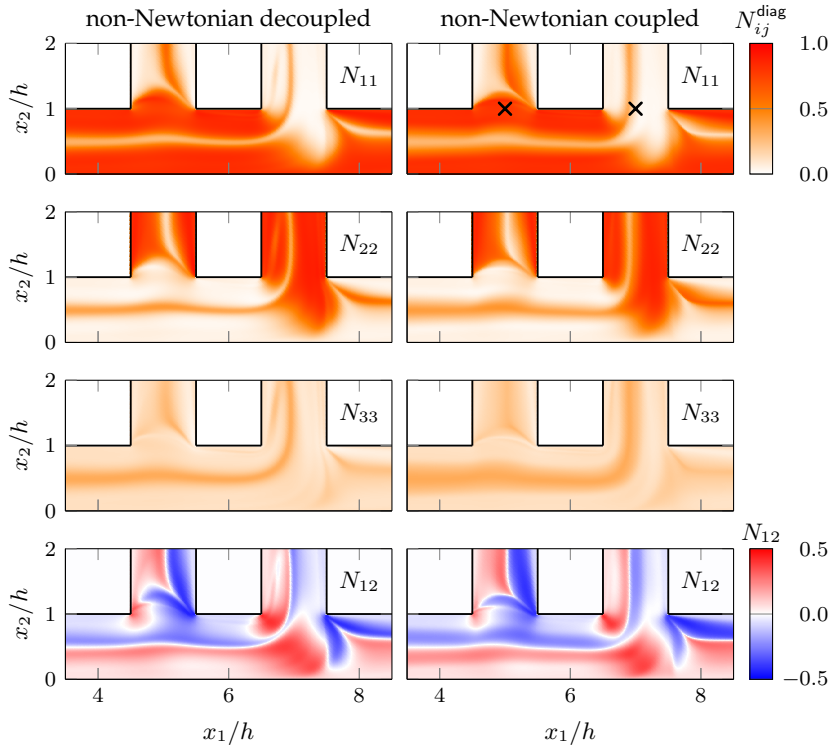

Figure 3.3: Fiber orientation field $\boldsymbol{N}$ in the area of interest with respect to non-Newtonian matrix behavior during mold-filling (left column: decoupled approach, right column: coupled approach), adapted from Karl et al. (2023b).

the right rib and the horizontal channel are not completely filled at this particular time step. Once the left rib is filled, no fiber orientation evolution is present inside and the kinematics in the area below change into a shear-dominated one leading to an alignment in $\boldsymbol{e}_1$-direction. This horizontal shear is not present in the area below the right rib since the horizontal channel is filled before the right rib. Therefore, N_{22} is the favored fiber orientation below the right rib caused by vertical shear and

a deflection of the flow. In the following, the filling behavior of the two ribs is investigated further in a comparative manner.

In the top-right plot of Fig. 3.3, two points are marked for which the temporal fiber orientation evolution is investigated. For the point in the left rib, the diagonal components of $\boldsymbol{N}$ are plotted over time in Fig. 3.4(a) and for the right rib in Fig. 3.4(b), respectively. The analysis is restricted to the coupled non-Newtonian approach. Starting from the isotropic initial state marked with ①, the fiber orientation starts to evolve once the phase front, which is represented by ψ, passes the two considered points. In time interval ② shortly behind the phase front, a transient orientation state is shown for both points. Subsequently, the orientation evolves towards an asymptotic state at ③, which describes the mold-filling process of both ribs and the horizontal channel without any part of the cavity being completely filled. It should be noted that the asymptotic state only depends on the given kinematics, the aspect ratio of the fibers, and the fiber-fiber interaction strength as discussed on an analytical basis by Karl et al. (2021b). Since the kinematics are different

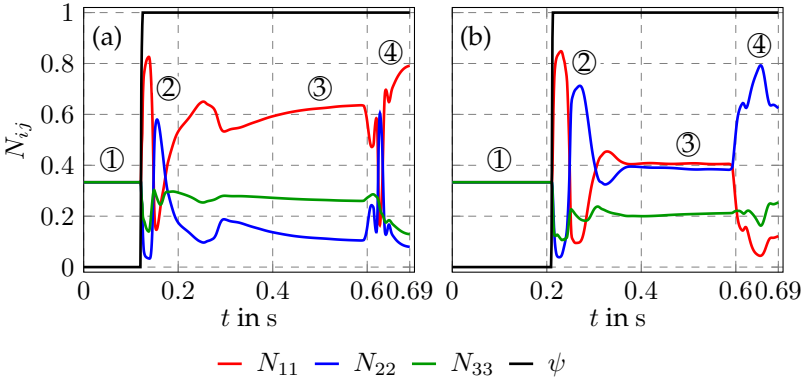

Figure 3.4: Temporal evolution of orientation tensor components N_{11}, N_{22}, N_{33}, and phase parameter ψ at the beginning of the left rib in (a) and of the right rib in (b) (non-Newtonian coupled, points marked in top right plot of Fig. 3.3), adapted from Karl et al. (2023b).

at the two points during time interval ③, also the orientation states differ. Note that the orientation states observed during time interval ③ correspond to the states that would occur if the flow through the cavity at both points was stationary, or in other words, if a two-phase simulation of the actual mold-filling process is not carried out. At approximately $t = 0.58\,\mathrm{s}$, the left rib is completely filled with suspension and, as already described before, the kinematics change to a shear-dominated one in the area around the considered point. This also affects the orientation evolution in the right rib at this time step since the flow is accelerating in the horizontal channel. Already a short time later, at approximately $t = 0.62\,\mathrm{s}$, the horizontal channel is also completely filled, leading to a complete deflection of the flow into the right rib. Until the cavity is completely filled at $t = 0.69\,\mathrm{s}$, this change in kinematics leads to a new orientation state at ④ defining the anisotropy of the manufactured part after fluid-solid transition. Since state ④ is clearly different from ③, the necessity of simulating the actual mold-filling becomes apparent. A simulation based purely on the steady-state flow through the geometry cannot represent this change in kinematics due to the filling process and predicts the fiber orientation differently. Therefore, the filling of individual areas of the cavity must necessarily be taken into account in order to correctly predict the evolution of the fiber orientation and the associated anisotropy.

In order to further quantify the mentioned differences between ③ and ④ in view of fiber orientation, the local anisotropic viscosity is investigated in the coupled approach. For this purpose, the following two measures e_{v} and $e_{\mathsf{v,aniso}}$ are defined, which quantify the difference between ③ (left rib fills quasi-stationary at $t = 0.5\,\mathrm{s}$) and ④ (shear-dominated flow below left rib at $t = 0.69\,\mathrm{s}$)

$$e_{\mathsf{v}} = \frac{\|\bar{\mathbb{V}}_{0.5} - \bar{\mathbb{V}}_{0.69}\|}{\|\bar{\mathbb{V}}_{0.5}\|} \cdot 100\,\%, \quad e_{\mathsf{v,aniso}} = \frac{\|\bar{\mathbb{V}}_{0.5,\mathsf{aniso}} - \bar{\mathbb{V}}_{0.69,\mathsf{aniso}}\|}{\|\bar{\mathbb{V}}_{0.5,\mathsf{aniso}}\|} \cdot 100\,\%. \tag{3.25}$$

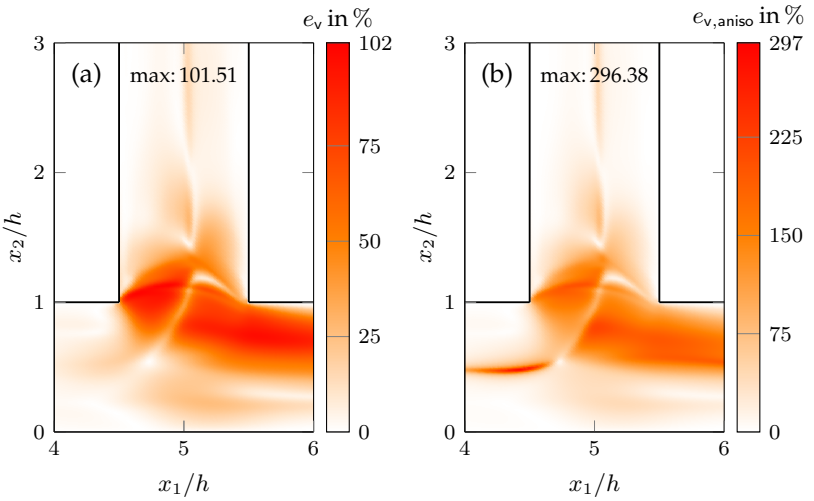

Figure 3.5: Viscosity measure e_v in (a) and the corresponding viscous anisotropy measure $e_{v,aniso}$ in (b) regarding the left rib and the difference between two different filling states, both for the coupled non-Newtonian case, adapted from Karl et al. (2023b).

The total viscosity difference is represented by e_v, whereas $e_{v,aniso}$ addresses the change of anisotropy, both as a scalar measure for simplicity. The anisotropic part of $\bar{\mathbb{V}}$ is defined as follows similar to, e.g., Bertóti and Böhlke (2017)

$$\bar{\mathbb{V}}_{aniso} = \bar{\mathbb{V}} - (\bar{\mathbb{V}} \cdot \mathbb{P}_1)\mathbb{P}_1 - \frac{1}{5}(\bar{\mathbb{V}} \cdot \mathbb{P}_2)\mathbb{P}_2, \tag{3.26}$$

with $\mathbb{P}_1$ representing the identity on spherical second-order tensors and with the identity on deviatoric second-order tensors $\mathbb{P}_2$, see Sec. 2.3.1. In Fig. 3.5, the viscosity measures defined in Eq. (3.25) are shown for the left rib. The results indicate that the difference in fiber orientation between ③ and ④ significantly affects the local effective viscosity and also significantly changes the degree of anisotropy.

In the following, the analysis is restricted to the comparisons shown in Fig. 3.6 with the fiber orientation differences defined similar to the previous study of Karl et al. (2021a). In Fig. 3.6, vertical differences address the effects of flow-fiber coupling for both viscosity models, whereas horizontal differences account for the effect of the viscosity models for both decoupled and flow-fiber coupled approach. For all four cases, the range of values is given with respect to the area of interest shown in Fig. 3.1.

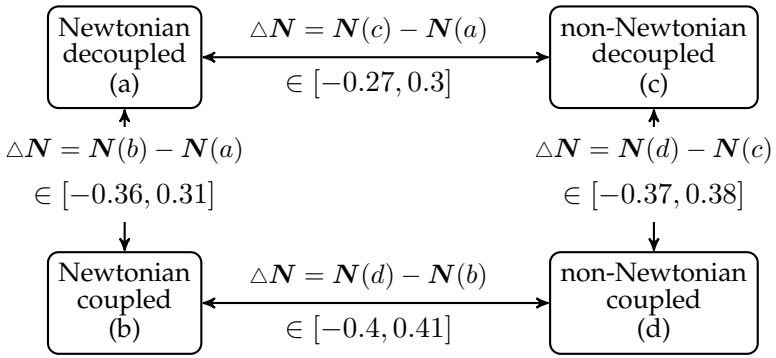

Figure 3.6: Fiber orientation difference $\triangle \boldsymbol{N}$ and ranges of values with respect to the different mold-filling approaches, adapted from Karl et al. (2023b).

For the sake of clarity, only the difference fields regarding the pure effects of flow-fiber coupling for each viscosity model are provided in the present section. In Fig. 3.7, the local orientation difference between the decoupled and the coupled approach is shown for the Newtonian case. The same difference is shown in Fig. 3.8 for the non-Newtonian matrix fluid. Areas highlighted in red indicate an alignment which is higher in the coupled case and blue areas indicate a higher alignment in the decoupled case. By comparing Figs. 3.7 and 3.8, it can be observed that the difference fields have similar characteristics for both considered matrix viscosity models. Regarding the possible interval $[0, 1]$ of N_{11}, N_{22}, and

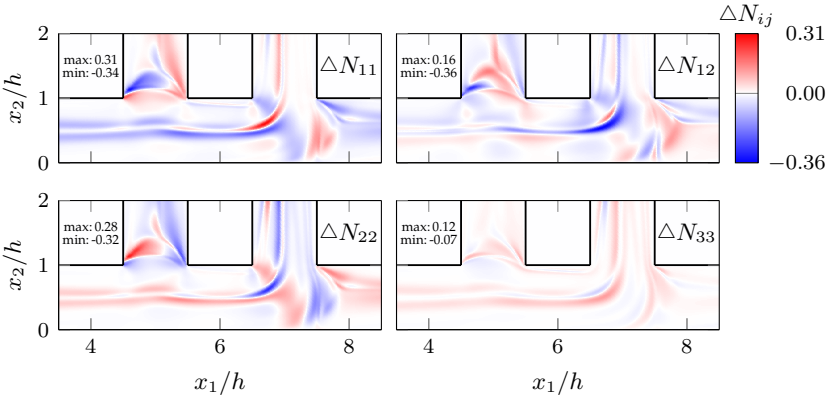

Figure 3.7: Difference field $\triangle \boldsymbol{N} = \boldsymbol{N}^{\text{coupled}}_{\text{Newtonian}} - \boldsymbol{N}^{\text{decoupled}}_{\text{Newtonian}}$ in the area of interest, adapted from Karl et al. (2023b).

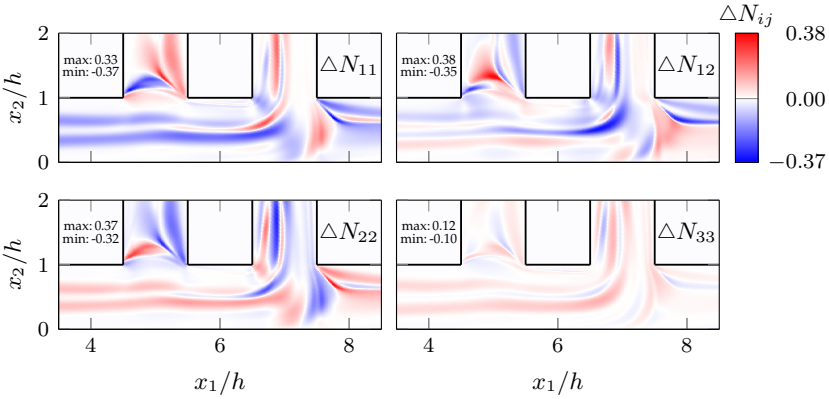

Figure 3.8: Difference field $\triangle \boldsymbol{N} = \boldsymbol{N}^{\text{coupled}}_{\text{nonNewtonian}} - \boldsymbol{N}^{\text{decoupled}}_{\text{nonNewtonian}}$ in the area of interest, adapted from Karl et al. (2023b).

N_{33}, the local effect of flow-fiber coupling ranges from $-36\,\%$ to $+31\,\%$ for the Newtonian case and from $-37\,\%$ to $+38\,\%$ for the non-Newtonian case and, therefore, can be evaluated as significant. It can be seen that the

flow-fiber coupling has approximately the same effect for both viscosity models. In the non-Newtonian case, the differences are slightly more distinct. However, this does not mean that the fiber orientation in the coupled case is almost identical for both viscosity models. In the coupled case, for example, the choice of viscosity model has a greater influence on the local fiber orientation than the flow-fiber coupling. This can be seen in Fig.3.6 in view of the given ranges of values. Therefore, not only the coupling is crucial for the local evolution of the fiber orientation, but also the consideration of the shear-thinning behavior.

Based on Fig. B.3.2 in App. B.3.1, where additional fiber orientation results are provided, the local orientation differences with respect to different viscosity models in the coupled approach range from $-40\,\%$ to $+41\,\%$, regarding the possible interval $[0, 1]$ of N_{11}, N_{22}, and N_{33}. In addition, Fig. B.3.1 in App. B.3.1 shows the effect of the viscosity model for the decoupled approach with local orientation differences $-27\,\%$ to $+30\,\%$. Therefore, it can be stated that for both the decoupled and the coupled approach, the viscosity model has a great influence on the local fiber orientation state. Furthermore, the relevance of the viscosity model changes with the flow-fiber coupling, as the range of values increases compared to the decoupled case. Please note that the latter statement only holds for flow cases in which the shear rate is sufficiently high to cause significant shear-thinning in the matrix fluid. This is given under the selected process conditions and is addressed in App. B.3.1 in the context of Fig. B.3.3.

3.3.2 Coupling effects on the stress field [17]

The fiber orientation fields investigated before are now used in finite element simulations for the solid composite. Independent of the fluid model during mold-filling, the solid composite is modeled linear elastic

[17] This section is directly taken from Karl et al. (2023b).

with its anisotropy completely defined by $\boldsymbol{N}$ and $\mathbb{N}$. Thus, this study docks directly to the results of Karl et al. (2021a), who analyze the coupling effects on the local elastic anisotropy, but not the stress field in the solid composite under load. Analogous to the previous section, Fig. 3.9 addresses the four investigated cases and the corresponding comparisons. In the following, the non-dimensional stress difference field $\triangle\bar{\boldsymbol{\sigma}}^*$ is considered with the respective definitions given in Fig. 3.9. Note that these definitions must be applied for each stress component $ij = 11, 12, \ldots$ individually. Again, horizontal differences address the influence of the viscosity model during mold-filling for both decoupled and coupled approach, whereas vertical differences consider the effect of coupling for both viscosity models.

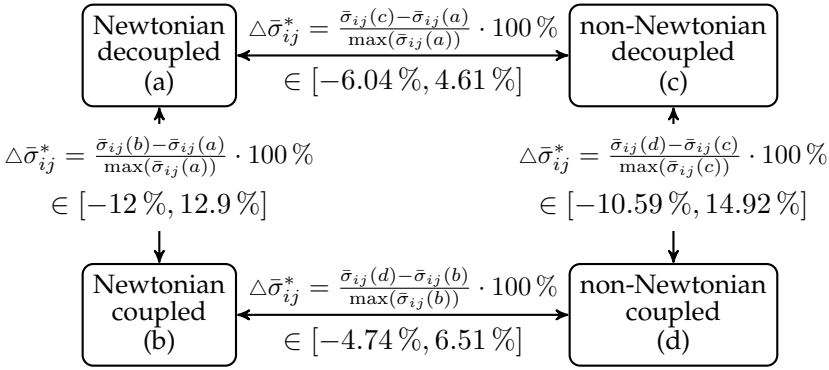

Figure 3.9: Non-dimensional stress difference $\triangle\boldsymbol{\sigma}^*$ and ranges of values with respect to the different mold-filling approaches, adapted from Karl et al. (2023b).

As a supplement to the discussion at hand, Fig. B.3.4 in App. B.3.2 shows the stress field for both the decoupled and the coupled approach regarding the non-Newtonian case during mold-filling. The corresponding stress difference field is given in Fig. 3.10 with the range of values from $-10.59\,\%$ to $+14.92\,\%$. Analogous to the previous section, only

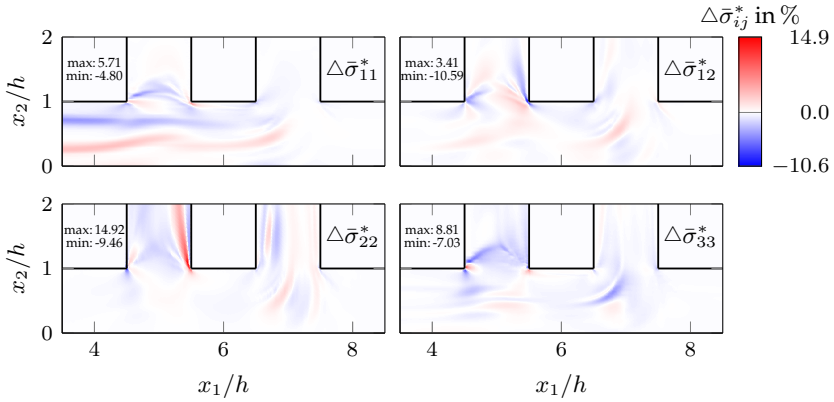

Figure 3.10: Difference field $\triangle\bar{\boldsymbol{\sigma}}^* = (\bar{\boldsymbol{\sigma}}^{\text{coupled}}_{\text{nonNewt.}} - \bar{\boldsymbol{\sigma}}^{\text{decoupled}}_{\text{nonNewt.}}) \cdot 100\,\%/\max(\bar{\boldsymbol{\sigma}}^{\text{decoupled}}_{\text{nonNewtonian}})$ in the area of interest, adapted from Karl et al. (2023b).

the non-dimensional stress difference fields regarding the pure effects of flow-fiber coupling for each viscosity model are considered in the section at hand. For the Newtonian viscosity, Fig. 3.11 addresses these coupling effects with the range $-12\,\%$ to $+12.9\,\%$. All components not shown are zero due to the plane strain state and $N_{13} = N_{23} = 0$. Both ranges indicate that the coupling effect on the fiber orientation evolution during mold-filling has a significant influence on the local stress of the solid composite under load after fluid-solid transition. Please note that normalization is done with each maximum stress component, which emphasizes the importance of the coupling in the context of the specified ranges. If stress peaks occur locally due to the geometry, even small differences in fiber orientation caused by flow-fiber coupling during mold-filling can lead to distinct differences in the stress field. This is the case in the area of the left rib in combination with distinct differences in fiber orientation. There, kinematically complex flow conditions are additionally present, which lead to distinct differences in the fiber orientation, since viscous anisotropy effects are fully present. Even

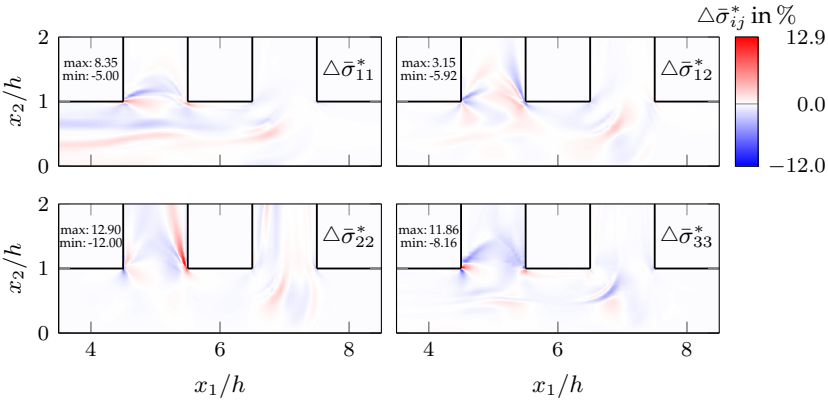

Figure 3.11: Difference field $\triangle\bar{\boldsymbol{\sigma}}^* = (\bar{\boldsymbol{\sigma}}^{\text{coupled}}_{\text{Newtonian}} - \bar{\boldsymbol{\sigma}}^{\text{decoupled}}_{\text{Newtonian}}) \cdot 100\,\%/\max(\bar{\boldsymbol{\sigma}}^{\text{decoupled}}_{\text{Newtonian}})$ in the area of interest, adapted from Karl et al. (2023b).

a small load without stress peaks can lead to significant differences in the local stress in such areas, as is the case, e.g., in the area under the right rib. In summary, also in the context of the stress distribution, both the necessity of coupling and the consideration of shear-thinning matrix behavior are confirmed.

The difference fields regarding the influence of the viscosity model can be found in App. B.3.2. For the decoupled case, the range of the local stress difference is $-6.04\,\%$ to $+4.61\,\%$ as shown in Fig. B.3.5 and for the coupled case, this range is $-4.74\,\%$ to $+6.51\,\%$ as shown in Fig. B.3.6. As a consequence, it can be stated that different viscosity models during mold-filling significantly affect the local stress both for the decoupled and the coupled approach. Compared to the previous section, the relevance of the viscosity model does not change remarkably with flow-fiber coupling, as the range of values is comparable to the decoupled case. However, the difference between the stress fields based on the different viscosity models is not negligible. More details can be found in App. B.3.2.

3.4 Summary and conclusions [18]

This study investigates the effects of flow-fiber coupling during mold-filling with respect to the stress field in the manufactured solid composite after fluid-solid transition. The two-phase mold-filling simulation of the fiber suspension is carried out with the finite volume solver OpenFOAM® based on an extended VOF solver interIsoFoam (OpenFOAM®, 2021). Various methods for numerical stabilization are implemented. The fiber orientation taken from mold-filling simulations is used for the solid composite defining its local anisotropic elastic behavior. The fiber orientation during mold-filling is simulated both with Newtonian and non-Newtonian matrix behavior and also with and without flow-fiber coupling. Both the viscous fiber suspension and the solid fiber reinforced composite are modeled micromechanically in a unified manner using the MT mean-field model (Mori and Tanaka, 1973) with respect to the formulation given in, e.g., Benveniste (1987), Brylka (2017) (p. 38), Hessman et al. (2021), Bertóti and Böhlke (2017), Bertóti et al. (2021), and Karl and Böhlke (2022) as the underlying publication of Sec. 2.6. The simulation of the solid composite is carried out with the finite element solver Abaqus® (Dassault Systèmes®, 2020) using an implemented subroutine for the anisotropic elastic behavior.

The present study is based on the following main assumptions. The fiber geometry is assumed to be constant and the fibers are treated as rigid bodies during mold-filling. Based on the Folgar-Tucker equation with isotropic fiber-fiber interaction referring to Folgar and Tucker III (1984) and Advani and Tucker III (1987), the fiber orientation tensor of the first kind and of second order (Kanatani, 1984) is assumed to be a sufficient measure of anisotropy. The closure problem is treated by using the IBOF closure proposed by Chung and Kwon (2002b) both for the Folgar-Tucker

[18] This section consists of parts from Karl et al. (2023b). Additional text passages have been added.

equation and for orientation averaging. The mold-filling process is modeled incompressible, isothermal, and without fluid-solid transition. To account for two different polymer matrix behaviors during mold-filling, the polymer matrix is modeled as a generalized Newtonian fluid, see Sec. 2.3.1, with embedded rigid fibers, whereas the solid composite and the fibers are modeled linear elastic. Both the fiber suspension and the solid composite are homogenized on the scale of a grid cell, which is seen as a representative volume element including all assumptions listed in Sec. 2.6. The present study is based on a double-rib geometry as a generic injection molding geometry.

Regarding the implemented methods for numerical stabilization, the implicit-explicit splitting is concluded to be important. If it is possible with a solver to treat the coupling term completely implicitly in the linear momentum balance, the highest possible stability will be obtained. However, this is not possible in OpenFOAM®, so further methods have to be implemented to allow flow-fiber coupled simulations with high fiber volume fractions and aspect ratios. Under-relaxation of the explicit part of the coupling term is found to be a powerful method for flows in which low relaxation factors can be used without negatively influencing the solution behavior. When only relatively high relaxation factors can be used, a combination with the method of spatial restriction of the coupling term is recommended. Furthermore, the described treatment of the viscous stress can be used to improve the convergence of the pressure solver. It can be concluded that the stabilization of the code strongly depends on the given problem and that a coordination of the methods is necessary. In this study, the combination of all described stabilization methods leads to a robust numerical behavior, provided that the adaptation of the methods is problem-specific. Since this is difficult a priori, extensive preliminary studies are recommended for a given flow case.

The simulation results can be summarized as follows and the associated conclusions can be drawn:

- **Viscosity effects I.** For both the decoupled and the coupled cases, the choice of the viscosity model has a non-negligible influence on the fiber orientation (decoupled: $-27\,\%$ to $+30\,\%$, coupled: $-40\,\%$ to $+41\,\%$) and on the stress field in the solid composite (decoupled: $-6\,\%$ to $+4.6\,\%$, coupled: $-4.7\,\%$ to $+6.5\,\%$). Since real polymer melts show shear-thinning behavior, the need for this modeling can be quantifiably justified. In this context, it is noted that a non-Newtonian behavior of the fiber suspension at the macroscale is caused by the connection between the fiber orientation evolution and the effective anisotropic viscosity and is not necessarily caused by a non-Newtonian matrix fluid. This statement is related to Kailasam and Ponte Castañeda (1998) and is consistent with the observed flattening of the velocity profile, typical of non-Newtonian fluids, in various studies using Newtonian matrix fluids discussed in Sec. 1.2.1.
- **Viscosity effects II.** The differences in fiber orientation between the viscosity models are greater in the coupled case than in the decoupled case. In this context, the differences in the stress field in the decoupled and coupled case are comparable. It can be concluded that the relevance of the shear-thinning behavior increases with coupling.
- **Flow-fiber coupling effects.** For both viscosity models considered, it is shown that the coupling has a significant influence on the fiber orientation (Newtonian: $-36\,\%$ to $+31\,\%$, non-Newtonian: $-37\,\%$ to $+38\,\%$) and on the stress field (Newtonian: $-12\,\%$ to $+12.9\,\%$, non-Newtonian: $-10.6\,\%$ to $+14.9\,\%$). Based on the fact that the anisotropic viscosity model describes the real fiber suspension more physically than neglecting of fiber-induced viscous anisotropy, the implementation of flow-fiber coupling is recommended.

- **Viscosity effects III.** The influence of flow-fiber coupling is quite comparable for both viscosity models. Only the comparison between the two viscosity models reveals the necessity of the shear-thinning behavior.
- **Actual mold-filling process.** The two-phase simulation approach leads to distinct differences in the local fiber orientation compared to the steady-state flow through the geometry. Therefore, changes in the kinematics due to the actual filling process must be predicted by the simulation setup in order to estimate the local anisotropic properties.

Finally, it should be noted that the assumptions described before are aimed at considering only the effects of flow-fiber coupling on the fiber orientation and thus on the stress field in the solid. Influences that are more complex than the viscous behavior of the matrix are therefore not taken into account, such as the effects of temperature, fiber-induced anisotropic heat conduction, and fluid-solid transition. In this context, the recent publication of Dietemann and Bierwisch (2022) indicates that accurate rheological modeling has a greater impact on fiber orientation, and thus on the resulting stress field, than complex modeling of orientation dynamics. In addition, the anisotropic mechanical behavior in this chapter is estimated based on mean-field homogenization, which has advantages in terms of computational effort. In particular, the mold-filling simulation requires a computationally efficient estimation of the anisotropic viscosity at each grid cell. On the other hand, critical stress peaks in the highly heterogeneous microstructure are not resolved by mean-field methods, as is the case with full-field approaches, see App. A. As a consequence, the conclusions above have to be interpreted in this context. Moreover, it is noted that injection molding processes are often modeled as flows through narrow gaps, as discussed by, e.g., Tucker III (1991). In the present chapter, this so-called Hele-Shaw simplification, see, e.g., Spurk and

Aksel (2020) (pp. 282–283) and Sec. 1.2.1, is deliberately omitted because the geometry under consideration is complex. An additional point is that the short-fiber orientation dynamics can be influenced by small wall distances in such a way that the movement of the fibers is restricted. In the literature this is referred to as confined flow, for which the modeling of fiber orientation evolution is adapted in the studies of, e.g., Perez et al. (2016) and Scheuer et al. (2016). Regarding these so-called wall effects, additional reference is made to, e.g., Ingber and Mondy (1994), Ozolins and Strautins (2014), and Li et al. (2021). In this context it is noted that the present study assumes that the short-fiber orientation evolves without any geometric constraints. This assumption is supported by the fact that the fibers are approximately 5 to 25 times shorter than the characteristic length $h = 2.5\,\mathrm{mm}$ of the considered rib geometry, since the fixed aspect ratio $\alpha = 20$ and the diameter range of glass fibers from $5\,\mu\mathrm{m}$ to $24\,\mu\mathrm{m}$ (Schürmann, 2007) (p. 28) results in a total fiber length of $0.1\,\mathrm{mm}$ to $0.48\,\mathrm{mm}$.

In the context of cavities with small wall distances, the question of the necessity of flow-fiber coupling must be asked. According to Advani and Tucker III (1987), the parameter values $\alpha = 20$ and $c_\mathrm{F} = 0.2$ chosen in this chapter are common values for fiber suspensions and, based on the model of Dinh and Armstrong (1984), they highlight the strongly anisotropic viscosity for these parameters. Although Advani and Tucker III (1987) motivate the flow-fiber coupled approach as a thorough procedure, they also mention that especially for cavities with small wall distances the decoupled approach may be adequate. It is shown in Sec. B.4 in App. B that the simulation setup considered in this chapter corresponds to the general narrow gap flow (Tucker III, 1991), which legitimizes the applied fully coupled approach in 3D without simplifications, see also Tucker III (2022a) (pp. 196–198).

Chapter 4

Symmetric quadratic closure

Contents overview. This chapter regards the second topic of this thesis, which deals with the development and investigation of new closure methods as a further element of the micromechanical modeling of short-fiber orientation dynamics. After introducing the common QC as a starting point, the matrix notation of fourth-order tensors is briefly discussed as a fundamental part, which is the basis for the implementation in this thesis. The prediction quality of the common QC is analyzed and based on this, two versions of a novel symmetric QC are proposed, the first version for estimating effective anisotropic properties and the second version for predicting orientation evolution.

4.1 Standard quadratic closure [1]

The closure function of the standard QC reads (Doi, 1981; Advani and Tucker III, 1987; 1990)

$$\mathbb{F}(\boldsymbol{N}) = \boldsymbol{N} \otimes \boldsymbol{N}. \tag{4.1}$$

To motivate the symmetric quadratic closure (SQC) as a simple improvement of the standard QC, the section at hand addresses the accuracy of QC in view of approximating exemplary orientation states. As a first

[1] This section consists of parts from Karl et al. (2021b). Additional text passages have been added.

step, details about the matrix representation of fourth-order orientation tensors are provided.

Throughout this thesis, fourth-order tensors are implemented in the normalized Voigt notation with the base system $\mathbb{B}_{ij} = \boldsymbol{B}_i \otimes \boldsymbol{B}_j$ and the six orthonormal second-order base tensors $\boldsymbol{B}_i$ $(i = 1, \ldots, 6)$ defined as follows (Böhlke and Brüggemann, 2001)

$$\begin{aligned} \boldsymbol{B}_1 &= \boldsymbol{e}_1 \otimes \boldsymbol{e}_1, & \boldsymbol{B}_4 &= \sqrt{2}\,\mathrm{sym}(\boldsymbol{e}_2 \otimes \boldsymbol{e}_3), \\ \boldsymbol{B}_2 &= \boldsymbol{e}_2 \otimes \boldsymbol{e}_2, & \boldsymbol{B}_5 &= \sqrt{2}\,\mathrm{sym}(\boldsymbol{e}_1 \otimes \boldsymbol{e}_3), \\ \boldsymbol{B}_3 &= \boldsymbol{e}_3 \otimes \boldsymbol{e}_3, & \boldsymbol{B}_6 &= \sqrt{2}\,\mathrm{sym}(\boldsymbol{e}_1 \otimes \boldsymbol{e}_2). \end{aligned} \tag{4.2}$$

By using Eq. (4.2), the normalized fourth-order tensor $\mathbb{N}$ reads as follows referring to Böhlke and Brüggemann (2001) in the adapted matrix formulation proposed by Voigt (1910) (pp. 584–587)

$$\begin{aligned} \mathbb{N} &= \begin{pmatrix} N_{1111} & N_{1122} & N_{1133} & \sqrt{2}N_{1123} & \sqrt{2}N_{1113} & \sqrt{2}N_{1112} \\ & N_{2222} & N_{2233} & \sqrt{2}N_{2223} & \sqrt{2}N_{2213} & \sqrt{2}N_{2212} \\ & & N_{3333} & \sqrt{2}N_{3323} & \sqrt{2}N_{3313} & \sqrt{2}N_{3312} \\ & & & 2N_{2323} & 2N_{2313} & 2N_{2312} \\ & & & & 2N_{1313} & 2N_{1312} \\ \mathrm{sym} & & & & & 2N_{1212} \end{pmatrix} \mathbb{B}_{ij} \\ &= \begin{pmatrix} N_{1111} & N_{1122} & N_{1133} & \sqrt{2}N_{1123} & \sqrt{2}N_{1113} & \sqrt{2}N_{1112} \\ & N_{2222} & N_{2233} & \sqrt{2}N_{2223} & \sqrt{2}N_{2213} & \sqrt{2}N_{2212} \\ & & N_{3333} & \sqrt{2}N_{3323} & \sqrt{2}N_{3313} & \sqrt{2}N_{3312} \\ & & & 2N_{2233} & 2N_{3312} & 2N_{2213} \\ & & & & 2N_{1133} & 2N_{1123} \\ \mathrm{sym} & & & & & 2N_{1122} \end{pmatrix} \mathbb{B}_{ij}. \end{aligned} \tag{4.3}$$

It should be noted that the notation above is also known as the Mandel notation (Mandel, 1965) and additional reference is made to, e.g., Fedorov (1968) (pp. 12–18), Mehrabadi and Cowin (1990), and Cowin and

Mehrabadi (1992). As addressed by, e.g., Böhlke and Brüggemann (2001), the notation above has the advantage over Voigt's notation in that the eigenvalues, eigentensors, and invariants of the 6×6 matrix correspond to those of the underlying fourth-order tensor. The first line of Eq. (4.3) refers to the standard normalized Voigt notation of fourth-order tensors having both minor symmetries and the main symmetry leading to 21 independent components in case of maximum anisotropy (Böhlke and Brüggemann, 2001). Using both the full index symmetry of $\mathbb{N}$ and the trace condition, the second line of Eq. (4.3) can be formulated with respect to 14 independent components in case of maximum anisotropy as described by, e.g., Bauer et al. (2023). Both lines of Eq. (4.3) differ in how to apply the QC, e.g.,

$$N_{1212} \approx N_{12}N_{12} \neq N_{11}N_{22} \approx N_{1122}. \tag{4.4}$$

Therefore, both lines of Eq. (4.3) induce a different approximation error, which also depends on the orientation state, regarding the index symmetry which cannot be avoided when the QC is used. Throughout this work, the second line of Eq. (4.3) is used for the fourth-order fiber orientation tensor. In the following, the exact unidirectional (UD), isotropic (ISO), and planar isotropic (PI) orientation states are explored to assess the approximation error induced by the QC

$$\begin{aligned}
\mathbb{N}_{\mathsf{UD}} &= \boldsymbol{e}_1 \otimes \boldsymbol{e}_1 \otimes \boldsymbol{e}_1 \otimes \boldsymbol{e}_1, \\
\mathbb{N}_{\mathsf{ISO}} &= \frac{1}{3}\mathbb{P}_1 + \frac{2}{15}\mathbb{P}_2, \\
\mathbb{N}_{\mathsf{PI}} &= \frac{3}{8}(\boldsymbol{e}_1^{\otimes 4} + \boldsymbol{e}_2^{\otimes 4}) + \frac{1}{8}(\boldsymbol{e}_1^{\otimes 2} \otimes \boldsymbol{e}_2^{\otimes 2} + \boldsymbol{e}_2^{\otimes 2} \otimes \boldsymbol{e}_1^{\otimes 2}) + \frac{1}{8}\boldsymbol{e}_1 \otimes \boldsymbol{e}_2 \otimes \boldsymbol{e}_1 \otimes \boldsymbol{e}_2.
\end{aligned} \tag{4.5}$$

Please note that the tensors given in Eq. (4.5) have to be transformed to the normalized Voigt notation. The closure input, or in other words the analytical second-order orientation tensors $\boldsymbol{N}$ related to the fourth-order

orientation tensors $\mathbb{N}$ given in Eq. (4.5), are as follows

$$\boldsymbol{N}_{\mathsf{UD}} = \boldsymbol{e}_1^{\otimes 2}, \qquad \boldsymbol{N}_{\mathsf{ISO}} = \frac{1}{3}\boldsymbol{I}, \qquad \boldsymbol{N}_{\mathsf{PI}} = \frac{1}{2}(\boldsymbol{e}_1^{\otimes 2} + \boldsymbol{e}_2^{\otimes 2}). \tag{4.6}$$

For the common fiber orientation states given in Eqs. (4.5) and (4.6), reference is made to, e.g., Moakher and Basser (2015). Furthermore, three different experimentally measured fourth-order orientation tensors are used to investigate the error of the QC. In this work, the tensors $\mathbb{N}(0°)$, $\mathbb{N}(45°)$, and $\mathbb{N}(90°)$ are used with the appropriate closure input $\boldsymbol{N}(0°)$, $\boldsymbol{N}(45°)$, and $\boldsymbol{N}(90°)$ of Kehrer et al. (2020). Note that the corresponding components given in Tab. 5 of Kehrer et al. (2020) have to be transformed to the normalized Voigt notation. As already addressed before, algebraic operations acting on $\mathbb{N}$ are valid only under this condition. To make this thesis self-contained, the fiber orientation tensors related to Kehrer et al. (2020) are provided in App. C.1. The following error measure $e(\mathbb{N}_{\mathsf{closure}}, \mathbb{N})$ is used for the closure investigation with $\mathbb{N}$ based on the analytical tensors given Eq. (4.5) and on the experimental data $\mathbb{N}(0°)$, $\mathbb{N}(45°)$, and $\mathbb{N}(90°)$ referring to Kehrer et al. (2020)

$$e = \frac{\|\mathbb{N}_{\mathsf{closure}}(\boldsymbol{N}) - \mathbb{N}\|}{\|\mathbb{N}\|}. \tag{4.7}$$

For comparison, the IBOF closure proposed by Chung and Kwon (2002b) is used and should not be reviewed in the present chapter. The IBOF closure is chosen to represent modern closure approaches based on parameter fitting to match the results of ODF level computations. Regarding ODF level computations, the reader is referred to the studies of, e.g., Mezi et al. (2019a), Férec et al. (2020), and to further works discussed in Sec. 1.2.3. In Tab. 4.1, the results corresponding to Eq. (4.7) are shown for the chosen fiber orientation states. Please note that the tensors given in Eq. (4.6) and $\boldsymbol{N}(0°)$, $\boldsymbol{N}(45°)$, and $\boldsymbol{N}(90°)$ provided in App. C.1 are used as closure inputs.

$\mathbb{N}$	$e(\mathbb{N}_{\mathsf{QC}}, \mathbb{N})$	$e(\mathbb{N}_{\mathsf{IBOF}}, \mathbb{N})$
UD	0.00	$6.5 \cdot 10^{-4}$
ISO	0.54	$2.2 \cdot 10^{-15}$
PI	0.58	$5.9 \cdot 10^{-5}$
$0°$	0.36	0.14
$45°$	0.34	0.16
$90°$	0.38	0.16

Table 4.1: Error measure e for QC and IBOF for different fiber orientation states $\mathbb{N}$, adapted from Karl et al. (2021b).

As already established in the literature, e.g., Advani and Tucker III (1987) and Dupret and Verleye (1999) and as shown in Tab. 4.1, the QC leads to exact results when the fibers are strictly aligned. When the fiber orientation state turns out to be isotropic or PI, the QC leads to errors that are much higher than for the IBOF closure. For measured fiber orientation states that are close to PI referring to Kehrer et al. (2020), the QC gives errors that are approximately two times higher than the IBOF-related errors. Compared to the exact orientation states, the difference between these two closures decreased for the measured orientation data.

4.2 Symmetric quadratic closure [2]

Building on the previous section, the SQC is proposed to improve the prediction accuracy while maintaining the algebraically simple quadratic representation. It should be noted that the prediction accuracy of a closure in view of approximating the fourth-order orientation tensor $\mathbb{N}$ is directly linked to the prediction accuracy of anisotropic mechanical properties via the orientation average of Advani and Tucker III (1987).

[2] This section consists of parts from Karl et al. (2021b). Additional text passages have been added.

The SQC is developed in two versions, the first version delivering better predictions of effective mechanical properties, the second version of flow-induced orientation evolution. As already addressed in Secs. 1.2.2 and 1.3.2, the proposed SQC joins, e.g., the symmetric quadratic closures proposed by Kröger et al. (2008) and Kim et al. (2015). In view of approximating the entire closure term of the Folgar-Tucker equation (2.43), the second version of the proposed SQC follows the idea of Hinch and Leal (1976).

4.2.1 First version for estimating effective properties [3]

Based on one term of the generalized HYB closure introduced by Petty et al. (1999), the first step towards an improvement of QC contains the symmetrization of $\boldsymbol{N}\otimes\boldsymbol{N}$ ensuring the complete index symmetry, or in other words, the computation of a fourth-order orientation tensor that is symmetric in all index pairs

$$\mathrm{sym}(\boldsymbol{N}\otimes\boldsymbol{N}) = \frac{1}{3}\big(\boldsymbol{N}\otimes\boldsymbol{N} + \boldsymbol{N}\square\boldsymbol{N} + (\boldsymbol{N}\square\boldsymbol{N})^{\mathsf{T_R}}\big). \tag{4.8}$$

Based on Eq. (4.8), the second step of improvement is defined by normalizing Eq. (4.8) so that the trace condition $\mathrm{tr}(\mathbb{N}) = \mathbb{N}\cdot\mathbb{I} = 1$, discussed in Sec. 2.5 in the context of the closure problem fundamentals, is fulfilled leading to the closure function of the first version of SQC

$$\mathbb{F}(\boldsymbol{N}) = \frac{\mathrm{sym}(\boldsymbol{N}\otimes\boldsymbol{N})}{\frac{1}{3}(1+2\|\boldsymbol{N}\|^2)}. \tag{4.9}$$

The normalization factor used in Eq. (4.9) results from

$$\mathrm{tr}(\mathrm{sym}(\boldsymbol{N}\otimes\boldsymbol{N})) = \mathrm{sym}(\boldsymbol{N}\otimes\boldsymbol{N})\cdot(\boldsymbol{I}\square\boldsymbol{I}), \tag{4.10}$$

[3] This section consists of parts from Karl et al. (2021b). Additional text passages have been added.

which leads to the sought representation by applying $\mathrm{tr}(\boldsymbol{N}) = 1$

$$\begin{aligned}\mathrm{tr}(\mathrm{sym}(\boldsymbol{N}\otimes\boldsymbol{N})) &= \frac{1}{3}(N_{ij}N_{kl} + N_{ik}N_{lj} + N_{il}N_{kj})\delta_{ik}\delta_{lj} \\ &= \frac{1}{3}(N_{ii}N_{jj} + 2N_{ij}N_{ij}) \\ &= \frac{1}{3}(1 + 2\|\boldsymbol{N}\|^2). \end{aligned} \tag{4.11}$$

It should be pointed out that compared to the original QC, the following fundamental properties listed in, e.g., Petty et al. (1999) have been lost at the expense of the two improvement steps already described

$$\mathbb{N}[\boldsymbol{I}] \neq \boldsymbol{N}, \qquad \mathrm{tr}(\mathbb{N}[\boldsymbol{D}]) \neq \boldsymbol{D}\cdot\boldsymbol{N}, \tag{4.12}$$

with $\mathbb{N}$ approximated based on the closure function of SQC given in Eq. (4.9). In the framework of estimating the effective anisotropic behavior based on given orientation states $\boldsymbol{N}$, the complete index symmetry and the trace condition are more important than fulfilling the conditions given in Eq. (4.12). As already addressed in Sec. 2.5, it is clarified that for exact tensors $\boldsymbol{N}$ and $\mathbb{N}$, the trace conditions $\mathrm{tr}(\mathbb{N}) = 1$ and $\mathrm{tr}(\boldsymbol{N}) = 1$ are connected as follows by using the complete index symmetry of $\mathbb{N}$ and the property $\mathbb{N}[\boldsymbol{I}] = \boldsymbol{N}$

$$\begin{aligned}\mathrm{tr}(\mathbb{N}) = \mathbb{N}\cdot\mathbb{I} = N_{ijkl}\delta_{ik}\delta_{lj} = N_{ijij} = N_{iijj} = \boldsymbol{I}\cdot\mathbb{N}[\boldsymbol{I}] \\ = \boldsymbol{I}\cdot\boldsymbol{N} = \mathrm{tr}(\boldsymbol{N}) = 1. \end{aligned} \tag{4.13}$$

This is not the case for SQC since the contraction condition is violated $\mathbb{N}[\boldsymbol{I}] \neq \boldsymbol{N}$. Please note that the closure function $\mathbb{F}(\boldsymbol{N})$ given in Eq. (4.9) cannot be used to close the Folgar-Tucker equation, since $\mathrm{tr}(\dot{\boldsymbol{N}}) = 0$ is violated. For that reason, Eq. (4.9) is a method to subsequently calculate $\mathbb{N}$ based on a given $\boldsymbol{N}$ and refers to the well-known closure procedure compactly represented by a fourth-order tensor function $\mathbb{N} \approx \mathbb{F}(\boldsymbol{N})$.

4.2.2 Second version for predicting orientation evolution [4]

The second version of SQC is developed in order to be used in the Folgar-Tucker equation describing the fiber orientation evolution. In contrast to the first version of SQC, the second version approximates the linear mapping $\mathbb{N}[\boldsymbol{D}]$, called closure term, appearing in the Folgar-Tucker equation. Using a general function $\boldsymbol{G}$, this closure scheme reads $\mathbb{N}[\boldsymbol{D}] \approx \boldsymbol{G}(\boldsymbol{N}, \boldsymbol{D})$. One important property is that the orientation tensor $\mathbb{N}$ can only be computed independently of the strain-rate tensor $\boldsymbol{D}$, if the function $\boldsymbol{G}$ is linear in $\boldsymbol{D}$. In all other cases, $\mathbb{N}$ depends on the deformation process. As already addressed in Sec. 1.2.2, the current approach of approximating $\mathbb{N}[\boldsymbol{D}]$ has been pursued already by Hinch and Leal (1976), who distinguish between intense (isotropic states, C_I large) and weak (aligned states, C_I small) fiber-fiber interactions, which is also addressed by Advani and Tucker III (1990). Hinch and Leal (1976) obtained the so-called composite closure by approximating these two extreme alignment states via an interpolation. Advani and Tucker III (1990) provide a comprehensive description of such closures, which approximate $\mathbb{N}[\boldsymbol{D}]$ instead of $\mathbb{N}$, and they extracted expressions for $\mathbb{N}$ for the previously mentioned linearity of $\boldsymbol{G}$ with respect to $\boldsymbol{D}$. Note that the term $\mathbb{N}[\boldsymbol{D}]$ does not only occur in the Folgar-Tucker equation, but also in material models, e.g., Eqs. (3.3) and (3.4), predicting the anisotropic viscous behavior of fiber suspensions. As a consequence, using the scheme $\mathbb{N}[\boldsymbol{D}] \approx \boldsymbol{G}(\boldsymbol{N}, \boldsymbol{D})$, the influence of the deformation process on the viscous anisotropy is improved by SQC compared to QC in the context of flow-fiber coupling.

The procedure of finding the closure function $\boldsymbol{G}(\boldsymbol{N}, \boldsymbol{D})$ preserving $\mathrm{tr}(\boldsymbol{N}) = 1$ in the context of SQC is given in App. C.2. The idea is to

[4] This section consists of parts from Karl et al. (2021b). Additional text passages have been added.

introduce a scalar factor $\kappa(\boldsymbol{N}, \boldsymbol{D})$ associated with the closure term in the Folgar-Tucker equation. The quantity κ is determined by forcing $\mathrm{tr}(\dot{\boldsymbol{N}}) = 0$. Based on the analysis shown in App. C.2, the following expression holds for κ depending on the local flow and orientation state

$$\kappa = \begin{cases} 0, & \boldsymbol{N} = \boldsymbol{N}_{\mathsf{ISO}} \text{ and/or } \boldsymbol{D} = \boldsymbol{0}, \\ \dfrac{6\boldsymbol{N}\cdot\boldsymbol{D}}{\boldsymbol{N}\cdot\boldsymbol{D} + 2\boldsymbol{D}\cdot\boldsymbol{N}^2}, & \boldsymbol{N} \neq \boldsymbol{N}_{\mathsf{ISO}}, \boldsymbol{D} \neq \boldsymbol{0}. \end{cases} \tag{4.14}$$

It is important to note that κ depends only on the direction of $\boldsymbol{D}$ and not on the magnitude $\|\boldsymbol{D}\|$. Since the normalization factor used in Eq. (4.9) cancels out as shown in App. C.2, the Folgar-Tucker equation (2.43) with SQC and κ defined in Eq. (4.14) reads

$$\begin{aligned} \dot{\boldsymbol{N}} &= \boldsymbol{W}\boldsymbol{N} - \boldsymbol{N}\boldsymbol{W} + \xi\big(\boldsymbol{D}\boldsymbol{N} + \boldsymbol{N}\boldsymbol{D} - \kappa\,\mathrm{sym}(\boldsymbol{N}\otimes\boldsymbol{N})[\boldsymbol{D}]\big) \\ &\quad + 2C_{\mathsf{I}}\dot{\gamma}(\boldsymbol{I} - 3\boldsymbol{N}) \\ &= \boldsymbol{W}\boldsymbol{N} - \boldsymbol{N}\boldsymbol{W} + \xi\big(\boldsymbol{D}\boldsymbol{N} + \boldsymbol{N}\boldsymbol{D} - \frac{\kappa}{3}(\boldsymbol{N}\cdot\boldsymbol{D})\boldsymbol{N} - \frac{2\kappa}{3}\boldsymbol{N}\boldsymbol{D}\boldsymbol{N}\big) \\ &\quad + 2C_{\mathsf{I}}\dot{\gamma}(\boldsymbol{I} - 3\boldsymbol{N}). \end{aligned} \tag{4.15}$$

Detailed information concerning the case distinction of κ can be found in App. C.2. Please note that only incompressible flows are considered.

4.3 Results and discussion [5]

In the following, the quality of SQC is investigated by considering the analytical orientation states given in Sec. 4.1 and the experimental data given in App. C.1 referring to Kehrer et al. (2020). The respective closure-induced error $e(\mathbb{N}_{\mathsf{closure}}, \mathbb{N})$ defined in Eq. (4.7) is given in Tab. 4.2.

[5] This section consists of parts from Karl et al. (2021b). Additional text passages have been added.

Based on the results, a significant improvement of the original QC can be observed for all considered examplary orientation states. For all analytically given orientation states, SQC leads to smaller errors than the IBOF closure.

$\mathbb{N}$	$e(\mathbb{N}_{\mathsf{QC}}, \mathbb{N})$	$e(\mathbb{N}_{\mathsf{SQC}}, \mathbb{N})$	$e(\mathbb{N}_{\mathsf{IBOF}}, \mathbb{N})$
UD	0.00	0.00	$6.5 \cdot 10^{-4}$
ISO	0.54	$2.3 \cdot 10^{-16}$	$2.2 \cdot 10^{-15}$
PI	0.58	$9.1 \cdot 10^{-17}$	$5.9 \cdot 10^{-5}$
$0°$	0.36	0.22	0.14
$45°$	0.34	0.20	0.16
$90°$	0.38	0.20	0.16

Table 4.2: Error measure e for QC, SQC, and IBOF for different fiber orientation states $\mathbb{N}$, adapted from Karl et al. (2021b).

To illustrate the quality of SQC compared to QC and IBOF, the direction-dependent normalized effective Young's modulus $\bar{E}(\varphi)/E_{\mathsf{M}}$ is shown in Fig. 4.1 based on the measured data of Kehrer et al. (2020) provided in App. C.1. Regarding the underlying computation, reference is made to the context of Eq. (5.53) for the effective stiffness tensor and to Eq. (5.54) for the direction-dependent effective Young's modulus. The angle $\varphi \in [0, 2\pi)$ represents the tensile direction restricted to the $\boldsymbol{e}_1$–$\boldsymbol{e}_2$-plane. Glass fiber-reinforced UPPH matrix material is considered with the following values for Young's modulus E and Poisson's ratio ν (Kehrer et al., 2020)

$$E_{\mathsf{M}} = 3.4\,\mathrm{GPa}, \quad \nu_{\mathsf{M}} = 0.385, \quad E_{\mathsf{F}} = 73\,\mathrm{GPa}, \quad \nu_{\mathsf{F}} = 0.22. \tag{4.16}$$

Throughout this section, $c_{\mathsf{F}} = 0.1$ and $\alpha = 10$ are used to represent anisotropic properties. The black curves in Fig. 4.1 refer to the measured fiber orientation data $\boldsymbol{N}$ and $\mathbb{N}$ (Kehrer et al., 2020) as a direct input of the stiffness prediction. All other curves represent stiffness predictions

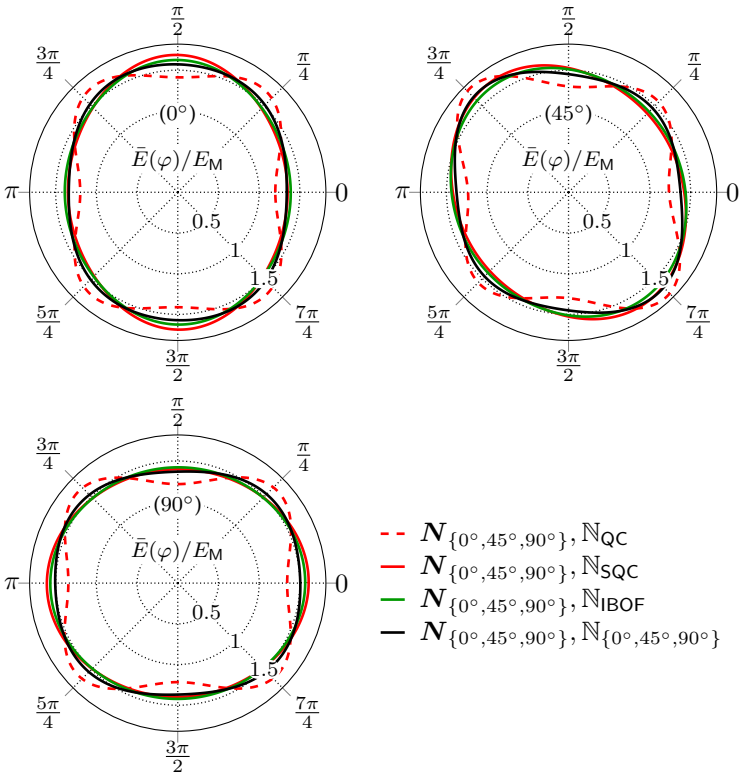

Figure 4.1: Comparison of QC, SQC, and IBOF in view of the direction-dependent normalized effective Young's modulus in the $\boldsymbol{e}_1$–$\boldsymbol{e}_2$-plane, adapted from Karl et al. (2021b).

based on the measured $\boldsymbol{N}$ (Kehrer et al., 2020) and three different closure methods for approximating $\mathbb{N}$. The results show that there are only small differences between SQC and IBOF, whereas SQC is superior to IBOF in terms of implementation and computational effort. This statement is supported by the results in the Secs. 5.4.2 and 5.4.3 in the following chapter 5, where an additional fiber orientation state and a new composite with different material parameters are considered and the computational effort is analyzed for various closures.

The performance of SQC as a closure of the Folgar-Tucker equation (2.43) is shown in Fig. 4.2 for a simple shear flow as given in Sec. 5.4.1. For comparison, the results referring to the QC and to the IBOF closure are given additionally. Since the simple shear flow is homogeneous, the Folgar-Tucker equation reduces to an ordinary differential equation for $\boldsymbol{N}$ which is integrated with a fourth-order Runge-Kutta method (Deuflhard and Bornemann, 2008) (pp. 140–153) in this chapter with the fixed time step size $\triangle t = 0.01\,\mathrm{s}$. The components N_{ij} are plotted over the total shear $\dot{\gamma}t$. The results in Fig. 4.2(a) refer to $\alpha = 10$ and $C_\mathrm{I} = 0.005$ and show that SQC improves the results of QC significantly if the IBOF-related results are seen as an evaluation basis. To conclude this section, the results for a simple shear flow with $\alpha \to \infty$ and $C_\mathrm{I} = 0.005$ are shown in Fig. 4.2(b). It can be observed that, in relation to IBOF, the quality of the SQC-predicted fiber orientation state has improved for $\alpha \to \infty$ compared to the results shown in Fig. 4.2(a).

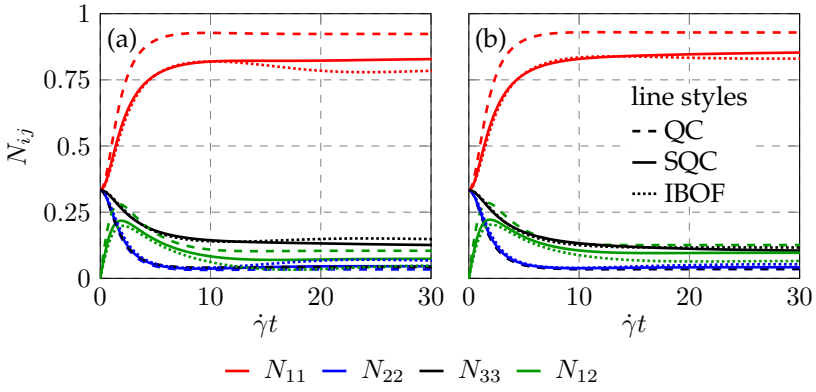

Figure 4.2: Evolution of the orientation tensor components N_{ij} plotted over the total shear $\dot{\gamma}t$ in a simple shear flow for QC, SQC, and IBOF based on $C_\mathrm{I} = 0.005$, $\alpha = 10$ in (a), and $\alpha \to \infty$ in (b), adapted from Karl et al. (2021b).

4.4 Summary and conclusions [6]

At the beginning of this chapter, the matrix notation of fourth-order tensors is revisited and restricted to fully symmetric fourth-order fiber orientation tensors. Based on a scalar error measure, the prediction accuracy of QC is investigated for the standard orientation states UD, PI, and ISO. In addition, three measured fiber orientation states related to Kehrer et al. (2020) serve as a basis for the investigation. The recognized drawbacks of QC are improved by postulating a normalized fully symmetric QC, the first version of SQC, which enhances the predicted material symmetry. This approach is validated by comparing the results with IBOF-related predictions. Furthermore, the introduced closure preserves the simple quadratic structure and proves to be a fast and accurate method for estimating the anisotropic behavior of fiber suspensions and fiber reinforced composites. In this context, Karl et al. (2021b) show through additional investigations how the prediction of effective viscous and elastic properties can be improved if the first version of SQC is used instead of QC. To do this, Karl et al. (2021b) use their derived analytical expressions for the asymptotic fiber orientation states of the Folgar-Tucker equation (2.43) to predict the corresponding anisotropic mechanical properties, based on both QC and SQC. The asymptotic orientation states are specified for different flow conditions and depend on both the aspect ratio α of the fibers and on the fiber interaction parameter C_I.

An adaptation of the new closure is developed for its use in the Folgar-Tucker equation, which represents the second version of SQC. In this context, an additional scalar parameter depending on the local orientation and the kinematic state is introduced. The result is a simple closure function approach depending on the deformation process, based on the

[6] This section consists of parts from Karl et al. (2021b). Additional text passages have been added.

idea originally introduced by Hinch and Leal (1976) and also discussed by Advani and Tucker III (1990), of approximating the second-order closure term $\mathbb{N}[\boldsymbol{D}]$ instead of the fourth-order orientation tensor $\mathbb{N}$. Using an explicit integration scheme, the improvement of QC by SQC in the context of fiber orientation evolution governed by the Folgar-Tucker equation is demonstrated in a simple shear flow for two different aspect ratios and a fixed fiber-fiber interaction parameter.

Chapter 5

Symmetric implicit closures

Contents overview. Following the previous chapter, this chapter describes the development of a novel closure approach, which is referred to as the fully symmetric implicit closure. First, the implicit closure concept is introduced in general, and subsequently two special cases are discussed. These special cases are the implicit formulations of classical closures, namely the quadratic and the hybrid closure. Both closures are discussed in terms of their solution procedure, which involves the reduction to the solution of a non-linear 1D problem, their realizability by an ODF, and their accuracy both in predicting orientation evolution and in estimating effective anisotropic viscous and elastic properties.

5.1 Implicit closure approach [1]

The novel implicit closure approach consists of using the property $\mathbb{N}[\boldsymbol{I}] = \boldsymbol{N}$, referring to the contraction condition introduced in Sec. 2.4.1, in terms of an arbitrary fully symmetric closure function $\mathbb{F}$ with an unknown positive semi-definite and symmetric tensor $\boldsymbol{B}$, called implicit closure tensor, instead of $\boldsymbol{N}$ as the argument such that the contraction condition

$$\mathbb{F}(\boldsymbol{B})[\boldsymbol{I}] = \boldsymbol{N} \tag{5.1}$$

[1] This section consists of parts from Karl et al. (2023a). Additional text passages have been added.

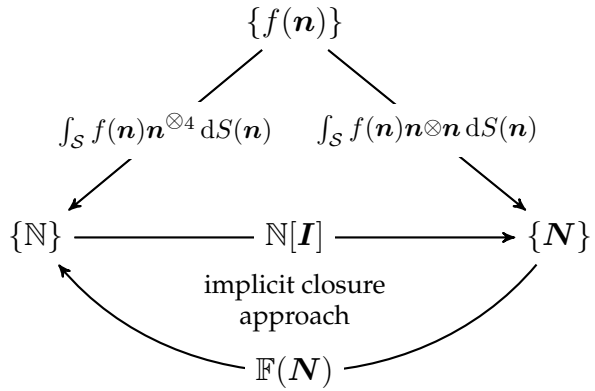

Figure 5.1: Graphical representation of the relationship between the ODF f and the fiber orientation tensors $\boldsymbol{N}$ and $\mathbb{N}$ for a realizable closure function $\mathbb{F}(\boldsymbol{N})$, adapted from Karl et al. (2023a).

is satisfied. Equation (5.1) implies that $\boldsymbol{B}$ is a function of $\boldsymbol{N}$ for a chosen closure function.[2] In order to approximate the fourth-order orientation tensor $\mathbb{N}$ in terms of $\mathbb{F}(\boldsymbol{B})$, the equation

$$\boldsymbol{F}(\boldsymbol{B}) = \boldsymbol{0} \tag{5.2}$$

has to be solved for the tensor $\boldsymbol{B}$ with the function $\boldsymbol{F}(\boldsymbol{B})$ defined as follows

$$\boldsymbol{F}(\boldsymbol{B}) = \mathbb{F}(\boldsymbol{B})[\boldsymbol{I}] - \boldsymbol{N}. \tag{5.3}$$

In general, $\boldsymbol{F}(\boldsymbol{B})$ is non-linear in $\boldsymbol{B}$, which is why Newton's method is used as follows

$$\boldsymbol{B}_{n+1} = \boldsymbol{B}_n - \left(\frac{\partial \boldsymbol{F}(\boldsymbol{B}_n)}{\partial \boldsymbol{B}_n}\right)^{-1} [\boldsymbol{F}(\boldsymbol{B}_n)] \tag{5.4}$$

[2] Formally, the approximation $\mathbb{N} \approx \mathbb{F}(\boldsymbol{N})$ is replaced by $\mathbb{N} \approx \mathbb{G}(\boldsymbol{B})$. In general, the tensors $\boldsymbol{B}$ and $\boldsymbol{N}$ are connected via $\boldsymbol{G}(\boldsymbol{B}) = \boldsymbol{N}$ leading to the alternative formulation of the closure approximation $\mathbb{F}(\boldsymbol{N}) = \mathbb{G}(\boldsymbol{G}^{-1}(\boldsymbol{N}))$ with the general functions $\boldsymbol{G}$ and $\mathbb{G}$.

similar to the well-known basic scheme given in, e.g., Deuflhard (2011) (p. 22) with an appropriate initial guess, e.g., $\boldsymbol{B}_0 = \boldsymbol{N}$ and n as the iteration index. The relationship previously addressed in Sec. 2.4.1 between the ODF f and the fiber orientation tensors $\boldsymbol{N}$ and $\mathbb{N}$ is shown graphically for a realizable closure function $\mathbb{F}(\boldsymbol{N})$ in Fig. 5.1. In particular, it is illustrated that the implicit closure approach is located between the fiber orientation tensors $\boldsymbol{N}$ and $\mathbb{N}$ based on the contraction property $\mathbb{N}[\boldsymbol{I}] = \boldsymbol{N}$. As discussed in Sec. 2.5, the second-order fiber orientation tensor $\boldsymbol{N}$ is assumed to be known with all its algebraic properties exactly fulfilled within the closure scheme described before.

5.2 The fully symmetric implicit quadratic closure

5.2.1 Definition [3]

The closure function for the symmetric implicit quadratic closure (SIQ) reads as follows

$$\mathbb{F}(\boldsymbol{B}) = \mathrm{sym}(\boldsymbol{B}\otimes\boldsymbol{B}) = \frac{1}{3}\big(\boldsymbol{B}\otimes\boldsymbol{B} + \boldsymbol{B}\square\boldsymbol{B} + (\boldsymbol{B}\square\boldsymbol{B})^{\mathsf{T}_\mathrm{R}}\big). \tag{5.5}$$

By inserting Eq. (5.5) into Eq. (5.3), the function $\boldsymbol{F}(\boldsymbol{B})$ is derived for the SIQ closure as follows, given in both symbolic and in index notation

$$\begin{aligned} \boldsymbol{F}(\boldsymbol{B}) &= \frac{1}{3}\big(\mathrm{tr}(\boldsymbol{B})\boldsymbol{B} + 2\boldsymbol{B}^2\big) - \boldsymbol{N}, \\ F_{ij}(\boldsymbol{B}) &= \frac{1}{3}(B_{kk}B_{ij} + 2B_{ik}B_{kj}) - N_{ij}. \end{aligned} \tag{5.6}$$

[3] This section is directly taken from Karl et al. (2023a).

5.2.2 Solution procedure [4]

In this section it is shown that Eq. (5.2) with $\boldsymbol{F}(\boldsymbol{B})$ given in Eq. (5.6) admits a symmetric positive semi-definite solution $\boldsymbol{B}$ for any given symmetric positive semi-definite orientation tensor $\boldsymbol{N}$. A constructive approach is used which turns out to be useful for numerical computations. This approach also shows that the solution is in fact unique.

By using the abbreviation $s = \mathrm{tr}(\boldsymbol{B})/4$, the defining Eq. (5.6) can be written in the form

$$\boldsymbol{B}^2 + 2s\boldsymbol{B} = \frac{3}{2}\boldsymbol{N}, \tag{5.7}$$

which can be reformulated by completing the square as follows

$$(\boldsymbol{B} + s\boldsymbol{I})^2 = \frac{3}{2}\boldsymbol{N} + s^2\boldsymbol{I}. \tag{5.8}$$

Since $\boldsymbol{N}$ is positive semi-definite, as addressed in Sec. 2.4.1, the following representation of the sought tensor $\boldsymbol{B}$ can be obtained

$$\boldsymbol{B} = \sqrt{\frac{3}{2}\boldsymbol{N} + s^2\boldsymbol{I}} - s\boldsymbol{I}. \tag{5.9}$$

It should be noted that for computing $\boldsymbol{B}$ based on Eq. (5.9), only the scalar variable s has to be determined. In order to derive an equation for s, the trace of both sides of Eq. (5.9) is taken, yielding

$$4s = \mathrm{tr}\left(\sqrt{\frac{3}{2}\boldsymbol{N} + s^2\boldsymbol{I}}\right) - sd, \tag{5.10}$$

with $d = 2, 3$ representing the spatial dimension of the considered problem. To proceed, it is noted that the tensors $\boldsymbol{N}$ and $\boldsymbol{B}$ share the same eigensystem. That $\boldsymbol{N}$ and $\boldsymbol{B}$ commute and thus are jointly diagonizable is shown by multiplying Eq. (5.6) on the left and on the right by the

[4] This section is directly taken from Karl et al. (2023a).

tensor $\boldsymbol{B}$ leading to

$$\boldsymbol{N}\boldsymbol{B} = \frac{1}{3}\big(\mathrm{tr}(\boldsymbol{B})\boldsymbol{B}^2 + 2\boldsymbol{B}^3\big) = \boldsymbol{B}\boldsymbol{N}. \tag{5.11}$$

With λ_i representing the given eigenvalues of $\boldsymbol{N}$, the defining Eq. (5.10) for s becomes

$$(d+4)s = \sum_{i=1}^{d} \sqrt{\frac{3\lambda_i}{2} + s^2}. \tag{5.12}$$

Once Eq. (5.12) is solved for s, the eigenvalues μ_i of $\boldsymbol{B}$ can be computed based on the following equation representing Eq. (5.9) in the eigensystem of $\boldsymbol{B}$

$$\mu_i = \sqrt{\frac{3\lambda_i}{2} + s^2} - s. \tag{5.13}$$

The eigenvalues μ_i refer to the diagonal matrix $\tilde{B}_{ij}$ as the eigensystem representation of B_{ij} with $B_{ij} = Q_{ik}\tilde{B}_{kl}Q^{\mathsf{T}}_{lj}$ being the eigendecomposition of B_{ij} with an orthogonal matrix $Q_{ij} \in \mathrm{Orth}^+$.

For any $\lambda_i \geq 0$, Eq. (5.12) is uniquely solvable. Indeed, the following continuous function is considered

$$f : \mathbb{R}_{\geq 0} \to \mathbb{R}, \quad s \mapsto (d+4)s - \sum_{i=1}^{d} \sqrt{\frac{3\lambda_i}{2} + s^2}, \tag{5.14}$$

whose roots s correspond to solutions of Eq. (5.13). Estimating the derivative of the function f from below

$$f'(s) = d + 4 - \sum_{i=1}^{d} \frac{s}{\sqrt{\frac{3\lambda_i}{2} + s^2}} = 4 + \sum_{i=1}^{d} \underbrace{\left(1 - \frac{s}{\sqrt{\frac{3\lambda_i}{2} + s^2}}\right)}_{\geq 0} \geq 4, \tag{5.15}$$

it is observed that the function f is strongly monotone. Indeed, due to $\lambda_i \geq 0$, the following inequality holds

$$\sqrt{\frac{3\lambda_i}{2} + s^2} \geq s \quad \text{implies} \quad 1 \geq \frac{s}{\sqrt{\frac{3\lambda_i}{2} + s^2}}. \tag{5.16}$$

Thus, any root of the function f is unique. To show the existence of a root, it is observed that

$$f(0) = -\sum_{i=1}^{d} \sqrt{\frac{3\lambda_i}{2}} \leq 0. \tag{5.17}$$

Furthermore, the estimate (5.15) implies

$$f(s) = f(0) + \int_0^s f'(\tau)\,\mathrm{d}\tau \geq f(0) + 4s \to \infty \tag{5.18}$$

as $s \to \infty$. In particular, f attains the value 0 and Eq. (5.12) is solvable. Concerning the uniqueness, notice that $\boldsymbol{B}$ is determined, by the mean-value theorem, solely from computed s and given $\boldsymbol{N}$, see Eq. (5.9). Moreover, Eq. (5.12) for s is uniquely solvable. Thus, there is only one solution $\boldsymbol{B}$ to Eq. (5.6).

5.2.3 Realizability by a fiber orientation distribution [5]

In two and three spatial dimensions ($d = 2, 3$), each completely symmetric fourth-order tensor $\mathbb{N}$ can be written in the form

$$\mathbb{N} = \sum_{i=1}^{l} \kappa_i\, \boldsymbol{r}_i \otimes \boldsymbol{r}_i \otimes \boldsymbol{r}_i \otimes \boldsymbol{r}_i \tag{5.19}$$

[5] This section is directly taken from Karl et al. (2023a).

for a non-negative integer l, non-negative numbers κ_i and vectors $\boldsymbol{r}_i \in \mathbb{R}^d$ $(i = 1, \ldots, l)$ if and only if the tensor $\mathbb{N}$ is completely symmetric and positive semi-definite in the sense

$$\boldsymbol{S} \cdot \mathbb{N}[\boldsymbol{S}] \geq 0, \quad \forall\, \boldsymbol{S} = \boldsymbol{S}^{\mathsf{T}}, \tag{5.20}$$

see Bauer et al. (2023). Thus, the SIQ closure given in Eq. (5.5) is realized by an ODF precisely if the following condition holds for all symmetric second-order tensors $\boldsymbol{S}$

$$\boldsymbol{S} \cdot \mathrm{sym}(\boldsymbol{B} \otimes \boldsymbol{B})[\boldsymbol{S}] \geq 0. \tag{5.21}$$

Next, it is shown that the condition holds provided that $\boldsymbol{B}$ is positive semi-definite. Using Eq. (5.5) in index notation, the following term is computed

$$\begin{aligned} 3\boldsymbol{S} \cdot \mathrm{sym}(\boldsymbol{B} \otimes \boldsymbol{B})[\boldsymbol{S}] &= S_{ij} B_{ij} B_{kl} S_{kl} + S_{ij} B_{ik} B_{lj} S_{kl} + S_{ij} B_{il} B_{kj} S_{kl} \\ &= S_{ij} B_{ij} S_{kl} B_{kl} + 2 S_{ij} B_{jl} S_{lk} B_{ki} \\ &= (\boldsymbol{S} \cdot \boldsymbol{B})^2 + 2\,\mathrm{tr}(\boldsymbol{S}\boldsymbol{B}\boldsymbol{S}\boldsymbol{B}). \end{aligned} \tag{5.22}$$

Both summands are non-negative. For the first summand, this is trivial. The assertion for the second summand follows from the fact that the following inequality holds for symmetric and positive semi-definite tensors $\boldsymbol{B}$ and $\boldsymbol{C}$

$$\boldsymbol{B} \cdot \boldsymbol{C} \geq 0. \tag{5.23}$$

Indeed, an eigendecomposition of the tensor $\boldsymbol{B}$ shows the inequality (5.23)

$$\boldsymbol{B} = \sum_{i=1}^{d} \mu_i\, \boldsymbol{r}_i \otimes \boldsymbol{r}_i, \qquad \boldsymbol{B} \cdot \boldsymbol{C} = \sum_{i=1}^{d} \underbrace{\mu_i}_{\geq 0} \underbrace{\boldsymbol{C} \cdot (\boldsymbol{r}_i \otimes \boldsymbol{r}_i)}_{\geq 0} \geq 0. \tag{5.24}$$

Applying this result to $\boldsymbol{B}$ and the symmetric and non-negative tensor $\boldsymbol{C} = \boldsymbol{SBS}$ gives the following result that the condition (5.21) holds

$$\mathrm{tr}(\boldsymbol{SBSB}) = \boldsymbol{B} \cdot (\boldsymbol{SBS}) = \boldsymbol{B} \cdot \boldsymbol{C} \geq 0 \tag{5.25}$$

and the SIQ closure is realizable. With a similar line of reasoning it can be shown that the SQC proposed in chapter 4 with the underlying publication Karl et al. (2021b) is also realizable with $\boldsymbol{N}$ instead of the implicit closure tensor $\boldsymbol{B}$ in view of the calculations outlined before.

5.2.4 Exactness for UD, ISO, and PI orientation states [6]

In this section it is considered whether the UD, ISO, and PI orientation states are exactly realized by the SIQ closure approach. For simplicity, it suffices to consider $\boldsymbol{N}$ and $\boldsymbol{B}$ in an eigensystem representation. Furthermore, is noted that $\mu_i = 0$ is a direct consequence of $\lambda_i = 0$ via the chain of equalities

$$\mu_i = \sqrt{\frac{3\lambda_i}{2} + s^2} - s = \sqrt{s^2} - s = 0. \tag{5.26}$$

In addition, the latter equation also shows that if multiple eigenvalues $\lambda_i = \lambda_j$ are given, the relation $\mu_i = \mu_j$ will follow directly.

First, the UD case is considered with $\lambda_1 = 1$ and $\lambda_2 = \lambda_3 = 0$. As a consequence, $\mu_2 = \mu_3 = 0$ holds and the equation for μ_1 reduces to $\mu_1^2 = 1 \leftrightarrow \mu_1 = 1$ by inserting $s = \mu_1/4$. Therefore, the SIQ closure $\mathbb{F}(\boldsymbol{B}) = \mathrm{sym}(\boldsymbol{B} \otimes \boldsymbol{B})$ results in the exact tensor for the UD case $\mathbb{N}_{\mathsf{UD}} = \boldsymbol{e}_1^{\otimes 4}$ as given in Eq. (4.5) referring to, e.g., Moakher and Basser (2015).

Second, the ISO case is considered with $\lambda_1 = \lambda_2 = \lambda_3 = \lambda = 1/3$ and, therefore, with the form $\boldsymbol{B} = \mu \boldsymbol{I}$ based on $\mu_1 = \mu_2 = \mu_3 = \mu$. The gov-

[6] This section is directly taken from Karl et al. (2023a).

erning Eq. (5.6) for the SIQ closure implies

$$\frac{1}{3}\boldsymbol{I} = \frac{1}{3}(3\mu^2\boldsymbol{I} + 2\mu^2\boldsymbol{I}) \quad \leftrightarrow \quad \frac{1}{3} = \mu^2 + \frac{2}{3}\mu^2, \tag{5.27}$$

leading to $1 = 5\mu^2$ with the physically consistent solution $\mu = 1/\sqrt{5}$, or $\boldsymbol{B} = \boldsymbol{I}/\sqrt{5}$, respectively. In a next step, this result is inserted into Eq. (5.5), leading to

$$\mathrm{sym}(\boldsymbol{B}\otimes\boldsymbol{B}) = \frac{1}{15}\big(\boldsymbol{I}\otimes\boldsymbol{I} + \boldsymbol{I}\square\boldsymbol{I} + (\boldsymbol{I}\square\boldsymbol{I})^{\mathsf{T_R}}\big) = \frac{1}{3}\mathbb{P}_1 + \frac{2}{15}\mathbb{P}_2 = \mathbb{N}_{\mathsf{ISO}}, \tag{5.28}$$

representing the exact expression for the isotropic fourth-order orientation tensor as given in Eq. (4.5) referring to, e.g., Moakher and Basser (2015).

Third, the PI case is considered with $\lambda_1 = \lambda_2 = \lambda = 1/2$ and $\lambda_3 = 0$. Therefore, the relations $\mu_1 = \mu_2 = \mu$ and $\mu_3 = 0$ hold. By using the governing Eq. (5.6) for the SIQ closure, it is deduced with the 2D identity tensor $\boldsymbol{I}_{(2)}$

$$\frac{1}{2}\boldsymbol{I}_{(2)} = \frac{1}{3}(2\mu^2\boldsymbol{I}_{(2)} + 2\mu^2\boldsymbol{I}_{(2)}) \quad \leftrightarrow \quad \frac{1}{2} = \frac{4}{3}\mu^2, \tag{5.29}$$

leading to the physically consistent solution $\mu = \sqrt{3/8}$ or $\boldsymbol{B} = \sqrt{3/8}\boldsymbol{I}_{(2)}$, respectively. Proceeding as for the previous cases, inserting this result into Eq. (5.5) leads to

$$\mathrm{sym}(\boldsymbol{B}\otimes\boldsymbol{B}) = \frac{1}{8}\big(\boldsymbol{I}_{(2)}\otimes\boldsymbol{I}_{(2)} + \boldsymbol{I}_{(2)}\square\boldsymbol{I}_{(2)} + (\boldsymbol{I}_{(2)}\square\boldsymbol{I}_{(2)})^{\mathsf{T_R}}\big), \tag{5.30}$$

or equivalently

$$\mathrm{sym}(\boldsymbol{B}\otimes\boldsymbol{B})_{ijkl} = \frac{1}{8}(\delta_{ij}\delta_{kl} + \delta_{ik}\delta_{lj} + \delta_{il}\delta_{kj}), \tag{5.31}$$

$i, j, k, l \in \{1, 2\}$, which corresponds to the exact expression for the PI fourth-order orientation tensor as given in Eq. (4.5) referring to, e.g., Moakher and Basser (2015).

5.3 The fully symmetric implicit hybrid closure

5.3.1 Definition and solution procedure [7]

The second proposed closure combines the SIQ closure discussed in the previous Sec. 5.2 with the well-known HYB closure (Advani and Tucker III, 1987; 1990). This closure is named fully symmetric implicit hybrid closure (SIHYB) and fixes the lack of symmetry of the original HYB closure addressed by, e.g., Petty et al. (1999). The respective closure function reads

$$\mathbb{F}(\boldsymbol{B}) = (1-k)\big(-\frac{3}{35}\,\mathrm{sym}(\boldsymbol{I}\otimes\boldsymbol{I}) + \frac{6}{7}\,\mathrm{sym}(\boldsymbol{I}\otimes\boldsymbol{B})\big) + k\,\mathrm{sym}(\boldsymbol{B}\otimes\boldsymbol{B}), \tag{5.32}$$

with $k = 1 - 27\det(\boldsymbol{N})$ for 3D fiber orientation states. The 2D case proceeds similarly by adapting the definition of k and the prefactors of the linear part in Eq. (5.32) as given in, e.g., Advani and Tucker III (1990). Analogous to the SIQ closure, the function $\boldsymbol{F}(\boldsymbol{B})$ defined in Eq. (5.3) is formulated as follows given both in symbolic and in index notation for the SIHYB closure in order to compute the tensor $\boldsymbol{B}$ based on Eq. (5.2)

$$\boldsymbol{F}(\boldsymbol{B}) = \frac{1-k}{7}\big(\mathrm{tr}(\boldsymbol{B}) - 1\big)\boldsymbol{I} + \big(1 - k + \frac{k}{3}\mathrm{tr}(\boldsymbol{B})\big)\boldsymbol{B} + \frac{2k}{3}\boldsymbol{B}^2 - \boldsymbol{N},$$

[7] This section is directly taken from Karl et al. (2023a).

$$F_{ij}(\boldsymbol{B}) = \frac{1-k}{7}(B_{nn}-1)\delta_{ij} + (1-k+\frac{k}{3}B_{nn})B_{ij} + \frac{2k}{3}B_{in}B_{nj} - N_{ij}. \tag{5.33}$$

Similar to SIQ, SIHYB can be reduced to a 1D formulation as shown in App. D.1. It should by noted that the symmetric HYB closure proposed by Petty et al. (1999) differs in the quadratic term and, in particular, no implicit formulation is addressed.

5.3.2 Exactness for UD, ISO, and PI orientation states [8]

For the UD case, $k = 1$ holds and the SIHYB closure corresponds to the SIQ closure, for which the exactness for UD is shown in Sec. 5.2.4. For the ISO case, $k = 0$ follows, leading to the linear equation for $\boldsymbol{B}$

$$\frac{1}{7}\big(\mathrm{tr}(\boldsymbol{B})-1\big)\boldsymbol{I} + \boldsymbol{B} - \frac{1}{3}\boldsymbol{I} = \boldsymbol{0}. \tag{5.34}$$

As a consequence, $\boldsymbol{B}$ is also isotropic with $\boldsymbol{B} = \mu\boldsymbol{I}$ leading to $\mu = 1/3$. By inserting the latter result into the linear part of Eq. (5.32), the isotropic fourth-order orientation tensor is obtained. In a 3D description, a PI orientation state leads to $k = 1$ with SIHYB corresponding to SIQ. As already addressed in Sec. 5.2.4, the SIQ closure is exact for PI.

5.3.3 Realizability by a fiber orientation distribution [9]

Since the realizability by an ODF is shown before for the SIQ closure, LIN as the second part of the SIHYB closure is discussed in the section at hand. As pointed out by Bauer and Böhlke (2022b), LIN represents a purely algebraic assumption. In addition, the corresponding fourth-order orientation tensor of the third kind (Kanatani, 1984), representing

[8] This section is directly taken from Karl et al. (2023a).
[9] This section is directly taken from Karl et al. (2023a).

a measure of anisotropy, is zero. It is also addressed by Bauer and Böhlke (2022b) that LIN may violate the allowed parameter space. As a consequence, orientation states exist for which LIN predicts non-realizable fourth-order orientation tensors. Since HYB is based on a linear interpolation between LIN and QC, the realizability by an ODF is not ensured, in general. Nevertheless, the SIHYB closure approach is used in the following Sec. 5.4 together with the SIQ closure in order to investigate the applicability in view of orientation evolution and prediction of anisotropic viscous and elastic properties.

5.4 Numerical examples

5.4.1 Prediction of fiber orientation evolution [10]

In the present section, the proposed SIQ and SIHYB closures are investigated with respect to the predicted orientation evolution. For clarity, only a simple shear flow is considered, with the strain-rate tensor $\boldsymbol{D}$ and the spin tensor $\boldsymbol{W}$ prescribed as follows

$$\boldsymbol{D} = \frac{\dot{\gamma}}{2}(\boldsymbol{e}_1 \otimes \boldsymbol{e}_2 + \boldsymbol{e}_2 \otimes \boldsymbol{e}_1), \qquad \boldsymbol{W} = \frac{\dot{\gamma}}{2}(\boldsymbol{e}_1 \otimes \boldsymbol{e}_2 - \boldsymbol{e}_2 \otimes \boldsymbol{e}_1). \tag{5.35}$$

The tensor $\boldsymbol{D}$ is the symmetric part of the velocity gradient $\boldsymbol{L} = \dot{\gamma}\, \boldsymbol{e}_1 \otimes \boldsymbol{e}_2$ and $\boldsymbol{W}$ is the skew-symmetric part of $\boldsymbol{L}$, respectively. The shear rate $\dot{\gamma}$ can be chosen arbitrarily since the results are considered in view of the total shear $\dot{\gamma}t$, $t_0 = 0$. The orientation evolution is subject to the Folgar-Tucker equation discussed in Sec. 2.4.2 and referring to Folgar and Tucker III (1984) and Advani and Tucker III (1987). Depending on the closure approach in use, the closure function $\mathbb{F}$ refers to $\mathbb{F}(\boldsymbol{B})$ in

[10] This section consists of parts from Karl et al. (2023a). Additional text passages have been added.

terms of the proposed implicit closures SIQ and SIHYB. Regarding the classical closures, the closure function $\mathbb{F}$ refers to $\mathbb{F}(\boldsymbol{N})$. In this chapter, the following closures and ODF estimations are considered in order to compare the results with the SIQ and SIHYB closures:

- Quadratic closure (QC) (Doi, 1981; Advani and Tucker III, 1987; 1990)

$$\mathbb{F}(\boldsymbol{N}) = \boldsymbol{N} \otimes \boldsymbol{N} \tag{5.36}$$

- Second version of the symmetric quadratic closure (SQC) for fiber orientation evolution description derived in chapter 4

$$2\mathbb{F}(\boldsymbol{N}) = \kappa \operatorname{sym}(\boldsymbol{N} \otimes \boldsymbol{N}) \tag{5.37}$$

with

$$\kappa = \begin{cases} 0, & \boldsymbol{N} = \boldsymbol{N}_{\mathsf{ISO}}, \boldsymbol{D} = \boldsymbol{0} \\ \dfrac{6\boldsymbol{N} \cdot \boldsymbol{D}}{\boldsymbol{N} \cdot \boldsymbol{D} + 2\boldsymbol{D} \cdot \boldsymbol{N}^2}, & \boldsymbol{N} \neq \boldsymbol{N}_{\mathsf{ISO}}, \boldsymbol{D} \neq \boldsymbol{0} \end{cases} \tag{5.38}$$

- Hybrid closure (HYB) (Advani and Tucker III, 1987; 1990)

$$\begin{aligned} \mathbb{F}(\boldsymbol{N}) &= (1-k)\big(-\frac{3}{35}\operatorname{sym}(\boldsymbol{I} \otimes \boldsymbol{I}) + \frac{6}{7}\operatorname{sym}(\boldsymbol{I} \otimes \boldsymbol{N})\big) + k\boldsymbol{N} \otimes \boldsymbol{N}, \\ k &= 1 - 27\det(\boldsymbol{N}) \end{aligned} \tag{5.39}$$

- Invariant-based optimal fitting closure (IBOF) with β_1 to β_6 depending on the invariants of $\boldsymbol{N}$ (Chung and Kwon, 2002b)

$$\begin{aligned} \mathbb{F}(\boldsymbol{N}) = {} & \beta_1 \operatorname{sym}\big(\boldsymbol{I} \otimes \boldsymbol{I}\big) + \beta_2 \operatorname{sym}\big(\boldsymbol{I} \otimes \boldsymbol{N}\big) \\ & + \beta_3 \operatorname{sym}\big(\boldsymbol{N} \otimes \boldsymbol{N}\big) + \beta_4 \operatorname{sym}\big(\boldsymbol{I} \otimes \boldsymbol{N}^2\big) \\ & + \beta_5 \operatorname{sym}\big(\boldsymbol{N} \otimes \boldsymbol{N}^2\big) + \beta_6 \operatorname{sym}\big(\boldsymbol{N}^2 \otimes \boldsymbol{N}^2\big) \end{aligned} \tag{5.40}$$

- Maximum entropy closure (MEM) based on the Bingham distribution (Jaynes, 1957; Bingham, 1974; Chaubal and Leal, 1998; van Gurp, 1998; Müller and Böhlke, 2016) [11]

$$f(\boldsymbol{n})_{\mathsf{MEM}} = c\exp\big(\tilde{\boldsymbol{G}}\cdot(\boldsymbol{n}\otimes\boldsymbol{n})\big) = \exp\big(\boldsymbol{G}\cdot(\boldsymbol{n}\otimes\boldsymbol{n})\big) \tag{5.41}$$

- Fast exact closure based on the angular central Gaussian distribution (ACG) (Tyler, 1987; Montgomery-Smith et al., 2011a;b), also known as the natural closure (NAT) of Verleye and Dupret (1993)

$$f(\boldsymbol{n})_{\mathsf{ACG}} = \frac{1}{4\pi}\big(\boldsymbol{G}\cdot(\boldsymbol{n}\otimes\boldsymbol{n})\big)^{-\frac{3}{2}} \tag{5.42}$$

As pointed out by, e.g., Mehta and Schneider (2022), the tensor $\boldsymbol{G}$ has to be computed for both the MEM and ACG closure based on

$$\mathbf{0} = \boldsymbol{N} - \int_{\mathcal{S}} f(\boldsymbol{n})\boldsymbol{n}\otimes\boldsymbol{n}\,\mathrm{d}S(\boldsymbol{n}), \tag{5.43}$$

with $f(\boldsymbol{n})$ representing either Eq. (5.41) or (5.42). For details about the ACG solution procedure, the reader is referred to, e.g., Mehta and Schneider (2022). For the MEM solution procedure, further details can be found in, e.g., Müller and Böhlke (2016). In this chapter, the numerical integration scheme of Lebedev and Laikov (1999) is used with the implementation of Parrish (2021) for evaluating the integrals over the unit sphere $\mathcal{S}$ in order to determine $\boldsymbol{G}$ and the sought tensor $\mathbb{N}$. The maximum number of 5810 integration points on $\mathcal{S}$ is used, and the tolerance for ACG and MEM is set to 10^{-8}. The initial guess $s_0 = 0.25$ is fixed for both SIQ and SIHYB.

[11] In the recent publication of Papenfuß (2022), an explicit MEM-based estimation of $f(\boldsymbol{n})$ is proposed using a function regarding the underlying information-theoretic entropy.

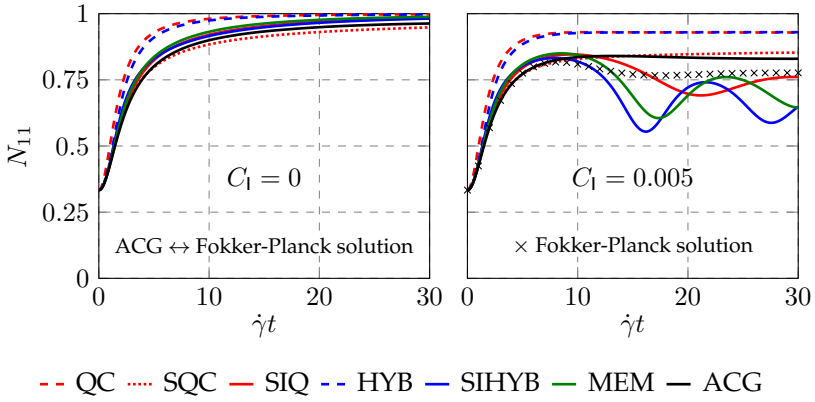

Figure 5.2: Evolution of the orientation tensor component N_{11} plotted over the total shear $\dot{\gamma}t$ for two different values of fiber interaction parameter C_I with respect to different closure approximations in a simple shear flow, adapted from Karl et al. (2023a).

In Fig. 5.2, the evolution of the orientation component N_{11} is shown for the fiber interaction parameters $C_\mathrm{I} = 0$ and $C_\mathrm{I} = 0.005$ in response to the total shear $\dot{\gamma}t$. In addition, the shape parameter $\xi = 1$ ($\alpha \to \infty$) is fixed. The Folgar-Tucker equation is integrated with a fourth-order Runge-Kutta method (Deuflhard and Bornemann, 2008) (pp. 140–153) and a time step size of $\triangle t = 0.01\,\mathrm{s}$. As a reference solution without closure-induced errors, the numerical solution of the Fokker-Planck equation referring to Fokker (1914) and Planck (1917) for the ODF $f(t, \boldsymbol{x}, \boldsymbol{n})$ additionally depending on the spatial position $\boldsymbol{x}$ and the time t extended by the isotropic diffusion term on the unit sphere $\mathcal{S}$ as given in, e.g., Montgomery-Smith et al. (2011b) and Lohmann (2016)

$$\dot{f} + \mathrm{div}_\mathcal{S}(f\dot{\boldsymbol{n}}) = C_\mathrm{I}\dot{\gamma}\Delta_\mathcal{S}(f) \tag{5.44}$$

is also shown in Fig. 5.2. In Eq. (5.44), $\dot{\gamma}$ and C_I refer to the definitions in the context of the Folgar-Tucker equation given in Sec. 2.4.2, $\dot{f}$ represents the material time derivative with respect to t and $\boldsymbol{x}$. The divergence

and the Laplacian on the unit sphere are denoted by $\mathrm{div}_{\mathcal{S}}(\cdot)$ and $\Delta_{\mathcal{S}}(\cdot)$. Tucker's implementation (Tucker III, 2021) is used for the numerical solution of Eq. (5.44) with 150×150 grid points on the unit hemisphere and a maximum Courant number of 0.1. The well-known periodic behavior of the orientation tensor illustrated in, e.g., Altan and Tang (1993) and Montgomery-Smith et al. (2011a), which is also called Jeffery orbits (Ingber and Mondy, 1994) referring to Jeffery's equation (Jeffery, 1922; Junk and Illner, 2007), is not present for $C_{\mathrm{I}} = 0$ in the left part of Fig. 5.2 since the period length referring to Jeffery (1922) and given as follows (Montgomery-Smith et al., 2011a)

$$T = \frac{2\pi}{\|\boldsymbol{D}\|\sqrt{1-\xi^2}} = \frac{2\pi}{\dot{\gamma}\sqrt{1-\xi^2}} \tag{5.45}$$

is infinitely large for $\xi = 1$ ($\alpha \to \infty$). On the other hand, a non-zero fiber interaction parameter $C_{\mathrm{I}} = 0.005$ reduces the high alignment level of the vanishing fiber interaction parameter $C_{\mathrm{I}} = 0$ due to the present diffusive effect towards the isotropic state. The behavior of the common closures is well studied in the literature and, therefore, not the focus of the present chapter: For QC and HYB see, e.g., Advani and Tucker III (1987; 1990), SQC is discussed in chapter 4 based on Karl et al. (2021b), IBOF is addressed in, e.g., Chung and Kwon (2002b), Mezi et al. (2019a), and Férec et al. (2020), and ACG is discussed in Montgomery-Smith et al. (2011a). In summary, QC and HYB overestimate the alignment of the fibers and SQC is a useful ad-hoc improvement of QC. In particular, the ACG closure is exact for the case of absent fiber-fiber interaction (Verleye and Dupret, 1993; Montgomery-Smith et al., 2011a;b) and thus represents the solution of the Fokker-Planck equation for a vanishing fiber interaction parameter $C_{\mathrm{I}} = 0$, and the IBOF closure approximates the ACG-related orientation results closely. Therefore, the IBOF results are not shown in Fig. 5.2. It should be noted that the overshoot of IBOF and ACG with respect to the Fokker-Planck solution is well known

(Chung and Kwon, 2002b; Férec et al., 2020). Regarding the proposed implicit closures and the MEM-related results, a distinct oscillatory orientation behavior is observed for $C_\mathrm{I} = 0.005$ compared to all other shown closures. The oscillations increase in the order SIQ→MEM→SIHYB. In particular, IBOF and ACG also show a weak oscillatory orientation behavior with one single peak at $\dot{\gamma}t \approx 10$. In contrast, a vanishing fiber interaction parameter $C_\mathrm{I} = 0$ leads to a stable solution behavior as shown in the left plot in Fig. 5.2. This suggests that for SIQ, SIHYB, and MEM the fiber interaction parameter C_I has a destabilizing effect and induces the oscillations due to the interaction between the closure term and the diffusion term in the Folgar-Tucker equation. Surprisingly, the proposed implicit closures show very good agreement with the MEM approach. In conclusion, SIQ and SIHYB are capable of replacing the MEM in terms of a low-cost computation. In this context, SIHYB is more accurate than SIQ in terms of approximating the MEM results with respect to orientation evolution. As a supplement to Fig. 5.2, the evolution of the remaining orientation tensor components for the considered simple shear flow are provided in Fig. D.2.1 in App. D.2.

To further investigate the oscillatory behavior, the ACG, MEM, and both new closures SIQ and SIHYB are compared with each other for various interaction parameters C_I. In addition, the solution of the Fokker-Planck equation is used as the reference in Fig. 5.3 showing the orientation evolution of the tensor component N_{11} with respect to the total shear $\dot{\gamma}t$. The results, which are limited to N_{11} for the sake of a compact representation, show that both proposed implicit closures behave similar to MEM over the considered range of the fiber interaction parameter C_I. With decreasing values of the fiber interaction parameter C_I the period length of the oscillation increases and for $C_\mathrm{I} = 5 \cdot 10^{-5}$ and $C_\mathrm{I} = 5 \cdot 10^{-6}$ oscillations induced by parameter values $C_\mathrm{I} > 0$ are not observed in the shown range of total shear. For SIQ, the amplitude of the oscillations halved at a total shear $\dot{\gamma}t \approx 1000$, while for SIHYB this

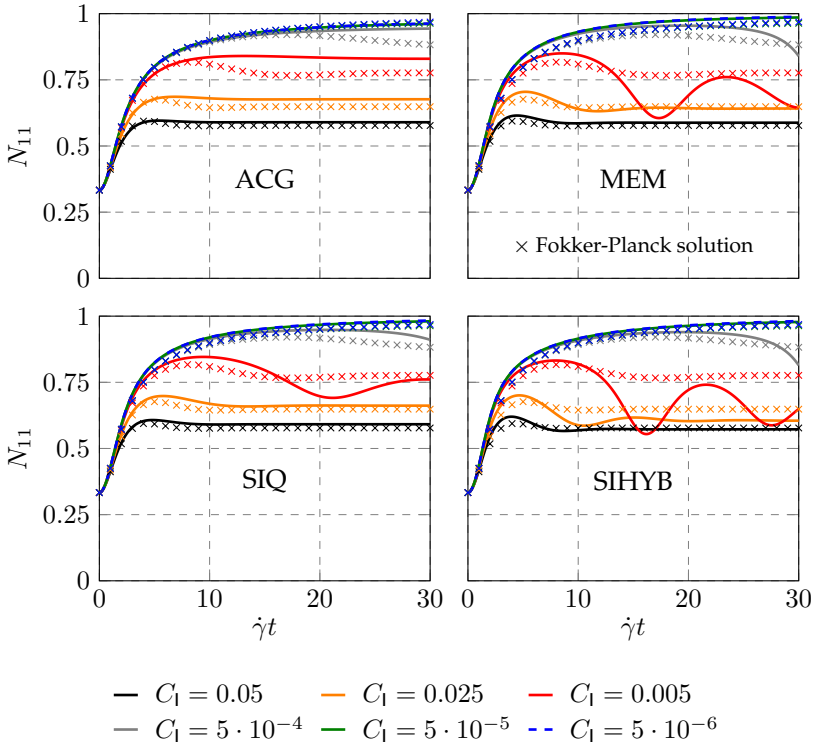

Figure 5.3: Evolution of the orientation tensor component N_{11} plotted over the total shear $\dot{\gamma}t$ for different values of fiber interaction parameter C_I with respect to ACG, MEM, SIQ, and SIHYB in a simple shear flow, adapted from Karl et al. (2023a).

occurs at a total shear $\dot{\gamma}t \approx 1700$. For high values of C_I (higher than 0.05, which is typically not realized in physical situations) the oscillations are damped due to the strong diffusion towards the isotropic state. For typical values of C_I in the interval $[5 \cdot 10^{-4}, 5 \cdot 10^{-3}]$ the oscillations for MEM, SIQ, and SIHYB are distinct in the shown range and lead to inadequate accuracy of the orientation tensor results compared to the Fokker-Planck solution. It should be noted that the fiber interaction parameter C_I is typically selected accounting for the fiber aspect ratio

and the fiber volume fraction as addressed in Bay (1991) (pp. 117–120) and Phan-Thien et al. (2002), where typical values of C_I can be found. Additional computational experiments regarding the widely used RSC model proposed by Wang et al. (2008) and the ARD model of Phelps and Tucker III (2009) show that the oscillations are still present with the oscillations of SIHYB being more distinct compared to SIQ. The results of these additional computational experiments are provided in Figs. D.2.2 and D.2.3 in App. D.2.

As already addressed, the proposed SIQ and SIHYB closures behave like the MEM closure. This empirical observation may be backed up by theoretical arguments. In general, the closure principle of the MEM is based on maximizing the information-theoretic entropy η which leads to an ODF that is as isotropic (or as uniform) as possible (Tucker III, 2022b), but reproduces a given finite number of statistical moments. In the recent publication of Papenfuß (2022), the series expansion

$$\eta = \eta_0 + \frac{1}{2}\eta_2 \operatorname{tr}(\boldsymbol{N}'^2) + \frac{1}{6}\eta_3 \operatorname{tr}(\boldsymbol{N}'^3) + \mathcal{O}(\boldsymbol{N}'^4) \tag{5.46}$$

of the information-theoretic entropy (Jaynes, 1957; Tucker III, 2022b)

$$\eta = -\int_{\mathcal{S}} f(\boldsymbol{n}) \ln(f(\boldsymbol{n})) \,\mathrm{d}S(\boldsymbol{n}) \tag{5.47}$$

is considered in terms of the symmetric and traceless (also known as irreducible) second-order fiber orientation tensor of the third kind $\boldsymbol{N}'$ (Kanatani, 1984). It should be noted that orientation tensors of the third kind represent measures of anisotropy. Therefore, the η_0-term in Eq. (5.46) represents the isotropic part and all other terms of the power series in Eq. (5.46) contain information about the microstructure's anisotropy. Papenfuß (2022) derived the following lowest order MEM approximation for the irreducible fourth-order orientation tensor $\mathbb{N}'$

based on the series expansion in Eq. (5.46)

$$\mathbb{N}' \approx \frac{4\eta_2^2}{315}(\boldsymbol{N}'\otimes\boldsymbol{N}')'. \tag{5.48}$$

Equation (5.48) is reformulated as follows in terms of $\mathbb{N}$ and $\boldsymbol{N}$ using the relationships between the tensors $\mathbb{N}$ and $\mathbb{N}'$ and between the tensors $\boldsymbol{N}$ and $\boldsymbol{N}'$ given in Kanatani (1984) and Advani and Tucker III (1987)

$$\mathbb{N} \approx -\frac{3}{35}\,\mathrm{sym}(\boldsymbol{I}\otimes\boldsymbol{I}) + \frac{6}{7}\,\mathrm{sym}(\boldsymbol{I}\otimes\boldsymbol{N}) + \frac{4\eta_2^2}{315}\boldsymbol{\Delta}_{\langle 8\rangle}\Big[\Big(\boldsymbol{N}-\frac{\boldsymbol{I}}{3}\Big)\otimes\Big(\boldsymbol{N}-\frac{\boldsymbol{I}}{3}\Big)\Big], \tag{5.49}$$

with $\boldsymbol{\Delta}_{\langle 8\rangle}$ as the identity on irreducible fourth-order tensors. Equation (5.49) states that the lowest order approximation of the MEM closure refers to a fully symmetric expression of linear and quadratic order in the orientation tensor $\boldsymbol{N}$. Thus, the proposed implicit closures SIQ and SIHYB may be interpreted as lowest order MEM approximations accounting for the constraint $\mathbb{N}[\boldsymbol{I}] = \boldsymbol{N}$ which refers to the formulation $\mathbb{F}(\boldsymbol{N})[\boldsymbol{I}] = \boldsymbol{N}$ in terms of the closure function $\mathbb{F}$. The difference to the MEM lies in the implicit procedure represented by replacing the orientation tensor $\boldsymbol{N}$ by the closure tensor $\boldsymbol{B}$ in the closure function $\mathbb{F}$. It is noticed in the computational experiments that SIHYB is a better approximation of the MEM compared to SIQ. This is because SIHYB is closer to the lowest order approximation of MEM than SIQ due to the combination of linear and quadratic terms in the hybrid approach. Interestingly, the classical QC and HYB closures do not show oscillations. However, these closures do not have the required full index symmetry and, therefore, cannot be understood as a lowest order approximation of the MEM.

The recent publication of Tucker III (2022b) also addresses non-physical oscillations of the MEM closure in a simple shear flow for typical fiber interaction parameter values C_I. It is stated that the MEM closure, or

the underlying Bingham distribution, is not an optimal approximation of ODFs which evolve during flow processes. As SIQ and SIHYB may be considered as approximations of the MEM, it does not come as a surprise that these closures feature oscillations in a simple shear flow, as well. It should be noted that the MEM closure is evaluated as accurate by Chaubal and Leal (1998) and Feng et al. (1998) with respect to non-approximated solutions for liquid-crystalline polymers. However, these studies are based on a different orientation evolution equation, which differs from the Folgar-Tucker equation by a nematic term. That the MEM closure based on the Bingham distribution in Eq. (5.41) can be used to close orientation evolution equations with either nematic or non-nematic terms is mentioned in the recent publication of Corona et al. (2023). It is also mentioned that although the ODF following Eq. (5.41) has the required properties, accuracy is not necessarily guaranteed. The inaccurate prediction of the orientation evolution based on the Bingham distribution is attributed by Corona et al. (2023) to the symmetry of the closure tensor $\boldsymbol{G}$ in Eq. (5.41), which cannot describe the orientation evolution in flows which lead to skewed orientation distributions. In general, Corona et al. (2023) compare different closure approaches $\mathbb{N} \approx \mathbb{F}(\boldsymbol{N})$ in a simple shear flow on an experimental basis, considering a suspension with embedded rigid rods of different volume fractions. The ODF was measured in 3D and was used to compute the fourth-order orientation tensor $\mathbb{N}$. The study compares this tensor with the result of different closure functions $\mathbb{F}(\boldsymbol{N})$ with the input $\boldsymbol{N}$ computed with the experimentally determined ODF. The results of Corona et al. (2023) indicate that no superior closure can be identified, but sufficiently accurate estimates are possible under the chosen closure functions.

To conclude this section, reference is made to Montgomery-Smith (2011a;b; 2023) addressing instabilities (growth of perturbations) of Jeffery's equation in the context of flow-fiber coupling caused by fiber-induced anisotropic viscosity in the balance of linear momentum.

5.4.2 Prediction of anisotropic viscosity and stiffness [12]

In this section, all considered closure approximations are compared in terms of predicting the viscous and elastic anisotropy for the following measured orientation state [13] related to Müller et al. (2016)

$$N_{ij} = \begin{pmatrix} 0.392 & 0.111 & -0.006 \\ 0.111 & 0.584 & -0.005 \\ -0.006 & -0.005 & 0.024 \end{pmatrix}. \tag{5.50}$$

The matrix representation of the respective measured fourth-order orientation tensor $\mathbb{N}$ in Voigt notation (Voigt, 1910) (pp. 584–587), which is called the non-normalized notation in this thesis and is also addressed in Cowin (1989), reads as follows

$$N_{ijkl} = \begin{pmatrix} 0.2780 & 0.1060 & 0.0080 & -0.0007 & -0.0049 & 0.0474 \\ 0.1060 & 0.4680 & 0.0100 & -0.0035 & -0.0007 & 0.0622 \\ 0.0080 & 0.0100 & 0.0060 & -0.0007 & 0.0000 & 0.0014 \\ -0.0007 & -0.0035 & -0.0007 & 0.0100 & 0.0015 & -0.0010 \\ -0.0049 & -0.0007 & 0.0000 & 0.0015 & 0.0080 & -0.0010 \\ 0.0474 & 0.0622 & 0.0014 & -0.0010 & -0.0010 & 0.1060 \end{pmatrix}. \tag{5.51}$$

It should be noted that $\mathbb{N}$ given in Eq. (5.51) has to be transferred to the normalized Voigt notation first in order to apply tensor operations, see Sec. 4.1 and the references therein. The non-normalized Voigt notation for the exemplary orientation states is chosen in this thesis in order to provide the components of the fourth-order orientation tensor $\mathbb{N}$ directly without prefactors. In addition, the SQC closure derived in chapter 4 based on the underlying publication Karl et al. (2021b) for estimating

[12] This section consists of parts from Karl et al. (2023a). Additional text passages have been added.

[13] Internal database, Institute of Engineering Mechanics, Chair for Continuum Mechanics, Karlsruhe Institute of Technology (KIT).

the effective anisotropic behavior reads in its first version

$$\mathbb{F}(\boldsymbol{N}) = \frac{\mathrm{sym}(\boldsymbol{N}\otimes\boldsymbol{N})}{\frac{1}{3}(1+2\|\boldsymbol{N}\|^2)}, \tag{5.52}$$

whereas all other closures listed in Sec. 5.4.1 remain unchanged. In general, the matrix representation of the fourth-order orientation tensor $\mathbb{N}$ is based on proposing the complete index symmetry first and then approximating the components depending on the closure in use. For details, the reader is referred to Sec. 4.1. For the matrix material, polypropylene (PP) is considered with the Young's modulus $E_\mathsf{M} = 1.6\,\mathrm{GPa}$ and Poisson's ratio $\nu_\mathsf{M} = 0.4$ (Schürmann, 2007) (p. 132). Glass fibers serve as the reinforcement material with $E_\mathsf{F} = 73\,\mathrm{GPa}$ and $\nu_\mathsf{F} = 0.22$ (Schürmann, 2007) (p. 30). Both the matrix and the fibers are assumed to be isotropic with homogeneous elastic properties. Based on the data of Müller et al. (2016), the mean fiber aspect ratio $\alpha \approx 26$ is used in combination with the fiber volume fraction $c_\mathsf{F} = 0.13$ (PP-GF30). For predicting the effective properties, the mean-field model of Mori and Tanaka (1973) is used for both the effective stiffness tensor $\bar{\mathbb{C}}$ and the effective viscosity tensor $\bar{\mathbb{V}}$ similar to Eqs. (3.3) and (3.11) based on the assumptions and fundamentals addressed in Sec. 2.6

$$\begin{aligned}
\bar{\mathbb{C}} &= \mathbb{C}_\mathsf{M} + c_\mathsf{F}\Big(c_\mathsf{F}\delta\mathbb{C}^{-1} + c_\mathsf{M}\Big\langle\big(\delta\mathbb{C}^{-1} + \mathbb{P}_0^\mathsf{S}\big)^{-1}\Big\rangle_\mathsf{F}^{-1}\Big)^{-1}, \\
\bar{\mathbb{V}} &= \mathbb{V}_\mathsf{M} + \frac{c_\mathsf{F}}{c_\mathsf{M}}\Big\langle\big(\mathbb{P}_0^\mathsf{S}\big)^{-1}\Big\rangle_\mathsf{F}.
\end{aligned} \tag{5.53}$$

In Eq. (5.53), the abbreviation $\delta\mathbb{C} = \mathbb{C}_\mathsf{F} - \mathbb{C}_\mathsf{M}$ is used with the index F indicating the fiber phase and M referring to the matrix phase, respectively. The polarization tensors in Eq. (5.53) share the same notation and for the solid, reference is made to, e.g., Ponte Castañeda and Willis (1995). The incompressible representation for the fiber suspension is provided in Eqs. (E.19) and (E.20) in App. E.4. To account for the fiber orientation state, the operator $\langle\cdot\rangle_\mathsf{F}$ refers to the orientation averaging

procedure introduced by Advani and Tucker III (1987) based on Eq. (2.81) for the involved transversely isotropic tensors. For the ODF-based closures, the fourth-order orientation tensor $\mathbb{N}$ is computed first based on its definition in Eq. (2.41) with the numerical integration over the unit sphere described in the previous Sec. 5.4.1. The results presented in this section are based on the following scalar representation of the effective directional Young's modulus $\bar{E}$ and the direction-dependent shear viscosity $\bar{\mu}$ referring to Böhlke and Brüggemann (2001) with the analogy between the shear modulus and the shear viscosity as used by, e.g., Bertóti and Böhlke (2017), Karl et al. (2021a), Karl et al. (2021b), and Karl and Böhlke (2022)

$$\begin{aligned} \frac{1}{\bar{E}(\boldsymbol{d})} &= (\boldsymbol{d}\otimes\boldsymbol{d}) \cdot \big(\bar{\mathbb{C}}^{-1}[\boldsymbol{d}\otimes\boldsymbol{d}]\big), \\ \frac{1}{2\bar{\mu}(\boldsymbol{d},\boldsymbol{p})} &= \sqrt{2}\,\mathrm{sym}(\boldsymbol{d}\otimes\boldsymbol{p}) \cdot \big(\bar{\mathbb{V}}^{-1}[\sqrt{2}\,\mathrm{sym}(\boldsymbol{d}\otimes\boldsymbol{p})]\big). \end{aligned} \tag{5.54}$$

In Eq. (5.54), the tensile or the shear direction is indicated by $\boldsymbol{d}$ and $\boldsymbol{p}$ stands for normal vector of the shear plane. In this study, both $\bar{E}(\boldsymbol{d})$ and

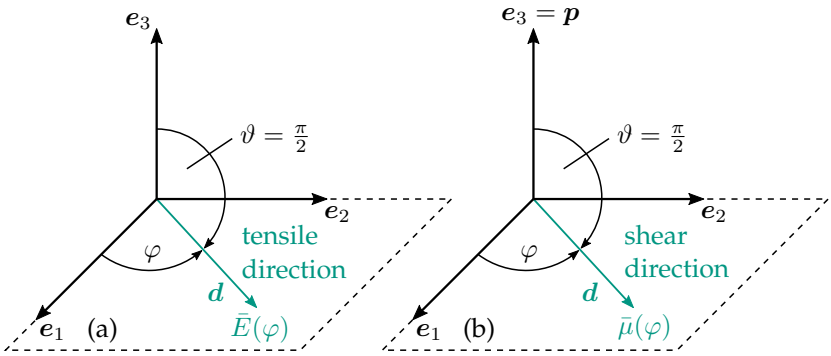

Figure 5.4: Visualization of the direction-dependent effective Young's modulus $\bar{E}(\varphi)$ in (a) and of the effective shear viscosity $\bar{\mu}(\varphi)$ in (b), restricted to the $\boldsymbol{e}_1$–$\boldsymbol{e}_2$-plane ($\vartheta = \pi/2$) parameterized by $\varphi \in [0, 2\pi)$, adapted from Karl and Böhlke (2022).

$\bar{\mu}(\boldsymbol{d}, \boldsymbol{p})$ are restricted to the $\boldsymbol{e}_1$–$\boldsymbol{e}_2$-plane with $\boldsymbol{p} = \boldsymbol{e}_3$. As a consequence, the argument list of $\bar{E}$ and $\bar{\mu}$ is reduced to an angle $\varphi \in [0, 2\pi)$. These two measures of anisotropy $\bar{E}(\varphi)$ and $\bar{\mu}(\varphi)$ are illustrated in Fig. 5.4. Please note that Eq. (5.54) only represents the instantaneous anisotropic viscosity and any reorientation of the fibers is not considered as described in Sec. 2.6.1. Further information about mean-field homogenization can be found in Sec. 2.6.

In Fig. 5.5, the direction-dependent normalized effective Young's modulus $\bar{E}(\varphi)/E_\mathsf{M}$ is shown for all considered closure approximations. By comparing the closure-related results with the stiffness prediction based on the exact fourth-order orientation tensor (μCT), the predictive capabilities of the closures can be assessed. In the following, the μCT-curve is assumed to represent the exact result. The anisotropic elastic behavior is not predicted well by both QC, see Sec. 4.3, and HYB based on the missing total index symmetry of the respective closure function. As already shown in Sec. 4.3, the SQC improves the QC-related results significantly, but the IBOF closure still achieves a better approximation of the real anisotropic stiffness. In contrast, the proposed implicit closures SIQ and SIHYB deviate only slightly from the IBOF closure, which in turn approximates the ACG closure. As discussed in the previous Sec. 5.4.1 for the fiber orientation evolution, it is observed that both implicit closures are capable of substituting the MEM closure also in terms of predicting anisotropic elastic properties.

In Fig. 5.6, the direction-dependent normalized effective shear viscosity $\bar{\mu}(\varphi)/\mu_\mathsf{M}$ is shown for all considered closure approximations. In particular, the performance of different closure approximations in terms of anisotropic viscosity models is important in the context of flow-fiber coupled mold-filling simulation. Further details about flow-fiber coupling can be found in the publications discussed in Sec. 1.2.1 and in chapter 3. Compared to Fig. 5.5, the proposed implicit closures deviate more from μCT, IBOF, and ACG regarding the viscous anisotropy. Both

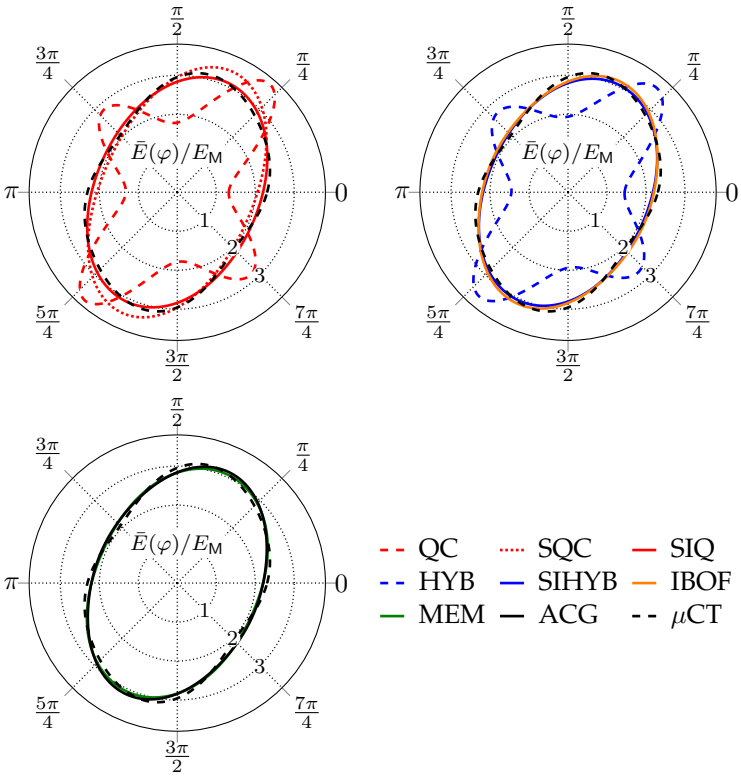

Figure 5.5: Direction-dependent normalized effective Young's modulus $\bar{E}(\varphi)/E_\mathrm{M}$ in the $\boldsymbol{e}_1$–$\boldsymbol{e}_2$-plane for the considered orientation state with respect to different closure approximations, adapted from Karl et al. (2023a).

IBOF and ACG predict the effective viscosity accurately based on the prediction with the measured orientation tensor in use. It is observed that both implicit closures improve the prediction compared to their explicit formulation. In case of QC and HYB, no anisotropy errors related to the violated full index symmetry of both closures are present. Using QC leads to a small overestimation, whereas HYB predicts the highest effective viscosity. SQC leads to a slight underestimation and

SIQ lies between QC and SQC. In view of approximating the results of the MEM closure, SIQ is more suitable than SIHYB in case of anisotropic viscosity. In addition, SIQ is evaluated as more accurate compared to SIHYB.

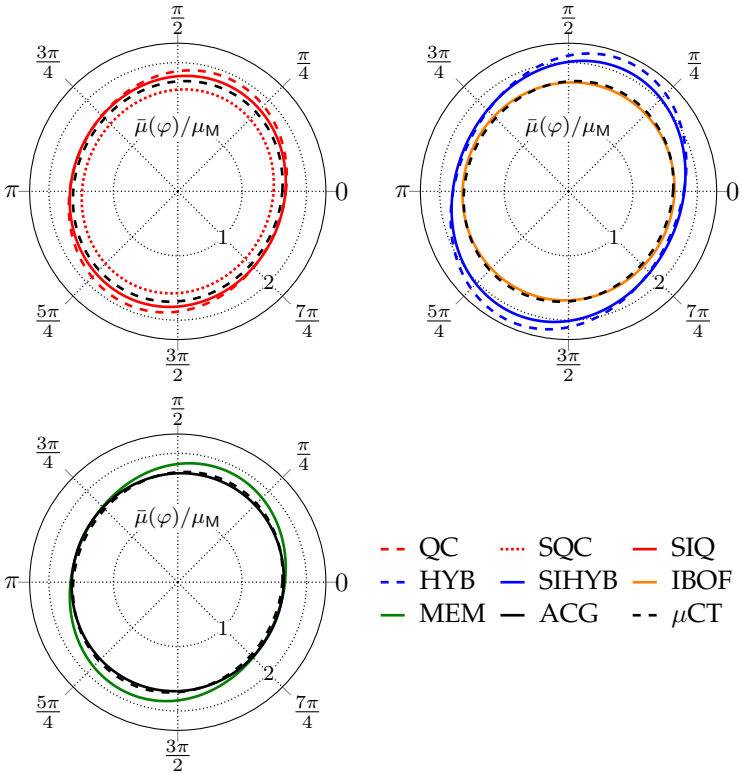

Figure 5.6: Direction-dependent normalized effective shear viscosity $\bar{\mu}(\varphi)/\mu_M$ in the e_1–e_2-plane for the considered orientation state with respect to different closure approximations, adapted from Karl et al. (2023a).

Closure	t_c in s	t_rel in %
MEM	0.31688170	486024
ACG	0.11489970	176230
SIHYB	0.00011718	180
SIQ	0.00007490	115
IBOF	0.00006520	100
HYB	0.00001681	26
SQC	0.00000697	11
QC	0.00000186	3

Table 5.1: Absolute computation time t_c and approximate relative computation time t_rel for all considered closure approximations, adapted from Karl et al. (2023a).

5.4.3 Computational effort [14]

Finally, to evaluate the numerical effort of the different closures, the absolute computational time t_c needed to approximate the fourth-order fiber orientation tensor $\mathbb{N}$ for a specific closure is measured relative to the computational time of the IBOF closure $t_\mathsf{c}^\mathsf{IBOF}$. With both measures at hand, the relative computational time t_rel is defined as follows

$$t_\mathsf{rel} = \frac{t_\mathsf{c}}{t_\mathsf{c}^\mathsf{IBOF}}. \tag{5.55}$$

In the case of orientation evolution, the data refer to the effort in each time integration step, whereas for the prediction of anisotropic properties the fourth-order fiber orientation tensor $\mathbb{N}$ only needs to be calculated once. Table 5.1 lists the timings recorded on a Lenovo ThinkPad X1 Yoga with Intel® Core™ i7-10510U CPU (1.80 GHz) and 16 GB RAM using MATLAB®. As previously reported in Sec. 5.4.1, 5810 integration points on the unit sphere are used for MEM and ACG, the tolerance is fixed to 10^{-8} and the initial guess of Newton's method for SIQ and SIHYB is

[14] This section is directly taken from Karl et al. (2023a).

$s_0 = 0.25$. The results show that the highest numerical effort is required by MEM, followed by ACG. The closures HYB, SQC, and QC come with the least effort. In addition, the computational effort for IBOF and the new closures SIQ and SIHYB are in the same order of magnitude. It is noted that no runtime-optimized implementation of MEM (Luo et al., 2018) and ACG (Montgomery-Smith et al., 2011a;b) is used.

5.5 Summary and conclusions [15]

In the present chapter, a novel implicit closure approach is proposed based on the contraction condition $\mathbb{N}[\boldsymbol{I}] = \boldsymbol{N}$ involving orientation tensors of the first kind (Kanatani, 1984; Advani and Tucker III, 1987). By considering fully symmetric approximations, additional requirements are fulfilled, namely the trace condition and the consistency with the flow, see Sec. 2.5, in view of the trace-preserving property of the Folgar-Tucker equation (Folgar and Tucker III, 1984; Advani and Tucker III, 1987). Two fully symmetric implicit closures are investigated representing an innovative class of closure approaches, namely the symmetric implicit quadratic closure (SIQ) and the symmetric implicit hybrid closure (SIHYB). The SIQ closure approach extends the symmetric quadratic closure (SQC) proposed in chapter 4 with the underlying publication Karl et al. (2021b) and SIHYB combines both approaches in view of the classical HYB closure of Advani and Tucker III (1987; 1990). The present analysis shows that SIQ represents a realizable closure meaning that it is based on an ODF. In contrast, the SIHYB approach is not based on an ODF in general, since the linear part represents a non-realizable closure (Bauer and Böhlke, 2022b). Both proposed implicit closures are able to exactly compute the correct fourth-order

[15] This section consists of parts from Karl et al. (2023a). Additional text passages have been added.

orientation tensor for the UD, ISO, and PI case. In the context of fiber orientation evolution in a simple shear flow and the prediction of the effective viscous and elastic anisotropy for a given orientation state, SIQ and SIHYB are compared with well-known closure schemes. In the following, the results are summarized and the related conclusions are drawn:

- **Orientation dynamics.** In case of orientation evolution, the SIQ and SIHYB closures show oscillatory behavior, closely following the MEM referring to Jaynes (1957), Bingham (1974), Chaubal and Leal (1998), van Gurp (1998), and Müller and Böhlke (2016) over the entire considered range of the fiber interaction parameter C_I. The SIHYB approach is capable of approximating the MEM results with respect to lower computational cost. Of course, MEM is able to be extended to known higher-order orientation tensors improving the approximation, which is not possible for SIHYB. In contrast to the estimation of the effective stiffness, the fiber orientation evolution is not well-approximated compared to IBOF and ACG, even for typical values of the fiber interaction parameter C_I in the interval $[5 \cdot 10^{-4}, 5 \cdot 10^{-3}]$, see Bay (1991) (p. 119). Likewise, the accuracy of SIQ and SIHYB compared to the solution of the Fokker-Planck equation is rated as insufficient. In addition, the oscillations of SIQ and SIHYB also occur in the more relevant RSC (Wang et al., 2008) and ARD (Phelps and Tucker III, 2009) models as illustrated in Sec. D.2. This allows the conclusion that the implicit approaches in a non-stabilized formulation should not be used in engineering practice for orientation evolution predictions. This is in line with the discussion in Sec. 2.5 in relation to Advani and Tucker III (1987) that the fulfillment of all algebraic properties is a necessary but not a sufficient criterion for a closure.

- **MEM approximation.** The MEM-approximating property of the proposed SIQ and SIHYB closures originates from an approximation of the lowest-order MEM formulation recently published by Papenfuß (2022).
- **Effective stiffness prediction.** For estimating the effective stiffness with different closure approaches, the computational experiments demonstrate that the implicit closures strongly improve the results compared to their explicit formulation. Both SIQ and SIHYB are capable of approximating the MEM prediction and the results are close to the IBOF and ACG. Overall, there is a rather good agreement with the prediction of effective stiffness based on the measured fourth-order orientation tensor, which is considered accurate.
- **Limitation of material symmetry.** Provided that all necessary algebraic conditions are satisfied by the closure, excluding QC and HYB, the anisotropy plots of Figs. 5.5 and 5.6 look similar for all applied closures. The considered common closures and the new approaches SIQ and SIHYB depend on the intrinsically orthotropic second-order fiber orientation tensor. This implies the orthotropic symmetry of the closed fourth-order orientation tensor. Therefore, orthotropy is the highest possible degree of anisotropy predicted by the new closure approach. This issue is discussed in the recent publications of Bauer and Böhlke (2022a) and Tucker III (2022b). Conversely, this apparent restriction means that the quality of standard closures depending on the second-order fiber orientation tensor should not be judged solely on the basis of estimating the effective properties. In order to comprehend the quality of closures holistically, the behavior with regard to the prediction of the fiber orientation evolution in flow simulations must also be examined. A closure that is suitable for engineering practice is characterized by the fact that both the effective properties and the orientation evolution are predicted accurately.

- **Effective viscosity prediction.** Analogously, the implicit closures strongly improve the predictions of the effective viscosity compared to their explicit formulation. However, the difference between the implicit closures and IBOF or ACG is more distinct in the case of anisotropic linear viscous properties compared to the estimation of the effective stiffness. In this context, SIQ is capable of approximating the MEM results and an overall good agreement of SIQ with the measured data is observed.
- **1D formulation.** Since both SIQ and SIHYB can be reduced to Newton's method in 1D, these closures are simple to compute and represent accurate approximations with respect to anisotropic property predictions.

Chapter 6

Mean-field formulation of short-fiber orientation dynamics

Contents overview. This chapter represents the third and final part of the micromechanical modeling of short-fiber orientation dynamics. First, the generalized evolution equation for the fiber orientation tensor of arbitrary order is derived based on mean-field modeling. This approach allows the consideration of the anisotropic microstructure in the orientation evolution equation itself. Subsequently, the generalized evolution equation is specified for a selection of different mean-field models. The respective evolution equations for the second-order fiber orientation tensor are investigated for a simple shear flow.

6.1 Fiber orientation tensor evolution

6.1.1 Generalized formulation [1]

As a starting point for deriving a generalized fiber orientation tensor evolution equation, the orientation average given in Advani and Tucker III (1987) of an arbitrary second-order microstructure tensor $\boldsymbol{A}(\boldsymbol{n})$ is

[1] This section consists of parts from Karl and Böhlke (2024). Additional text passages have been added.

considered similar to Eq. (2.80)

$$\langle \boldsymbol{A} \rangle_{\mathsf{F}} = \int_{\mathcal{S}} f(\boldsymbol{n}, t) \boldsymbol{A}(\boldsymbol{n}) \, \mathrm{d}S(\boldsymbol{n}). \tag{6.1}$$

The argument $\boldsymbol{x}$, which represents the spatial dependence of the ODF f, is omitted for a more compact notation. Following the work of Böhlke (2006) for polycrystals, the time derivative of $\langle \boldsymbol{A} \rangle_{\mathsf{F}}$ is considered according to

$$\frac{\mathrm{d}}{\mathrm{d}t} \langle \boldsymbol{A} \rangle_{\mathsf{F}} = \frac{\mathrm{d}}{\mathrm{d}t} \int_{\mathcal{S}} f(\boldsymbol{n}, t) \boldsymbol{A}(\boldsymbol{n}) \, \mathrm{d}S(\boldsymbol{n}). \tag{6.2}$$

As shown in App. E.1, Eq. (6.2) can be transformed into the following generalized evolution equation for the orientation tensor $\mathbb{N}_{\langle n \rangle}$ of arbitrary even order n by substituting the tensor $\boldsymbol{A}$ with $\boldsymbol{n}^{\otimes n}$

$$\dot{\mathbb{N}}_{\langle n \rangle} = \int_{\mathcal{S}} f(\boldsymbol{n}, t) (\boldsymbol{n}^{\otimes n})^{\cdot} \, \mathrm{d}S(\boldsymbol{n}), \tag{6.3}$$

with the corresponding derivative

$$(\boldsymbol{n}^{\otimes n})^{\cdot} = \dot{\boldsymbol{n}} \otimes \boldsymbol{n}^{\otimes (n-1)} + \boldsymbol{n} \otimes \dot{\boldsymbol{n}} \otimes \boldsymbol{n}^{\otimes (n-2)} + \ldots + \boldsymbol{n}^{\otimes (n-1)} \otimes \dot{\boldsymbol{n}}. \tag{6.4}$$

It should be noted that the rate $\dot{\boldsymbol{n}}$, which represents the material time derivative of $\boldsymbol{n}$ similar to Eq. (2.16), is a constitutive quantity when considering the analogous approach by Böhlke (2006) for polycrystals. Following Favaloro (2020), the local fiber spin tensor $\boldsymbol{W}_{\mathsf{F}}$ is used to express the rate via $\dot{\boldsymbol{n}} = \boldsymbol{W}_{\mathsf{F}} \boldsymbol{n}$, which allows the abbreviation

$$(\boldsymbol{n}^{\otimes n})^{\cdot} = \boldsymbol{W}_{\mathsf{F}} \boxtimes (\boldsymbol{n}^{\otimes n}). \tag{6.5}$$

The operator $\boxtimes$ is defined as follows (Böhlke, 2006)

$$\begin{aligned} (\boldsymbol{n}^{\otimes n})^{\cdot}_{ijk\ldots l} = {} & W^{\mathsf{F}}_{im} n_m n_j n_k \ldots n_l + W^{\mathsf{F}}_{jm} n_i n_m n_k \ldots n_l \\ & + W^{\mathsf{F}}_{km} n_i n_j n_m \ldots n_l + \ldots + W^{\mathsf{F}}_{lm} n_i n_j n_k \ldots n_m. \end{aligned} \tag{6.6}$$

As will be shown in the following part of this section, $\boldsymbol{W}_{\mathsf{F}}$ and, therefore, the rate $(\boldsymbol{n}^{\otimes n})^{\cdot}$ depends on the effective spin, the local strain rate, and the anisotropic environment of the fiber. With Eq. (6.5), the fiber orientation tensor evolution equation of arbitrary even order n can be compactly formulated as follows

$$\dot{\mathbb{N}}_{\langle n\rangle} = \int_{\mathcal{S}} f(\boldsymbol{n},t)\boldsymbol{W}_{\mathsf{F}}\boxtimes(\boldsymbol{n}^{\otimes n})\,\mathrm{d}S(\boldsymbol{n}). \tag{6.7}$$

It is noted that Eq. (6.7) is related to the generalized evolution equation for arbitrary statistical moments in terms of texture coefficients for polycrystals as derived by Böhlke (2006). It is interesting to see that the algebraic structure is equal with respect to the set of orthogonal tensors $\mathrm{SO3}$ and the unit sphere $\mathcal{S}$, and that the spin localization of the polycrystal analogy referring to, e.g., Lipinski and Berveiller (1989), Adams and Field (1991), and Lebensohn and Tomé (1993) is a crucial constitutive quantity that needs to be modeled.

In order to incorporate the microstructure into the evolution equation (6.7), the localization (or concentration) relation for the fiber spin tensor $\boldsymbol{W}_{\mathsf{F}}$ is addressed in the following. This serves as a starting point for the subsequent application of arbitrary mean-field homogenization models. The approach of Adams and Field (1991) is applied to viscous suspensions throughout this chapter, considering the quasi-static balance of linear momentum without body forces, the constitutive law for linear viscous suspensions, the compatibility condition inside the volume V, and the incompressibility condition

$$\begin{aligned} \boldsymbol{0} &= \mathrm{div}(\boldsymbol{\sigma}), & \boldsymbol{\sigma} &= -p\boldsymbol{I} + \mathbb{V}[\boldsymbol{D}], \\ \boldsymbol{0} &= \mathrm{rot}(\mathrm{rot}^{\mathsf{T}}(\boldsymbol{D})), & 0 &= \mathrm{tr}(\boldsymbol{D}). \end{aligned} \tag{6.8}$$

In this system of equations, the operator $\mathrm{rot}(\cdot)$ refers to the rotation, also referred to as $\mathrm{curl}(\cdot)$. It is assumed that the constant macroscopic velocity gradient $\bar{\boldsymbol{L}}$ and the constant macroscopic pressure $\bar{p}$ are applied on the

boundary ∂V (Adams and Field, 1991). For the sake of clarity, the discussion of the fundamental assumptions of mean-field homogenization is omitted here, and reference is made to Sec. 2.6.1. Based on the approach for linear elastic solids referring to Hashin and Shtrikman (1962a;b), Walpole (1966a;b), and Willis (1977), a homogeneous reference viscosity $\mathbb{V}_0$ is introduced and the corresponding viscous stress polarization $\boldsymbol{\tau}$ and the constitutive law read

$$\boldsymbol{\tau} = (\mathbb{V} - \mathbb{V}_0)[\boldsymbol{D}], \qquad \boldsymbol{\sigma} = -p\boldsymbol{I} + \mathbb{V}_0[\boldsymbol{D}] + \boldsymbol{\tau}. \tag{6.9}$$

Using Eq. (6.9), the static balance of linear momentum without body forces can be reformulated for viscous suspensions similar to elastic solids, see, e.g., Willis (1981), Lipinski and Berveiller (1989), and Adams and Field (1991)

$$\mathbf{0} = -\mathrm{grad}(p) + \mathrm{div}(\mathbb{V}_0[\boldsymbol{D}]) + \mathrm{div}(\boldsymbol{\tau}), \tag{6.10}$$

with the pressure boundary condition $p(\boldsymbol{x}) = \bar{p}$, $\boldsymbol{x} \in \partial V$, and the velocity boundary condition $\boldsymbol{v}(\boldsymbol{x}) = \bar{\boldsymbol{v}}$, $\boldsymbol{x} \in \partial V$. The formal solution of Eq. (6.10) can be expressed conveniently in index notation as follows with Green's functions $\boldsymbol{g}(\boldsymbol{x}, \boldsymbol{x}')$ and $\boldsymbol{G}(\boldsymbol{x}, \boldsymbol{x}')$, see, e.g., Willis (1981), Lipinski and Berveiller (1989), and Adams and Field (1991)

$$\begin{aligned} p(\boldsymbol{x}) &= \bar{p} - \int_V \frac{\partial g_i(\boldsymbol{x}, \boldsymbol{x}')}{\partial x'_j} \tau_{ij}(\boldsymbol{x}') \,\mathrm{d}V(\boldsymbol{x}'), \\ v_i(\boldsymbol{x}) &= \bar{v}_i - \int_V \frac{\partial G_{ik}(\boldsymbol{x}, \boldsymbol{x}')}{\partial x'_l} \tau_{kl}(\boldsymbol{x}') \,\mathrm{d}V(\boldsymbol{x}'), \end{aligned} \tag{6.11}$$

with the boundary values $\boldsymbol{g}(\boldsymbol{x}, \boldsymbol{x}') = \mathbf{0}$, $\boldsymbol{x} \in \partial V$, and $\boldsymbol{G}(\boldsymbol{x}, \boldsymbol{x}') = \mathbf{0}$, $\boldsymbol{x} \in \partial V$. Since the pressure in the incompressible case represents only a reaction force, its calculation is not considered here. The components of the local velocity gradient $\boldsymbol{L}$ follow directly from the components of the

local velocity $\boldsymbol{v}$ in Eq. (6.11) (Lipinski and Berveiller, 1989)

$$\begin{aligned} L_{ij}(\boldsymbol{x}) &= \bar{L}_{ij} - \int_V \frac{\partial^2 G_{ik}(\boldsymbol{x},\boldsymbol{x}')}{\partial x'_l \partial x_j} \tau_{kl}(\boldsymbol{x}')\,\mathrm{d}V(\boldsymbol{x}') \\ &= \bar{L}_{ij} - \int_V \frac{\partial^2 G_{im}(\boldsymbol{x},\boldsymbol{x}')}{\partial x'_n \partial x_j} I^{\mathsf{S}}_{mnkl} \tau_{kl}(\boldsymbol{x}')\,\mathrm{d}V(\boldsymbol{x}') \\ &= \bar{L}_{ij} - \int_V \Gamma_{ijkl}(\boldsymbol{x},\boldsymbol{x}')\tau_{kl}(\boldsymbol{x}')\,\mathrm{d}V(\boldsymbol{x}'). \end{aligned} \tag{6.12}$$

In the last step, the kernel of the integral is abbreviated by $\mathbb{\Gamma} \mathrel{\widehat{=}} \Gamma_{ijkl}$ which typically is symmetrized in the right index pair leading to the compact symbolic notation of Eq. (6.12) similar to Willis (1977; 1981)

$$\begin{aligned} \mathbb{\Gamma}\{\boldsymbol{\tau}\} : \boldsymbol{\tau} &\mapsto \int_V \mathbb{\Gamma}(\boldsymbol{x},\boldsymbol{x}')[\boldsymbol{\tau}(\boldsymbol{x}')]\,\mathrm{d}V(\boldsymbol{x}'), \\ \boldsymbol{L}(\boldsymbol{x}) &= \bar{\boldsymbol{L}} - \mathbb{\Gamma}\{\boldsymbol{\tau}\}. \end{aligned} \tag{6.13}$$

In order to derive localization relations for the strain-rate tensor $\boldsymbol{D} = \mathrm{sym}(\boldsymbol{L})$ and for the spin tensor $\boldsymbol{W} = \mathrm{skw}(\boldsymbol{L})$, the integral operator $\mathbb{\Gamma}$ is either skew-symmetrized (A) or symmetrized (S) in the left index pair (Adams and Field, 1991) which is denoted by $\mathbb{\Gamma}^{\mathsf{A}} = \mathbb{I}^{\mathsf{A}}\mathbb{\Gamma}$ and $\mathbb{\Gamma}^{\mathsf{S}} = \mathbb{I}^{\mathsf{S}}\mathbb{\Gamma}$, respectively. Here, $\mathbb{I}^{\mathsf{A}}$ refers to the identity on skew-symmetric second-order tensors. Similar to Eq. (6.13), it is written

$$\boldsymbol{D}(\boldsymbol{x}) = \bar{\boldsymbol{D}} - \mathbb{\Gamma}^{\mathsf{S}}\{\boldsymbol{\tau}\}, \qquad \boldsymbol{W}(\boldsymbol{x}) = \bar{\boldsymbol{W}} - \mathbb{\Gamma}^{\mathsf{A}}\{\boldsymbol{\tau}\}. \tag{6.14}$$

The integral operations of Eq. (6.14) can be transformed into linear mappings by taking into account the following points referring to, e.g., Willis (1977; 1981):

1) By considering an infinite volume V_∞ of a statistically homogeneous composite, $\mathbb{\Gamma}^{\mathsf{S,A}}(\boldsymbol{x},\boldsymbol{x}')$ is replaced by the infinite translation-invariant operator $\mathbb{\Gamma}^{\mathsf{S,A}}_\infty(\boldsymbol{x}-\boldsymbol{x}')$. It should be noted that the super-

script „S,A“ represents an abbreviation meaning either S or A, not both in the sense of a composition.

2) The localization relations (6.14) must fulfill $\langle \boldsymbol{D} \rangle = \bar{\boldsymbol{D}}$ and $\langle \boldsymbol{W} \rangle = \bar{\boldsymbol{W}}$ implying that the volume average of the integral operations vanishes: $\langle \mathbb{I}^{\mathsf{S}}\{\boldsymbol{\tau}\} \rangle = \mathbf{0}$ and $\langle \mathbb{I}^{\mathsf{A}}\{\boldsymbol{\tau}\} \rangle = \mathbf{0}$. This is ensured by defining the integral operator $\mathbb{I}^{\mathsf{S,A}}\{\boldsymbol{\tau}\}$ on the fluctuation of the viscous stress polarization field $\boldsymbol{\tau} - \langle \boldsymbol{\tau} \rangle$

$$\mathbb{I}^{\mathsf{S,A}}\{\boldsymbol{\tau}\} : \boldsymbol{\tau} \mapsto \int_V \mathbb{I}_{\infty}^{\mathsf{S,A}}(\boldsymbol{x} - \boldsymbol{x}')[\boldsymbol{\tau}(\boldsymbol{x}') - \langle \boldsymbol{\tau} \rangle] \, \mathrm{d}V(\boldsymbol{x}'). \tag{6.15}$$

3) The viscous stress polarization $\boldsymbol{\tau}$ is assumed to be constant in each of the phases. If no long-range order and ellipsoidal two-point statistics are assumed, the integral operator (6.15) can be further simplified

$$\begin{aligned} \mathbb{I}^{\mathsf{S,A}}\{\boldsymbol{\tau}\} : \boldsymbol{\tau} &\mapsto \int_V \mathbb{I}_{\infty}^{\mathsf{S,A}}(\boldsymbol{x}) \, \mathrm{d}V(\boldsymbol{x})[\boldsymbol{\tau} - \langle \boldsymbol{\tau} \rangle], \\ \mathbb{P}_0^{\mathsf{S,A}} &= \int_V \mathbb{I}_{\infty}^{\mathsf{S,A}}(\boldsymbol{x}) \, \mathrm{d}V(\boldsymbol{x}). \end{aligned} \tag{6.16}$$

The tensor $\mathbb{P}_0^{\mathsf{S,A}}$ is called polarization tensor according to, e.g., Walpole (1981), and is either symmetric in the left index pair (S) or skew-symmetric (A) in the left index pair. It should be noted that both tensors $\mathbb{P}_0^{\mathsf{S,A}}$ are symmetric in the right index pair. Based on Eq. (6.16), the localization relations (6.14) read as the following linear mappings as derived by Adams and Field (1991)

$$\boldsymbol{D} = \bar{\boldsymbol{D}} - \mathbb{P}_0^{\mathsf{S}}[\boldsymbol{\tau} - \langle \boldsymbol{\tau} \rangle], \qquad \boldsymbol{W} = \bar{\boldsymbol{W}} - \mathbb{P}_0^{\mathsf{A}}[\boldsymbol{\tau} - \langle \boldsymbol{\tau} \rangle], \tag{6.17}$$

which correspond to the expressions derived similarly by, e.g., Avazmohammadi and Ponte Castañeda (2015) in the context of deformable particles in Newtonian fluids, but Eq. (6.17) additionally considers the

volume average $\langle \boldsymbol{\tau} \rangle$, which will be shown below to be connected to the orientation average. The fiber spin tensor $\boldsymbol{W}_{\mathsf{F}}$ needed for Eq. (6.7) can be computed based on Eq. (6.17) specified for the fiber phase as follows

$$\boldsymbol{W}_{\mathsf{F}} = \bar{\boldsymbol{W}} - \mathbb{P}_0^{\mathsf{A}}[\boldsymbol{\tau}_{\mathsf{F}} - \langle \boldsymbol{\tau} \rangle]. \tag{6.18}$$

For the special case of two-phase fiber suspensions, the volume-averaged viscous stress polarization reads similar to the volume averages given in Eq. (2.74)

$$\langle \boldsymbol{\tau} \rangle = c_{\mathsf{M}} \langle \boldsymbol{\tau} \rangle_{\mathsf{M}} + c_{\mathsf{F}} \langle \boldsymbol{\tau} \rangle_{\mathsf{F}}, \tag{6.19}$$

with the volume fraction of the matrix c_{M} and of the fibers c_{F}. The homogeneous reference viscosity is set to the matrix viscosity $\mathbb{V}_0 = \mathbb{V}_{\mathsf{M}}$ similar to Kailasam and Ponte Castañeda (1998) and Avazmohammadi and Ponte Castañeda (2015), which leads to a vanishing polarization field in the matrix phase $\langle \boldsymbol{\tau} \rangle_{\mathsf{M}} = \boldsymbol{0}$. Therefore, the volume average of the viscous stress polarization reads $\langle \boldsymbol{\tau} \rangle = c_{\mathsf{F}} \langle \boldsymbol{\tau} \rangle_{\mathsf{F}}$. The non-zero polarization field of the fiber phase

$$\boldsymbol{\tau}_{\mathsf{F}} = (\mathbb{V}_{\mathsf{F}} - \mathbb{V}_{\mathsf{M}})[\boldsymbol{D}_{\mathsf{F}}] = \delta\mathbb{V}[\boldsymbol{D}_{\mathsf{F}}] = \delta\mathbb{V}\mathbb{A}_{\mathsf{F}}[\bar{\boldsymbol{D}}] \tag{6.20}$$

depends on the strain-rate localization tensor $\mathbb{A}_{\mathsf{F}}$ of the fiber and the difference $\delta\mathbb{V} = \mathbb{V}_{\mathsf{F}} - \mathbb{V}_{\mathsf{M}}$. Herein, the local strain-rate tensor $\boldsymbol{D}_{\mathsf{F}}$ of the fiber is computed with the constant macroscopic strain-rate tensor $\bar{\boldsymbol{D}}$ via $\boldsymbol{D}_{\mathsf{F}} = \mathbb{A}_{\mathsf{F}}[\bar{\boldsymbol{D}}]$. As a result, the fiber spin tensor given in Eq. (6.18) can be computed as follows

$$\begin{aligned}
\boldsymbol{W}_{\mathsf{F}} &= \bar{\boldsymbol{W}} - \mathbb{P}_0^{\mathsf{A}}[\boldsymbol{\tau}_{\mathsf{F}} - c_{\mathsf{F}} \langle \boldsymbol{\tau} \rangle_{\mathsf{F}}] \\
&= \bar{\boldsymbol{W}} - \mathbb{P}_0^{\mathsf{A}}(\delta\mathbb{V}\mathbb{A}_{\mathsf{F}} - c_{\mathsf{F}} \langle \delta\mathbb{V}\mathbb{A} \rangle_{\mathsf{F}})[\bar{\boldsymbol{D}}] \\
&= \bar{\boldsymbol{W}} - \mathbb{P}_0^{\mathsf{A}}\delta\mathbb{V}\mathbb{A}_{\mathsf{F}}[\bar{\boldsymbol{D}}] + c_{\mathsf{F}} \langle \mathbb{P}_0^{\mathsf{A}}\delta\mathbb{V}\mathbb{A} \rangle_{\mathsf{F}}[\bar{\boldsymbol{D}}] \\
&= \bar{\boldsymbol{W}} - \boldsymbol{W}_{\mathsf{local}} + \bar{\boldsymbol{W}}_{\mathsf{mean}}.
\end{aligned} \tag{6.21}$$

The first term $\bar{\boldsymbol{W}}$ refers to the macroscopic or far-field spin tensor of the flow, which is a constant contribution to the fiber spin tensor $\boldsymbol{W}_{\mathsf{F}}$. The second term $\boldsymbol{W}_{\mathsf{local}}$ refers to an additional spin concentration according to, e.g., Kailasam and Ponte Castañeda (1998) and Wetzel and Tucker III (2001). Since only the macroscopic strain-rate tensor $\bar{\boldsymbol{D}}$ is involved, this term induces a local fiber spin depending on the local direction of the fiber even in the presence of spin-free macroscopic flow (Wetzel and Tucker III, 2001). Also the geometry of the fibers is involved in the fiber spin tensor via the polarization tensors as stated by, e.g., Kailasam and Ponte Castañeda (1998). The third term $\bar{\boldsymbol{W}}_{\mathsf{mean}}$ contains the orientation average operator $\langle\cdot\rangle_{\mathsf{F}}$ introduced in Eq. (6.1) which accounts for the interaction between the fibers by considering the mean fiber orientation of the suspension as an anisotropic environment. It is noted that this is a constant contribution to the fiber spin only if the effective orientation itself is constant. However, in any real process, a single fiber does not have a constant anisotropic environment, as the flow generally changes the effective orientation over time. In addition, the third term also induces a spin even in the presence of spin-free macroscopic flow. The contributions $\boldsymbol{W}_{\mathsf{local}}$ and $\bar{\boldsymbol{W}}_{\mathsf{mean}}$ to the fiber spin tensor have different signs since together they define a fluctuation field of the spin which is derived from the convergence criterion of the integral operator in the context of Eq. (6.15). Whether $\boldsymbol{W}_{\mathsf{local}}$ and $\bar{\boldsymbol{W}}_{\mathsf{mean}}$ accelerate or decelerate the local spin with respect to $\bar{\boldsymbol{W}}$ depends on the kinematics in a complex way, the actual fiber direction, and the mean orientation of the fiber suspension. The three different contributions to the fiber spin tensor $\boldsymbol{W}_{\mathsf{F}}$ are illustrated in Fig. 6.1, where a representative volume element V is depicted. The macroscopic tensors $\bar{\boldsymbol{W}}$ and $\bar{\boldsymbol{D}}$ are prescribed at the boundary ∂V (green). The term $\boldsymbol{W}_{\mathsf{local}}$ is associated with the single fiber (blue) and depends on its orientation $\boldsymbol{n}$ and aspect ratio α via the skew-symmetric polarization tensor $\mathbb{P}_0^{\mathsf{A}}$, see App. E.4. In addition, $\boldsymbol{W}_{\mathsf{local}}$ contains the viscosity of both phases, and depending on which mean-field model for $\mathbb{A}_{\mathsf{F}}$ is applied, additional dependencies may be given, see

Sec. 2.6.4. The term $\bar{\boldsymbol{W}}_{\mathsf{mean}}$ refers to the anisotropic environment of the single fiber (gray). This term depends on the fiber volume fraction c_{F} of the suspension, regardless of which mean-field model is applied. In addition to the viscosity of both phases, the effective aspect ratio α and the effective ODF f of the suspension are included. Note that there is no dependence on the direction of all surrounding individual fibers, as these are considered as an ensemble via the orientation average $\langle\cdot\rangle_{\mathsf{F}}$ and only constant aspect ratios are assumed in this thesis.

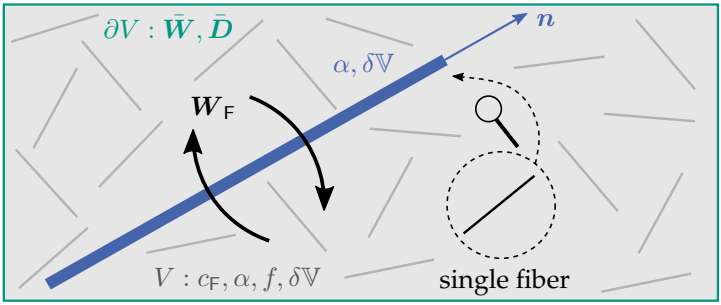

Figure 6.1: Graphical illustration of the fiber spin tensor contributions: The macroscopic tensors $\bar{\boldsymbol{W}}$ and $\bar{\boldsymbol{D}}$ at the boundary ∂V (■), the local contribution $\boldsymbol{W}_{\mathsf{local}} = \mathbb{P}_0^{\mathsf{A}}\delta\mathbb{V}\mathbb{A}_{\mathsf{F}}[\bar{\boldsymbol{D}}]$ (■), and the contribution of the anisotropic environment $\bar{\boldsymbol{W}}_{\mathsf{mean}} = c_{\mathsf{F}}\langle\mathbb{P}_0^{\mathsf{A}}\delta\mathbb{V}\mathbb{A}\rangle_{\mathsf{F}}[\bar{\boldsymbol{D}}]$ (■), adapted from the graphical abstract of Karl and Böhlke (2024) published online at `https://doi.org/10.1016/j.ijmecsci.2023.108771`, retrieved on August 26, 2024.

The generalized fiber orientation evolution equation (6.7) can be specified by using the fiber spin tensor given in Eq. (6.21)

$$\begin{aligned}\dot{\mathbb{N}}_{\langle n\rangle} = \bar{\boldsymbol{W}}\boxtimes\mathbb{N}_{\langle n\rangle} - \int_{\mathcal{S}} f(\boldsymbol{n},t)\big(\mathbb{P}_0^{\mathsf{A}}\delta\mathbb{V}\mathbb{A}_{\mathsf{F}}[\bar{\boldsymbol{D}}]\big)\boxtimes(\boldsymbol{n}^{\otimes n})\,\mathrm{d}S(\boldsymbol{n})\\ + c_{\mathsf{F}}\int_{\mathcal{S}} f(\boldsymbol{n},t)\big(\langle\mathbb{P}_0^{\mathsf{A}}\delta\mathbb{V}\mathbb{A}\rangle_{\mathsf{F}}[\bar{\boldsymbol{D}}]\big)\boxtimes(\boldsymbol{n}^{\otimes n})\,\mathrm{d}S(\boldsymbol{n}).\end{aligned} \tag{6.22}$$

To conclude this section it should be noted that Eq. (6.22) is given exactly with regard to the assumptions addressed before and that the

study is limited to a linear homogenization approach. The evolution equation (6.22) is not presented in closed form since the ODF f has to be estimated in engineering practice. In addition, the tensors $\mathbb{P}_0^{\mathsf{A}}$ and $\mathbb{A}_{\mathsf{F}}$ are approximated by using mean-field models. It is emphasized that Eq. (6.22) allows the application of arbitrary mean-field models for the localization tensor $\mathbb{A}_{\mathsf{F}}$, a selection of which is presented below.

6.1.2 Reconsideration of Jeffery's equation [2]

The motion of one single spheroidal rigid fiber in a Newtonian matrix fluid without Brownian motion, inertia effects, and hydrodynamic interaction, see Sec. 2.4.2, is covered by the Jeffery equation (Jeffery, 1922; Junk and Illner, 2007). Since one fiber is considered whose size is small compared to the size of the considered volume (Jeffery, 1922), the fiber spin tensor given in Eq. (6.21) can be simplified by applying $c_{\mathsf{F}} \to 0$

$$\boldsymbol{W}_{\mathsf{F}} = \bar{\boldsymbol{W}} - \mathbb{P}_0^{\mathsf{A}} \delta \mathbb{V} \mathbb{A}_{\mathsf{F}} [\bar{\boldsymbol{D}}]. \tag{6.23}$$

The suitable mean-field model for the localization tensor $\mathbb{A}_{\mathsf{F}}$ is DD following Wetzel (1999) (pp. 48–49, 267–269) and Wetzel and Tucker III (2001), which is also addressed in the following Sec. 6.1.3. As a result, the fiber spin tensor can be written as follows by using $\mathbb{A}_{\mathsf{F}}$ given in, e.g., Tucker III and Liang (1999) and in Sec. 2.6.4

$$\begin{aligned} \boldsymbol{W}_{\mathsf{F}} &= \bar{\boldsymbol{W}} - \mathbb{P}_0^{\mathsf{A}} \delta \mathbb{V} \big(\mathbb{I}^{\mathsf{S}} + \mathbb{P}_0^{\mathsf{S}} \delta \mathbb{V} \big)^{-1} [\bar{\boldsymbol{D}}] \\ &= \bar{\boldsymbol{W}} - \mathbb{P}_0^{\mathsf{A}} \big(\delta \mathbb{V}^{-1} + \mathbb{P}_0^{\mathsf{S}} \big)^{-1} [\bar{\boldsymbol{D}}]. \end{aligned} \tag{6.24}$$

The rigid fiber assumption $\mathbb{V}_{\mathsf{F}} \to \infty$ or, in other words, a vanishing fluidity $\delta \mathbb{V}^{-1}$, as one of the fundamental assumptions of mean-field

[2] This section consists of parts from Karl and Böhlke (2024). Additional text passages have been added.

homogenization described in Sec. 2.6.1, leads to the following fiber spin tensor $\boldsymbol{W}_{\mathsf{F}}$ and to an equation for the rate $\dot{\boldsymbol{n}}$ reading

$$\begin{aligned}\boldsymbol{W}_{\mathsf{F}} &= \bar{\boldsymbol{W}} - \mathbb{P}_0^{\mathsf{A}}\big(\mathbb{P}_0^{\mathsf{S}}\big)^{-1}[\bar{\boldsymbol{D}}],\\ \dot{\boldsymbol{n}} &= \bar{\boldsymbol{W}}\boldsymbol{n} - \mathbb{P}_0^{\mathsf{A}}\big(\mathbb{P}_0^{\mathsf{S}}\big)^{-1}[\bar{\boldsymbol{D}}]\boldsymbol{n}.\end{aligned} \tag{6.25}$$

It is shown in App. E.2 that the polarization tensor-based notation of Eq. (6.25) corresponds to the following equivalent formulation of Wetzel (1999) (pp. 48–49) and Wetzel and Tucker III (2001)

$$\begin{aligned}\boldsymbol{W}_{\mathsf{F}} &= \bar{\boldsymbol{W}} + \mathbb{J}_{\mathsf{F}}[\bar{\boldsymbol{D}}],\\ \dot{\boldsymbol{n}} &= \bar{\boldsymbol{W}}\boldsymbol{n} + \mathbb{J}_{\mathsf{F}}[\bar{\boldsymbol{D}}]\boldsymbol{n},\end{aligned} \tag{6.26}$$

with the tensor $\mathbb{J}_{\mathsf{F}}$ introduced as Jeffery tensor in this chapter reading

$$\mathbb{J}_{\mathsf{F}} = \frac{1}{2}\xi\big(\boldsymbol{I}\square(\boldsymbol{n}\otimes\boldsymbol{n}) + (\boldsymbol{I}\square(\boldsymbol{n}\otimes\boldsymbol{n}))^{\mathsf{T}_{\mathsf{R}}} - (\boldsymbol{n}\otimes\boldsymbol{n})\square\boldsymbol{I} - ((\boldsymbol{n}\otimes\boldsymbol{n})\square\boldsymbol{I})^{\mathsf{T}_{\mathsf{R}}}\big). \tag{6.27}$$

In Eq. (6.27), the shape parameter $\xi = (\alpha^2-1)/(\alpha^2+1)$ of the fibers depends on the fiber aspect ratio α. Combining Eqs. (6.26) and (6.27) leads to the following common representation as given in Wetzel (1999) (pp. 48–49) and Wetzel and Tucker III (2001)

$$\begin{aligned}\boldsymbol{W}_{\mathsf{F}} &= \bar{\boldsymbol{W}} + \xi\big((\bar{\boldsymbol{D}}\boldsymbol{n})\otimes\boldsymbol{n} - \boldsymbol{n}\otimes(\bar{\boldsymbol{D}}\boldsymbol{n})\big),\\ \dot{\boldsymbol{n}} &= \bar{\boldsymbol{W}}\boldsymbol{n} + \xi\big(\bar{\boldsymbol{D}}\boldsymbol{n} - (\boldsymbol{n}\otimes\boldsymbol{n}\otimes\boldsymbol{n})[\bar{\boldsymbol{D}}]\big).\end{aligned} \tag{6.28}$$

Finally, the generalized Jeffery equation (JE) for the fiber orientation tensor of arbitrary even order n can be derived by using the fiber spin tensor $\boldsymbol{W}_{\mathsf{F}}$ given in Eq. (6.28) in Eq. (6.7) combined with the fiber orientation tensor definition given in Eq. (2.41) leading to

$$\dot{\mathbb{N}}_{\langle n\rangle} = \bar{\boldsymbol{W}}\boxtimes\mathbb{N}_{\langle n\rangle} + \xi\big(\bar{\boldsymbol{D}}\boxtimes\mathbb{N}_{\langle n\rangle} - n\mathbb{N}_{\langle n+2\rangle}[\bar{\boldsymbol{D}}]\big). \tag{6.29}$$

To conclude this section, the generalization of the Folgar-Tucker equation referring to Folgar and Tucker III (1984) and Advani and Tucker III (1987) is addressed. In order to model the respective fiber interaction, the following diffusion term on the unit sphere is considered at the level of the Fokker-Planck equation already addressed in Eq. (5.44)

$$D = C_\mathrm{I}\dot{\gamma}\Delta_{\mathcal{S}}(f(\boldsymbol{n},t)). \tag{6.30}$$

The parameter C_I refers to the fiber interaction parameter, the generalized shear rate is represented by $\dot{\gamma}$, and $\Delta_{\mathcal{S}}(\cdot)$ stands for the Laplacian on the unit sphere. The corresponding diffusion term (or interaction term) of order n can be obtained by integrating $D\boldsymbol{n}^{\otimes n}$ over the unit sphere

$$\mathbb{D}_{\langle n\rangle} = C_\mathrm{I}\dot{\gamma}\int_{\mathcal{S}} \boldsymbol{n}^{\otimes n}\Delta_{\mathcal{S}}(f(\boldsymbol{n},t))\,\mathrm{d}S(\boldsymbol{n}). \tag{6.31}$$

For $n=2$, this procedure involving Eqs. (6.30) and (6.31) is described by, e.g., Férec et al. (2017b). By transferring the following equivalence for arbitrary periodic functions $a(\boldsymbol{n})$ and $b(\boldsymbol{n})$ on the unit sphere (Sillem, 2010) (p. 19)

$$\int_{\mathcal{S}} a(\boldsymbol{n})\Delta_{\mathcal{S}}(b(\boldsymbol{n}))\,\mathrm{d}S(\boldsymbol{n}) = \int_{\mathcal{S}} b(\boldsymbol{n})\Delta_{\mathcal{S}}(a(\boldsymbol{n}))\,\mathrm{d}S(\boldsymbol{n}), \tag{6.32}$$

the alternative formulation of the interaction term (6.31) reads

$$\mathbb{D}_{\langle n\rangle} = C_\mathrm{I}\dot{\gamma}\int_{\mathcal{S}} f(\boldsymbol{n},t)\Delta_{\mathcal{S}}(\boldsymbol{n}^{\otimes n})\,\mathrm{d}S(\boldsymbol{n}). \tag{6.33}$$

The Laplacian on the unit sphere $\Delta_{\mathcal{S}}(\boldsymbol{n}^{\otimes n})$ can be computed analytically using the rules of calculus on the unit sphere as shown in App. E.3 for the special case of $n=2$. Applying this procedure to the general case in

Eq. (6.33) leads to the generalized Folgar-Tucker interaction term

$$\mathbb{D}_{\langle n\rangle} = 2C_{\mathrm{I}}\dot{\gamma}\left(\frac{(n-1)n}{2}\,\mathrm{sym}(\boldsymbol{I}\otimes\mathbb{N}_{\langle n-2\rangle}) - \left(n+\frac{(n-1)n}{2}\right)\mathbb{N}_{\langle n\rangle}\right), \quad (6.34)$$

defining the generalized Folgar-Tucker equation

$$\dot{\mathbb{N}}_{\langle n\rangle} = \bar{\boldsymbol{W}}\boxtimes\mathbb{N}_{\langle n\rangle} + \xi\big(\bar{\boldsymbol{D}}\boxtimes\mathbb{N}_{\langle n\rangle} - n\mathbb{N}_{\langle n+2\rangle}[\bar{\boldsymbol{D}}]\big) + \mathbb{D}_{\langle n\rangle}. \quad (6.35)$$

Furthermore, special emphasis is put on the following additional remarks:

1) As described by, e.g., Papenfuß (2019), the orientation of rigid-rod molecules in liquid crystals is related to the orientation of rigid fibers contained in fiber suspensions. Analogously, orientation tensors, or alignment tensors representing orientation tensors of the third kind (Kanatani, 1984), as statistical moments of the underlying ODF are used to describe the macroscopic orientation state.
2) In terms of a complete reconstruction of the ODF from its statistical moments, Papenfuß (2019) derived the evolution equation for the orientation tensor of arbitrary order for liquid crystals. Micro-level effects such as potentials and molecular interactions were excluded and the general equation includes components from flow, diffusion, and nematic parts. Hill (1999) considered rigid-rod molecules in liquid crystals analogously and also formulated the evolution equation for the statistical moment of arbitrary order. In contrast to Papenfuß (2019), the equation of Hill (1999) also contains components from an electric field, a magnetic field, and a dipole field and thus considers additional effects on the micro level.
3) The studies of Hill (1999) and Papenfuß (2019) generalize the collision tensor considered by Latz et al. (2010) to an arbitrary

tensor order. It should be noted that the collision tensor consists of two opposing mechanisms: Diffusion as a driving force towards an isotropic state and the nematic part forcing an alignment.

4) The generalized Folgar-Tucker equation (6.35) derived in this chapter is related in parts to the equations of Hill (1999) and Papenfuß (2019) and can be understood as its counterpart in the usual fiber community notation.

In the following, the interaction term (6.34) based on diffusion on the unit sphere is not considered since the micromechanical models addressed in the next sections are to be compared with the unmodified Jeffery equation (6.29) as done similarly by Férec et al. (2014) to investigate the behavior of their fiber interaction terms.

6.1.3 Dilute distribution [3]

Similar to the derivation of the Jeffery equation in Sec. 6.1.2, the strain-rate localization tensor of DD as given in, e.g., Tucker III and Liang (1999) and in Sec. 2.6.4

$$\mathbb{A}_{\mathsf{F}} = \left(\mathbb{I}^{\mathsf{S}} + \mathbb{P}_0^{\mathsf{S}}\delta\mathbb{V}\right)^{-1} \tag{6.36}$$

is used in the general expression (6.21) for the fiber spin tensor. The difference to the derivation of Jeffery's equation is that the volume fraction of the fibers $c_{\mathsf{F}} \ll 1$ is non-zero and the associated term is not neglected. Therefore, the spin localization for DD after a slight modification reads as follows

$$\begin{aligned}\boldsymbol{W}_{\mathsf{F}} = \bar{\boldsymbol{W}} &- \mathbb{P}_0^{\mathsf{A}}\left(\delta\mathbb{V}^{-1} + \mathbb{P}_0^{\mathsf{S}}\right)^{-1}[\bar{\boldsymbol{D}}] \\ &+ c_{\mathsf{F}}\left\langle \mathbb{P}_0^{\mathsf{A}}\left(\delta\mathbb{V}^{-1} + \mathbb{P}_0^{\mathsf{S}}\right)^{-1}[\bar{\boldsymbol{D}}]\right\rangle_{\mathsf{F}}.\end{aligned} \tag{6.37}$$

[3] This section consists of parts from Karl and Böhlke (2024). Additional text passages have been added.

Applying the assumption of rigid fibers with a vanishing fluidity $\delta\mathbb{V}^{-1}$ as before, the expression above yields

$$\boldsymbol{W}_{\mathsf{F}} = \bar{\boldsymbol{W}} - \mathbb{P}_0^{\mathsf{A}}\big(\mathbb{P}_0^{\mathsf{S}}\big)^{-1}[\bar{\boldsymbol{D}}] + c_{\mathsf{F}}\Big\langle \mathbb{P}_0^{\mathsf{A}}\big(\mathbb{P}_0^{\mathsf{S}}\big)^{-1}[\bar{\boldsymbol{D}}]\Big\rangle_{\mathsf{F}}. \tag{6.38}$$

Based on the considerations given in App. E.2, the expression above is equivalent to the following compact form

$$\boldsymbol{W}_{\mathsf{F}} = \bar{\boldsymbol{W}} + \mathbb{J}_{\mathsf{F}}[\bar{\boldsymbol{D}}] - c_{\mathsf{F}}\Big\langle \mathbb{J}_{\mathsf{F}}[\bar{\boldsymbol{D}}]\Big\rangle_{\mathsf{F}}, \tag{6.39}$$

with the Jeffery tensor $\mathbb{J}_{\mathsf{F}}$ given in Eq. (6.27) depending on the fiber aspect ratio and the direction of the spheroidal fiber. The operator $\langle\cdot\rangle_{\mathsf{F}}$ refers to Eq. (6.1) as the orientation average (Advani and Tucker III, 1987) and can be computed directly based on the convenient form of $\mathbb{J}_{\mathsf{F}}[\bar{\boldsymbol{D}}]$ with the second-order fiber orientation tensor $\boldsymbol{N}$

$$\boldsymbol{W}_{\mathsf{F}} = \bar{\boldsymbol{W}} + \xi\big((\bar{\boldsymbol{D}}\boldsymbol{n})\otimes\boldsymbol{n} - \boldsymbol{n}\otimes(\bar{\boldsymbol{D}}\boldsymbol{n})\big) - c_{\mathsf{F}}\xi(\bar{\boldsymbol{D}}\boldsymbol{N} - \boldsymbol{N}\bar{\boldsymbol{D}}). \tag{6.40}$$

It should be noted that the last term on the right-hand side represents a constant contribution with respect to the fiber direction $\boldsymbol{n}$ to the fiber spin tensor for a given ODF and a given macroscopic strain-rate tensor. Its algebraic structure can be traced back to the orientation-averaged form of the tensor $\mathbb{J}_{\mathsf{F}}$ given in Eq. (6.27), as analogously considered by Favaloro (2020) in the context of the Mori-Tanaka model, which is discussed in the next Sec. 6.1.4. In view of the orientation evolution of a single fiber

$$\dot{\boldsymbol{n}} = \bar{\boldsymbol{W}}\boldsymbol{n} + \xi\big(\bar{\boldsymbol{D}}\boldsymbol{n} - (\boldsymbol{n}\otimes\boldsymbol{n}\otimes\boldsymbol{n})[\bar{\boldsymbol{D}}]\big) - c_{\mathsf{F}}\xi(\bar{\boldsymbol{D}}\boldsymbol{N} - \boldsymbol{N}\bar{\boldsymbol{D}})\boldsymbol{n}, \tag{6.41}$$

it becomes clear that this constant tensor represents the anisotropic environment of a single fiber in a micromechanical sense. If it is taken into account that this term follows from $\mathbb{P}_0^{\mathsf{A}}[\langle\boldsymbol{\tau}\rangle]$ in Eq. (6.18) via $c_{\mathsf{F}}\langle\mathbb{P}_0^{\mathsf{A}}\delta\mathbb{V}\mathbb{A}\rangle_{\mathsf{F}}[\bar{\boldsymbol{D}}]$ in Eq. (6.21), it becomes apparent that the convergence criterion of the

integral operator $\langle \mathbb{I}^{\mathsf{A}}\{\boldsymbol{\tau}\}\rangle = \mathbf{0}$ embodies the micromechanical interaction of a single fiber with its anisotropic environment, which is not represented in the Jeffery approach. In order to derive the evolution equation for the fiber orientation tensor of arbitrary even order n for DD, the fiber spin tensor given in Eq. (6.40) is used in Eq. (6.7). The resulting equation can be expressed as follows based on the fiber orientation tensor definition (2.41)

$$\begin{aligned}\dot{\mathbb{N}}_{\langle n\rangle} = \bar{\boldsymbol{W}}\boxtimes\mathbb{N}_{\langle n\rangle} + \xi\big(\bar{\boldsymbol{D}}\boxtimes\mathbb{N}_{\langle n\rangle} - n\mathbb{N}_{\langle n+2\rangle}[\bar{\boldsymbol{D}}]\big)\\ - c_{\mathsf{F}}\xi(\bar{\boldsymbol{D}}\boldsymbol{N} - \boldsymbol{N}\bar{\boldsymbol{D}})\boxtimes\mathbb{N}_{\langle n\rangle}.\end{aligned} \tag{6.42}$$

The derived interaction term in Eq. (6.42) is fully symmetric, similar to the generalized Folgar-Tucker term given in Eq. (6.34), but in contrast it takes into account the fiber volume fraction, the fiber geometry, and it includes the kinematics in terms of the tensor $\bar{\boldsymbol{D}}$.

6.1.4 Mori-Tanaka model [4]

In case of the MT mean-field model referring to Mori and Tanaka (1973) and Benveniste (1987), the following strain-rate localization tensor is used for viscous suspensions based on Eq. (2.85). Since one single fiber is considered, the localization tensor $\mathbb{A}_{\mathsf{SIP}}$ as given in Eqs. (2.83) or (6.36) is used in Eq. (2.85) instead of the orientation-averaged localization tensor $\langle\mathbb{A}_{\mathsf{SIP}}\rangle_{\mathsf{F}}$, which leads to

$$\begin{aligned}\mathbb{A}_{\mathsf{F}} &= \mathbb{A}_{\mathsf{SIP}}\big(c_{\mathsf{M}}\mathbb{I}^{\mathsf{S}} + c_{\mathsf{F}}\mathbb{A}_{\mathsf{SIP}}\big)^{-1}\\ &= \big(c_{\mathsf{F}}\mathbb{I}^{\mathsf{S}} + c_{\mathsf{M}}\mathbb{A}_{\mathsf{SIP}}^{-1}\big)^{-1}\\ &= \big(\mathbb{I}^{\mathsf{S}} + c_{\mathsf{M}}\mathbb{P}_0^{\mathsf{S}}\delta\mathbb{V}\big)^{-1}.\end{aligned} \tag{6.43}$$

[4] This section consists of parts from Karl and Böhlke (2024). Additional text passages have been added.

In the last step, the expression for the SIP localization tensor in Eq. (6.36) is used. Following the computation steps already presented, the fiber spin tensor reads as follows

$$\begin{aligned}\boldsymbol{W}_{\mathsf{F}} = \bar{\boldsymbol{W}} &- \mathbb{P}_0^{\mathsf{A}}\big(\delta\mathbb{V}^{-1} + c_{\mathsf{M}}\mathbb{P}_0^{\mathsf{S}}\big)^{-1}[\bar{\boldsymbol{D}}] \\ &+ c_{\mathsf{F}}\Big\langle \mathbb{P}_0^{\mathsf{A}}\big(\delta\mathbb{V}^{-1} + c_{\mathsf{M}}\mathbb{P}_0^{\mathsf{S}}\big)^{-1}[\bar{\boldsymbol{D}}]\Big\rangle_{\mathsf{F}},\end{aligned} \tag{6.44}$$

which, for rigid fibers, can be simplified to

$$\boldsymbol{W}_{\mathsf{F}} = \bar{\boldsymbol{W}} - \frac{1}{c_{\mathsf{M}}}\mathbb{P}_0^{\mathsf{A}}\big(\mathbb{P}_0^{\mathsf{S}}\big)^{-1}[\bar{\boldsymbol{D}}] + \frac{c_{\mathsf{F}}}{c_{\mathsf{M}}}\Big\langle \mathbb{P}_0^{\mathsf{A}}\big(\mathbb{P}_0^{\mathsf{S}}\big)^{-1}[\bar{\boldsymbol{D}}]\Big\rangle_{\mathsf{F}}. \tag{6.45}$$

With the equality $\mathbb{J}_{\mathsf{F}} = -\mathbb{P}_0^{\mathsf{A}}\big(\mathbb{P}_0^{\mathsf{S}}\big)^{-1}$ shown in App. E.2, the expression above for the fiber spin tensor reads as follows with the orientation average operator $\langle\cdot\rangle_{\mathsf{F}}$ defined by Eq. (6.1)

$$\begin{aligned}\boldsymbol{W}_{\mathsf{F}} &= \bar{\boldsymbol{W}} + \frac{1}{c_{\mathsf{M}}}\mathbb{J}_{\mathsf{F}}[\bar{\boldsymbol{D}}] - \frac{c_{\mathsf{F}}}{c_{\mathsf{M}}}\Big\langle \mathbb{J}_{\mathsf{F}}[\bar{\boldsymbol{D}}]\Big\rangle_{\mathsf{F}} \\ &= \bar{\boldsymbol{W}} + \frac{\xi}{c_{\mathsf{M}}}\big((\bar{\boldsymbol{D}}\boldsymbol{n})\otimes\boldsymbol{n} - \boldsymbol{n}\otimes(\bar{\boldsymbol{D}}\boldsymbol{n})\big) - \frac{\xi c_{\mathsf{F}}}{c_{\mathsf{M}}}(\bar{\boldsymbol{D}}\boldsymbol{N} - \boldsymbol{N}\bar{\boldsymbol{D}}),\end{aligned} \tag{6.46}$$

which corresponds to the result of Favaloro (2020) in a different notation. The derivation of the rate $\dot{\boldsymbol{n}}$ regarding the direction of a single fiber embedded in an anisotropic suspension is straightforward. By using Eq. (6.46), the modified Jeffery equation based on the MT model reads similar to Favaloro (2020)

$$\dot{\boldsymbol{n}} = \bar{\boldsymbol{W}}\boldsymbol{n} + \frac{\xi}{c_{\mathsf{M}}}\big(\bar{\boldsymbol{D}}\boldsymbol{n} - (\boldsymbol{n}\otimes\boldsymbol{n}\otimes\boldsymbol{n})[\bar{\boldsymbol{D}}]\big) - \frac{\xi c_{\mathsf{F}}}{c_{\mathsf{M}}}(\bar{\boldsymbol{D}}\boldsymbol{N} - \boldsymbol{N}\bar{\boldsymbol{D}})\boldsymbol{n}. \tag{6.47}$$

In the last step, the fiber spin tensor (6.46) is used in Eq. (6.7) in order to derive the evolution equation for the fiber orientation tensor of arbitrary

even order

$$\dot{\mathbb{N}}_{\langle n\rangle} = \bar{\boldsymbol{W}}\boxtimes\mathbb{N}_{\langle n\rangle} + \frac{\xi}{c_{\mathsf{M}}}\big(\bar{\boldsymbol{D}}\boxtimes\mathbb{N}_{\langle n\rangle} - n\mathbb{N}_{\langle n+2\rangle}[\bar{\boldsymbol{D}}]\big) - \frac{\xi c_{\mathsf{F}}}{c_{\mathsf{M}}}(\bar{\boldsymbol{D}}\boldsymbol{N} - \boldsymbol{N}\bar{\boldsymbol{D}})\boxtimes\mathbb{N}_{\langle n\rangle}. \tag{6.48}$$

It is noted that Eq. (6.48) generalizes the expression for the special case of order $n = 2$ given in Favaloro (2020). Furthermore, the derivation of Eq. (6.48) in this chapter differs by a generalized approach that allows the use of arbitrary mean-field models via arbitrary strain-rate localization tensors $\mathbb{A}_{\mathsf{F}}$.

6.1.5 Ponte Castañeda-Willis model [5]

The PCW model (Ponte Castañeda and Willis, 1995) is based on the idea of considering different inclusion geometries with different spatial distributions. To realize this, two different polarization tensors are introduced: One for the inclusion (i) and the other one for the spatial distribution (d). For the special case of one single inclusion geometry with one single distribution, both the skew symmetric (A) and symmetric (S) polarization tensors read (Ponte Castañeda, 2021)

$$\mathbb{P}_0^{\mathsf{A},\mathsf{S}} = \frac{1}{c_{\mathsf{M}}}\big(\mathbb{P}_{\mathsf{i}}^{\mathsf{A},\mathsf{S}} - c_{\mathsf{F}}\mathbb{P}_{\mathsf{d}}^{\mathsf{A},\mathsf{S}}\big). \tag{6.49}$$

Inserting the symmetric tensor given in Eq. (6.49) into the localization tensor of MT, the localization tensor of PCW is obtained (Ponte Castañeda and Willis, 1995; Ponte Castañeda, 2021)

$$\mathbb{A}_{\mathsf{F}} = \big(\mathbb{I}^{\mathsf{S}} + (\mathbb{P}_{\mathsf{i}}^{\mathsf{S}} - c_{\mathsf{F}}\mathbb{P}_{\mathsf{d}}^{\mathsf{S}})\delta\mathbb{V}\big)^{-1}, \tag{6.50}$$

[5] This section consists of parts from Karl and Böhlke (2024). Additional text passages have been added.

which is also given in Kailasam and Ponte Castañeda (1998) for the special case of two phases. The direct use of Eqs. (6.49) and (6.50) in the general expression (6.21) for the fiber spin tensor leads to the following results simplified for a vanishing fluidity $\delta\mathbb{V}^{-1}$ for rigid fibers

$$\begin{aligned}\boldsymbol{W}_{\mathsf{F}} = \bar{\boldsymbol{W}} &- \frac{1}{c_{\mathsf{M}}}\left(\mathbb{P}_{\mathsf{i}}^{\mathsf{A}} - c_{\mathsf{F}}\mathbb{P}_{\mathsf{d}}^{\mathsf{A}}\right)\left(\mathbb{P}_{\mathsf{i}}^{\mathsf{S}} - c_{\mathsf{F}}\mathbb{P}_{\mathsf{d}}^{\mathsf{S}}\right)^{-1}[\bar{\boldsymbol{D}}] \\ &+ \frac{c_{\mathsf{F}}}{c_{\mathsf{M}}}\left\langle\left(\mathbb{P}_{\mathsf{i}}^{\mathsf{A}} - c_{\mathsf{F}}\mathbb{P}_{\mathsf{d}}^{\mathsf{A}}\right)\left(\mathbb{P}_{\mathsf{i}}^{\mathsf{S}} - c_{\mathsf{F}}\mathbb{P}_{\mathsf{d}}^{\mathsf{S}}\right)^{-1}[\bar{\boldsymbol{D}}]\right\rangle_{\mathsf{F}}. \end{aligned} \tag{6.51}$$

It should be noted that Eq. (6.51) corresponds to the special case of one single inclusion geometry with one single distribution given in Ponte Castañeda (2021) if rigid particles are considered and thus elastic components of the stress inside the particles are not present. In addition, the spin localization in Eq. (6.51) is related to Kailasam and Ponte Castañeda (1998) for the special case of rigid inclusions. However, in contrast, the spin localization (6.51) for this special case takes the anisotropic environment of the particle into account in an additional, orientation-averaged term $\langle\cdot\rangle_{\mathsf{F}}$. This also results in a modified evolution equation (6.54) for the direction of a single fiber compared to the relation given in Ponte Castañeda (2021) regarding deformable particles, and the same holds for the inclusion orientation relations given in Kailasam and Ponte Castañeda (1998).

In the following, the additional spin tensor depending on the fiber direction $\boldsymbol{n}$

$$\boldsymbol{\Omega}(\boldsymbol{n}) = \left(\mathbb{P}_{\mathsf{i}}^{\mathsf{A}}(\boldsymbol{n}) - c_{\mathsf{F}}\mathbb{P}_{\mathsf{d}}^{\mathsf{A}}(\boldsymbol{n})\right)\left(\mathbb{P}_{\mathsf{i}}^{\mathsf{S}}(\boldsymbol{n}) - c_{\mathsf{F}}\mathbb{P}_{\mathsf{d}}^{\mathsf{S}}(\boldsymbol{n})\right)^{-1}[\bar{\boldsymbol{D}}] \tag{6.52}$$

is introduced for convenience. With this abbreviation at hand, the computation of the constant orientation-averaged tensor in Eq. (6.51) representing the fiber's anisotropic environment can be expressed compactly as follows

$$\boldsymbol{\Omega}_{\mathsf{F}} = \int_{\mathcal{S}} f(\boldsymbol{p}, t)\boldsymbol{\Omega}(\boldsymbol{p})\,\mathrm{d}S(\boldsymbol{p}). \tag{6.53}$$

It should be noted that the integration variable on the unit sphere is deliberately changed to $\boldsymbol{p}$ to avoid confusion with the fiber direction $\boldsymbol{n}$. Without any further simplifications, the equation for the single fiber reads as follows

$$\dot{\boldsymbol{n}} = \bar{\boldsymbol{W}}\boldsymbol{n} - \frac{1}{c_{\mathsf{M}}}\boldsymbol{\Omega}(\boldsymbol{n})\boldsymbol{n} + \frac{c_{\mathsf{F}}}{c_{\mathsf{M}}}\boldsymbol{\Omega}_{\mathsf{F}}\boldsymbol{n}. \tag{6.54}$$

A combination of Eq. (6.51) with Eq. (6.7) leads to the generalized evolution equation for the fiber orientation tensor of arbitrary even order for the PCW model

$$\dot{\mathbb{N}}_{\langle n\rangle} = \bar{\boldsymbol{W}}\boxtimes\mathbb{N}_{\langle n\rangle} - \frac{1}{c_{\mathsf{M}}}\int_{\mathcal{S}} f(\boldsymbol{n},t)\boldsymbol{\Omega}(\boldsymbol{n})\boxtimes(\boldsymbol{n}^{\otimes n})\,\mathrm{d}S(\boldsymbol{n}) + \frac{c_{\mathsf{F}}}{c_{\mathsf{M}}}\boldsymbol{\Omega}_{\mathsf{F}}\boxtimes\mathbb{N}_{\langle n\rangle}. \tag{6.55}$$

Furthermore, special emphasis is put on the following additional remarks:

1) For the special case $\mathbb{P}_{\mathsf{i}}^{\mathsf{A},\mathsf{S}} = \mathbb{P}_{\mathsf{d}}^{\mathsf{A},\mathsf{S}}$, the strain-rate localization tensor (6.50) reduces to the MT approach as described in the literature (Ponte Castañeda and Willis, 1995; Du and Zheng, 2002). Therefore, the orientation evolution equation (6.55) also corresponds to the MT approach (6.48) for this special case. For $c_{\mathsf{F}} \to 0$, the distribution becomes irrelevant in Eqs. (6.50) and (6.51) and the DD model is recovered as described by Kailasam and Ponte Castañeda (1998) with the spin localization relation (6.38), if the orientation-averaged contribution is not neglected and, therefore, differs from Jeffery's model given in Eq. (6.25).
2) For simplicity, it is possible to assume a spheroidal distribution of the fibers via an additional distribution aspect ratio α_{d}. Since the fibers are also modeled as spheroids with the aspect ratio $\alpha_{\mathsf{i}} = \alpha$, all four polarization tensors $\mathbb{P}_{\mathsf{i,d}}^{\mathsf{A},\mathsf{S}}$ can be computed identically. In App. E.4, an efficient computation procedure is shown avoiding an encapsulated integration over the unit sphere in the integral

term of Eq. (6.55). As an alternative to a constant spheroidal distribution, an additional evolution equation for a distribution tensor can be solved (Ponte Castañeda, 2021), with a correspondingly adjusted computation of the polarization tensors $\mathbb{P}_{\mathsf{d}}^{\mathsf{A,S}}$. It is stated by Kailasam and Ponte Castañeda (1998) that the impact of the distribution evolution could be relevant for high volume fractions.

3) It should be noted that both aspect ratios $\alpha_{\mathsf{i,d}}$, which refer to the assumption of both spheroidal fibers and distribution, cannot be chosen independently of each other. For a given fiber volume fraction c_{F} and a fiber geometry α_{i}, the following bounds for α_{d} must not be violated (Ponte Castañeda and Willis, 1995)

$$\alpha_{\mathsf{d}}^{\mathsf{min}} = \alpha_{\mathsf{i}} \sqrt{c_{\mathsf{F}}}, \qquad \alpha_{\mathsf{d}}^{\mathsf{max}} = \frac{\alpha_{\mathsf{i}}}{c_{\mathsf{F}}}. \tag{6.56}$$

For a more general formulation of this so-called no-overlap hypothesis in the case of different orientation and distribution, see Kailasam and Ponte Castañeda (1998).

4) In consideration of the already shown connection between the Jeffery tensor $\mathbb{J}_{\mathsf{F}}$ and the polarization tensors $\mathbb{P}_0^{\mathsf{A,S}}$ via $\mathbb{J}_{\mathsf{F}} = -\mathbb{P}_0^{\mathsf{A}} \left(\mathbb{P}_0^{\mathsf{S}}\right)^{-1}$, see App. E.2, it is concluded that PCW leads to the following distribution-corrected Jeffery tensor

$$\mathbb{J}_{\mathsf{F,d}} = -\left(\mathbb{P}_{\mathsf{i}}^{\mathsf{A}} - c_{\mathsf{F}} \mathbb{P}_{\mathsf{d}}^{\mathsf{A}}\right) \left(\mathbb{P}_{\mathsf{i}}^{\mathsf{S}} - c_{\mathsf{F}} \mathbb{P}_{\mathsf{d}}^{\mathsf{S}}\right)^{-1}. \tag{6.57}$$

This interpretation complements the statements of Kailasam and Ponte Castañeda (1998) and Ponte Castañeda (2021) that the special case of Jeffery's equation is included in the considered approach. This assumes $\mathbb{P}_{\mathsf{i}}^{\mathsf{A,S}} = \mathbb{P}_{\mathsf{d}}^{\mathsf{A,S}}$ and the limit $c_{\mathsf{F}} \to 0$. The present study builds on Kailasam and Ponte Castañeda (1998) and Ponte Castañeda (2021) in the sense that a general evolution equation for the fiber orientation tensor of arbitrary order is derived which, unlike

conventional approaches, takes into account the distribution of the fibers.

5) Compared to the models considered previously, the intrinsic closure problem that the evolution equation for $\mathbb{N}_{\langle n \rangle}$ depends on the next higher order orientation tensor $\mathbb{N}_{\langle n+2 \rangle}$, see Advani and Tucker III (1987), is present in Eq. (6.55) in the form of an unknown ODF f. As already discussed in the literature review in Sec. 1.2.2, function-based approaches like ACG or the Jeffery distribution, MEM, or an ellipse radius distribution can be applied.

6.1.6 Effective medium approach [6]

The last method considered in this chapter is the effective medium approach (EM) with the basic idea of embedding a single inclusion (DD) in a suspension with the (unknown) effective viscosity $\bar{\mathbb{V}}$ as described by, e.g., Kanaun and Levin (2008) (p. 162). As a result, the strain-rate localization tensor given in Eq. (6.36) reads as follows which is also addressed in Sec. 2.6.4

$$\bar{\mathbb{A}}_{\mathsf{F}} = \left(\mathbb{I}^{\mathsf{S}} + \bar{\mathbb{P}}_0^{\mathsf{S}} \delta\bar{\mathbb{V}}\right)^{-1}, \tag{6.58}$$

with the abbreviation $\delta\bar{\mathbb{V}} = \mathbb{V}_{\mathsf{F}} - \bar{\mathbb{V}}$. Since the expression has the same algebraic structure as in the case of DD and the fluidity $\delta\bar{\mathbb{V}}^{-1}$ also vanishes for rigid fibers, the fiber spin tensor reads as follows

$$\boldsymbol{W}_{\mathsf{F}} = \bar{\boldsymbol{W}} - \bar{\mathbb{P}}_0^{\mathsf{A}} \left(\bar{\mathbb{P}}_0^{\mathsf{S}}\right)^{-1} [\bar{\boldsymbol{D}}] + c_{\mathsf{F}} \left\langle \bar{\mathbb{P}}_0^{\mathsf{A}} \left(\bar{\mathbb{P}}_0^{\mathsf{S}}\right)^{-1} [\bar{\boldsymbol{D}}] \right\rangle_{\mathsf{F}}. \tag{6.59}$$

The polarization tensors $\bar{\mathbb{P}}_0^{\mathsf{A,S}}$ depend on the effective, in general anisotropic, viscosity tensor $\bar{\mathbb{V}}$ and must be computed by numerically integrating Eq. (E.15) in App. E.4. Therefore, no further simplifications

[6] This section is directly taken from Karl and Böhlke (2024).

of Eq. (6.59) are possible. With the additional spin tensor depending on the fiber direction $\boldsymbol{n}$

$$\bar{\boldsymbol{\Omega}}(\boldsymbol{n}) = \bar{\mathbb{P}}_0^{\mathsf{A}}(\boldsymbol{n})\big(\bar{\mathbb{P}}_0^{\mathsf{S}}(\boldsymbol{n})\big)^{-1}[\bar{\boldsymbol{D}}] \tag{6.60}$$

and with its constant orientation-averaged representation

$$\bar{\boldsymbol{\Omega}}_{\mathsf{F}} = \int_{\mathcal{S}} f(\boldsymbol{p},t)\bar{\boldsymbol{\Omega}}(\boldsymbol{p})\,\mathrm{d}S(\boldsymbol{p}), \tag{6.61}$$

the evolution equation for a single fiber can be compactly expressed by

$$\dot{\boldsymbol{n}} = \bar{\boldsymbol{W}}\boldsymbol{n} - \bar{\boldsymbol{\Omega}}(\boldsymbol{n})\boldsymbol{n} + c_{\mathsf{F}}\bar{\boldsymbol{\Omega}}_{\mathsf{F}}\boldsymbol{n}. \tag{6.62}$$

Again, the integration variable in Eq. (6.61) is changed to $\boldsymbol{p}$ to avoid confusion with the fiber direction $\boldsymbol{n}$. A combination of Eq. (6.59) with Eq. (6.7) leads to the following generalized orientation evolution equation of arbitrary even order based on the EM approach

$$\dot{\mathbb{N}}_{\langle n\rangle} = \bar{\boldsymbol{W}}\boxtimes\mathbb{N}_{\langle n\rangle} - \int_{\mathcal{S}} f(\boldsymbol{n},t)\bar{\boldsymbol{\Omega}}(\boldsymbol{n})\boxtimes(\boldsymbol{n}^{\otimes n})\,\mathrm{d}S(\boldsymbol{n}) + c_{\mathsf{F}}\bar{\boldsymbol{\Omega}}_{\mathsf{F}}\boxtimes\mathbb{N}_{\langle n\rangle}. \tag{6.63}$$

Furthermore, special emphasis is put on the following additional remarks:

1) Similar to the PCW model, Eq. (6.63) is not closed since the ODF f is unknown. Based on suitable approaches addressed in Sec. 6.1.5, the function f has to be approximated.
2) In analogy to all previous considerations, in particular to App. E.2, the following effective Jeffery tensor can be defined

$$\bar{\mathbb{J}}_{\mathsf{F}} = -\bar{\mathbb{P}}_0^{\mathsf{A}}\big(\bar{\mathbb{P}}_0^{\mathsf{S}}\big)^{-1}. \tag{6.64}$$

3) Unlike the PCW model, it is not possible to avoid encapsulated integration in Eq. (6.63). In this context, encapsulated means

that for each integration point on $\mathcal{S}$ in Eq. (6.63), two complete integrations over $\mathcal{S}$ must be performed to evaluate the tensor $\bar{\boldsymbol{\Omega}}(\boldsymbol{n})$ as given in Eq. (6.60).

4) In contrast to all previously discussed orientation models, the effective viscosity tensor $\bar{\mathbb{V}}$ must be calculated explicitly in order to integrate the orientation evolution equation (6.63). Below, SC and DS are listed with the adaptation to fiber suspensions with rigid fibers as discussed in Sec. 2.6.4

$$\begin{aligned} \bar{\mathbb{V}}_{\mathsf{SC}} &= \mathbb{V}_{\mathsf{M}} + c_{\mathsf{F}} \left\langle \left(\bar{\mathbb{P}}_0^{\mathsf{S}}\right)^{-1} \right\rangle_{\mathsf{F}}, \\ \frac{\mathrm{d}\bar{\mathbb{V}}_{\mathsf{DS}}}{\mathrm{d}c_{\mathsf{F}}} &= \frac{1}{1-c_{\mathsf{F}}} \left\langle \left(\bar{\mathbb{P}}_0^{\mathsf{S}}\right)^{-1} \right\rangle_{\mathsf{F}}. \end{aligned} \tag{6.65}$$

It should be noted that, in general, Eq. (6.65) represents implicit expressions for the effective viscosity tensor $\bar{\mathbb{V}}$ and that Eq. (6.63) is not limited to these two methods.

5) The computation of the effective viscosity based on Eq. (6.65) must be performed at each time step during the integration of Eq. (6.63). A fully explicit approach proves to be practical in order to decouple the computation of $\bar{\mathbb{V}}$ and $\mathbb{N}_{\langle n \rangle}$ in each time step, since both tensors are coupled via the ODF in the orientation average of Eq. (6.65).

6.2 Numerical example and discussion

6.2.1 Considered orientation evolution equations [7]

In order to examine the differences between the various mean-field models addressed before, the present section is limited to the following

[7] This section consists of parts from Karl and Böhlke (2024). Additional text passages have been added.

equations for the evolution of the second-order fiber orientation tensor

$$
\begin{aligned}
\dot{\boldsymbol{N}}_{\mathsf{JE}} &= \bar{\boldsymbol{W}}\boldsymbol{N} - \boldsymbol{N}\bar{\boldsymbol{W}} + \xi\big(\bar{\boldsymbol{D}}\boldsymbol{N} + \boldsymbol{N}\bar{\boldsymbol{D}} - 2\mathbb{N}[\bar{\boldsymbol{D}}]\big),\\
\dot{\boldsymbol{N}}_{\mathsf{DD}} &= \bar{\boldsymbol{W}}\boldsymbol{N} - \boldsymbol{N}\bar{\boldsymbol{W}} + \xi\big(\bar{\boldsymbol{D}}\boldsymbol{N} + \boldsymbol{N}\bar{\boldsymbol{D}} - 2\mathbb{N}[\bar{\boldsymbol{D}}]\big)\\
&\quad - c_{\mathsf{F}}\xi(\bar{\boldsymbol{D}}\boldsymbol{N}^2 + \boldsymbol{N}^2\bar{\boldsymbol{D}} - 2\boldsymbol{N}\bar{\boldsymbol{D}}\boldsymbol{N}),\\
\dot{\boldsymbol{N}}_{\mathsf{MT}} &= \bar{\boldsymbol{W}}\boldsymbol{N} - \boldsymbol{N}\bar{\boldsymbol{W}} + \frac{\xi}{c_{\mathsf{M}}}\big(\bar{\boldsymbol{D}}\boldsymbol{N} + \boldsymbol{N}\bar{\boldsymbol{D}} - 2\mathbb{N}[\bar{\boldsymbol{D}}]\big)\\
&\quad - \frac{c_{\mathsf{F}}\xi}{c_{\mathsf{M}}}(\bar{\boldsymbol{D}}\boldsymbol{N}^2 + \boldsymbol{N}^2\bar{\boldsymbol{D}} - 2\boldsymbol{N}\bar{\boldsymbol{D}}\boldsymbol{N}),\\
\dot{\boldsymbol{N}}_{\mathsf{PCW}} &= \bar{\boldsymbol{W}}\boldsymbol{N} - \boldsymbol{N}\bar{\boldsymbol{W}} - \frac{1}{c_{\mathsf{M}}}\int_{\mathcal{S}} f(\boldsymbol{n},t)\big(\boldsymbol{\Omega}(\boldsymbol{n}\otimes\boldsymbol{n}) - (\boldsymbol{n}\otimes\boldsymbol{n})\boldsymbol{\Omega}\big)\,\mathrm{d}S(\boldsymbol{n})\\
&\quad + \frac{c_{\mathsf{F}}}{c_{\mathsf{M}}}(\boldsymbol{\Omega}_{\mathsf{F}}\boldsymbol{N} - \boldsymbol{N}\boldsymbol{\Omega}_{\mathsf{F}}),\\
\dot{\boldsymbol{N}}_{\mathsf{EM}} &= \bar{\boldsymbol{W}}\boldsymbol{N} - \boldsymbol{N}\bar{\boldsymbol{W}} - \int_{\mathcal{S}} f(\boldsymbol{n},t)\big(\bar{\boldsymbol{\Omega}}(\boldsymbol{n}\otimes\boldsymbol{n}) - (\boldsymbol{n}\otimes\boldsymbol{n})\bar{\boldsymbol{\Omega}}\big)\,\mathrm{d}S(\boldsymbol{n})\\
&\quad + c_{\mathsf{F}}(\bar{\boldsymbol{\Omega}}_{\mathsf{F}}\boldsymbol{N} - \boldsymbol{N}\bar{\boldsymbol{\Omega}}_{\mathsf{F}}).
\end{aligned}
\tag{6.66}
$$

It should be noted that the spin tensors $\boldsymbol{\Omega}$ and $\bar{\boldsymbol{\Omega}}$ depend on the integration variable $\boldsymbol{n}$. The respective definitions are given in Eq. (6.52) for the PCW model and in Eq. (6.60) for the EM approach. In addition, the following equations are solved in parallel with those given in Eq. (6.66) to track a single fiber embedded in the fiber suspension

$$
\begin{aligned}
\dot{\boldsymbol{n}}_{\mathsf{JE}} &= \bar{\boldsymbol{W}}\boldsymbol{n} + \xi\big(\bar{\boldsymbol{D}}\boldsymbol{n} - (\boldsymbol{n}\otimes\boldsymbol{n}\otimes\boldsymbol{n})[\bar{\boldsymbol{D}}]\big),\\
\dot{\boldsymbol{n}}_{\mathsf{DD}} &= \bar{\boldsymbol{W}}\boldsymbol{n} + \xi\big(\bar{\boldsymbol{D}}\boldsymbol{n} - (\boldsymbol{n}\otimes\boldsymbol{n}\otimes\boldsymbol{n})[\bar{\boldsymbol{D}}]\big) - c_{\mathsf{F}}\xi(\bar{\boldsymbol{D}}\boldsymbol{N} - \boldsymbol{N}\bar{\boldsymbol{D}})\boldsymbol{n},\\
\dot{\boldsymbol{n}}_{\mathsf{MT}} &= \bar{\boldsymbol{W}}\boldsymbol{n} + \frac{\xi}{c_{\mathsf{M}}}\big(\bar{\boldsymbol{D}}\boldsymbol{n} - (\boldsymbol{n}\otimes\boldsymbol{n}\otimes\boldsymbol{n})[\bar{\boldsymbol{D}}]\big) - \frac{\xi c_{\mathsf{F}}}{c_{\mathsf{M}}}(\bar{\boldsymbol{D}}\boldsymbol{N} - \boldsymbol{N}\bar{\boldsymbol{D}})\boldsymbol{n},\\
\dot{\boldsymbol{n}}_{\mathsf{PCW}} &= \bar{\boldsymbol{W}}\boldsymbol{n} - \frac{1}{c_{\mathsf{M}}}\boldsymbol{\Omega}(\boldsymbol{n})\boldsymbol{n} + \frac{c_{\mathsf{F}}}{c_{\mathsf{M}}}\boldsymbol{\Omega}_{\mathsf{F}}\boldsymbol{n},\\
\dot{\boldsymbol{n}}_{\mathsf{EM}} &= \bar{\boldsymbol{W}}\boldsymbol{n} - \bar{\boldsymbol{\Omega}}(\boldsymbol{n})\boldsymbol{n} + c_{\mathsf{F}}\bar{\boldsymbol{\Omega}}_{\mathsf{F}}\boldsymbol{n}.
\end{aligned}
\tag{6.67}
$$

Before presenting and discussing the respective results, the following section deals with the settings for the numerical computation of the considered fiber orientation evolution equations.

6.2.2 Settings [8]

The numerical example is limited to a simple shear flow with the effective velocity gradient $\bar{\boldsymbol{L}} = \dot{\gamma}\, \boldsymbol{e}_1 \otimes \boldsymbol{e}_2$, leading to the effective strain-rate tensor $\bar{\boldsymbol{D}}$ and spin tensor $\bar{\boldsymbol{W}}$

$$\bar{\boldsymbol{D}} = \frac{\dot{\gamma}}{2}(\boldsymbol{e}_1 \otimes \boldsymbol{e}_2 + \boldsymbol{e}_2 \otimes \boldsymbol{e}_1), \qquad \bar{\boldsymbol{W}} = \frac{\dot{\gamma}}{2}(\boldsymbol{e}_1 \otimes \boldsymbol{e}_2 - \boldsymbol{e}_2 \otimes \boldsymbol{e}_1). \tag{6.68}$$

All orientation evolution equations are integrated with an explicit fourth-order Runge-Kutta method (Deuflhard and Bornemann, 2008) (pp. 140–153) with the fixed time step $\triangle t = 0.05\,\mathrm{s}$. The isotropic initial condition $\boldsymbol{N}_0 = \boldsymbol{I}/3$ and the initial fiber direction $\boldsymbol{n}_0 = (1\ 1\ 1)^{\mathsf{T}}/\sqrt{3}\,\boldsymbol{e}_i$ is fixed. The evolution equations for the second-order orientation tensor are closed by using the ACG closure referring to, e.g., Tyler (1987) and Montgomery-Smith et al. (2011a) with the tolerance of 10^{-8}. The respective integrations over the unit sphere are based on a Lebedev grid (Lebedev and Laikov, 1999) using the implementation of Parrish (2021). The implementation of the ACG closure refers to the adapted integration scheme of Goldberg et al. (2017), which is also addressed by, e.g., Hessman et al. (2021). For JE, DD, MT, and PCW, the maximum number of 5810 integration points is chosen, as this does not negatively affect the computation time. For the EM approach, which is limited to DS as mean-field model, 974 integration points are chosen in order to ensure a sufficiently high accuracy with a reasonable computational effort. DS is also integrated with an explicit fourth-order Runge-Kutta method,

[8] This section consists of parts from Karl and Böhlke (2024). Additional text passages have been added.

consistent with previous chapters, with the fixed volume fraction step $\triangle c_\mathsf{F} = 0.01$ and the initial solution $\bar{\mathbb{V}}_0 = 3\mu_\mathsf{v}\mathbb{P}_1 + 2\mu_\mathsf{s}\mathbb{P}_2$. Similar to the previous study by Karl and Böhlke (2022), the shear viscosity of the matrix is set to $\mu_\mathsf{s} = 1\,\mathrm{Pas}$ and the matrix volume viscosity $\mu_\mathsf{v} = 10^6\,\mathrm{Pas}$ is fixed. The solution of DS refers to the expression $\mathbb{P}_2\bar{\mathbb{V}}\mathbb{P}_2$ similar to Karl and Böhlke (2022) and is consistent with the stabilized implementation of the anisotropic viscous stress in Eq. (3.21) in the context of flow-fiber coupling. As an example, the fiber volume fraction c_F is varied between the values 0.02 and 0.15 and the fiber aspect ratio $\alpha = 10$ is fixed.[9] Due to the chosen fiber aspect ratio, the fiber volume fractions correspond to the semi-concentrated regime ($\alpha^{-2} < c_\mathsf{F} < \alpha^{-1} \Leftrightarrow 0.01 < c_\mathsf{F} < 0.1$) and to the concentrated regime ($\alpha^{-1} \leq c_\mathsf{F} \Leftrightarrow 0.1 \leq c_\mathsf{F}$) according to Tucker III (1991). It should be noted that, even for the concentrated regime, the used mean-field approach covers only a purely hydrodynamic interaction between the fibers, as stated by Ponte Castañeda (2021). For the PCW model, the aspect ratio of the inclusion α_i refers to $\alpha = 10$ and the distribution aspect ratios $\alpha_\mathsf{d}^\mathsf{min}$ and $\alpha_\mathsf{d}^\mathsf{max}$ are computed based on Eq. (6.56) for each fiber volume fraction. Typically $\alpha \to \infty$ is chosen, which is not done in the present chapter for the following reasons. On the one hand, it is to be investigated how different mean-field models affect the periodic orientation behavior, which is not present for the infinite aspect ratio $\alpha \to \infty$. On the other hand, for $\alpha \to \infty$ the distribution aspect ratios of the PCW model are infinite as well, which makes the PCW model equal to the MT model. Another arising issue is that $\alpha \to \infty$ leads to a singularity in the computation of the polarization tensor for anisotropic matrix viscosities according to Eq. (E.15) for the EM approach.

[9] For example, if polypropylene (PP) is chosen as the matrix material and glass is chosen as the fiber material, then the fiber volume fraction of 0.02 to 0.15 corresponds to a fiber mass fraction of 0.05 to 0.33 based on the mass densities $\rho_\mathsf{M} = 910\,\mathrm{kg/m^3}$ and $\rho_\mathsf{F} = 2540\,\mathrm{kg/m^3}$ (Schürmann, 2007) (pp. 30, 132). The highest volume fraction thus corresponds to the standard composite material PP-GF30.

c_F	DD	MT	PCW($\alpha_\mathsf{d}^\mathsf{min}$)	PCW($\alpha_\mathsf{d}^\mathsf{max}$)	EM
0.02	0.881	0.917	0.947	0.916	0.826
0.05	0.855	0.930	0.968	0.928	0.812
0.1	0.826	0.948	0.979	0.944	0.795
0.15	0.805	0.962	0.983	0.957	0.782

Table 6.1: For DD, MT, PCW, and EM, the maximum values of the orientation tensor component N_{11} are given for different fiber volume fractions c_F. The maximum values of N_{11} refer to the considered interval of the total shear $\dot{\gamma}t \in [0, 30]$, adapted from Karl and Böhlke (2024).

6.2.3 Results and discussion [10]

In Fig. 6.2, the evolution of the fiber orientation tensor component N_{11} is shown with respect to the total shear $\dot{\gamma}t$. In the range of approximately $\dot{\gamma}t < 5$ it can be seen that the investigated models differ only slightly, while for the range of approximately $\dot{\gamma}t > 5$ a strongly different behavior can be seen. For the MT and PCW models, the maximum values of N_{11} increase with an increasing fiber volume fraction. This behavior corresponds to the tendency observed in the recent studies Gilormini and Chinesta (2019) and Favaloro (2020). For the DD and EM models, in contrast, a decrease of the maximum value of N_{11} can be seen with an increasing fiber volume fraction. The maximum values of N_{11} with respect to the considered mean-field models and fiber volume fractions are given in Tab. 6.1. Furthermore, the PCW($\alpha_\mathsf{d}^\mathsf{min}$) model shows the least periodic reorientation behavior for the selected settings. In general, the orientation evolution is greatly influenced by the consideration of the spatial distribution of the fibers. With an increasing fiber volume fraction, the period length for the MT and PCW($\alpha_\mathsf{d}^\mathsf{max}$) models increases, whereas the period length for the DD and EM models decreases. The

[10] This section consists of parts from Karl and Böhlke (2024). Additional text passages have been added.

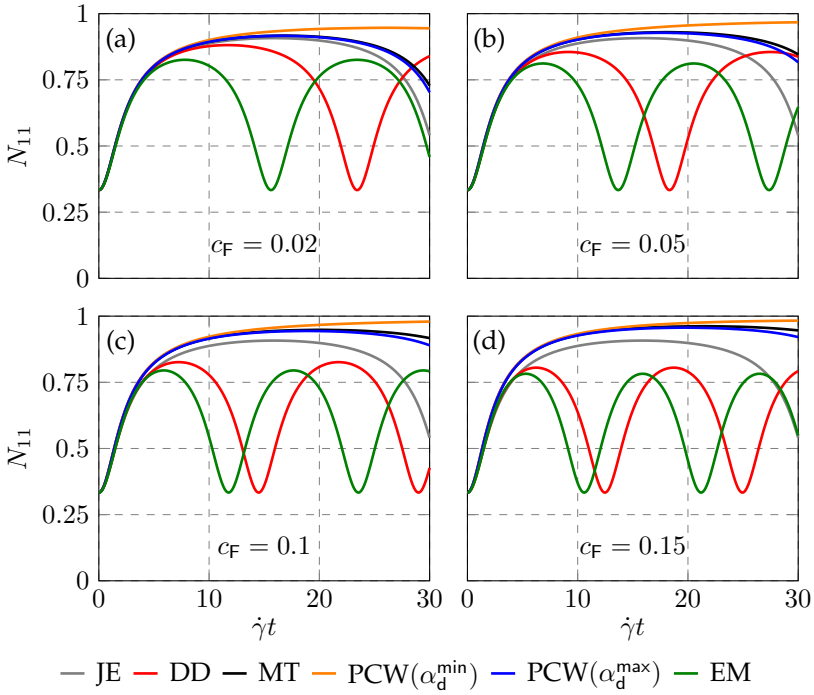

Figure 6.2: For DD, MT, PCW, and EM, the evolution of the orientation tensor component N_{11} in a simple shear flow is plotted over the total shear $\dot{\gamma}t$. The results of the Jeffery equation (JE) are given for comparison. Different fiber volume fractions c_F are considered: 0.02 in (a), 0.05 in (b), 0.1 in (c), and 0.15 in (d), adapted from Karl and Böhlke (2024).

evolution of the remaining components N_{22}, N_{33}, and N_{12} is shown in Fig. E.5.1 in App. E.5.

The behavior of a single fiber embedded in the fiber suspension, whose effective orientation behavior is shown in Fig. 6.2, is discussed in the following. In Fig. 6.3(a), the orientation evolution of a single fiber is shown on the unit sphere for the fiber volume fraction $c_F = 0.15$ of the surrounding fiber suspension. Figure 6.3(b) shows the projection of the orientation path on the $\boldsymbol{e}_1$–$\boldsymbol{e}_2$-plane. Although the total shear acting on

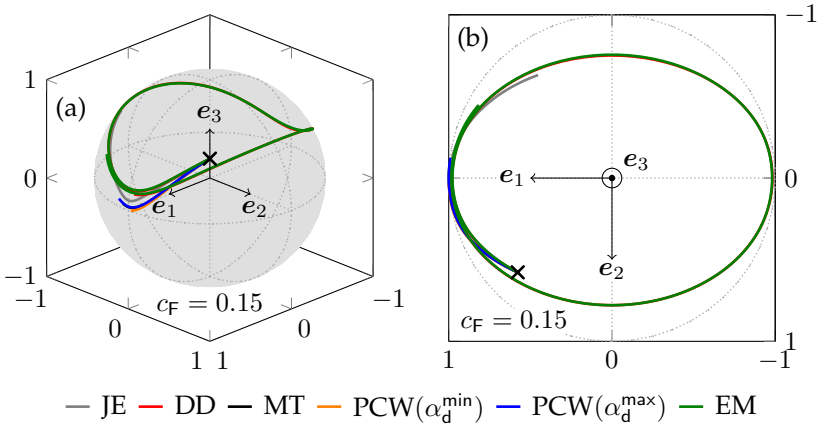

Figure 6.3: For the fiber volume fraction $c_F = 0.15$, the orientation behavior of a single fiber is shown in a simple shear flow for DD, MT, PCW, and EM. The Jeffery model (JE) is considered as a reference. The initial fiber orientation is marked with $\times$. In (a), the orientation path of the single fiber is plotted on the unit sphere. The respective projection on the e_1–e_2-plane is shown in (b), adapted from Karl and Böhlke (2024).

the fiber is the same for all considered mean-field models, there are clear differences in the reorientation behavior. These differences correspond to the effective behavior shown in Fig. 6.2. On the one hand, the longest path on the unit sphere is shown for DD and EM, which is related to the strongly pronounced periodic behavior visualized in Fig. 6.2. For MT and PCW(α_d^{max}), the weaker periodic behavior becomes apparent at the end of the path. For PCW(α_d^{min}), on the other hand, the largest period length of the reorientation is shown by the quasi-static final state in the considered range of total shear. The result of the classical Jeffery equation, measured by path length, lies between the results of DD, EM and MT, PCW(α_d^{max}). As a supplement, the orientation evolution of a single fiber for all other considered fiber volume fractions is shown in Fig. E.5.2 in App. E.5.

It should be noted that the DD model is only valid in the dilute regime. Investigations with different fiber volume fractions showed that the

results of DD already deviate significantly from those of the MT model for fiber volume fractions higher than 10^{-3}. As a supplement, the respective orientation evolution is shown in Fig. E.5.3 in App. E.5. The MT model shows the behavior of slowing down the orientation dynamics with an increasing fiber volume fraction. The opposite behavior of DD shows that the respective linearized approach and the associated micromechanical assumption of non-interacting single fibers, see, e.g., Tucker III and Liang (1999), is not appropriate and must be evaluated as non-physical. Interestingly, the application of the EM model shows qualitatively the same orientation dynamics and the periodic behavior is more sensitive to increasing fiber volume fractions compared to the DD model. The DD and EM models are connected via a similar basic structure of the orientation evolution equation. This can be recognized on the one hand by the linear scaling with the fiber volume fraction and on the other hand by the concept of the EM model, as a single inclusion is embedded in the medium with the effective viscosity. The observed amplifying effect of EM on the periodic reorientation can be attributed to the fact that the inherent SC approach tends to overestimate the effective viscosity, as indicated by the results of, e.g., Thevenin and Perreux (1996) and Karl and Böhlke (2022). In addition, the spin localizations of the DD and EM models only include the macroscopic strain rate, while the spin localization of MT, as a special case of PCW, is derived based on the effective matrix strain rate (Mori and Tanaka, 1973; Benveniste, 1987; Tucker III and Liang, 1999), which is indicated in the present study to be crucial for the fiber orientation evolution. The discussion before is supported by the statement of Kailasam and Ponte Castañeda (1998) in a way that the DD model leads to inaccuracies, especially when the orientation dynamics of inclusions are taken into account in the macroscopic modeling of composites. The behavior of DD and EM in a simple shear flow for increasing fiber volume fraction shown in Fig. 6.2 occurs similarly in the model used by Férec et al. (2014). The respective evolution equation for $\boldsymbol{N}$ contains interaction tensor terms (Férec et al.,

2009) that scale linearly with the fiber volume fraction and a friction parameter. As the value of this product increases, e.g., by increasing the fiber volume fraction under constant friction, the evolution of N_{11} shown in Férec et al. (2014) shares the behavior of DD and EM shown in Fig. 6.2.

To conclude the numerical example, the results of the derived mean-field based fiber orientation evolution equations in the context of slow orientation dynamics are briefly investigated. Based on the discussion before, the upcoming analysis is limited to the JE, MT, and PCW models for selected fiber volume fractions. Following Favaloro (2020), the observed slower orientation dynamics of real fiber suspensions are realized by using the reduction tensor $\mathbb{R}$ with the reduction parameter $\kappa \in [0, 1]$ and the right eigenvectors $\boldsymbol{r}_i$ of the second-order orientation tensor $\boldsymbol{N}$

$$\mathbb{R} = \mathbb{I}^{\mathsf{S}} + (\kappa - 1) \sum_{i=1}^{3} \boldsymbol{r}_i \otimes \boldsymbol{r}_i \otimes \boldsymbol{r}_i \otimes \boldsymbol{r}_i. \tag{6.69}$$

The orientation dynamics predicted by the JE, MT, and PCW models are slowed down by the use of the reduced strain-rate tensor $\mathbb{R}[\bar{\boldsymbol{D}}]$ (Favaloro, 2020) instead of the unmodified strain-rate tensor $\bar{\boldsymbol{D}}$ in the respective orientation evolution equation. In this context, Jeffery's model given in Eq. (6.29) refers to the RSC model proposed by Wang et al. (2008) with a neglected Folgar-Tucker fiber interaction term (Folgar and Tucker III, 1984; Advani and Tucker III, 1987), which is given in Eq. (6.34). Figure 6.4 shows the evolution of the fiber orientation tensor component N_{11} with respect to the total shear $\dot{\gamma}t$ for the exemplary reduction parameter $\kappa = 0.3$. Note that the smaller κ, the more intense the respective slowdown effect. The results show that an increasing fiber volume fraction has a significant effect on the orientation evolution predicted by the slowed down mean-field models. Here, PCW($\alpha_{\mathsf{d}}^{\mathsf{min}}$) shows the least pronounced changes with an increasing fiber volume fraction, whereas the results of MT and PCW($\alpha_{\mathsf{d}}^{\mathsf{max}}$) strongly depend on

the fiber volume fraction for a total shear $\dot{\gamma}t > 40$. Analogous to Fig. 6.2, vanishing differences between the MT and PCW models are shown for high volume fractions and the effect of spatial distribution decreases, but is evaluated as significant in the context of slow orientation dynamics.

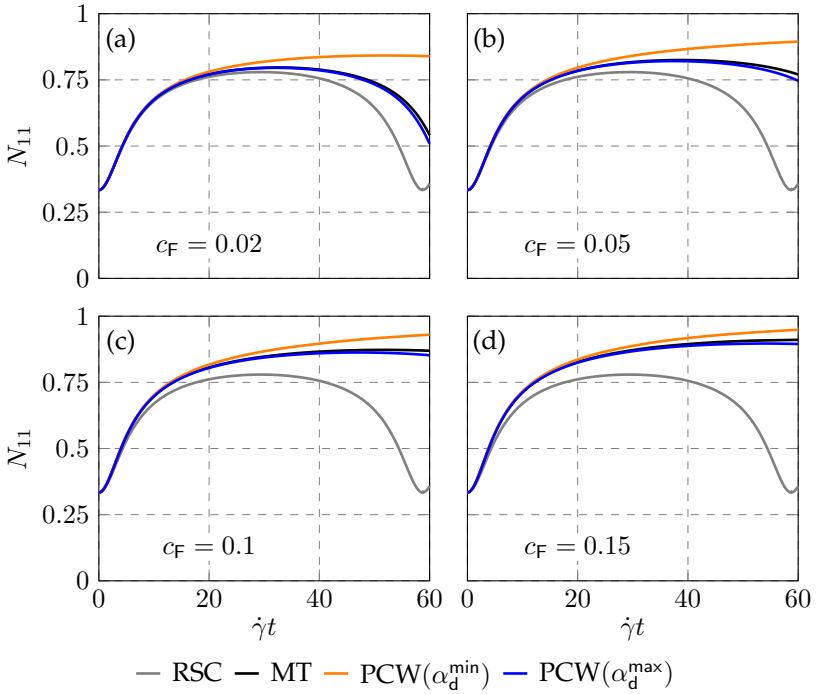

Figure 6.4: For MT and PCW, the evolution of the orientation tensor component N_{11} in a simple shear flow is plotted over the total shear $\dot{\gamma}t$. The reduction parameter $\kappa = 0.3$ is used for slowing down the orientation dynamics. The results of the reduced-strain closure model without fiber interaction (RSC) are given for comparison. Different fiber volume fractions c_F are considered: 0.02 in (a), 0.05 in (b), 0.1 in (c), and 0.15 in (d), adapted from Karl and Böhlke (2024).

6.2.4 Discussion of the closure problem [11]

In the present chapter, the ACG closure referring to, e.g., Tyler (1987) and Montgomery-Smith et al. (2011a) is assumed to be valid. As discussed by Favaloro (2020), it should be noted that common closures for the micromechanically motivated new orientation evolution equations do not necessarily lead to the same quality of results as known from the conventional orientation evolution equations. Precise quantitative statements about how much the predicted orientation state varies when using different closures based on the reconstruction of the ODF f require extensive parameter studies. For the MEM (Jaynes, 1957; Chaubal and Leal, 1998; van Gurp, 1998) based on the Bingham distribution (Bingham, 1974), oscillations are expected in a simple shear flow as described by Tucker III (2022b) and as shown in Sec. 5.4.1. Based on the results given in Nabergoj et al. (2022) for a simple shear flow, it can be concluded that the ellipse radius closure behaves qualitatively similar to the IBOF closure proposed by Chung and Kwon (2002b) with slight quantitative deviations from the predicted alignment. This observation can be transferred to the ACG closure, since the IBOF closure is an approximation of the ACG closure (Chung and Kwon, 2002b).

Future work could address the issue of finding an appropriate closure method and also consider non-orthotropic approaches (Tucker III, 2022b), which are so far only known for planar orientation states. There are two possible approaches to assessing the suitability of a closure for the mean-field based orientation evolution equations derived in this chapter. On the one hand, the approach of Favaloro (2020) can be used, where the orientation evolution of a statistically representative ensemble of single fibers is considered. Since the single-fiber equations do not require a closure, a comparison of the averaged orientation state

[11] This section is directly taken from Karl and Böhlke (2024).

can be made with, e.g., the orientation state predicted by the second-order orientation evolution equations using a specific closure. On the other hand, a closure can be evaluated using the higher-order evolution equations derived in this work. The idea here is to use a specific closure approach and compare the higher-order orientation state at the end of the time integration with a reconstruction of this tensor based on the time integration result of a lower-order orientation evolution equation.

In order to identify a reliable combination of mean-field modeling and a closure method, further studies need to be carried out in the context of comparing numerical with experimental results. Future research should focus on implementing the derived evolution equations in mold-filling software and comparing the numerical results of the mean-field models with measured fiber orientation states in manufactured parts. In this context, specific extensions of the models can be considered in order to be in line with experimental data. A pragmatic first step would be to add the isotropic diffusion term similar to the classical Folgar-Tucker equation (6.35) and to fit the interaction parameter C_I to the experimental results. Therefore, the present work can serve as a basis for the development of micromechanically motivated and practical orientation models taking into account the anisotropic fiber suspension.

6.3 Summary and conclusions [12]

This chapter deals with the micromechanical foundation of fiber orientation tensor evolution equations and presents a novel formula (6.22) for the evolution of orientation tensors of arbitrary even order. Using a linear homogenization approach, the general orientation evolution equation (6.22) is derived in a first step and allows the application

[12] This section consists of parts from Karl and Böhlke (2024). Additional text passages have been added.

of a variable mean-field models via the corresponding strain-rate localization tensor. Thus, the anisotropic character of the incompressible fiber suspension is algebraically taken into account in the orientation evolution equation, which is an extension of the classical approaches of Jeffery (Jeffery, 1922; Junk and Illner, 2007) and, e.g., Folgar and Tucker (Folgar and Tucker III, 1984; Advani and Tucker III, 1987). The idea of using mean-field homogenization and incorporating anisotropy effects in the modeling of fiber orientation tensor dynamics is based on, e.g., Wetzel and Tucker III (2001), Gilormini and Chinesta (2019), and Favaloro (2020). In a second step, the evolution equations for the orientation tensor are specified for the dilute distribution model (DD), see, e.g., Tucker III and Liang (1999), the Mori-Tanaka model (MT), see, e.g., Mori and Tanaka (1973) and Benveniste (1987), the approach of Ponte Castañeda and Willis (1995) (PCW), and for the effective medium approach (EM) discussed by Kanaun and Levin (2008) (pp. 162–172). Both Jeffery's equation and the Folgar-Tucker equation of arbitrary tensor order are addressed as special cases of the formulated generalized mean-field approach and discussed both in the context of the dilute model (Wetzel, 1999; Wetzel and Tucker III, 2001) and in the context of the related field of liquid crystals (Hill, 1999; Papenfuß, 2019). The present work is limited to rigid spheroidal short fibers embedded in a Newtonian matrix fluid under Stokes flow conditions. Brownian motion and inertia effects are not taken into account. The interaction between the fibers is modeled hydrodynamically by the chosen mean-field approach (Ponte Castañeda, 2021). In the following, the conclusions of the present study are summarized and grouped thematically:

- **Orientation dynamics and application.** For industrially relevant fiber volume fractions, DD leads to non-physical orientation dynamics and cannot be recommended. Not only because of the high computational cost of the EM model due to the encapsulated integration

over the unit sphere, but also because the results of the EM model are similar to those of the DD model, EM cannot be recommended for engineering practice. For relevant fiber volume fractions and neglected spatial distribution of the fibers, the MT model is recommended. This is justified by the fact that with this model the common engineering approach $\alpha \to \infty$ can be used and that the MT approach is valid for higher fiber volume fractions, see Benveniste (1987). In addition, the periodic behavior is not present for $\alpha \to \infty$ on the basis of Jeffery's period length given in Eq. (5.45). In contrast, the PCW approach has the additional advantage over the MT model that the spatial distribution of the fibers is taken into account in the derived orientation tensor evolution equation. Furthermore, for relevant fiber volume fractions, e.g., $c_\mathsf{F} > 0.1$, the PCW($\alpha_\mathsf{d}^{\mathsf{min}}$) model shows a weak periodic orientation behavior for finite fiber aspect ratios and can therefore be recommended for predicting the alignment of fibers under spatial distribution effects. The effects of the spatial distribution itself are rated as significant and their consideration opens up the possibility of a new way of computing the evolution of fiber orientation tensors. For engineering applications, one could consider stabilizing the weak periodic behavior of the PCW($\alpha_\mathsf{d}^{\mathsf{min}}$) model by a very small Folgar-Tucker fiber interaction term in the sense of an artificial diffusion term. This would have the advantages that fitting of this additional term to experimental data would be possible and that micromechanical effects including the spatial distribution of the embedded fibers could be taken into account in the derived fiber orientation tensor evolution equations of arbitrary order.

- **Slow orientation dynamics.** The proposed micromechanical approach can serve as a basis for understanding the mechanics behind phenomenological models, such as the RSC model proposed by Wang et al. (2008) or the ARD model developed by Phelps and Tucker III (2009). In the present study, slowed orientation dynamics are

investigated in the context of different mean-field models by using a modified strain-rate tensor as described by Favaloro (2020). Herein, the derived equations can be seen as a generalization of the RSC model (Wang et al., 2008) based on a consistent micromechanical approach that takes into account the anisotropic behavior of fiber suspensions. The investigation of a simple shear flow shows that the predicted fiber orientation strongly depends on the fiber volume fraction. In addition, the mean-field model itself plays an important role, where the consideration of the spatial distribution of the fibers in the evolution equation can be considered as crucial.

- **Micromechanical foundation of the Jeffery tensor.** From an algebraic point of view, the present work shows that the Jeffery tensor $\mathbb{J}_{\mathsf{F}}$, which localizes the additional contribution $\mathbb{J}_{\mathsf{F}}[\bar{\boldsymbol{D}}]$ to the spin tensor $\boldsymbol{W}_{\mathsf{F}}$ and leads to Jeffery's equation (6.28), is related to the skew-symmetric and symmetric polarization tensors $\mathbb{P}_0^{\mathsf{A},\mathsf{S}}$. Thus, the work of Wetzel (1999) and Wetzel and Tucker III (2001) is complemented in that the Jeffery equation is derived from a general mean-field formulation considered in the present study. In this context, reference is made to Kailasam and Ponte Castañeda (1998) and Ponte Castañeda (2021) who emphasize that Jeffery's model is included in their homogenization approach for the special case of rigid particles in dilute suspensions, see Sec. 1.2.3. For the PCW model, the distribution-corrected Jeffery tensor $\mathbb{J}_{\mathsf{F},\mathsf{d}}$ and for the EM model the effective Jeffery tensor $\bar{\mathbb{J}}_{\mathsf{F}}$ are specified in this context in the present work.
- **Algebraic interpretation of the anisotropic interaction term.** The general micromechanical formulation of the fiber orientation evolution equation (6.22) in this work allows the interpretation that the consideration of the anisotropic environment of the fiber or, in other words, the anisotropic interaction between fibers is related to the convergence criterion of the integral operator $\langle \mathbb{I}^{\mathsf{A}}\{\boldsymbol{\tau}\}\rangle = \mathbf{0}$ in the context of the spin localization relation (6.14) and Eq. (6.15).

Chapter 7

Concluding remarks and outlook

This publication-based thesis deals with the micromechanical modeling of the orientation evolution of short-fiber suspensions, which is called orientation dynamics. The modeling is divided into three parts and is limited to mean-field homogenization approaches referring to the underlying publication Karl and Böhlke (2022). The first part addresses the consideration of the fiber-induced anisotropic viscosity during mold-filling, which is called flow-fiber coupling, with reference to Karl et al. (2023b). The description of the fiber orientation state via orientation tensors contains a closure problem (Advani and Tucker III, 1987), which is discussed in the second part of this thesis. With reference to Karl et al. (2021b) and Karl et al. (2023a), an improved quadratic closure and a novel implicit closure concept are developed and investigated. The modeling of the orientation dynamics is completed in the third part of this thesis by the general micromechanical formulation of the evolution equations for the fiber orientation tensor of arbitrary order with the underlying publication Karl and Böhlke (2024). The key findings of each of these three parts are summarized below:

- **Flow-fiber coupling.** Both the coupling itself and the choice of the viscosity model have a significant influence on the predicted fiber orientation for a given geometry, compared to the decoupled approach. The influence of the coupling is surprisingly apparent throughout the simulation chain up to the prediction of the stress field and

emphasizes the significance of the coupled approach. The differences between the Newtonian and non-Newtonian matrix modeling are more pronounced in the coupled case. The results also show that the two-phase mold-filling simulation strongly influences the predicted fiber orientation field compared to the steady-state prediction.

- **Closure approximations.** The two proposed versions of the symmetric quadratic closure (SQC) lead to an improvement of the common quadratic closure (Doi, 1981) with respect to the estimation of effective mechanical properties and the prediction of orientation evolution. The prediction of effective properties is further improved by both the symmetric quadratic (SIQ) and symmetric hybrid implicit closures (SIHYB). SIQ and SIHYB can be formulated as a 1D problem, which reduces their computational cost to the order of magnitude of the well-known IBOF closure (Chung and Kwon, 2002b), while the computational time of SQC is an order of magnitude less. It turns out that SIQ and SIHYB approximate the maximum entropy closure (Jaynes, 1957; Chaubal and Leal, 1998) via its leading terms (Papenfuß, 2022). As a result, the oscillations of the maximum entropy closure (Tucker III, 2022b) also occur in SIQ and SIHYB, making these models unsuitable for predicting the orientation dynamics.
- **Orientation dynamics.** The evolution equation of the fiber orientation tensor of arbitrary order is formulated based on mean-field homogenization. This generalized evolution equation is specified for selected mean-field models. In particular, the application of the model of Ponte Castañeda and Willis (1995) in the derived generalized evolution equation allows the consideration of the spatial fiber distribution. The results show that the latter has a significant influence on the reorientation behavior in a simple shear flow. In this context, and due to its acceptable computational effort, the model of Ponte Castañeda and Willis (1995) can be recommended besides the Mori-Tanaka model (Mori and Tanaka, 1973; Benveniste, 1987), which is also valid beyond

the dilute regime. The notation based on polarization tensors used throughout this thesis is transferred to the fundamental structure of the evolution equations of the orientation tensor by showing the equivalence to the spin concentration tensor of Wetzel (1999) (pp. 48–49, 269, 318–321) and Wetzel and Tucker III (2001). This tensor, called Jeffery tensor in the present thesis, is extended with respect to the spatial fiber distribution as well as with respect to the consideration of the anisotropic matrix for the effective medium approach (Kanaun and Levin, 2008) (pp. 162–172). From the generalized mean-field based derivation it is concluded that the fiber-fiber interaction term arises from the micromechanical convergence criterion, see, e.g., Willis (1977), for solving the homogenization problem.

The findings of this work described before are based on assumptions and simplifications that need to be critically discussed in the context of the application to industrial problems.

The present thesis assumes a constant mean fiber aspect ratio for the geometric description of the spheroidal fibers. In other words, the real length distribution of the fibers, see Tucker III (2022a) (pp. 40–42), is not taken into account and the embedded fibers are modeled as monodisperse. The reorientation ability of all fibers is assumed to be unrestricted based on the micromechanically formulated fiber orientation evolution equations. In particular, long fibers included in real length distributions cannot freely reorient in thin-walled cavities, see Sec. 3.4 and the references therein. Further studies can focus on incorporating such restriction effects in the mean-field based evolution equations for the fiber orientation tensor of arbitrary order. In order to approximate real length distributions over different discrete values, see Tucker III (2022a) (p. 40), the model of Ponte Castañeda and Willis (1995) can be used to take so-called inclusion families into account (Ponte Castañeda, 2021) to formulate the corresponding mean-field

based evolution equation for the fiber orientation tensor of arbitrary order.

Phase transition from liquid to solid, which occurs in real injection molding processes, is not considered in the present work in order to investigate the effects of flow-fiber coupling in isolation and without the superposition of other physical phenomena. The assumption of an isothermal process is also emphasized here, which needs to be reconsidered in the context of modeling phase transitions. It is known that the degree of alignment near the cavity walls is higher when the phase transition is not considered compared to simulation setups in which the phase transition is implemented (Oumer and Mamat, 2012). This is due to a so-called frozen layer that grows from the wall into the cavity and in which there is no longer any flow that could lead to a reorientation of the fibers, see also Bay (1991) (p. 25). It is discussed by Oumer and Mamat (2012), referring to VerWeyst (1998), that the consideration of phase transition counteracts the effects of flow-fiber coupling. However, in contrast, it would be interesting to quantify the effects of flow-fiber coupling, taking into account phase transition during mold-filling, on the stress field in the loaded solid composite in an insightful further investigation. In this context, the question arises to what extent the knowledge gained can be transferred to real industrial components with complex shapes and whether the effects of flow-fiber coupling can be clearly identified.

With regard to an extended fully coupled simulation chain, a next step may consider the mean-field based fiber orientation evolution equations in a mold-filling simulation, since all of the three main aspects of this thesis are deliberately studied separately for the purpose of fundamental understanding. The micromechanically motivated fiber-fiber interaction term is to be suitably modified in order to be able to be fitted to experimental data and to get rid of the periodic orientation dynamics. As discussed in Secs. 6.2.4 and 6.3, the fiber interaction

parameter related to the model proposed by Folgar and Tucker III (1984) can be used. In addition, a combination of this Folgar-Tucker interaction term with a nematic term can also be used similar to Latz et al. (2010). The higher-order formulation of this combined term can be derived by means of the Maier-Saupe potential given by Latz et al. (2010), and implemented in combination with Eq. (6.34). The use of a nematic term as a possible modification can also be motivated based on Férec et al. (2009; 2014). The same algebraic structure of the interaction terms of the present mean-field approach and the interaction terms of Férec et al. (2009; 2014) can be identified based on the special case of the evolution equation for the second-order fiber orientation tensor. In this context, reference is made to Favaloro (2020), who deals with the special case of second-order based on the Mori-Tanaka model and also draws a connection to Férec et al. (2009; 2014). The interaction terms of Férec et al. (2009; 2014) include unknown second- and fourth-order interaction tensors, where the second-order interaction tensor is approximated by Férec et al. (2009) based on the Maier-Saupe nematic potential. At the positions of these interaction tensors in the overall interaction term, the mean-field approach of the present work leads to expressions including the known second-order fiber orientation tensor. Due to this algebraic similarity of the interaction terms of Férec et al. (2009; 2014) and the interaction terms of the present thesis, a proper nematic modification of the mean-field based evolution equations of this thesis may be proposed in future work.

The use of the mean-field based fiber orientation tensor evolution equations at high volume fractions must be questioned, because the inherent property of the mean-field approach is characterized by the fact that only hydrodynamic effects can be included, see Ponte Castañeda (2021), which may not be the only relevant phenomenon. In the context of Fig. 6.1 it must be discussed that the orientation state of the representative volume element, in which the fiber under consideration is

embedded, can only be considered homogeneously via the orientation average. In practical computations, the illustrated volume element represents a numerical grid cell, which does not allow any connection to the orientation state in neighboring cells. In other words, this means that the fiber orientation state evolves locally in each grid cell without being influenced by the orientation of the neighboring cells. Although studied in the context of Brownian rods and for dilute suspensions, the work of Issa et al. (2023) provides hints for a possible adaptation of the mean-field based fiber interaction of the present work. By considering anisotropic interaction, spatial derivatives of the second- and fourth-order orientation tensor, and thus not only gradient effects of the flow field, are included in the respective orientation evolution equation.

The proposed implicit closures in the form of both a fully symmetric quadratic and a fully symmetric hybrid closure function are only suitable for predicting anisotropic effective properties, since the orientation dynamics show distinct oscillations. Here, further studies are needed to investigate suitable, and most likely problem-adapted, fully symmetric closure functions beyond the quadratic and hybrid approaches, since common fitted closures are superior in terms of predicting the fiber orientation evolution. In particular, the possibility of reduction to a 1D problem similar to the quadratic and hybrid approach can be investigated for new closure functions, which may be advantageous in terms of computational time.

Appendix A

Appendix to chapter 2 - Fundamentals [1]

As a supplement to Sec. 2.6, this appendix provides an overview of selected studies in the field of mean-field homogenization with a special focus on the prediction of the anisotropic viscosity of fiber suspensions. Since mean-field homogenization has been developed mainly in the field of solid mechanics, an overview of selected studies is given first, before studies on the estimation of the effective viscosity are discussed. For a more detailed overview, the reader is referred to, e.g., Mura (1987), Nemat-Nasser and Hori (1993), Torquato (2002), and Kachanov and Sevostianov (2018).

The effective behavior of composites can be narrowed down by using various bounding methods. The coarsest bounds of the effective properties is given by the lower bound according to Reuss (1929) and the upper bound according to Voigt (1889). It is shown by Hill (1952) that the effective properties of the composite cannot violate these bounds. Hashin and Shtrikman (1962a;b; 1963) derived more precise bounds. The bounds of Hashin and Shtrikman are also addressed by, e.g., Walpole (1966a;b) and Willis (1977; 1981). A review of both the Voigt-Reuss bounds and the Hashin-Shtrikman bounds can be found in Hashin (1964; 1965).

[1] This section consists of parts from Karl and Böhlke (2022) and Karl and Böhlke (2024). Additional text passages have been added.

In contrast, mean-field models do not provide a range into which the effective properties of the composite fall, but rather an estimate. Based on Eshelby's single inclusion problem (Eshelby, 1957; 1959), the dilute distribution model (DD) discussed by, e.g., Russel (1973), Benveniste et al. (1991), Tucker III and Liang (1999), and Torquato (2002) (pp. 497–500) estimates the effective stiffness neglecting the interaction between the inclusions. Mori and Tanaka (1973) (MT) used Eshelby's result to model the interaction between the inclusions via the effective strain which refers to the effective matrix strain, see, e.g., Benveniste (1987) and Norris (1989). Based on the concept of Hershey (1954) and Kröner (1958) for crystal aggregates, Hill (1965) and Budiansky (1965) developed the so-called self-consistent method (SC) for matrix-based composites. The effective elastic properties described by SC are estimated by embedding a single inclusion in an infinitely large matrix having the unknown effective properties, which may be anisotropic. A further estimation of the effective properties of a composite is given by the differential scheme (DS). The basic idea is to add the inclusion phase incrementally into the matrix, whose elastic properties depend on the current inclusion volume fraction. In every step, the DD model described before is applied. This approach was first introduced by Roscoe (1952) using Einstein's estimate (Einstein, 1906) of suspensions containing rigid spheres of equal shape in a Newtonian matrix fluid. For macroscopically isotropic solid composites consisting of isotropic phases, DS was suggested by Roscoe (1973) and Boucher (1976). By using tensor calculus, McLaughlin (1977) formulated DS in order to treat two-phase linear elastic anisotropic composites consisting of anisotropic phases and homogeneously distributed inclusions. In addition to the more classical models described before, there are newer developments for estimating the effective elastic properties of composites. Ponte Castañeda and Willis (1995) derived explicit estimates of Hashin-Shtrikman type considering both the inclusion geometries and the spatial distribution of the inclusions. Hori and Nemat-Nasser (1993) introduced the double-inclusion model. The

basic idea is to embed an ellipsoidal inclusion in an infinite domain of matrix material. The inclusion itself again consists of two phases, one of which takes on the role of the matrix and the other the role of an inclusion. Aboutajeddine and Neale (2005) developed a new version of the double-inclusion model in order to generally consider multi-phase composites. In Hu and Weng (2000), the connection between the double-inclusion model and other mean-field estimates is addressed. Zheng and Du (2001) and Du and Zheng (2002) proposed the explicit interaction direct derivative model to consider multi-phase composites with interactive inclusions of different anisotropic behavior. Two-step homogenization approaches proposed by Pierard et al. (2004) divide the composite into domains which can be homogenized separately. Subsequently, a homogenization over all domains is done to estimate the effective anisotropic behavior. For a unified algebraic formulation of selected mean-field models, reference is made to Hessman et al. (2021). In this study, based on full-field simulations and experimental investigations, the MT model leads to reliable results.

Selected studies in the field of estimating the effective viscous behavior of suspensions using the mean-field models addressed before are discussed in the following. Note that the application of Eshelby's single inclusion problem (Eshelby, 1957; 1959) in early works in the field of homogenizing the effective viscosity of fluid mixtures is addressed in Sec. 1.2.3. The estimation of the effective viscosity of a suspension in which rigid spheres are embedded can be traced back to Einstein (1906). The derived formula, which was later corrected by Einstein (1911), is only valid for dilute suspensions and corresponds to DD, as described by Torquato (2002) (p. 499). For a review of early literature on both dilute and concentrated suspensions, reference is made to Hashin (1964). Note that DD is only a valid choice for inclusion volume fractions of $1\,\%$ or less (Tucker III and Liang, 1999). As addressed by Kachanov and Abedian (2015), Einstein's estimate violates the lower Hashin-Shtrikman bound

and an alternative expression can be found which leads to reliable results for particle volume fractions up to around 20 % to 30 %. This improved approach was generalized by Kachanov and Abedian (2015) to estimate the anisotropic viscosity of suspensions with embedded rigid particles. The special case of rigid inclusions of various spheroidal geometries and orientations is addressed in their work without accounting for particle-particle interaction. Before going on to discuss further work, it is worth emphasizing the comment of Kachanov and Abedian (2015) that the description of the anisotropic viscosity of suspensions is not widespread in the literature. This remark can be found in a similar form in works by other authors, such as Thevenin and Perreux (1996) and Schneider (2016). Periodic suspensions consisting of rigid UD fibers in a Newtonian matrix fluid are addressed with respect to homogenization by Périn and Lévy (1994) and governing equations for the special case of fiber-parallel flow are described. For this configuration, Périn (2004) addresses lower and upper bounds for the special case of macroscopic isotropy. Thevenin and Perreux (1996) applied the MT and the SC model for estimating the viscosity of fiber suspensions in the framework of two-phase fluid formulations and UD fiber orientation. In addition, the applicability of micromechanical methods from linear elasticity is addressed in their study. It is outlined that considering the fibers as rigid bodies, which is synonymous with an infinitely large viscosity, SC suffer from convergence problems in contrast to the MT approach. In addition, a procedure of modeling the matrix as a non-Newtonian fluid is discussed and was applied to the MT model. Estimates for different directional viscosities are compared for various fiber volume fractions. The conclusions of Thevenin and Perreux (1996) indicate that the MT approach and SC can be seen as a bounding estimation pair for the elongational and the in-plane viscosity of the fiber suspension with transversely isotropic material symmetry. From a physical point of view, the MT approach is evaluated to better represent the viscous behavior compared to SC. Bertóti and Böhlke (2017) used a two-step

Hashin-Shtrikman approach for the special case of rigid spheroidal inclusions and simulated a fiber set subject to Jeffery's equation for each individual fiber. Regarding four different flow cases, both the orientation evolution and the evolution of the effective viscosity tensor were investigated. For the viscous stress evolution, the differences between the mean-field model and the constitutive law of Dinh and Armstrong (1984) were studied. The results show that the chosen mean-field approach is sufficient to model the viscosity of the fiber suspension. The expression for the UD viscosity tensor for the special case of rigid fibers used by Bertóti and Böhlke (2017) is equivalent to the form given in Talbot and Willis (1992). Traxl et al. (2020) used non-linear homogenization in order to determine the effective viscosity of suspensions with various matrix behaviors and with different shapes of embedded inclusions or pores. The analogy to linear elasticity is addressed and DD, the MT model, and DS were applied. In the context of viscous suspensions, the fundamental Hill-Mandel condition (Hill, 1963; Mandel, 1980) is addressed in the work of Traxl et al. (2020). Ponte Castañeda (2021) applied a Hashin-Shtrikman-type homogenization in order to model the rheological behavior of suspensions with deformable inclusions embedded in Newtonian or viscoplastic matrix fluid. The constitutive behavior of the inclusions refers to viscoelastic or elasto-viscoplastic. In addition, different so-called inclusions families are addressed, with the evolution of the microstructure due to the flow kinematics being possible. Kammer et al. (2022) generalized the homogenization approach of Ponte Castañeda and Willis (1995) in order to approximate the effective viscosity of suspensions with isotropically distributed rigid spherical particles. Both Newtonian and viscoplastic matrix fluids were considered. An empirical scalar parameter was used to interpolate between the Ponte Castañeda and Willis estimates and SC estimates (Hill, 1965; Budiansky, 1965). It is shown that the proposed model agrees well with experimental results and that the empirical parameter can be interpreted as a representation of the polydisperse

character of the particle suspension. Kammer and Ponte Castañeda (2022) generalized the approach of Ponte Castañeda and Willis (1995) and the SC estimate (Hill, 1965; Budiansky, 1965) in parallel by using the same empirical scalar parameter introduced by Kammer et al. (2022) in order to interpolate between both methods. The further development of Kammer and Ponte Castañeda (2022) includes a general tensorial approach with the additional feature of considering different inclusion geometries, mechanical behaviors of the constituents, orientations, and distributions while fulfilling the necessary index symmetries of the effective tensors. In the context of this thesis, reference is made to their results of estimating the effective linear viscous behavior for both a statistically isotropic distribution of rigid spheres and an isotropic distribution of rigid ellipsoidal fibers in a Newtonian matrix fluid.

Full-field simulations, see, e.g., Schneider (2016), Bertóti et al. (2021), and Sterr et al. (2023) are not part of this study as they require a fully resolved microstructure. However, such computational intense approaches can be used to analyze the quality of the results of mean-field models. In the study of Bertóti et al. (2021), referring to the underlying doctoral thesis of Bertóti (2021), an orientation-averaged three parameter model based on the MT estimate was applied and compared with full-field simulations in view of the model parameters. The results indicate that the parameter approximation based on the MT approach is reliable for fiber volume fractions of $5\,\%$ or less and leads to lower viscosity values for higher fiber volume fractions compared to the full-field computations. However, the results also show that the algebraic form of the orientation-averaged effective viscosity tensor can be used with corrected parameters in order to minimize the error regarding the full-field predictions. It should be noted that the performance of various mean-field models beyond the MT approach was not investigated by Bertóti et al. (2021). The study of Sterr et al. (2023) builds on Bertóti et al. (2021) in view of investigating non-Newtonian viscosity of the matrix fluid in which rigid

fibers are embedded. Their results for various fiber volume fractions and for a fixed fiber aspect ratio indicate clear differences between the MT approach and the full-field simulations. It should be noted that the investigation of Sterr et al. (2023) is limited to a single transversely isotropic orientation state and to the MT model as a representation of mean-field modeling. In a recent publication, Sterr et al. (2025) use a combination of full-field simulations and machine learning to investigate the anisotropic viscosity of short-fiber suspensions with non-Newtonian matrix behavior for orientations beyond the transversely isotropic state. Four different model approaches are proposed and trained for an efficient estimation of the shear-rate dependent anisotropic viscosity at the macroscale.

In order to make this thesis self-contained, and in addition to the classical mean-field models addressed before, reference is made to selected further literature on anisotropic constitutive behavior of fiber suspensions. Regarding transversely isotropic material symmetry, Ericksen (1960) derived an expression for the stress tensor depending on the orientation of the embedded non-spherical particles. The work of Batchelor (1970) deals with suspensions with embedded ellipsoidal particles assuming a dilute regime and a corresponding formulation for the stress tensor is provided. The recent publication of Geißler et al. (2023) addresses the computation of the three transversely isotropic fluid model parameters of Ericksen (1960). For the special case of so-called slender rods, an improved expression is provided compared to the one proposed by Batchelor (1970). In addition, a novel approach incorporating non-Newtonian matrix behavior in the transversely isotropic fluid model is described. Batchelor (1971) addresses the constitutive modeling of fiber suspensions with an aligned orientation state beyond the interaction-free dilute regime. Gibson (1989) published a matrix representation of the constitutive law for transversely isotropic fiber suspensions and identified three independent viscosity parameters for the special case of incom-

pressibility. Gibson chose the inverse formulation of the constitutive behavior which means that the deformation rate is expressed in terms of the fluidity and the stress tensor. This convenient representation was used in the studies of Pipes et al. (1991a;b), where expressions for the three independent viscosities were derived depending on the fiber aspect ratio, the fiber content, the viscosity of the matrix fluid, and a geometric parameter. Pipes (1992) extended this approach for a transversely isotropic fiber suspension by considering non-Newtonian matrix behavior. Expressions for the directional viscosities of UD fiber suspensions were also derived by Christensen (1993). In order to model the anisotropic behavior of fiber suspensions beyond the transversely isotropic symmetry, Sommer et al. (2018) applied an orientation-averaged representation of the aforementioned constitutive law including the three independent viscosity parameters. The parallelism in view of the structure of the constitutive law with the work of, e.g., Hand (1962) is addressed, in which the anisotropic stress tensor is formulated in terms of the strain-rate tensor and a structural tensor. With today's knowledge of the work of Kanatani (1984) and Advani and Tucker III (1987), Hand's structural tensor can be identified as the fiber orientation tensor. The recent publication of Férec et al. (2023) should be mentioned in the context of Hand (1962). An ellipsoidal particle is considered by Férec et al. (2023), whose geometry differs from the idealized geometry of a spheroidal particle, which is commonly assumed to approximate fiber geometries. Based on a volumetric discretization, a so-called conformation tensor of second order is derived whose evolution equation is related to Hand's work. It is shown that the particle orientation evolution equation of Jeffery (1922) is included as a special case and therefore the approach of Férec et al. (2023) can be seen as a respective generalization in view of more complex particle geometries. In addition, Férec et al. (2023) provide an expression for the viscous stress tensor in the context of their novel approach.

Describing the anisotropic behavior of fiber suspensions with the direct use of orientation tensors is the basis of many models, e.g. that of Dinh and Armstrong (1984), Lipscomb II et al. (1988), Shaqfeh and Fredrickson (1990), and Phan-Thien and Graham (1991). The anisotropic viscosity model given in, e.g., Tucker III (1991), which is a special form of the Lipscomb model, was used by Munganga et al. (2000) to assess the thermodynamic consistency of various closure schemes based on both the isothermal Clausius-Duhem inequality given in Eq. (2.25) and the procedure of Coleman and Noll (1963). Finally, it should be mentioned that the dilute, semi-dilute, and concentrated regime appears in the literature as a subdivision with regard to the applicability of the different anisotropic viscosity models. The subdivision can be estimated from the fiber volume fraction and the aspect ratio, as shown, e.g., in Bay (1991) (p. 118), referring to the work of Doi and Edwards (1978), in Tucker III (1991), or in Petrie (1999), representing a review article in the context of the present section.

Appendix B

Appendix to chapter 3 - Flow-fiber coupling

B.1 Process parameters

Following Osswald and Rudolph (2015) (p. 63), the process temperature for PP is set to $\theta = 220\,^{\circ}\mathrm{C}$ or $\theta = 493\,\mathrm{K}$, respectively. Osswald and Rudolph (2015) (p. 70) provide the equation for the Cross model (Cross, 1965) as follows

$$\mu(\dot{\gamma}) = \frac{\mu_0}{1 + \left(\frac{\mu_0}{\tau^*}\dot{\gamma}\right)^{1-\tilde{n}}}. \tag{B.1}$$

The parameter $\tilde{n} = 0.251$ is given in Osswald and Rudolph (2015) (p. 71) and corresponds to the parameter $n = 0.749$ in Eq. (3.10) which refers to the solver implementation used in this thesis. The computation of the kinematic viscosity $\nu_0 = \mu_0/\rho_{\mathsf{M}}$ at the process temperature is based on the so-called Williams-Landel-Ferry equation (WLF) (Williams et al., 1955) as given in Osswald and Rudolph (2015) (p. 70)

$$\mu_0 = D_1 \exp\left(\frac{A_1(\theta - D_2)}{A_2 + \theta - D_2}\right), \tag{B.2}$$

with the parameters given as follows (Osswald and Rudolph, 2015) (p. 71)

$$A_1 = 2803.3, \qquad D_1 = 564\,\mathrm{Pa\,s},$$
$$A_2 = 165097.1\,\mathrm{K}, \qquad D_2 = 493\,\mathrm{K}.$$

The remaining parameter $m = 17.366 \cdot 10^{-3}\,\mathrm{s}$ in Eq. (3.10) is computed via $m = \mu_0/\tau^*$ with $\tau^* = 32477\,\mathrm{Pa}$ as given in the work of Osswald and Rudolph (2015) (p. 71).

The computation of the surface tension at the process temperature is based on the following relation (Osswald et al., 2006) (p. 125)

$$\sigma(\theta) = \sigma_{\mathsf{ref}} + \frac{\mathrm{d}\sigma}{\mathrm{d}\theta}(\theta - \theta_{\mathsf{ref}}), \tag{B.3}$$

with the reference surface tension $\sigma_{\mathsf{ref}} = 0.03\,\mathrm{N/m}$ at the reference temperature $\theta_{\mathsf{ref}} = 180\,^\circ\mathrm{C}$ or $\theta_{\mathsf{ref}} = 453\,\mathrm{K}$, respectively. For PP, the gradient is given as $\mathrm{d}\sigma/\mathrm{d}\theta = -5.8 \cdot 10^{-5}\,\mathrm{N/(mK)}$ following Osswald et al. (2006) (p. 125) and the chosen process temperature $\theta = 493\,\mathrm{K}$ leads to the value $\sigma \approx 0.028\,\mathrm{N/m}$ used in the simulation.

B.2 Implicit-explicit splitting of the Folgar-Tucker equation [1]

In this supplementary section, the implicit-explicit splitting of the Folgar-Tucker equation is addressed. The implicit-explicit splitting of the IBOF closure terms (Chung and Kwon, 2002b) is given based on the work of Heinen (2007) (p. 78) with respect to the symmetry-preserving representation of the previous study Karl et al. (2021a). It should be noted that the incompressibility condition $\mathrm{tr}(\bar{\boldsymbol{D}}) = 0$ is used in the closure terms. The Folgar-Tucker equation is solved for cells with

[1] This section is directly taken from Karl et al. (2023b).

$\psi > 0.99$ avoiding anisotropic effects in cells, which could neither be clearly assigned to the air phase nor to the suspension. In addition, the Folgar-Tucker equation is solved in every time step before solving the system of governing equations (3.6) with the following splitting

$$\underbrace{\frac{\partial \boldsymbol{N}}{\partial t} + \operatorname{div}(\boldsymbol{N} \otimes \bar{\boldsymbol{v}}) + 2\xi \mathbb{N}[\bar{\boldsymbol{D}}]_{\mathsf{impl}} + 6C_{\mathsf{I}}\dot{\bar{\gamma}}\boldsymbol{N}}_{\text{implicit}}$$
$$= \underbrace{\bar{\boldsymbol{W}}\boldsymbol{N} - \boldsymbol{N}\bar{\boldsymbol{W}} + \xi\big(\bar{\boldsymbol{D}}\boldsymbol{N} + \boldsymbol{N}\bar{\boldsymbol{D}} - 2\mathbb{N}[\bar{\boldsymbol{D}}]_{\mathsf{expl}}\big)}_{\text{explicit}} + \underbrace{2C_{\mathsf{I}}\dot{\bar{\gamma}}\boldsymbol{I}}_{\text{explicit}}. \tag{B.4}$$

The implicit-explicit splitting of the IBOF closure terms in the split Folgar-Tucker equation above reads as follows

$$\begin{aligned}
\mathbb{N}[\bar{\boldsymbol{D}}]_{\mathsf{impl}} &= \frac{\beta_3}{3}(\boldsymbol{N}\cdot\bar{\boldsymbol{D}})\boldsymbol{N} + \frac{\beta_5}{6}(\boldsymbol{S}\cdot\bar{\boldsymbol{D}})\boldsymbol{N},\\
\mathbb{N}[\bar{\boldsymbol{D}}]_{\mathsf{expl}} &= \frac{2\beta_1}{3}\bar{\boldsymbol{D}} + \frac{2\beta_3}{3}\boldsymbol{N}\bar{\boldsymbol{D}}\boldsymbol{N}\\
&\quad + \frac{\beta_2}{6}\big((\boldsymbol{N}\cdot\bar{\boldsymbol{D}})\boldsymbol{I} + 2\bar{\boldsymbol{D}}\boldsymbol{N} + 2\boldsymbol{N}\bar{\boldsymbol{D}}\big)\\
&\quad + \frac{\beta_4}{6}\big((\boldsymbol{S}\cdot\bar{\boldsymbol{D}})\boldsymbol{I} + 2\bar{\boldsymbol{D}}\boldsymbol{S} + 2\boldsymbol{S}\bar{\boldsymbol{D}}\big)\\
&\quad + \frac{\beta_5}{6}\big((\boldsymbol{N}\cdot\bar{\boldsymbol{D}})\boldsymbol{S} + 2\boldsymbol{N}\bar{\boldsymbol{D}}\boldsymbol{S} + 2\boldsymbol{S}\bar{\boldsymbol{D}}\boldsymbol{N}\big)\\
&\quad + \frac{\beta_6}{3}\big((\boldsymbol{S}\cdot\bar{\boldsymbol{D}})\boldsymbol{S} + 2\boldsymbol{S}\bar{\boldsymbol{D}}\boldsymbol{S}\big),
\end{aligned} \tag{B.5}$$

with the coefficients β_1 to β_6 depending on the invariants of $\boldsymbol{N}$ as given in Chung and Kwon (2002b) and the abbreviation $\boldsymbol{S} = \boldsymbol{N}^2$ or equivalently $S_{ij} = N_{ik}N_{kj}$. Both terms of the implicit closure part $\mathbb{N}[\bar{\boldsymbol{D}}]_{\mathsf{impl}}$ are linearized $(\boldsymbol{N}^n \cdot \bar{\boldsymbol{D}}^n)\boldsymbol{N}^{n+1}$ and $(\boldsymbol{S}^n \cdot \bar{\boldsymbol{D}}^n)\boldsymbol{N}^{n+1}$ as suggested by Heinen (2007) (p. 78), with n representing the time step index.

B.3 Supplementary results

B.3.1 Fiber orientation [2]

In addition to Sec. 3.3.1, Figs. B.3.1 and B.3.2 address the local fiber orientation difference with respect to viscosity modeling. Figure B.3.1 shows the difference between the non-Newtonian and Newtonian matrix fluid for the decoupled case, whereas Fig. B.3.2 address the same difference for the coupled case. The fields in both figures look similar. This is because for the decoupled case, the non-Newtonian fluid has a flatter velocity profile than the Newtonian fluid. This phenomenon is exactly the same in the coupled case, in which the flow-fiber coupling flattens the velocity profile as discussed in Sec. 1.2.1. In the coupled case, however, the non-Newtonian velocity profile flattens more than in the Newtonian case, which is why the characteristics of the difference field correspond to the decoupled approach.

The differences regarding the two matrix fluid behaviors are caused by different shear rates. Especially in the channel center region, flattening causes less shear leading to less fiber alignment in the main shear direction. This phenomenon can be seen for N_{11} in the horizontal channel region, where the Newtonian fluid results in higher values for N_{11} close to the center line compared to the non-Newtonian case (blue color). The same can be observed for N_{22} inside the right rib. Furthermore, the difference fields vanish near the channel walls, since the asymptotic orientation state is dominant there and only depends on the kinematics, the fiber aspect ratio α, and the fiber-fiber interaction strength C_I and not on the fluid model of the matrix. For further information regarding asymptotic states of the Folgar-Tucker equation, the reader is referred to Karl et al. (2021b).

[2] This section is directly taken from Karl et al. (2023b).

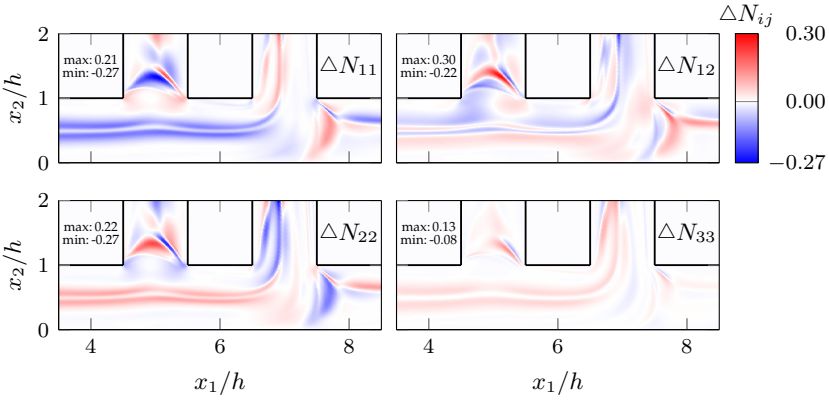

Figure B.3.1: Difference field $\triangle \boldsymbol{N} = \boldsymbol{N}^{\text{decoupled}}_{\text{nonNewtonian}} - \boldsymbol{N}^{\text{decoupled}}_{\text{Newtonian}}$ in the area of interest, adapted from Karl et al. (2023b).

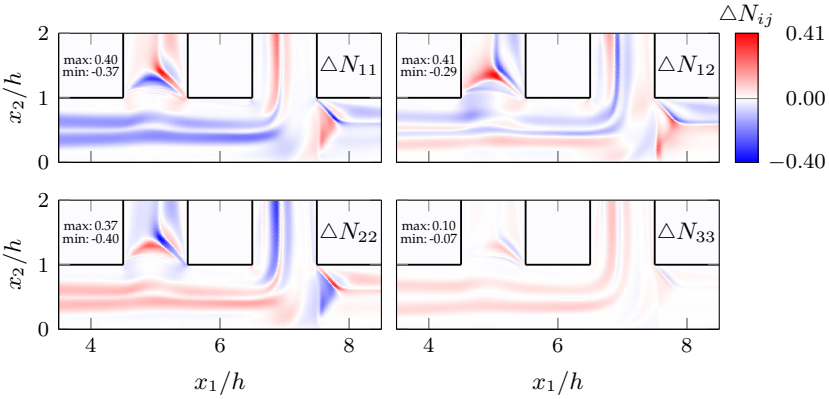

Figure B.3.2: Difference field $\triangle \boldsymbol{N} = \boldsymbol{N}^{\text{coupled}}_{\text{nonNewtonian}} - \boldsymbol{N}^{\text{coupled}}_{\text{Newtonian}}$ in the area of interest, adapted from Karl et al. (2023b).

The differences between the viscosity models addressed before depend on the shear-thinning behavior of the matrix fluid in the non-Newtonian case. In order to quantify this, Fig. B.3.3(a) shows the non-dimensional

viscosity $\mu(\dot{\bar{\gamma}}_\mathrm{M})/\mu_0$ based on the Cross-model given in Eq. (3.10). In addition, the field of the effective matrix shear rate $\dot{\bar{\gamma}}_\mathrm{M}$ is shown in Fig. B.3.3(b) with respect to the coupled non-Newtonian simulation during mold-filling ($t = 0.5\,\mathrm{s}$). It can be observed that the shear rate is locally so high that significant shear-thinning is present.

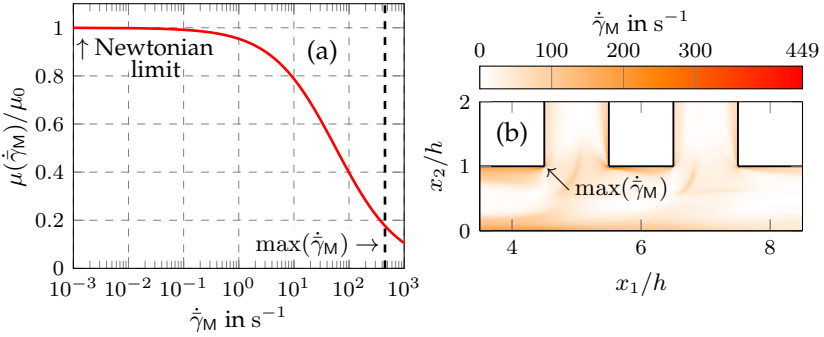

Figure B.3.3: Non-dimensional viscosity $\mu(\dot{\bar{\gamma}}_\mathrm{M})/\mu_0$ based on the Cross-model in (a) and effective matrix shear rate $\dot{\bar{\gamma}}_\mathrm{M}$ in the area of interest for the coupled non-Newtonian simulation during mold-filling ($t = 0.5\,\mathrm{s}$) in (b), adapted from Karl et al. (2023b).

B.3.2 Stress field [3]

In addition to the results of Sec. 3.3.2, the local effective stress field is given in Fig. B.3.4. The left column refers to the stress analysis for the decoupled simulation and the right column refers to the coupled approach, both for non-Newtonian matrix behavior during mold-filling. Since the elastic limit of the material used (PP-GF40) is 60.2 to $87.9\,\mathrm{MPa}$ (Ansys Granta EduPack®, 2022), the deformation is purely elastic.

[3] This section is directly taken from Karl et al. (2023b).

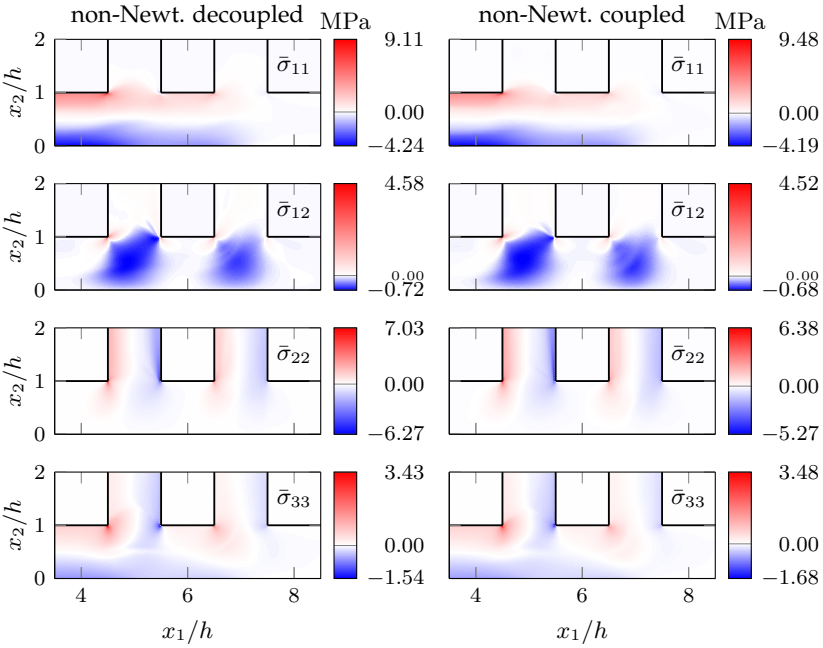

Figure B.3.4: Effective stress field $\bar{\sigma}$ in the area of interest with respect to non-Newtonian matrix behavior during mold-filling (left column: decoupled approach, right column: coupled approach), adapted from Karl et al. (2023b).

The non-dimensional stress difference field regarding both viscosity models for the decoupled approach is given in Fig. B.3.5. For the coupled approach, this difference field is shown in Fig. B.3.6. Due to the prescribed boundary conditions, see Sec. 3.2.1, effects of the viscosity model mainly can be limited to $\triangle\bar{\sigma}^*_{11}$ inside the horizontal channel and to $\triangle\bar{\sigma}^*_{22}$ inside the ribs. These differences are directly linked to the previous section and caused by the flattening of the velocity profile. This flattening affects the fiber alignment by a decreased shear rate in the center region of the channels which influences the local stiffness. These

local stiffness differences are represented by the local stress differences for the prescribed displacement boundary conditions.

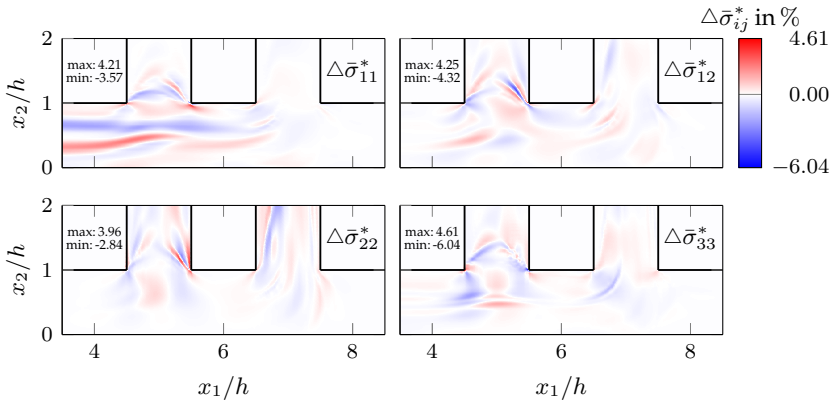

Figure B.3.5: Difference field $\triangle\bar{\boldsymbol{\sigma}}^* = (\bar{\boldsymbol{\sigma}}^{\text{decoupled}}_{\text{nonNewtonian}} - \bar{\boldsymbol{\sigma}}^{\text{decoupled}}_{\text{Newtonian}}) \cdot 100\,\%/\max(\bar{\boldsymbol{\sigma}}^{\text{decoupled}}_{\text{Newtonian}})$ in the area of interest, adapted from Karl et al. (2023b).

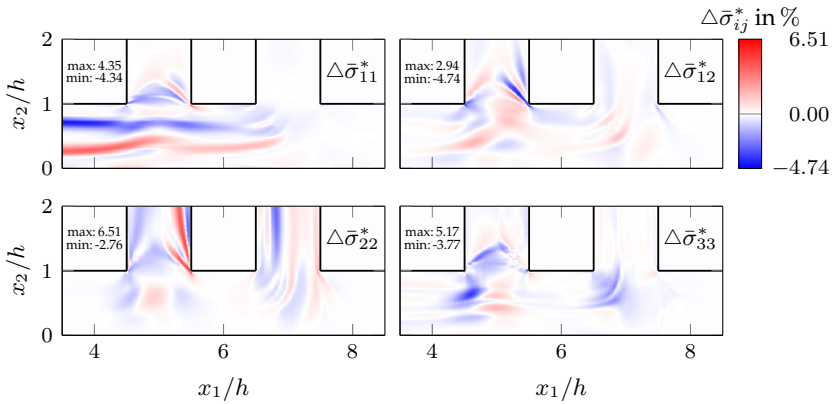

Figure B.3.6: Difference field $\triangle\bar{\boldsymbol{\sigma}}^* = (\bar{\boldsymbol{\sigma}}^{\text{coupled}}_{\text{nonNewtonian}} - \bar{\boldsymbol{\sigma}}^{\text{coupled}}_{\text{Newtonian}}) \cdot 100\,\%/\max(\bar{\boldsymbol{\sigma}}^{\text{coupled}}_{\text{Newtonian}})$ in the area of interest, adapted from Karl et al. (2023b).

B.4 Discussion of the flow regime

The discussion in the section at hand supplements Sec. 3.4 and the argumentation is based on Tucker III (1991) and Tucker III (2022a) (pp. 196–198). The following formulation of the viscous stress tensor represents the starting point (Tucker III, 2022a) (p. 182)

$$\boldsymbol{\sigma}_{\mathsf{v}} = 2\mu\boldsymbol{D} + 2\mu N_{\mathsf{p}}\mathbb{N}[\boldsymbol{D}], \tag{B.6}$$

with the parameter N_{p} called particle number. The mean-field approach given in Eqs. (3.3) and (3.4) is used in a formulation similar to Eq. (B.6)

$$\bar{\boldsymbol{\sigma}}_{\mathsf{v}} \approx 2\mu\bar{\boldsymbol{D}} + \frac{c_{\mathsf{F}}}{c_{\mathsf{M}}} b_1 \mathbb{N}[\bar{\boldsymbol{D}}]. \tag{B.7}$$

The coefficient b_1 is computed based on the orientation average of $(\mathbb{P}_0^{\mathsf{S}})^{-1}$ as given in Eq. (2.82). The components of the polarization tensor $\mathbb{P}_0^{\mathsf{S}}$ given in Eq. (E.20) indicate that the shear viscosity μ can be taken into account as a prefactor

$$\mathbb{P}_0^{\mathsf{S}} = \frac{1}{\mu}\tilde{\mathbb{P}}_0^{\mathsf{S}} \quad \leftrightarrow \quad \left(\mathbb{P}_0^{\mathsf{S}}\right)^{-1} = \mu\left(\tilde{\mathbb{P}}_0^{\mathsf{S}}\right)^{-1}. \tag{B.8}$$

The polarization tensor $\tilde{\mathbb{P}}_0^{\mathsf{S}}$ depends only on the fiber aspect ratio α, based on a modification of Eq. (E.20). By using Eq. (B.8) in the mean-field approach of Eq. (3.3), the following equivalent formulation of Eq. (B.7) is derived

$$\bar{\boldsymbol{\sigma}}_{\mathsf{v}} \approx 2\mu\bar{\boldsymbol{D}} + \mu\frac{c_{\mathsf{F}}}{c_{\mathsf{M}}} \tilde{b}_1 \mathbb{N}[\bar{\boldsymbol{D}}], \tag{B.9}$$

with $\tilde{b}_1$ depending on the components of $\left(\tilde{\mathbb{P}}_0^{\mathsf{S}}\right)^{-1}$. A comparison with Eq. (B.6) leads to the following value of the particle number

$$N_{\mathsf{p}} = \frac{c_{\mathsf{F}}}{c_{\mathsf{M}}}\frac{\tilde{b}_1}{2} \approx 21.87, \tag{B.10}$$

based on the chosen parameters $\alpha = 20$ and $c_\mathsf{F} = 0.2$. The decision whether or not the flow-fiber coupling is relevant requires the computation of $N_\mathsf{p}\delta^2$ according to Tucker III (1991). The value of δ^2 can be estimated as described by Tucker III (2022a) (p. 196) via

$$\delta^2 = N_{22}, \tag{B.11}$$

where N_{22} is the asymptotic orientation state in a simple shear flow perpendicular to the shear plane consistent with the coordinate system shown in Fig. 3.1. The solution of the Folgar-Tucker model with the IBOF closure, $\alpha = 20$, and $C_\mathsf{I} = 0.005$ according to chapter 3 leads to

$$\delta^2 = 0.056 \quad \leftrightarrow \quad \delta \approx 0.237, \tag{B.12}$$

which results in the sought parameter value

$$N_\mathsf{p}\delta^2 \approx 1.22. \tag{B.13}$$

To complete the discussion, the geometry must be included via the following ratio (Tucker III, 1991)

$$\epsilon = \frac{h/2}{L} = \frac{h/2}{4.5h} \approx 0.11. \tag{B.14}$$

The characteristic length $L = 4.5h$ is chosen because it represents the maximum length near the area of interest shown in Fig. 3.1 over which the fiber suspension flows undisturbed without deflection into the ribs. The computations above show that ϵ is in the order of magnitude of δ

$$N_\mathsf{p}\delta^2 \geq 1, \qquad\qquad \delta \sim \epsilon, \tag{B.15}$$

which corresponds to the general narrow gap flow of Tucker III (1991), also called regime III, for which a flow-fiber coupled approach in 3D is suggested, see also Tucker III (2022a) (p. 198).

Appendix C

Appendix to chapter 4 - Symmetric quadratic closure

C.1 Considered fiber orientation states

The following components of the chosen exemplary second-order fiber orientation tensors $\boldsymbol{N}(0°)$, $\boldsymbol{N}(45°)$, and $\boldsymbol{N}(90°)$ refer to Kehrer et al. (2020). These orientation states are used to investigate the proposed SQC in terms of estimating the anisotropic effective stiffness compared with QC and IBOF and read as follows

$$N_{ij}^{(0°)} = \begin{pmatrix} 0.3449 & -0.0084 & 0.0023 \\ -0.0084 & 0.6325 & 0.0056 \\ 0.0023 & 0.0056 & 0.0226 \end{pmatrix},$$

$$N_{ij}^{(45°)} = \begin{pmatrix} 0.4390 & -0.1164 & 0.0031 \\ -0.1164 & 0.5317 & 0.0047 \\ 0.0031 & 0.0047 & 0.0294 \end{pmatrix},$$

$$N_{ij}^{(90°)} = \begin{pmatrix} 0.5744 & 0.0046 & 0.0049 \\ 0.0046 & 0.3993 & -0.0008 \\ 0.0049 & -0.0008 & 0.0263 \end{pmatrix}. \tag{C.1}$$

The corresponding experimentally measured fourth-order fiber orientation tensors $\mathbb{N}(0°)$, $\mathbb{N}(45°)$, and $\mathbb{N}(90°)$ read as follows (Kehrer et al., 2020)

$$N_{ijkl}^{(0°)} \mathrel{\widehat{=}} \begin{pmatrix} 0.1981 & 0.1401 & 0.0067 & 0.0010 & 0.0012 & -0.0003 \\ 0.1401 & 0.4837 & 0.0087 & 0.0046 & 0.0005 & -0.0081 \\ 0.0067 & 0.0087 & 0.0072 & 0.0000 & 0.0006 & 0.0000 \\ 0.0010 & 0.0046 & 0.0000 & 0.0087 & 0.0000 & 0.0005 \\ 0.0012 & 0.0005 & 0.0006 & 0.0000 & 0.0067 & 0.0010 \\ -0.0003 & -0.0081 & 0.0000 & 0.0005 & 0.0010 & 0.1401 \end{pmatrix},$$

$$N_{ijkl}^{(45°)} \mathrel{\widehat{=}} \begin{pmatrix} 0.2689 & 0.1606 & 0.0095 & 0.0013 & 0.0015 & -0.0523 \\ 0.1606 & 0.3623 & 0.0088 & 0.0032 & 0.0005 & -0.0631 \\ 0.0095 & 0.0088 & 0.0111 & 0.0003 & 0.0010 & -0.0011 \\ 0.0013 & 0.0032 & 0.0003 & 0.0088 & -0.0011 & 0.0005 \\ 0.0015 & 0.0005 & 0.0010 & -0.0011 & 0.0095 & 0.0013 \\ -0.0523 & -0.0631 & -0.0011 & 0.0005 & 0.0013 & 0.1606 \end{pmatrix},$$

$$N_{ijkl}^{(90°)} \mathrel{\widehat{=}} \begin{pmatrix} 0.4144 & 0.1497 & 0.0103 & -0.0006 & 0.0031 & -0.0028 \\ 0.1497 & 0.2433 & 0.0064 & -0.0006 & 0.0008 & 0.0074 \\ 0.0103 & 0.0064 & 0.0096 & 0.0004 & 0.0010 & 0.0000 \\ -0.0006 & -0.0006 & 0.0004 & 0.0064 & 0.0000 & 0.0008 \\ 0.0031 & 0.0008 & 0.0010 & 0.0000 & 0.0103 & -0.0006 \\ -0.0028 & 0.0074 & 0.0000 & 0.0008 & -0.0006 & 0.1497 \end{pmatrix}. \tag{C.2}$$

Note that these matrix representations of the measured fourth-order fiber orientation tensors refer to the non-normalized Voigt notation given in, e.g., Voigt (1910) (pp.584–587) and Cowin (1989). As already addressed in Sec. 4.1 in the context of Eq. (4.3), the normalized matrix representation has to to be used to apply tensor operations.

C.2 SQC for orientation evolution description [1]

First of all, it is shown that the use of $\mathbb{N}$ approximated based on Eq. (4.9) violates the condition $\mathrm{tr}(\dot{\boldsymbol{N}}) = 0$. Based on this particular $\mathbb{N}$, the closure term in the Folgar-Tucker equation reads

$$\begin{aligned}\mathbb{N}[\boldsymbol{D}] &= \frac{\mathrm{sym}(\boldsymbol{N}\otimes\boldsymbol{N})[\boldsymbol{D}]}{\frac{1}{3}(1+2\|\boldsymbol{N}\|^2)} \\ &= \frac{1}{\frac{1}{3}(1+2\|\boldsymbol{N}\|^2)}\frac{1}{3}\big((\boldsymbol{N}\cdot\boldsymbol{D})\boldsymbol{N} + 2\boldsymbol{N}\boldsymbol{D}\boldsymbol{N}\big) \\ &= \frac{1}{1+2\|\boldsymbol{N}\|^2}\big((\boldsymbol{N}\cdot\boldsymbol{D})\boldsymbol{N} + 2\boldsymbol{N}\boldsymbol{D}\boldsymbol{N}\big). \end{aligned} \tag{C.3}$$

The condition $\mathrm{tr}(\mathbb{N}[\boldsymbol{D}]) = \boldsymbol{D}\cdot\boldsymbol{N}$ given in Eq. (4.12) is violated by this particular $\mathbb{N}$ since

$$\begin{aligned}\mathrm{tr}(\mathbb{N}[\boldsymbol{D}]) &= \frac{1}{1+2\|\boldsymbol{N}\|^2}\big(\boldsymbol{N}\cdot\boldsymbol{D} + 2\,\mathrm{tr}(\boldsymbol{N}\boldsymbol{D}\boldsymbol{N})\big) \\ &= \frac{1}{1+2\|\boldsymbol{N}\|^2}(\boldsymbol{N}\cdot\boldsymbol{D} + 2\boldsymbol{D}\cdot\boldsymbol{N}^2) \\ &\neq \boldsymbol{D}\cdot\boldsymbol{N}. \end{aligned} \tag{C.4}$$

Please note that $\mathrm{tr}(\boldsymbol{N}\boldsymbol{D}\boldsymbol{N}) = \boldsymbol{D}\cdot\boldsymbol{N}^2$ holds. The idea now is to introduce a scalar factor A in the following closure term of SQC

$$\mathbb{N}[\boldsymbol{D}] = \frac{A}{1+2\|\boldsymbol{N}\|^2}\big((\boldsymbol{N}\cdot\boldsymbol{D})\boldsymbol{N} + 2\boldsymbol{N}\boldsymbol{D}\boldsymbol{N}\big) \tag{C.5}$$

in such a way that the Folgar-Tucker equation is consistent in the sense of the trace conservation of $\boldsymbol{N}$

$$\frac{A}{1+2\|\boldsymbol{N}\|^2}(\boldsymbol{N}\cdot\boldsymbol{D} + 2\boldsymbol{D}\cdot\boldsymbol{N}^2) \stackrel{!}{=} \boldsymbol{D}\cdot\boldsymbol{N}. \tag{C.6}$$

[1] This section is directly taken from Karl et al. (2021b).

After a quick analysis, the process dependent scalar factor A can be eliminated and reads as follows

$$A = \frac{(1 + 2\|\boldsymbol{N}\|^2)\boldsymbol{N} \cdot \boldsymbol{D}}{\boldsymbol{N} \cdot \boldsymbol{D} + 2\boldsymbol{D} \cdot \boldsymbol{N}^2}. \tag{C.7}$$

By inserting Eq. (C.7) into Eq. (C.5), the sought closure function, which is non-linear in $\boldsymbol{D}$, is as follows

$$\begin{aligned}\mathbb{N}[\boldsymbol{D}] &= \frac{\boldsymbol{N} \cdot \boldsymbol{D}}{\boldsymbol{N} \cdot \boldsymbol{D} + 2\boldsymbol{D} \cdot \boldsymbol{N}^2}\big((\boldsymbol{N} \cdot \boldsymbol{D})\boldsymbol{N} + 2\boldsymbol{N}\boldsymbol{D}\boldsymbol{N}\big) \\ &= \frac{3\boldsymbol{N} \cdot \boldsymbol{D}}{\boldsymbol{N} \cdot \boldsymbol{D} + 2\boldsymbol{D} \cdot \boldsymbol{N}^2}\,\mathrm{sym}(\boldsymbol{N}\otimes\boldsymbol{N})[\boldsymbol{D}] \\ &= \boldsymbol{G}(\boldsymbol{N}, \boldsymbol{D}).\end{aligned} \tag{C.8}$$

It should be noted that the term $1 + 2\|\boldsymbol{N}\|^2$ introduced in Eq. (4.9) cancels out. The definition of κ given in Eq. (4.14) and applied in Eq. (4.15) is based on considering the complete closure term of the Folgar-Tucker equation

$$2\mathbb{N}[\boldsymbol{D}] \approx \kappa\,\mathrm{sym}(\boldsymbol{N}\otimes\boldsymbol{N})[\boldsymbol{D}], \qquad \kappa = \frac{6\boldsymbol{N} \cdot \boldsymbol{D}}{\boldsymbol{N} \cdot \boldsymbol{D} + 2\boldsymbol{D} \cdot \boldsymbol{N}^2}. \tag{C.9}$$

Looking at Eq. (C.9), the isotropic fiber orientation state $\boldsymbol{N}_{\mathsf{ISO}} = \boldsymbol{I}/3$ is critical for incompressible flows since $\mathrm{tr}(\boldsymbol{D}) = \boldsymbol{D} \cdot \boldsymbol{I} = 0$ causes a division by zero. For this case, $\kappa = 0$ is sufficient, resulting in the same strain-rate part of the Folgar-Tucker equation as for the QC which preserves $\mathrm{tr}(\boldsymbol{N}) = 1$. In addition, for flows with a vanishing strain-rate tensor $\boldsymbol{D} = \boldsymbol{0}$, the direction of the strain-rate tensor is not defined and $\kappa = 0$ also applies. During the simulations, non-trivial singularities of the form $\boldsymbol{D} \cdot \boldsymbol{N} \neq 0$ and $\boldsymbol{D} \cdot \boldsymbol{N} + 2\boldsymbol{D} \cdot \boldsymbol{N}^2 = 0$ must be excluded $\forall \boldsymbol{D} \neq \boldsymbol{0}$ and $\forall \boldsymbol{N} \neq \boldsymbol{N}_{\mathsf{ISO}}$. This is part of further research. These singularities do

exist, as the following example shows

$$D_{ij} = \begin{pmatrix} 1 & 0 & 0 \\ 0 & 1 & 0 \\ 0 & 0 & -2 \end{pmatrix}, \qquad N_{ij} = \begin{pmatrix} \frac{51-7\sqrt{33}}{20} & 0 & 0 \\ 0 & \frac{1}{10} & 0 \\ 0 & 0 & \frac{-33+7\sqrt{33}}{20} \end{pmatrix},$$

$$\boldsymbol{D} \cdot \boldsymbol{N} = \frac{119 - 21\sqrt{33}}{20}, \qquad 0 = \boldsymbol{D} \cdot \boldsymbol{N} + 2\boldsymbol{D} \cdot \boldsymbol{N}^2. \tag{C.10}$$

Any non-singular states $0 \approx \boldsymbol{D} \cdot \boldsymbol{N} + 2\boldsymbol{D} \cdot \boldsymbol{N}^2$ and $\boldsymbol{D} \cdot \boldsymbol{N} \neq 0$ must be treated numerically by small time steps to sufficiently resolve the rate $\dot{\boldsymbol{N}}$. Correction schemes used in other studies, e.g., Paschkewitz et al. (2004), Kuzmin (2018), and VerWeyst and Tucker III (2002) can be applied to ensure the necessary algebraic properties of the solution $\boldsymbol{N}$. The special case of 2D fiber orientation states and incompressible suspensions

$$N_{ij} = \begin{pmatrix} N_{11} & N_{12} \\ N_{12} & 1 - N_{11} \end{pmatrix}, \qquad D_{ij} = \begin{pmatrix} D_{11} & D_{12} \\ D_{12} & -D_{11} \end{pmatrix}, \tag{C.11}$$

leads to $\kappa = 2$, since $\boldsymbol{D} \cdot \boldsymbol{N} = \boldsymbol{D} \cdot \boldsymbol{N}^2$ holds. Please note that in this case $\boldsymbol{D} \neq \boldsymbol{0}$ and $\boldsymbol{N} \neq \boldsymbol{N}_{\mathsf{ISO}}$ is required in 2D. Otherwise, $\kappa = 0$ is valid for $\boldsymbol{D} = \boldsymbol{0}$ or $\boldsymbol{N} = \boldsymbol{N}_{\mathsf{ISO}}$ as already described.

Appendix D

Appendix to chapter 5 - Symmetric implicit closures

D.1 One-dimensional formulation of SIHYB [1]

Analogous to the SIQ closure, the SIHYB closure can also be formulated one-dimensionally, which allows the simple application of Newton's method. The closure function $\mathbb{F}(\boldsymbol{B})$ and the corresponding function $\boldsymbol{F}(\boldsymbol{B})$ whose roots $\boldsymbol{B}$ are sought read as follows according to Eqs. (5.32) and (5.33) with $k = 1 - 27\det(\boldsymbol{N})$

$$\begin{aligned}\mathbb{F}(\boldsymbol{B}) &= (1-k)\big(-\frac{3}{35}\operatorname{sym}(\boldsymbol{I}\otimes\boldsymbol{I}) + \frac{6}{7}\operatorname{sym}(\boldsymbol{I}\otimes\boldsymbol{B})\big) + k\operatorname{sym}(\boldsymbol{B}\otimes\boldsymbol{B}),\\ \boldsymbol{F}(\boldsymbol{B}) &= \frac{1-k}{7}\big(\operatorname{tr}(\boldsymbol{B})-1\big)\boldsymbol{I} + \big(1-k+\frac{k}{3}\operatorname{tr}(\boldsymbol{B})\big)\boldsymbol{B} + \frac{2k}{3}\boldsymbol{B}^2 - \boldsymbol{N}.\end{aligned} \tag{D.1}$$

Using the results already discussed in Sec. 5.3.2, the isotropic state ($k = 0$) leads to the linear Eq. (5.34) which has the unique solution $\boldsymbol{B} = \boldsymbol{N} = \boldsymbol{I}/3$. For the UD state ($k = 1$), the SIHYB closure reduces to the SIQ closure whose unique solution $\boldsymbol{B} = \boldsymbol{N} = \boldsymbol{e}_1 \otimes \boldsymbol{e}_1$ follows from the discussion in Sec. 5.2.4.

[1] This section is directly taken from Karl et al. (2023a).

For orientation-dependent parameter values $k \in (0,1)$, the 1D formulation of the SIHYB closure is derived as follows. By using both $s = \mathrm{tr}(\boldsymbol{B})/4$ analogously to SIQ and $\boldsymbol{F}(\boldsymbol{B}) = \boldsymbol{0}$, Eq. (D.1) can be written in the following form with the abbreviations $a(s,k)$ and $b(s,k)$

$$\begin{aligned} \boldsymbol{0} &= \boldsymbol{B}^2 + a\boldsymbol{B} + b\boldsymbol{I} - \frac{3}{2k}\boldsymbol{N}, \\ a &= \frac{3 + (4s-3)k}{2k}, \\ b &= \frac{3(1-k)(4s-1)}{14k}. \end{aligned} \tag{D.2}$$

Completing the square analogously to SIQ results in

$$\boldsymbol{0} = \left(\boldsymbol{B} + \frac{a}{2}\boldsymbol{I}\right)^2 + \left(b - \frac{a^2}{4}\right)\boldsymbol{I} - \frac{3}{2k}\boldsymbol{N}, \tag{D.3}$$

with the solution for the implicit closure tensor of SIHYB

$$\boldsymbol{B} = -\frac{a}{2}\boldsymbol{I} + \sqrt{\frac{3}{2k}\boldsymbol{N} + \left(\frac{a^2}{4} - b\right)\boldsymbol{I}}. \tag{D.4}$$

It should be noted that $\boldsymbol{BN} = \boldsymbol{NB}$ holds based on Eq. (D.2), which means that $\boldsymbol{N}$ and $\boldsymbol{B}$ commute and thus are jointly diagonizable. By computing the trace of both sides of Eq. (D.4), the implicit equation for s is derived

$$4s = -\frac{a}{2}d + \sum_{i=1}^{d}\sqrt{\frac{3\lambda_i}{2k} + \frac{a^2}{4} - b}. \tag{D.5}$$

Please note that a and b depend on s and $d = 2,3$ represents the spatial dimension. The eigenvalues μ_i of $\boldsymbol{B}$ can be computed with the solution s as follows

$$\mu_i = -\frac{a}{2} + \sqrt{\frac{3\lambda_i}{2k} + \frac{a^2}{4} - b}. \tag{D.6}$$

To apply Newton's method in 1D, the following function $f(s)$ is defined

$$f(s) = 4s + \frac{a}{2}d - \sum_{i=1}^{d} \sqrt{\frac{3\lambda_i}{2k} + \frac{a^2}{4} - b}, \tag{D.7}$$

with the corresponding derivative $f'(s)$ for $k \in (0, 1)$

$$f'(s) = 4 + \sum_{i=1}^{d} \left(1 - \frac{9(1-k) + 28sk}{28k\sqrt{\frac{3\lambda_i}{2k} + \frac{a^2}{4} - b}} \right). \tag{D.8}$$

It is shown in the following that the function f is strongly monotone and $f'(s) \geq 4$ holds referring to

$$1 - \frac{9(1-k) + 28sk}{28k\sqrt{\frac{3\lambda_i}{2k} + \frac{a^2}{4} - b}} \geq 0, \tag{D.9}$$

which is equal to the following inequality

$$28k\sqrt{\frac{3\lambda_i}{2k} + \frac{a^2}{4} - b} \geq 9(1-k) + 28sk. \tag{D.10}$$

Squaring both sides and using the definitions of $a(s, k)$ and $b(s, k)$ leads to the following condition which is independent of s

$$g(k) = 192k^2 + (1176\lambda_i - 552)k + 360 \geq 0, \tag{D.11}$$

with $\lambda_i \in [0, 1]$ and $k \in (0, 1)$. The lower bound $k \to 0$ results in $360 \geq 0$, while the upper bound $k \to 1$ results in $1176\lambda_i \geq 0$, $\lambda_i \in [0, 1]$. In general, the roots of the function g read for fixed λ_i

$$k_{1,2} = -\frac{49\lambda_i}{16} + \frac{23}{16} \pm \frac{7}{16}\sqrt{49\lambda_i^2 - 46\lambda_i + 1}. \tag{D.12}$$

The roots $k_{1,2}$ are real numbers only for $49\lambda_i^2 - 46\lambda_i + 1 \geq 0$, which is valid for

$$0 \leq \lambda_i \leq \frac{23}{49} - \frac{4\sqrt{30}}{49} \tag{D.13}$$

and

$$\frac{23}{49} + \frac{4\sqrt{30}}{49} \leq \lambda_i \leq 1. \tag{D.14}$$

For these intervals of λ_i, $k_{1,2} \notin (0, 1)$ holds and Eq. (D.11) is valid. As a consequence, the function f is strongly monotone with $f'(s) \geq 4$. The sought root s of the function f can be computed using Newton's method in 1D and $\boldsymbol{B}$ is obtained via Eq. (D.6) and a back transformation into the spatial coordinate system using the eigenvectors of the second-order fiber orientation tensor $\boldsymbol{N}$.

D.2 Supplementary results [2]

The following Fig. D.2.1 supplements Fig. 5.2 in Sec. 5.4.1 with the evolution of the fiber orientation tensor components N_{22}, N_{33}, and N_{12} for the interaction parameter values $C_\mathrm{I} = 0$ and $C_\mathrm{I} = 0.005$.

As a supplement to the discussion of the oscillatory behavior of the proposed implicit closures SIQ and SIHYB in Sec. 5.4.1, Fig. D.2.2 shows the evolution of the orientation tensor component N_{11} for different reduction parameters κ and for $C_\mathrm{I} = 0.005$ based on the RSC model proposed by Wang et al. (2008). The respective simulation results for the ARD model developed by Phelps and Tucker III (2009) are shown in Fig. D.2.3. Analogous to Sec. 5.4.1, a simple shear flow is considered and the shape parameter $\xi = 1$ ($\alpha \to \infty$) is fixed. For the ARD model, the parameter values given in Phelps and Tucker III (2009) are used.

[2] This section consists of parts from the supplementary material of Karl et al. (2023a) published online at `https://doi.org/10.1016/j.jnnfm.2023.105049`, retrieved on August 26, 2024. Additional text passages have been added.

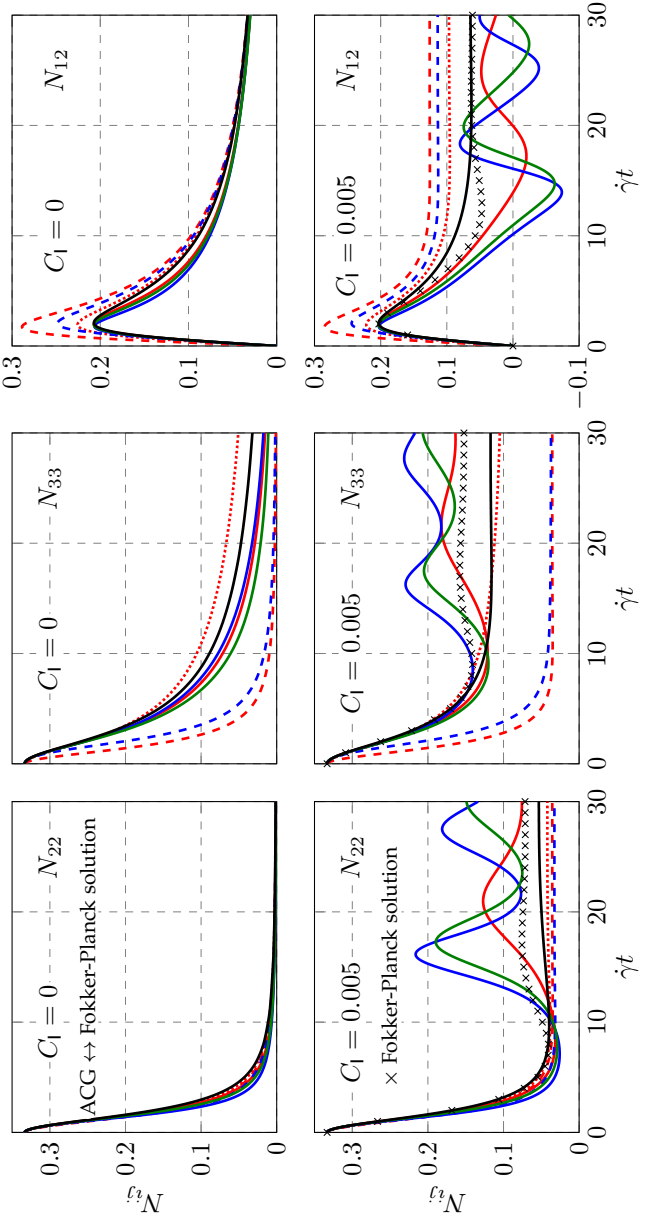

Figure D.2.1: Evolution of the orientation tensor components N_{22}, N_{33}, and N_{12} plotted over the total shear $\dot{\gamma}t$ for two different values of the parameter C_I with respect to different closures in a simple shear flow, adapted from the supplementary material of Karl et al. (2023a) published online at `https://doi.org/10.1016/j.jnnfm.2023.105049`, retrieved on August 26, 2024.

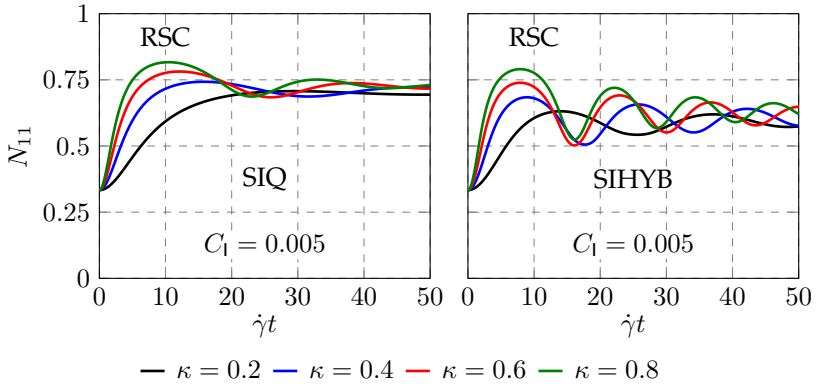

Figure D.2.2: Evolution of the orientation tensor component N_{11} plotted over the total shear $\dot{\gamma}t$ based on the RSC model for different reduction parameters κ with respect to SIQ and SIHYB in a simple shear flow.

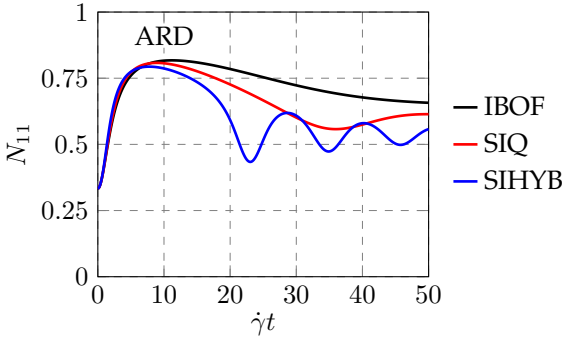

Figure D.2.3: Evolution of the orientation tensor component N_{11} plotted over the total shear $\dot{\gamma}t$ based on the ARD model with respect to SIQ, SIHYB, and IBOF in a simple shear flow.

Appendix E

Appendix to chapter 6 - Orientation dynamics

E.1 Supplement to the generalized orientation evolution [1]

Using Eq. (6.2) as a starting point, the derivation of Eq. (6.3) representing the generalized evolution equation for the orientation tensor $\mathbb{N}_{\langle n \rangle}$ of arbitrary even order n is given in the following. The derivation is methodically based on Böhlke (2006). Equation (6.2) can be reformulated with respect to the reference ODF by using the reorientation gradient $\boldsymbol{F}_{\mathcal{S}} \in \mathrm{Inv}^{+}$ on the unit sphere similar to the polycrystals-considering works of Kumar and Dawson (1996) and Böhlke (2006)

$$\boldsymbol{F}_{\mathcal{S}} = \frac{\partial \boldsymbol{n}}{\partial \boldsymbol{n}_0} = \frac{\partial \boldsymbol{\chi}_{\mathcal{S}}(\boldsymbol{n}_0, t)}{\partial \boldsymbol{n}_0}. \tag{E.1}$$

In Eq. (E.1), the function $\boldsymbol{\chi}_{\mathcal{S}}$ maps the reference orientation $\boldsymbol{n}_0$ to the actual orientation $\boldsymbol{n}$ via $\boldsymbol{n} = \boldsymbol{\chi}_{\mathcal{S}}(\boldsymbol{n}_0, t)$. The relation between $f(\boldsymbol{n}, t)$ and the reference distribution $f_0(\boldsymbol{n}_0)$

$$f(\boldsymbol{n}, t) = J_{\mathcal{S}}^{-1} f_0(\boldsymbol{n}_0) \tag{E.2}$$

[1] This section consists of parts from Karl and Böhlke (2024). Additional text passages have been added.

is implied by Eq. (2.40) based on the transformation rule of surface elements on the unit sphere reading $\mathrm{d}S(\boldsymbol{n}) = J_{\mathcal{S}}\mathrm{d}S_0(\boldsymbol{n})$ with the so-called Jacobian determinant $J_{\mathcal{S}}$ of the reorientation (Kumar and Dawson, 1996). As a consequence, Eq. (6.2) reads in the reference orientation

$$\begin{aligned}\frac{\mathrm{d}}{\mathrm{d}t}\langle \boldsymbol{A}\rangle_{\mathsf{F}} &= \frac{\mathrm{d}}{\mathrm{d}t}\int_{\mathcal{S}} J_{\mathcal{S}}^{-1} f_0(\boldsymbol{n}_0)\boldsymbol{A}(\boldsymbol{n}) J_{\mathcal{S}}\,\mathrm{d}S_0(\boldsymbol{n}) \\ &= \frac{\mathrm{d}}{\mathrm{d}t}\int_{\mathcal{S}} f_0(\boldsymbol{n}_0)\boldsymbol{A}(\boldsymbol{\chi}_{\mathcal{S}}(\boldsymbol{n}_0,t))\,\mathrm{d}S_0(\boldsymbol{n}).\end{aligned} \tag{E.3}$$

The time derivative is straightforward to compute by using the chain rule based on $\boldsymbol{A}(\boldsymbol{n}) = \boldsymbol{A}(\boldsymbol{\chi}_{\mathcal{S}}(\boldsymbol{n}_0,t))$

$$\frac{\mathrm{d}}{\mathrm{d}t}\langle \boldsymbol{A}\rangle_{\mathsf{F}} = \int_{\mathcal{S}} f_0(\boldsymbol{n}_0)\frac{\partial \boldsymbol{A}}{\partial \boldsymbol{\chi}_{\mathcal{S}}}\frac{\partial \boldsymbol{\chi}_{\mathcal{S}}}{\partial t}\,\mathrm{d}S_0(\boldsymbol{n}). \tag{E.4}$$

The transformation of Eq. (E.4) into the actual orientation leads to the desired formulation

$$\begin{aligned}\frac{\mathrm{d}}{\mathrm{d}t}\langle \boldsymbol{A}\rangle_{\mathsf{F}} &= \int_{\mathcal{S}} J_{\mathcal{S}} f(\boldsymbol{n},t)\frac{\partial \boldsymbol{A}}{\partial \boldsymbol{n}}\dot{\boldsymbol{n}}\,\mathrm{d}S_0(\boldsymbol{n}) \\ &= \int_{\mathcal{S}} f(\boldsymbol{n},t)\frac{\partial \boldsymbol{A}}{\partial \boldsymbol{n}}\dot{\boldsymbol{n}}\,\mathrm{d}S(\boldsymbol{n}) \\ &= \int_{\mathcal{S}} f(\boldsymbol{n},t)\dot{\boldsymbol{A}}(\boldsymbol{n})\,\mathrm{d}S(\boldsymbol{n}).\end{aligned} \tag{E.5}$$

With Eq. (E.5) at hand, the generalized evolution equation for the orientation tensor $\mathbb{N}_{\langle n\rangle}$ of arbitrary even order n is derived by substituting the tensor $\boldsymbol{A}$ in Eq. (E.5) with $\boldsymbol{n}^{\otimes n}$ leading to

$$\dot{\mathbb{N}}_{\langle n\rangle} = \int_{\mathcal{S}} f(\boldsymbol{n},t)(\boldsymbol{n}^{\otimes n})^{\cdot}\,\mathrm{d}S(\boldsymbol{n}). \tag{E.6}$$

E.2 Supplement to the Jeffery equation [2]

As a supplement to Sec. 6.1.2 it is formally shown in the following under the assumptions made, that the Jeffery equation (6.28) follows from the general spin localization (6.21). Methodically, the equivalence of the formulation (6.25) with the result (6.26) of Wetzel (1999) (pp. 48–49, 269, 318–321) and Wetzel and Tucker III (2001) is proven. The Jeffery tensor $\mathbb{J}_F$ is called vorticity concentration tensor in the underlying studies (Wetzel, 1999; Wetzel and Tucker III, 2001) and reads

$$\mathbb{J}_F = \Big(1 - \frac{\mu_F}{\mu_M}\Big)\mathbb{E}^A\Big(\mathbb{I}^S - \big(1 - \frac{\mu_F}{\mu_M}\big)\mathbb{E}^S\Big)^{-1}, \tag{E.7}$$

with the so-called alternative Eshelby tensor $\mathbb{E}^A$ and the common Eshelby tensor $\mathbb{E}^S$. Lebensohn and Tomé (1993) call $\mathbb{E}^A$ the Eshelby rotation tensor. The shear viscosities of the matrix and the fibers refer to μ_M and μ_F. A simple modification of Eq. (E.7) leads to the following equivalent representation

$$\mathbb{J}_F = -\mathbb{E}^A\frac{1}{2\mu_M}(2\mu_F - 2\mu_M)\big(\mathbb{I}^S + \mathbb{E}^S\frac{1}{2\mu_M}(2\mu_F - 2\mu_M)\big)^{-1}. \tag{E.8}$$

For the special case of incompressibility, the representation $\mathbb{V}_M = 2\mu_M\mathbb{P}_2$ and $\mathbb{V}_F = 2\mu_F\mathbb{P}_2$ in Eq. (E.8) can be used leading to

$$\mathbb{J}_F = -\mathbb{E}^A\mathbb{V}_M^{-1}(\mathbb{V}_F - \mathbb{V}_M)\big(\mathbb{I}^S + \mathbb{E}^S\mathbb{V}_M^{-1}(\mathbb{V}_F - \mathbb{V}_M)\big)^{-1}. \tag{E.9}$$

With the abbreviation $\delta\mathbb{V} = \mathbb{V}_F - \mathbb{V}_M$ and the expression for the polarization tensors $\mathbb{P}_0^{A,S} = \mathbb{E}^{A,S}\mathbb{V}_M^{-1}$ given in, e.g., Walpole (1981) (p. 196), the

[2] This section consists of parts from Karl and Böhlke (2024). Additional text passages have been added.

Jeffery tensor $\mathbb{J}_{\mathsf{F}}$, used in this thesis as an abbreviation, reads as follows

$$\begin{aligned}\mathbb{J}_{\mathsf{F}} &= -\mathbb{P}_0^{\mathsf{A}}\delta\mathbb{V}\big(\mathbb{I}^{\mathsf{S}} + \mathbb{P}_0^{\mathsf{S}}\delta\mathbb{V}\big)^{-1} \\ &= -\mathbb{P}_0^{\mathsf{A}}\big(\delta\mathbb{V}^{-1} + \mathbb{P}_0^{\mathsf{S}}\big)^{-1},\end{aligned} \tag{E.10}$$

which can be further simplified based on the rigid fiber assumption (vanishing fluidity $\delta\mathbb{V}^{-1}$), as addressed in Sec. 2.6, leading to the sought equivalence

$$\mathbb{J}_{\mathsf{F}} = -\mathbb{P}_0^{\mathsf{A}}\big(\mathbb{P}_0^{\mathsf{S}}\big)^{-1}. \tag{E.11}$$

In the context of the model proposed by Ponte Castañeda and Willis (1995), it is discussed in Sec. 6.1.5 that the notation of the spin localization based on the polarization tensors $\mathbb{P}_0^{\mathsf{A}}$ and $\mathbb{P}_0^{\mathsf{S}}$ for rigid inclusions of one single geometry can also be found, e.g., in Kailasam and Ponte Castañeda (1998) and Ponte Castañeda (2021). Equation (E.11) now serves to use $\mathbb{J}_{\mathsf{F}}$ based on Wetzel and Tucker III (2001) given in Eq. (6.27) and, combined with the orientation averaging procedure described by Advani and Tucker III (1987), to formulate the evolution equation for the fiber orientation tensor of arbitrary order for various mean-field models. By using $\mathbb{J}_{\mathsf{F}}$ instead of the polarization tensors $\mathbb{P}_0^{\mathsf{A}}$ and $\mathbb{P}_0^{\mathsf{S}}$, the algebraic structure of the evolution equation for the fiber orientation tensor can be further specified.

E.3 Laplacian on the unit sphere [3]

As a supplement to the derivation of the generalized fiber interaction term (6.34) involving the computation of the Laplacian on the unit sphere $\Delta_{\mathcal{S}}(\boldsymbol{n}^{\otimes n})$ based on Eq. (6.33), the special case of $n = 2$ is considered in the following. Regarding the rules of calculus, reference is made to,

[3] This section consists of parts from Karl and Böhlke (2024). Additional text passages have been added.

e.g., Sillem (2010) (pp. 17–21). In index notation, the Laplacian for $n = 2$ reads

$$\begin{aligned}\big(\Delta_{\mathcal{S}}(\boldsymbol{n}\otimes\boldsymbol{n})\big)_{ij} &= \frac{\partial^2 n_i n_j}{\partial n_k \partial n_k} = \frac{\partial}{\partial n_k}\left(\frac{\partial n_i n_j}{\partial n_k}\right) = \frac{\partial}{\partial n_k}\left(\frac{\partial n_i}{\partial n_k} n_j + n_i \frac{\partial n_j}{\partial n_k}\right) \\ &= \frac{\partial}{\partial n_k}\big((\delta_{ik} - n_i n_k) n_j + n_i(\delta_{jk} - n_j n_k)\big) \\ &= \frac{\partial}{\partial n_k}(\delta_{ik} n_j + n_i \delta_{jk} - 2 n_i n_j n_k). \end{aligned} \tag{E.12}$$

If the same procedure is applied again and taking $\delta_{kk} = 3$ and $n_k n_k = 1$ into account, this leads to

$$\begin{aligned}\big(\Delta_{\mathcal{S}}(\boldsymbol{n}\otimes\boldsymbol{n})\big)_{ij} &= 2(\delta_{ij} - 3 n_i n_j), \\ \Delta_{\mathcal{S}}(\boldsymbol{n}\otimes\boldsymbol{n}) &= 2(\boldsymbol{I} - 3\boldsymbol{n}\otimes\boldsymbol{n}), \end{aligned} \tag{E.13}$$

based on Sillem (2010) (p. 19). If this term is integrated over the unit sphere as described by, e.g., Férec et al. (2017b), the well-known second-order fiber interaction term (Folgar and Tucker III, 1984; Advani and Tucker III, 1987) follows, taking into account the properties of the ODF f and the definition of the second-order fiber orientation tensor $\boldsymbol{N}$

$$\mathbb{D}_{\langle 2\rangle} = 2C_{\mathrm{I}}\dot{\gamma} \int_{\mathcal{S}} f(\boldsymbol{n})(\boldsymbol{I} - 3\boldsymbol{n}\otimes\boldsymbol{n}) \,\mathrm{d}S = 2C_{\mathrm{I}}\dot{\gamma}(\boldsymbol{I} - 3\boldsymbol{N}). \tag{E.14}$$

The fourth-order interaction term $\mathbb{D}_{\langle 4\rangle}$ can be found in, e.g., Advani and Tucker III (1987) and Jack and Smith (2005; 2006). The algebraic structure of the general expression (6.34) becomes clear in the analytical computation up to sixth-order interaction tensor $\mathbb{D}_{\langle 6\rangle}$ based on the fiber-fiber interaction model proposed by Folgar and Tucker III (1984).

E.4 Polarization tensors [4]

General definition. In contrast to the JE, DD, and MT models discussed in Secs. 6.1.2 to 6.1.4, the polarization tensors $\mathbb{P}_0^{\mathsf{A},\mathsf{S}}(\boldsymbol{n})$ must be computed explicitly for the PCW and EM models. In general, the polarization tensors for a spheroidal inclusion aligned with direction $\boldsymbol{n}$ are defined as follows referring to, e.g., Willis (1977; 1981)

$$\mathbb{P}_0^{\mathsf{A},\mathsf{S}} = \frac{1}{4\pi \det(\boldsymbol{Z}(\boldsymbol{n}))} \int_{\mathsf{S}} \frac{\mathbb{H}^{\mathsf{A},\mathsf{S}}(\mathbb{V}, \boldsymbol{p})}{\|\boldsymbol{Z}^{-1}(\boldsymbol{n})\boldsymbol{p}\|^3} \, \mathrm{d}S(\boldsymbol{p}), \tag{E.15}$$

with the abbreviations

$$\mathbb{H}^{\mathsf{A},\mathsf{S}} = \mathbb{I}^{\mathsf{A},\mathsf{S}}\big(\boldsymbol{K}^{-1} \square (\boldsymbol{p} \otimes \boldsymbol{p})\big)\mathbb{I}^{\mathsf{S}}, \qquad K_{ij} = V_{ikjl}\, p_k\, p_l \tag{E.16}$$

and the reformulation used by, e.g., Ponte Castañeda and Willis (1995)

$$\big(\boldsymbol{p} \cdot (\boldsymbol{Z}^{-\mathsf{T}} \boldsymbol{Z}^{-1} \boldsymbol{p})\big)^{\frac{3}{2}} = \big((\boldsymbol{Z}^{-1}\boldsymbol{p}) \cdot (\boldsymbol{Z}^{-1}\boldsymbol{p})\big)^{\frac{3}{2}} = \|\boldsymbol{Z}^{-1}\boldsymbol{p}\|^3. \tag{E.17}$$

The integration variable in Eq. (E.15) is represented by $\boldsymbol{p}$ to avoid confusion with the spheroidal inclusion direction $\boldsymbol{n}$ and the shape of the inclusion is represented by the shape tensor $\boldsymbol{Z}$. In general, the viscosity tensor of the matrix $\mathbb{V}$ can be arbitrarily anisotropic. As described by, e.g., Ponte Castañeda (2021), the tensor $\boldsymbol{Z}$ can be formulated in terms of the aspect ratios of an ellipsoidal inclusion with respect to its eigensystem. This eigensystem can be replaced by considering a reference shape tensor $\boldsymbol{Z}_0$ with the largest aspect ratio pointing in the fixed direction $\boldsymbol{n} = \boldsymbol{e}_1$. Since the present thesis uses the inverted definition of $\boldsymbol{Z}$ compared to Ponte Castañeda (2021), this reference shape tensor reads $\boldsymbol{Z}_0 = \alpha^{-1}\boldsymbol{e}_1 \otimes \boldsymbol{e}_1 + \boldsymbol{e}_2 \otimes \boldsymbol{e}_2 + \boldsymbol{e}_3 \otimes \boldsymbol{e}_3$ depending on

[4] This section consists of parts from Karl and Böhlke (2024). Additional text passages have been added.

one single aspect ratio α for the special case of spheroidal fibers. For an arbitrary direction $\boldsymbol{n}$, the components $Z_{ij}(\boldsymbol{n})$ must be computed via $Z_{ij}(\boldsymbol{n}) = Q_{ik}(\boldsymbol{n}) Z^0_{kl} Q^{\mathsf{T}}_{lj}(\boldsymbol{n})$. The computation of $Q_{ij}(\boldsymbol{n})$ is based on the angles $\vartheta \in [0, \pi]$ and $\varphi \in [0, 2\pi)$ of the spherical coordinate system which can be computed with the known direction $\boldsymbol{n}$ from geometric considerations. The components $Q_{ij}(\boldsymbol{n})$ are computed as follows

$$Q_{ij} = \begin{pmatrix} \sin(\vartheta)\cos(\varphi) & \cos(\vartheta)\cos(\varphi) & -\sin(\varphi) \\ \sin(\vartheta)\sin(\varphi) & \cos(\vartheta)\sin(\varphi) & \cos(\varphi) \\ \cos(\vartheta) & -\sin(\vartheta) & 0 \end{pmatrix}. \tag{E.18}$$

The columns refer to the basis vectors of the spherical coordinate system $\{\boldsymbol{e}_r, \boldsymbol{e}_\vartheta, \boldsymbol{e}_\varphi\}$, which are used in the transformation rule for quadratic matrices as given in, e.g., Arens et al. (2015) (pp. 628, 966–970).

Efficient computation for the PCW model. For the special case of an isotropic and incompressible matrix fluid, the symmetric reference polarization tensor $\mathbb{P}^{\mathsf{S}}_0(\boldsymbol{e}_1)$ can be computed as follows (Ponte Castañeda and Willis, 1995) in normalized Voigt or Mandel notation

$$\mathbb{P}^{\mathsf{S}}_0(\boldsymbol{e}_1)_{ijkl} = \begin{pmatrix} P_1 & P_2 & P_2 & 0 & 0 & 0 \\ P_2 & P_3 + P_4 & P_3 - P_4 & 0 & 0 & 0 \\ P_2 & P_3 - P_4 & P_3 + P_4 & 0 & 0 & 0 \\ 0 & 0 & 0 & 2P_4 & 0 & 0 \\ 0 & 0 & 0 & 0 & 2P_5 & 0 \\ 0 & 0 & 0 & 0 & 0 & 2P_5 \end{pmatrix}, \tag{E.19}$$

see Sec. 4.1, with the components simplified for incompressibility following Karl and Böhlke (2022)

$$P_1 = \frac{h(\alpha) - 2\alpha^2 + 2\alpha^2 h(\alpha)}{2(1-\alpha^2)\mu}, \qquad P_2 = \frac{2\alpha^2 - h(\alpha) - 2\alpha^2 h(\alpha)}{4(1-\alpha^2)\mu},$$
$$P_3 = \frac{h(\alpha) - 2\alpha^2 + 2\alpha^2 h(\alpha)}{8(1-\alpha^2)\mu}, \qquad P_4 = \frac{3h(\alpha) - 2\alpha^2}{16(1-\alpha^2)\mu},$$

$$P_5 = \frac{2 - 3h(\alpha) + 2\alpha^2 - 3\alpha^2 h(\alpha)}{8(1-\alpha^2)\mu}, \quad h(\alpha) = \frac{\alpha\big(\alpha\sqrt{\alpha^2-1} - \operatorname{arcosh}(\alpha)\big)}{(\alpha^2-1)^{3/2}}. \tag{E.20}$$

For geometrically generalized expressions for this special case, please refer to Avazmohammadi and Ponte Castañeda (2015). Instead of integrating Eq. (E.15), $\mathbb{P}_0^{\mathsf{S}}(\boldsymbol{e}_1)$ can be simply computed and the transformation rule given in Kuzmin (2018) (p. 3047) formulated in Voigt notation can be used, see, e.g., Voigt (1910) (pp. 584–587) and Cowin (1989), leading to the sought rotated polarization tensor $\mathbb{P}_0^{\mathsf{S}}(\boldsymbol{n})$. It should be noted that the rotation matrix Q_{ij} of Kuzmin (2018) refers to Q_{ij}^{T} given in Eq. (E.18). Next, the Jeffery tensor $\mathbb{J}_{\mathsf{F}}(\boldsymbol{n})$ depending on the direction $\boldsymbol{n}$ can be computed as given in Eq. (6.27). By using the shown equivalence (E.11), the sought rotated polarization tensor $\mathbb{P}_0^{\mathsf{A}}(\boldsymbol{n})$ is computed via

$$\mathbb{P}_0^{\mathsf{A}}(\boldsymbol{n}) = -\mathbb{J}_{\mathsf{F}}(\boldsymbol{n})\mathbb{P}_0^{\mathsf{S}}(\boldsymbol{n}). \tag{E.21}$$

To conclude, it should be noted that the described procedure refers to the assumption that both the inclusions (i) and the distribution (d) are modeled as spheroids with the aspect ratios α_{i} and α_{d}, respectively.

E.5 Supplementary results [5]

Figure E.5.1 shows the evolution of the orientation tensor components N_{22}, N_{33}, and N_{12} for the considered mean-field models and fiber volume fractions as a supplement to Fig. 6.2 in Sec. 6.2.3. Figure E.5.2 shows the orientation evolution of a single fiber on the unit sphere for different fiber volume fractions of the surrounding fiber suspension as a supplement to Fig. 6.3 in Sec. 6.2.3.

[5] This section consists of parts from Karl and Böhlke (2024). Additional text passages have been added.

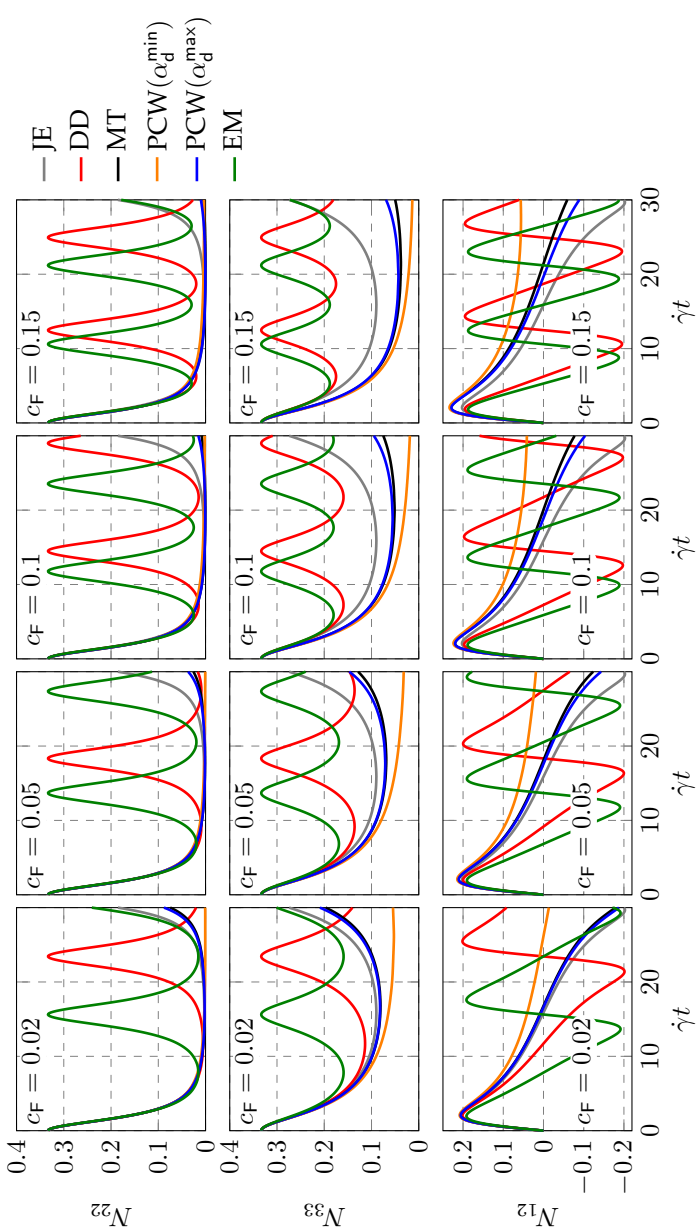

Figure E.5.1: For DD, MT, PCW, and EM, the evolution of the orientation tensor components N_{22}, N_{33}, and N_{12} in a simple shear flow is plotted over the total shear $\dot{\gamma}t$. Each line refers to the respective orientation tensor component. The results of the Jeffery equation (JE) are given for comparison. The different fiber volume fractions refer to the respective column, adapted from Karl and Böhlke (2024).

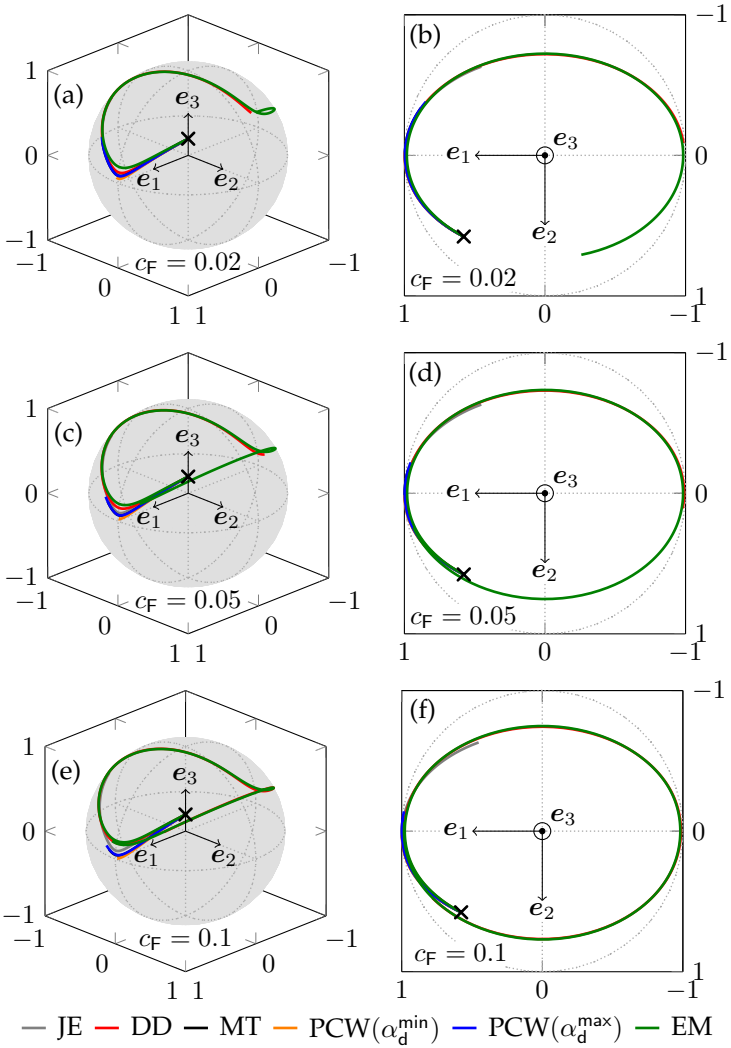

Figure E.5.2: For different fiber volume fractions, the orientation behavior of a single fiber is shown in a simple shear flow for DD, MT, PCW, and EM. The Jeffery model (JE) is considered as a reference. The initial fiber orientation is marked with $\times$. In (a), (c), (e), the orientation path of the single fiber is plotted on the unit sphere. The respective projection on the e_1–e_2-plane is shown in (b), (d), (f), adapted from Karl and Böhlke (2024).

As a supplement to the discussion of DD in Sec. 6.2.3, Fig. E.5.3 shows the evolution of the orientation tensor component N_{11} for JE, DD, and MT with respect to the fiber volume fractions $c_\mathsf{F} = 10^{-3}$ and $c_\mathsf{F} = 5 \cdot 10^{-3}$. The deviation between DD and MT is already evident for $c_\mathsf{F} = 5 \cdot 10^{-3}$, while Jeffery's model (JE) is shown as a comparison that predicts the orientation evolution independent of the fiber volume fraction.

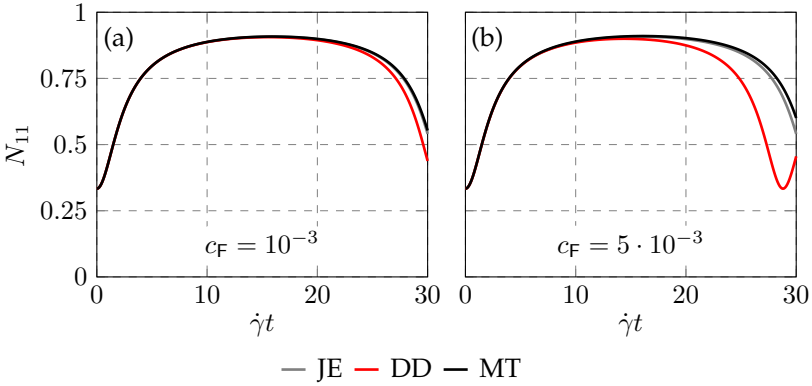

Figure E.5.3: For the models JE, DD, and MT, the evolution of the orientation tensor components N_{11} in a simple shear flow is plotted over the total shear $\dot{\gamma}t$ for the fiber volume fraction $c_\mathsf{F} = 10^{-3}$ in (a) and for $c_\mathsf{F} = 5 \cdot 10^{-3}$ in (b).

Bibliography

Aboutajeddine, A., Neale, K. W., 2005. The double-inclusion model: A new formulation and new estimates. Mechanics of Materials 37 (2–3), 331–341.

Abtahi, S. A., Elfring, G. J., 2019. Jeffery orbits in shear-thinning fluids. Physics of Fluids 31 (10), Article 103106.

Adams, B. L., Field, D. P., 1991. A statistical theory of creep in polycrystalline materials. Acta Metallurgica et Materialia 39 (10), 2405–2417.

Advani, S. G., Tucker III, C. L., 1987. The use of tensors to describe and predict fiber orientation in short fiber composites. Journal of Rheology 31 (8), 751–784.

Advani, S. G., Tucker III, C. L., 1990. Closure approximations for three-dimensional structure tensors. Journal of Rheology 34 (3), 367–386.

Akbar, S., Altan, M. C., 1992. On the solution of fiber orientation in two-dimensional homogeneous flows. Polymer Engineering & Science 32 (12), 810–822.

Al-Qudsi, A., Çelik, H., Neuhaus, J., Hopmann, C., 2022. A comparative study between fiber orientation closure approximations and a new orthotropic closure. Polymer Composites 43 (11), 7669–7700.

Altan, M. C., Güçeri, S. I., Pipes, R. B., 1992. Anisotropic channel flow of fiber suspensions. Journal of Non-Newtonian Fluid Mechanics 42 (1–2), 65–83.

Altan, M. C., Subbiah, S., Güçeri, S. I., Pipes, R. B., 1990. Numerical prediction of three-dimensional fiber orientation in Hele-Shaw flows. Polymer Engineering & Science 30 (14), 848–859.

Altan, M. C., Tang, L., 1993. Orientation tensors in simple flows of dilute suspensions of non-Brownian rigid ellipsoids, comparison of analytical and approximate solutions. Rheologica Acta 32 (3), 227–244.

Ansys Granta EduPack®, 2022. Datasheet for PP-GF40. Retrieved on July 12, 2022. https://www.ansys.com/de-de/products/materials/granta-edupack.

Arens, T., Hettlich, F., Karpfinger, C., Kockelkorn, U., Lichtenegger, K., Stachel, H., 2015. Mathematik, 3rd Edition. Springer Spektrum, Berlin, Heidelberg.

Ashby, M. F., 2006. Materials Selection in Mechanical Design: Das Original mit Übersetzungshilfen, 3rd Edition. Springer Spektrum, Berlin, Heidelberg, 1. Auflage der deutschen Easy-Reading-Ausgabe.

Atkinson, K., 1982. Numerical integration on the sphere. The Journal of the Australian Mathematical Society. Series B. Applied Mathematics 23 (3), 332–347.

Avazmohammadi, R., Ponte Castañeda, P., 2015. The rheology of non-dilute dispersions of highly deformable viscoelastic particles in Newtonian fluids. Journal of Fluid Mechanics 763, 386–432.

Batchelor, G. K., 1970. The stress system in a suspension of force-free particles. Journal of Fluid Mechanics 41 (3), 545–570.

Batchelor, G. K., 1971. The stress generated in a non-dilute suspension of elongated particles by pure straining motion. Journal of Fluid Mechanics 46 (4), 813–829.

Bauer, J. K., Böhlke, T., 2022a. On the dependence of orientation averaging mean field homogenization on planar fourth-order fiber orientation tensors. Mechanics of Materials 170, Article 104307.

Bauer, J. K., Böhlke, T., 2022b. Variety of fiber orientation tensors. Mathematics and Mechanics of Solids 27 (7), 1185–1211.

Bauer, J. K., Böhlke, T., 2023. Fiber orientation distributions based on planar fiber orientation tensors of fourth order. Mathematics and Mechanics of Solids 28 (3), 773–794.

Bauer, J. K., Schneider, M., Böhlke, T., 2023. On the phase space of fourth-order fiber-orientation tensors. Journal of Elasticity 153 (2), 161–184.

Bažant, Z. P., Oh, B. H., 1986. Efficient numerical integration on the surface of a sphere. Zeitschrift für Angewandte Mathematik und Mechanik 66 (1), 37–49.

Bay, R. S., 1991. Fiber Orientation in Injection Molded Composites: A Comparison of Theory and Experiment. PhD thesis, University of Illinois at Urbana-Champaign.

Benveniste, Y., 1987. A new approach to the application of Mori-Tanaka's theory in composite materials. Mechanics of Materials 6 (2), 147–157.

Benveniste, Y., Dvorak, G. J., Chen, T., 1991. On diagonal and elastic symmetry of the approximate effective stiffness tensor of heterogeneous media. Journal of the Mechanics and Physics of Solids 39 (7), 927–946.

Bertóti, R., Böhlke, T., 2017. Flow-induced anisotropic viscosity in short FRPs. Mechanics of Advanced Materials and Modern Processes 3 (1), Article 1.

Bertóti, R., 2021. Modeling the Flow-Induced Anisotropic Effective Viscosity of Fiber Suspensions by Mean-Field and Full-Field Homogenization. Doctoral thesis, Karlsruher Institut für Technologie (KIT).

Bertóti, R., Wicht, D., Hrymak, A., Schneider, M., Böhlke, T., 2021. A computational investigation of the effective viscosity of short-fiber reinforced thermoplastics by an FFT-based method. European Journal of Mechanics - B/Fluids 90, 99–113.

Bilby, B. A., Eshelby, J. D., Kundu, A. K., 1975. The change of shape of a viscous ellipsoidal region embedded in a slowly deforming matrix having a different viscosity. Tectonophysics 28 (4), 265–274.

Bilby, B. A., Kolbuszewski, M. L., 1977. The finite deformation of an inhomogeneity in two-dimensional slow viscous incompressible flow. Proceedings of the Royal Society of London. Series A. Mathematical and Physical Sciences 355 (1682), 335–353.

Bingham, C., 1974. An antipodally symmetric distribution on the sphere. The Annals of Statistics 2 (6), 1201–1225.

Bird, R. B., Curtiss, C. F., Armstrong, R. C., Hassager, O., 1987. Dynamics of Polymeric Liquids: Volume 2 - Kinetic Theory, 2nd Edition. Wiley, New York [a.o.].

Böhlke, T., 2006. Texture simulation based on tensorial Fourier coefficients. Computers & Structures 84 (17–18), 1086–1094.

Böhlke, T., Brüggemann, C., 2001. Graphical representation of the generalized Hooke's law. Technische Mechanik 21 (2), 145–158.

Böhlke, T., Henning, F., Hrymak, A., Kärger, L., Weidenmann, K., Wood, J. T., 2019. Continuous-Discontinuous Fiber-Reinforced Polymers: An Integrated Engineering Approach. Hanser, München.

Böhlke, T., Jöchen, K., Piat, R., Langhoff, T.-A., Tsukrov, I., Reznik, B., 2010. Elastic properties of pyrolytic carbon with axisymmetric textures. Technische Mechanik 30 (4), 343–353.

Borzacchiello, D., Abisset-Chavanne, E., Chinesta, F., Keunings, R., 2016. Orientation kinematics of short fibres in a second-order viscoelastic fluid. Rheologica Acta 55 (5), 397–409.

Borzenko, E. I., Shrager, G. R., 2015. Effect of the type of boundary conditions on the three-phase contact line on the flow characteristics during filling of the channel. Journal of Applied Mechanics and Technical Physics 56 (2), 167–176.

Boucher, S., 1976. Modules effectifs de matériaux composites quasi homogènes et quasi isotropes, constitués d'une matrice élastique et d'inclusions élastiques. II. Cas des concentrations finies en inclusions. Revue M 22 (1), 31–36.

Brackbill, J. U., Kothe, D. B., Zemach, C., 1992. A continuum method for modeling surface tension. Journal of Computational Physics 100 (2), 335–354.

Bretherton, F. P., 1962. The motion of rigid particles in a shear flow at low Reynolds number. Journal of Fluid Mechanics 14 (2), 284–304.

Breuer, K., Stommel, M., Korte, W., 2019. Analysis and evaluation of fiber orientation reconstruction methods. Journal of Composites Science 3 (3), Article 67.

Brunn, P., 1977. The slow motion of a rigid particle in a second-order fluid. Journal of Fluid Mechanics 82 (3), 529–547.

Brylka, B., 2017. Charakterisierung und Modellierung der Steifigkeit von langfaserverstärktem Polypropylen. Doctoral thesis, Schriftenreihe Kontinuumsmechanik im Maschinenbau Band 10, Karlsruher Institut für Technologie (KIT).

Buck, F., Brylka, B., Müller, V., Müller, T., Weidenmann, K. A., Hrymak, A. N., Henning, F., Böhlke, T., 2015. Two-scale structural mechanical modeling of long fiber reinforced thermoplastics. Composites Science and Technology 117, 159–167.

Budiansky, B., 1965. On the elastic moduli of some heterogeneous materials. Journal of the Mechanics and Physics of Solids 13 (4), 223–227.

Carlson, B. C., 1995. Numerical computation of real or complex elliptic integrals. Numerical Algorithms 10 (1), 13–26.

Carlson, B. C., Notis, E. M., 1981. Algorithm 577 - Algorithms for incomplete elliptic integrals [S21]. ACM Transactions on Mathematical Software 7 (3), 398–403.

Chang, R.-Y., Yang, W.-H., 2001. Numerical simulation of mold filling in injection molding using a three-dimensional finite volume approach. International Journal for Numerical Methods in Fluids 37 (2), 125–148.

Chaubal, C. V., Leal, L. G., 1998. A closure approximation for liquid-crystalline polymer models based on parametric density estimation. Journal of Rheology 42 (1), 177–201.

Chawla, K. K., 2019. Composite Materials: Science and Engineering, 4th Edition. Springer, Cham.

Chen, H., Wapperom, P., Baird, D. G., 2019a. A model incorporating the effects of flow type on fiber orientation for flows with mixed flow kinematics. Journal of Rheology 63 (3), 455–464.

Chen, H., Wapperom, P., Baird, D. G., 2019b. The use of flow type dependent strain reduction factor to improve fiber orientation predictions for an injection molded center-gated disk. Physics of Fluids 31 (12), Article 123105.

Christensen, R. M., 1993. Effective viscous flow properties for fiber suspensions under concentrated conditions. Journal of Rheology 37 (1), 103–121.

Chung, D. H., Kwon, T. H., 2001. Improved model of orthotropic closure approximation for flow induced fiber orientation. Polymer Composites 22 (5), 636–649.

Chung, D. H., Kwon, T. H., 2002a. Fiber orientation in the processing of polymer composites. Korea-Australia Rheology Journal 14 (4), 175–188.

Chung, D. H., Kwon, T. H., 2002b. Invariant-based optimal fitting closure approximation for the numerical prediction of flow-induced fiber orientation. Journal of Rheology 46 (1), 169–194.

Chung, D. H., Kwon, T. H., 2002c. Numerical studies of fiber suspensions in an axisymmetric radial diverging flow: The effects of modeling and numerical assumptions. Journal of Non-Newtonian Fluid Mechanics 107 (1–3), 67–96.

Cintra, J. S., Tucker III, C. L., 1995. Orthotropic closure approximations for flow-induced fiber orientation. Journal of Rheology 39 (6), 1095–1122.

Coleman, B. D., Noll, W., 1963. The thermodynamics of elastic materials with heat conduction and viscosity. Archive for Rational Mechanics and Analysis 13 (1), 167–178.

Corona, P. T., Dai, K., Helgeson, M. E., Leal, L. G., 2023. Testing orientational closure approximations in dilute and non-dilute suspensions with Rheo-SANS. Journal of Non-Newtonian Fluid Mechanics 315, Article 105014.

Courant, R., Friedrichs, K., Lewy, H., 1928. Über die partiellen Differenzengleichungen der mathematischen Physik. Mathematische Annalen 100 (1), 32–74.

Cowin, S. C., 1989. Properties of the anisotropic elasticity tensor. The Quarterly Journal of Mechanics and Applied Mathematics 42 (2), 249–266.

Cowin, S. C., Mehrabadi, M. M., 1992. The structure of the linear anisotropic elastic symmetries. Journal of the Mechanics and Physics of Solids 40 (7), 1459–1471.

Cox, R. G., 1986. The dynamics of the spreading of liquids on a solid surface. Part 1. Viscous flow. Journal of Fluid Mechanics 168, 169–194.

Cross, M. M., 1965. Rheology of non-Newtonian fluids: A new flow equation for pseudoplastic systems. Journal of Colloid Science 20 (5), 417–437.

Dassault Systèmes®, 2020. SIMULIA® User assistance for Abaqus® FEA. Retrieved on May 13, 2024. `https://help.3ds.com/HelpProductsDS.aspx`.

Deuflhard, P., 2011. Newton Methods for Nonlinear Problems: Affine Invariance and Adaptive Algorithms. Vol. 35 of Springer Series in Computational Mathematics. Springer, Berlin, Heidelberg.

Deuflhard, P., Bornemann, F., 2008. Numerische Mathematik 2: Gewöhnliche Differentialgleichungen, 3rd Edition. De Gruyter, Berlin, New York.

Deutsch, G. C., 1978. Automotive applications for advanced composite materials. In: Proceedings of the 23rd National Symposium of the Society for the Advanced of Materials and Process Engineering (May 2–4, 1978, Anaheim, California, USA), 34–61.

Dietemann, B., Bierwisch, C., 2022. Predicting particle orientation: Is an accurate flow field more important than the actual orientation model? Journal of Non-Newtonian Fluid Mechanics 310, Article 104927.

Dinh, S. M., Armstrong, R. C., 1984. A rheological equation of state for semiconcentrated fiber suspensions. Journal of Rheology 28 (3), 207–227.

Doghri, I., Tinel, L., 2005. Micromechanical modeling and computation of elasto-plastic materials reinforced with distributed-orientation fibers. International Journal of Plasticity 21 (10), 1919–1940.

Doi, M., 1981. Molecular dynamics and rheological properties of concentrated solutions of rodlike polymers in isotropic and liquid crystalline phases. Journal of Polymer Science: Polymer Physics Edition 19 (2), 229–243.

Doi, M., Edwards, S. F., 1978. Dynamics of rod-like macromolecules in concentrated solution. Part 1. Journal of the Chemical Society, Faraday Transactions 2: Molecular and Chemical Physics 74 (0), 560–570.

Du, D.-X., Zheng, Q.-S., 2002. A further exploration of the interaction direct derivative (IDD) estimate for the effective properties of multiphase composites taking into account inclusion distribution. Acta Mechanica 157 (1), 61–80.

Dupret, F., Verleye, V., 1999. Modelling the flow of fiber suspensions in narrow gaps. In: Advances in the Flow and Rheology of Non-Newtonian Fluids Part B. Vol. 8 of Rheology Series, 1347–1398. Elsevier, Amsterdam [a.o.].

Einarsson, J., Angilella, J. R., Mehlig, B., 2014. Orientational dynamics of weakly inertial axisymmetric particles in steady viscous flows. Physica D: Nonlinear Phenomena 278–279, 79–85.

Einarsson, J., Candelier, F., Lundell, F., Angilella, J. R., Mehlig, B., 2015. Rotation of a spheroid in a simple shear at small Reynolds number. Physics of Fluids 27 (6), Article 063301.

Einstein, A., 1906. Eine neue Bestimmung der Moleküldimensionen. Annalen der Physik 324 (2), 289–306.

Einstein, A., 1911. Berichtigung zu meiner Arbeit: „Eine neue Bestimmung der Moleküldimensionen“. Annalen der Physik 339 (3), 591–592.

Ericksen, J. L., 1960. Transversely isotropic fluids. Kolloid-Zeitschrift 173 (2), 117–122.

Eshelby, J. D., 1957. The determination of the elastic field of an ellipsoidal inclusion, and related problems. Proceedings of the Royal Society of London. Series A. Mathematical and Physical Sciences 241 (1226), 376–396.

Eshelby, J. D., 1959. The elastic field outside an ellipsoidal inclusion. Proceedings of the Royal Society of London. Series A. Mathematical and Physical Sciences 252 (1271), 561–569.

Farotti, E., Natalini, M., 2018. Injection molding. Influence of process parameters on mechanical properties of polypropylene polymer. A first study. In: Proceedings of the 46th Conference on Stress Analysis and Mechanical Engineering Design (September 6–9, 2017, Pisa, Italy). Vol. 8 of Procedia Structural Integrity, 256–264.

Favaloro, A. J., 2020. The rotation of rigid spheroids in a viscous fluid under mean-field effects. Journal of Non-Newtonian Fluid Mechanics 282, Article 104324.

Favaloro, A. J., Tseng, H.-C., Pipes, R. B., 2018. A new anisotropic viscous constitutive model for composites molding simulation. Composites Part A: Applied Science and Manufacturing 115, 112–122.

Favaloro, A. J., Tucker III, C. L., 2019. Analysis of anisotropic rotary diffusion models for fiber orientation. Composites Part A: Applied Science and Manufacturing 126, Article 105605.

Fedorov, F. I., 1968. Theory of Elastic Waves in Crystals. Plenum Press, New York, translated from Russian by J. E. S. Bradley.

Feng, J., Chaubal, C. V., Leal, L. G., 1998. Closure approximations for the Doi theory: Which to use in simulating complex flows of liquid-crystalline polymers? Journal of Rheology 42 (5), 1095–1119.

Ferziger, J. H., Perić, M., Street, R. L., 2020. Computational Methods for Fluid Dynamics, 4th Edition. Springer, Cham.

Fletcher, R. C., 2009. Deformable, rigid, and inviscid elliptical inclusions in a homogeneous incompressible anisotropic viscous fluid. Journal of Structural Geology 31 (4), 382–387.

Fokker, A. D., 1914. Die mittlere Energie rotierender elektrischer Dipole im Strahlungsfeld. Annalen der Physik 348 (5), 810–820.

Folgar, F., Tucker III, C. L., 1984. Orientation behavior of fibers in concentrated suspensions. Journal of Reinforced Plastics and Composites 3 (2), 98–119.

Férec, J., Abisset-Chavanne, E., Ausias, G., Chinesta, F., 2014. On the use of interaction tensors to describe and predict rod interactions in rod suspensions. Rheologica Acta 53 (5), 445–456.

Férec, J., Ausias, G., Advani, S. G., 2023. A tensorial form to describe the rheological properties of a rigid triaxial ellipsoid suspended in a Newtonian fluid. Journal of Non-Newtonian Fluid Mechanics 311, Article 104953.

Férec, J., Ausias, G., Heuzey, M. C., Carreau, P. J., 2009. Modeling fiber interactions in semiconcentrated fiber suspensions. Journal of Rheology 53 (1), 49–72.

Férec, J., Bertevas, E., Khoo, B. C., Ausias, G., Phan-Thien, N., 2017a. A rheological constitutive model for semiconcentrated rod suspensions in Bingham fluids. Physics of Fluids 29 (7), Article 073103.

Férec, J., Bertevas, E., Khoo, B. C., Ausias, G., Phan-Thien, N., 2017b. Steady-shear rheological properties for suspensions of axisymmetric particles in second-order fluids. Journal of Non-Newtonian Fluid Mechanics 239, 62–72.

Férec, J., Bertevas, E., Khoo, B. C., Ausias, G., Phan-Thien, N., 2021. Rigid fiber motion in slightly non-Newtonian viscoelastic fluids. Physics of Fluids 33 (10), Article 103320.

Férec, J., Heniche, M., Heuzey, M. C., Ausias, G., Carreau, P. J., 2008. Numerical solution of the Fokker-Planck equation for fiber suspensions: Application to the Folgar-Tucker-Lipscomb model. Journal of Non-Newtonian Fluid Mechanics 155 (1–2), 20–29.

Férec, J., Mezi, D., Advani, S. G., Ausias, G., 2020. Axisymmetric flow simulations of fiber suspensions as described by 3D probability distribution function. Journal of Non-Newtonian Fluid Mechanics 284, Article 104367.

Gajek, S., Schneider, M., Böhlke, T., 2021. An FE-DMN method for the multiscale analysis of short fiber reinforced plastic components. Computer Methods in Applied Mechanics and Engineering 384, Article 113952.

Gamet, L., Scala, M., Roenby, J., Scheufler, H., Pierson, J.-L., 2020. Validation of volume-of-fluid OpenFOAM® isoAdvector solvers using single bubble benchmarks. Computers & Fluids 213, Article 104722.

Geißler, P., Domurath, J., Ausias, G., Férec, J., Saphiannikova, M., 2023. Viscosity and dynamics of rigid axisymmetric particles in power-law fluids. Journal of Non-Newtonian Fluid Mechanics 311, Article 104963.

Gibson, A. G., 1989. Die entry flow of reinforced polymers. Composites 20 (1), 57–64.

Giesekus, H., 1962. Strömungen mit konstantem Geschwindigkeitsgradienten und die Bewegung von darin suspendierten Teilchen. Rheologica Acta 2 (2), 112–122.

Gilormini, P., Chinesta, F., 2019. Viscous drag and rod orientation kinematics in an orthotropic fluid. Journal of Non-Newtonian Fluid Mechanics 270, 96–103.

Gingold, R. A., Monaghan, J. J., 1977. Smoothed particle hydrodynamics: Theory and application to non-spherical stars. Monthly Notices of the Royal Astronomical Society 181 (3), 375–389.

Goldberg, N., Ospald, F., Schneider, M., 2017. A fiber orientation-adapted integration scheme for computing the hyperelastic Tucker average for short fiber reinforced composites. Computational Mechanics 60 (4), 595–611.

Görthofer, J., Meyer, N., Pallicity, T. D., Schöttl, L., Trauth, A., Schemmann, M., Hohberg, M., Pinter, P., Elsner, P., Henning, F., Hrymak, A., Seelig, T., Weidenmann, K., Kärger, L., Böhlke, T., 2019. Virtual process chain of sheet molding compound: Development, validation and perspectives. Composites Part B: Engineering 169, 133–147.

Guo, H., Song, K., Hilfer, R., 2022. A brief review of capillary number and its use in capillary desaturation curves. Transport in Porous Media 144 (1), 3–31.

Gupta, R., Fletcher, D. F., Haynes, B. S., 2010. Taylor flow in microchannels: A review of experimental and computational work. The Journal of Computational Multiphase Flows 2 (1), 1–31.

Gurtin, M. E., Fried, E., Anand, L., 2010. The Mechanics and Thermodynamics of Continua. Cambridge University Press, New York.

Haagh, G. A. A. V., van de Vosse, F. N., 1998. Simulation of three-dimensional polymer mould filling processes using a pseudo-concentration method. International Journal for Numerical Methods in Fluids 28 (9), 1355–1369.

Han, K.-H., Im, Y.-T., 1999. Modified hybrid closure approximation for prediction of flow-induced fiber orientation. Journal of Rheology 43 (3), 569–589.

Hand, G. L., 1962. A theory of anisotropic fluids. Journal of Fluid Mechanics 13 (1), 33–46.

Harper, C. A., 2000. Modern Plastics Handbook. McGraw-Hill, New York [a.o.].

Hashin, Z., 1964. Theory of mechanical behavior of heterogeneous media. Applied Mechanics Reviews 17 (1), 1–9.

Hashin, Z., 1965. Elasticity of random media. Transactions of The Society of Rheology 9 (1), 381–406.

Hashin, Z., Shtrikman, S., 1962a. On some variational principles in anisotropic and nonhomogeneous elasticity. Journal of the Mechanics and Physics of Solids 10 (4), 335–342.

Hashin, Z., Shtrikman, S., 1962b. A variational approach to the theory of the elastic behaviour of polycrystals. Journal of the Mechanics and Physics of Solids 10 (4), 343–352.

Hashin, Z., Shtrikman, S., 1963. A variational approach to the theory of the elastic behaviour of multiphase materials. Journal of the Mechanics and Physics of Solids 11 (2), 127–140.

Haupt, P., 2002. Continuum Mechanics and Theory of Materials, 2nd Edition. Springer, Berlin, Heidelberg, translated from German by Joan A. Kurth.

Heinen, K., 2007. Mikrostrukturelle Orientierungszustände strömender Polymerlösungen und Fasersuspensionen. Doctoral thesis, Technische Universität Dortmund.

Henning, F., Moeller, E., 2011. Handbuch Leichtbau: Methoden, Werkstoffe, Fertigung. Hanser, München, Wien.

Hershey, A. V., 1954. The elasticity of an isotropic aggregate of anisotropic cubic crystals. Journal of Applied Mechanics 21 (3), 236–240.

Hessman, P. A., Welschinger, F., Hornberger, K., Böhlke, T., 2021. On mean field homogenization schemes for short fiber reinforced composites: Unified formulation, application and benchmark. International Journal of Solids and Structures 230–231, Article 111141.

Hill, D. A., 1999. Evolution equations for arbitrary moments of the orientation distribution of rigid-rod molecules. Journal of Rheology 43 (6), 1635–1641.

Hill, R., 1952. The elastic behaviour of a crystalline aggregate. Proceedings of the Physical Society. Section A 65 (5), 349–354.

Hill, R., 1963. Elastic properties of reinforced solids: Some theoretical principles. Journal of the Mechanics and Physics of Solids 11 (5), 357–372.

Hill, R., 1965. A self-consistent mechanics of composite materials. Journal of the Mechanics and Physics of Solids 13 (4), 213–222.

Hill, R., 1967. The essential structure of constitutive laws for metal composites and polycrystals. Journal of the Mechanics and Physics of Solids 15 (2), 79–95.

Hinch, E. J., Leal, L. G., 1976. Constitutive equations in suspension mechanics. Part 2. Approximate forms for a suspension of rigid particles affected by Brownian rotations. Journal of Fluid Mechanics 76 (1), 187–208.

Hirt, C. W., Nichols, B. D., 1981. Volume of fluid (VOF) method for the dynamics of free boundaries. Journal of Computational Physics 39 (1), 201–225.

Hori, M., Nemat-Nasser, S., 1993. Double-inclusion model and overall moduli of multi-phase composites. Mechanics of Materials 14 (3), 189–206.

Howard, I. C., Brierley, P., 1976. On the finite deformation of an inhomogeneity in a viscous liquid. International Journal of Engineering Science 14 (12), 1151–1159.

Hu, G. K., Weng, G. J., 2000. The connections between the double-inclusion model and the Ponte Castañeda-Willis, Mori-Tanaka, and Kuster-Toksoz models. Mechanics of Materials 32 (8), 495–503.

Huang, C.-T., Lai, C.-H., 2020. Investigation on the coupling effects between flow and fibers on fiber-reinforced plastic (FRP) injection parts. Polymers 12 (10), Article 2274.

Huang, C.-T., Wang, J.-Z., Lai, C.-H., Hwang, S.-J., Huang, P.-W., Peng, H.-S., 2023. Correlation between fiber orientation and geometrical shrinkage of injected parts under the influence of flow-fiber coupling effect. International Journal of Precision Engineering and Manufacturing-Green Technology 10 (4), 1039–1060.

Huet, C., 1990. Application of variational concepts to size effects in elastic heterogeneous bodies. Journal of the Mechanics and Physics of Solids 38 (6), 813–841.

Huilgol, R. R., You, Z., 2006. On the importance of the pressure dependence of viscosity in steady non-isothermal shearing flows of compressible and incompressible fluids and in the isothermal fountain flow. Journal of Non-Newtonian Fluid Mechanics 136 (2–3), 106–117.

Hétu, J.-F., Gao, D. M., Garcia-Rejon, A., Salloum, G., 1998. 3D finite element method for the simulation of the filling stage in injection molding. Polymer Engineering & Science 38 (2), 223–236.

Ingber, M. S., Mondy, L. A., 1994. A numerical study of three-dimensional Jeffery orbits in shear flow. Journal of Rheology 38 (6), 1829–1843.

Ishimoto, K., 2020a. Helicoidal particles and swimmers in a flow at low Reynolds number. Journal of Fluid Mechanics 892, Article A11.

Ishimoto, K., 2020b. Jeffery orbits for an object with discrete rotational symmetry. Physics of Fluids 32 (8), Article 081904.

Issa, H., Natale, G., Ausias, G., Férec, J., 2023. Modeling and numerical simulations of Brownian rodlike particles with anisotropic translational diffusion. Physical Review Fluids 8 (3), Article 033302.

Issa, R. I., 1986. Solution of the implicitly discretised fluid flow equations by operator-splitting. Journal of Computational Physics 62 (1), 40–65.

Jack, D. A., Schache, B., Smith, D. E., 2010. Neural network-based closure for modeling short-fiber suspensions. Polymer Composites 31 (7), 1125–1141.

Jack, D. A., Smith, D. E., 2005. An invariant based fitted closure of the sixth-order orientation tensor for modeling short-fiber suspensions. Journal of Rheology 49 (5), 1091–1115.

Jack, D. A., Smith, D. E., 2006. Sixth-order fitted closures for short-fiber reinforced polymer composites. Journal of Thermoplastic Composite Materials 19 (2), 217–246.

Jack, D. A., Smith, D. E., 2007. The effect of fibre orientation closure approximations on mechanical property predictions. Composites Part A: Applied Science and Manufacturing 38 (3), 975–982.

Jaumann, G., 1911. Geschlossenes System physikalischer und chemischer Differenzialgesetze. Sitzungsberichte der Kaiserlichen Akademie der Wissenschaften Wien. Mathematisch-Naturwissenschaftliche Klasse (2a) 120, 385–530.

Jaynes, E. T., 1957. Information theory and statistical mechanics. Physical Review 106 (4), 620–630.

Jeffery, G. B., 1922. The motion of ellipsoidal particles immersed in a viscous fluid. Proceedings of the Royal Society of London. Series A 102 (715), 161–179.

Junk, M., Illner, R., 2007. A new derivation of Jeffery's equation. Journal of Mathematical Fluid Mechanics 9 (4), 455–488.

Kachanov, M., Abedian, B., 2015. On the isotropic and anisotropic viscosity of suspensions containing particles of diverse shapes and orientations. International Journal of Engineering Science 94, 71–85.

Kachanov, M., Sevostianov, I., 2018. Micromechanics of Materials, with Applications. Vol. 249 of Solid Mechanics and Its Applications. Springer, Cham.

Kailasam, M., Ponte Castañeda, P., 1998. A general constitutive theory for linear and nonlinear particulate media with microstructure evolution. Journal of the Mechanics and Physics of Solids 46 (3), 427–465.

Kammer, C., Blackwell, B., Arratia, P. E., Ponte Castañeda, P., 2022. A homogenization model for the rheology and local field statistics of suspensions of particles in yield stress fluids. Journal of Rheology 66 (3), 535–549.

Kammer, C., Ponte Castañeda, P., 2022. Variational estimates for the effective properties and field statistics of composites with variable particle interaction strengths. Journal of the Mechanics and Physics of Solids 167, Article 104996.

Kanatani, K.-I., 1984. Distribution of directional data and fabric tensors. International Journal of Engineering Science 22 (2), 149–164.

Kanaun, S. K., Levin, V. M., 2008. Self-Consistent Methods for Composites: Volume 1 - Static Problems. Vol. 148 of Solid Mechanics and Its Applications. Springer, Dordrecht.

Karl, T., Böhlke, T., 2022. Unified mean-field modeling of viscous short-fiber suspensions and solid short-fiber reinforced composites. Archive of Applied Mechanics 92 (12), 3695–3727.

Karl, T., Böhlke, T., 2024. Generalized micromechanical formulation of fiber orientation tensor evolution equations. International Journal of Mechanical Sciences 263, Article 108771.

Karl, T., Gatti, D., Böhlke, T., Frohnapfel, B., 2021a. Coupled simulation of flow-induced viscous and elastic anisotropy of short-fiber reinforced composites. Acta Mechanica 232 (6), 2249–2268.

Karl, T., Gatti, D., Frohnapfel, B., Böhlke, T., 2021b. Asymptotic fiber orientation states of the quadratically closed Folgar-Tucker equation and a subsequent closure improvement. Journal of Rheology 65 (5), 999–1022.

Karl, T., Schneider, M., Böhlke, T., 2023a. On fully symmetric implicit closure approximations for fiber orientation tensors. Journal of Non-Newtonian Fluid Mechanics 318, Article 105049.

Karl, T., Zartmann, J., Dalpke, S., Gatti, D., Frohnapfel, B., Böhlke, T., 2023b. Influence of flow-fiber coupling during mold-filling on the stress field in short-fiber reinforced composites. Computational Mechanics 71 (5), 991–1013.

Kehrer, L., Wood, J. T., Böhlke, T., 2020. Mean-field homogenization of thermoelastic material properties of a long fiber-reinforced thermoset and experimental investigation. Journal of Composite Materials 54 (25), 3777–3799.

Kim, Y., Bénard, A., Petty, C. A., 2015. Microstructure and rheology of rigid rod suspensions. Industrial & Engineering Chemistry Research 54 (16), 4497–4504.

Krauß, C., Bauer, J. K., Mitsch, J., Böhlke, T., Kärger, L., 2024. On the averaging and closure of fiber orientation tensors in virtual process chains. Journal of Elasticity 156 (1), 279–306.

Krauß, C., Kärger, L., 2022. Tensor interpolation in virtual manufacturing chains for fiber reinforced composites. International Journal of Mechanical Sciences 226, Article 107378.

Krochak, P. J., Olson, J. A., Martinez, D. M., 2009. Fiber suspension flow in a tapered channel: The effect of flow/fiber coupling. International Journal of Multiphase Flow 35 (7), 676–688.

Kröger, M., Ammar, A., Chinesta, F., 2008. Consistent closure schemes for statistical models of anisotropic fluids. Journal of Non-Newtonian Fluid Mechanics 149 (1–3), 40–55.

Kröner, E., 1958. Berechnung der elastischen Konstanten des Vielkristalls aus den Konstanten des Einkristalls. Zeitschrift für Physik 151 (4), 504–518.

Kugler, S. K., Dey, A. P., Saad, S., Cruz, C., Kech, A., Osswald, T., 2020a. A flow-dependent fiber orientation model. Journal of Composites Science 4 (3), Article 96.

Kugler, S. K., Kech, A., Cruz, C., Osswald, T., 2020b. Fiber orientation predictions - A review of existing models. Journal of Composites Science 4 (2), Article 69.

Kumar, A., Dawson, P. R., 1996. The simulation of texture evolution with finite elements over orientation space I. Development. Computer Methods in Applied Mechanics and Engineering 130 (3–4), 227–246.

Kuzmin, D., 2018. Planar and orthotropic closures for orientation tensors in fiber suspension flow models. SIAM Journal on Applied Mathematics 78 (6), 3040–3059.

Larsen, B. E., Fuhrman, D. R., Roenby, J., 2019. Performance of interFoam on the simulation of progressive waves. Coastal Engineering Journal 61 (3), 380–400.

Latz, A., Strautins, U., Niedziela, D., 2010. Comparative numerical study of two concentrated fiber suspension models. Journal of Non-Newtonian Fluid Mechanics 165 (13–14), 764–781.

Leal, L. G., 1975. The slow motion of slender rod-like particles in a second-order fluid. Journal of Fluid Mechanics 69 (2), 305–337.

Lebedev, V. I., 1977. Spherical quadrature formulas exact to orders 25–29. Siberian Mathematical Journal 18 (1), 99–107.

Lebedev, V. I., 1995. A quadrature formula for the sphere of 59th algebraic order of accuracy. Russian Academy of Sciences Doklady Mathematics 50 (2), 283–286.

Lebedev, V. I., Laikov, D. N., 1999. A quadrature formula for the sphere of the 131st algebraic order of accuracy. Russian Academy of Sciences Doklady Mathematics 59 (3), 477–481.

Lebedev, V. I., Skorokhodov, A. L., 1992. Quadrature formulas of orders 41, 47, and 53 for the sphere. Russian Academy of Sciences Doklady Mathematics 45 (3), 587–592.

Lebensohn, R. A., Tomé, C. N., 1993. A self-consistent anisotropic approach for the simulation of plastic deformation and texture development of polycrystals: Application to zirconium alloys. Acta Metallurgica et Materialia 41 (9), 2611–2624.

Lee, S., Shin, D., Kim, G., Ji, W., 2022. Numerical model for compression molding process of hybridly laminated thermoplastic composites based on anisotropic rheology. Composites Part C: Open Access 7, Article 100215.

Lee, S.-L., Liao, W.-C., 2008. Numerical simulation of a fountain flow on nonstaggered Cartesian grid system. International Journal of Heat and Mass Transfer 51 (9–10), 2433–2443.

Li, B., Guo, Y., Steeman, P., Bulters, M., Yu, W., 2021. Wall effect on the rheology of short-fiber suspensions under shear. Journal of Rheology 65 (6), 1169–1185.

Li, T., Luyé, J.-F., 2018. Optimization of fiber orientation model parameters in the presence of flow-fiber coupling. Journal of Composites Science 2 (4), Article 73.

Li, T., Luyé, J.-F., 2019. Flow-fiber coupled viscosity in injection molding simulations of short fiber reinforced thermoplastics. International Polymer Processing 34 (2), 158–171.

Linn, J., 2005. The Folgar-Tucker model as a differential algebraic system for fiber orientation calculation. Berichte des Fraunhofer-Instituts für Techno- und Wirtschaftsmathematik (ITWM) 75, 1–14.

Lipinski, P., Berveiller, M., 1989. Elastoplasticity of micro-inhomogeneous metals at large strains. International Journal of Plasticity 5 (2), 149–172.

Lipscomb II, G. G., Denn, M. M., Hur, D. U., Boger, D. V., 1988. The flow of fiber suspensions in complex geometries. Journal of Non-Newtonian Fluid Mechanics 26 (3), 297–325.

Liu, I.-S., 2002. Continuum Mechanics. Springer, Berlin, Heidelberg.

Lohmann, C., 2016. Efficient algorithms for constraining orientation tensors in Galerkin methods for the Fokker-Planck equation. Computers & Mathematics with Applications 71 (5), 1059–1073.

Lucy, L. B., 1977. A numerical approach to the testing of the fission hypothesis. The Astronomical Journal 82 (12), 1013–1024.

Luo, Y., Xu, J., Zhang, P., 2018. A fast algorithm for the moments of Bingham distribution. Journal of Scientific Computing 75 (3), 1337–1350.

Mandel, J., 1965. Generalisation de la theorie de plasticite de W. T. Koiter. International Journal of Solids and Structures 1 (3), 273–295.

Mandel, J., 1980. Généralization dans R9 de la régle du potential plastique pour un élément polycrystallin. Comptes Rendus de l'Académie des Sciences 290 (22), 481–484.

Marrucci, G., Grizzuti, N., 1984. Predicted effect of polydispersity on rodlike polymer behaviour in concentrated solutions. Journal of Non-Newtonian Fluid Mechanics 14, 103–119.

McLaughlin, R., 1977. A study of the differential scheme for composite materials. International Journal of Engineering Science 15 (4), 237–244.

Mehrabadi, M. M., Cowin, S. C., 1990. Eigentensors of linear anisotropic elastic materials. The Quarterly Journal of Mechanics and Applied Mathematics 43 (1), 15–41.

Mehta, A., Schneider, M., 2022. A sequential addition and migration method for generating microstructures of short fibers with prescribed length distribution. Computational Mechanics 70 (4), 829–851.

Meyer, N., Gajek, S., Görthofer, J., Hrymak, A., Kärger, L., Henning, F., Schneider, M., Böhlke, T., 2023. A probabilistic virtual process chain to quantify process-induced uncertainties in sheet molding compounds. Composites Part B: Engineering 249, Article 110380.

Meyer, N., Saburow, O., Hohberg, M., Hrymak, A. N., Henning, F., Kärger, L., 2020. Parameter identification of fiber orientation models based on direct fiber simulation with smoothed particle hydrodynamics. Journal of Composites Science 4 (2), Article 77.

Mezi, D., Ausias, G., Advani, S. G., Férec, J., 2019a. Fiber suspension in 2D nonhomogeneous flow: The effects of flow/fiber coupling for Newtonian and power-law suspending fluids. Journal of Rheology 63 (3), 405–418.

Mezi, D., Ausias, G., Grohens, Y., Férec, J., 2019b. Numerical simulation and modeling of the die swell for fiber suspension flows. Journal of Non-Newtonian Fluid Mechanics 274, Article 104205.

Moakher, M., Basser, P. J., 2015. Fiber orientation distribution functions and orientation tensors for different material symmetries. In: Visualization and Processing of Higher Order Descriptors for Multi-Valued Data. Mathematics and Visualization, 37–71. Springer, Cham.

Montgomery-Smith, S., 2011a. Perturbations of the coupled Jeffery-Stokes equations. Journal of Fluid Mechanics 681, 622–638.

Montgomery-Smith, S., 2011b. Perturbations of the coupled Jeffery-Stokes equations - Corrigendum. Retrieved on June 8, 2024. https://stephenmontgomerysmith.github.io/preprints/jeff-stokes-corrigendum.pdf.

Montgomery-Smith, S., 2023. Non-linear instability of periodic orbits of suspensions of thin fibers in fluids. Journal of Non-Newtonian Fluid Mechanics 313, Article 105001.

Montgomery-Smith, S., He, W., Jack, D. A., Smith, D. E., 2011a. Exact tensor closures for the three-dimensional Jeffery's equation. Journal of Fluid Mechanics 680, 321–335.

Montgomery-Smith, S., Jack, D. A., Smith, D. E., 2011b. The Fast Exact Closure for Jeffery's equation with diffusion. Journal of Non-Newtonian Fluid Mechanics 166 (7–8), 343–353.

Mori, T., Tanaka, K., 1973. Average stress in matrix and average elastic energy of materials with misfitting inclusions. Acta Metallurgica 21 (5), 571–574.

Müller, V., Böhlke, T., 2016. Prediction of effective elastic properties of fiber reinforced composites using fiber orientation tensors. Composites Science and Technology 130, 36–45.

Müller, V., Brylka, B., Dillenberger, F., Glöckner, R., Kolling, S., Böhlke, T., 2016. Homogenization of elastic properties of short-fiber reinforced composites based on measured microstructure data. Journal of Composite Materials 50 (3), 297–312.

Munganga, J. M. W., Reddy, B. D., Diatezua, K. J., 2000. Aspects of the thermodynamic stability of fibre suspension flows. Journal of Non-Newtonian Fluid Mechanics 92 (2–3), 135–150.

Mura, T., 1987. Micromechanics of Defects in Solids, 2nd Edition. Vol. 3 of Mechanics of Elastic and Inelastic Solids. Kluwer Academic Publishers, Dordrecht [a.o.].

Nabergoj, M., Urevc, J., Halilovič, M., 2022. Function-based reconstruction of the fiber orientation distribution function of short-fiber-reinforced polymers. Journal of Rheology 66 (1), 147–160.

Nemat-Nasser, S., Hori, M., 1993. Micromechanics: Overall Properties of Heterogeneous Materials. Vol. 37 of North-Holland Series in Applied Mathematics and Mechanics. North-Holland, Amsterdam [a.o.].

Noh, W. F., Woodward, P., 1976. SLIC (Simple Line Interface Calculation). In: Proceedings of the 5th International Conference on Numerical Methods in Fluid Dynamics (June 28 – July 2, 1976, Enschede, Netherlands). Vol. 59 of Lecture Notes in Physics, 330–340. Springer, Berlin, Heidelberg.

Norris, A. N., 1989. An examination of the Mori-Tanaka effective medium approximation for multiphase composites. Journal of Applied Mechanics 56 (1), 83–88.

Ogierman, W., 2022. Novel closure approximation for prediction of the effective elastic properties of composites with discontinuous reinforcement. Composite Structures 300, Article 116146.

Onat, E. T., Leckie, F. A., 1988. Representation of mechanical behavior in the presence of changing internal structure. Journal of Applied Mechanics 55 (1), 1–10.

OpenFOAM®, 2021. OpenFOAM documentation (version 2106). Retrieved on February 9, 2022. `https://www.openfoam.com/documentation/overview` and `https://www.openfoam.com/documentation/user-guide`.

Ospald, F., 2014. Numerical simulation of injection molding using OpenFOAM. Proceedings in Applied Mathematics and Mechanics 14 (1), 673–674.

Ospald, F., 2019. Contributions to the Simulation and Optimization of the Manufacturing Process and the Mechanical Properties of Short Fiber-Reinforced Plastic Parts. Doctoral thesis, Technische Universität Chemnitz.

Osswald, T., Rudolph, N., 2015. Polymer Rheology: Fundamentals and Applications. Hanser, München.

Osswald, T. A., Baur, E., Brinkmann, S., Oberbach, K., Schmachtenberg, E., 2006. International Plastics Handbook: The Resource for Plastics Engineers, 4th Edition. Hanser, München.

Oumer, A. N., Mamat, O., 2012. A study of fiber orientation in short fiber-reinforced composites with simultaneous mold filling and phase change effects. Composites Part B: Engineering 43 (3), 1087–1094.

Ozolins, A., Strautins, U., 2014. Simple models for wall effect in fiber suspension flows. Mathematical Modelling and Analysis 19 (1), 75–84.

Papenfuß, C., 2019. Mesoscopic continuum theory for liquid crystals. Atti della Accademia Peloritana dei Pericolanti - Classe di Scienze Fisiche, Matematiche e Naturali 97 (S1), Article A21.

Papenfuß, C., 2022. Maximum entropy closure relation for higher order alignment and orientation tensors compared to quadratic and hybrid closure. Journal of Modeling and Simulation of Materials 5 (1), 39–52.

Parrish, R., 2021. getLebedevSphere. MATLAB® Central File Exchange. Retrieved on July 6, 2021. `https://www.mathworks.com/matlabcentral/fileexchange/27097-getlebedevsphere`.

Paschkewitz, J. S., Dubief, Y., Dimitropoulos, C. D., Shaqfeh, E. S. G., Moin, P., 2004. Numerical simulation of turbulent drag reduction using rigid fibres. Journal of Fluid Mechanics 518, 281–317.

Perez, M., Scheuer, A., Abisset-Chavanne, E., Chinesta, F., Keunings, R., 2016. A multi-scale description of orientation in simple shear flows of confined rod suspensions. Journal of Non-Newtonian Fluid Mechanics 233, 61–74.

Petrie, C. J. S., 1999. The rheology of fibre suspensions. Journal of Non-Newtonian Fluid Mechanics 87 (2–3), 369–402.

Petty, C. A., Parks, S. M., Shao, S. M., 1999. Flow-induced alignment of fibers. In: Proceedings of 12th International Conference on Composite Materials (July 7–9, 1999, Paris, France), Article pap339.

Phan-Thien, N., Fan, X.-J., Tanner, R. I., Zheng, R., 2002. Folgar-Tucker constant for a fibre suspension in a Newtonian fluid. Journal of Non-Newtonian Fluid Mechanics 103 (2–3), 251–260.

Phan-Thien, N., Graham, A. L., 1991. A new constitutive model for fibre suspensions: Flow past a sphere. Rheologica Acta 30 (1), 44–57.

Phelps, J. H., Tucker III, C. L., 2009. An anisotropic rotary diffusion model for fiber orientation in short- and long-fiber thermoplastics. Journal of Non-Newtonian Fluid Mechanics 156 (3), 165–176.

Pierard, O., Friebel, C., Doghri, I., 2004. Mean-field homogenization of multi-phase thermo-elastic composites: A general framework and its validation. Composites Science and Technology 64 (10–11), 1587–1603.

Pipes, R. B., 1992. Anisotropic viscosities of an oriented fiber composite with a power-law matrix. Journal of Composite Materials 26 (10), 1536–1552.

Pipes, R. B., Hearle, J. W. S., Beaussart, A. J., Okine, R. K., 1991a. Influence of fiber length on the viscous flow of an oriented fiber assembly. Journal of Composite Materials 25 (10), 1379–1390.

Pipes, R. B., Hearle, J. W. S., Beaussart, A. J., Sastry, A. M., Okine, R. K., 1991b. A constitutive relation for the viscous flow of an oriented fiber assembly. Journal of Composite Materials 25 (9), 1204–1217.

Planck, M., 1917. Über einen Satz der statistischen Dynamik und seine Erweiterung in der Quantentheorie. Sitzungsberichte der Königlich-Preußischen Akademie der Wissenschaften zu Berlin 24, 324–341.

Ponte Castañeda, P., 2021. Anisotropic Oldroyd-type models for non-colloidal suspensions of viscoelastic particles in Newtonian and yield-stress fluids via homogenization. Journal of Non-Newtonian Fluid Mechanics 295, Article 104625.

Ponte Castañeda, P., Willis, J. R., 1995. The effect of spatial distribution on the effective behavior of composite materials and cracked media. Journal of the Mechanics and Physics of Solids 43 (12), 1919–1951.

Périn, F., 2004. Bounds and asymptotic results for the effective viscosity of a nondilute suspension of oriented fibres in longitudinal flow. International Journal of Engineering Science 42 (13–14), 1483–1502.

Périn, F., Lévy, T., 1994. Application of the homogenization method to a suspension of fibres. International Journal of Engineering Science 32 (8), 1253–1269.

Reuss, A., 1929. Berechnung der Fließgrenze von Mischkristallen auf Grund der Plastizitätsbedingung für Einkristalle. Zeitschrift für Angewandte Mathematik und Mechanik 9 (1), 49–58.

Roenby, J., Bredmose, H., Jasak, H., 2016. A computational method for sharp interface advection. Royal Society Open Science 3 (11), Article 160405.

Roscoe, R., 1952. The viscosity of suspensions of rigid spheres. British Journal of Applied Physics 3 (8), 267–269.

Roscoe, R., 1973. Isotropic composites with elastic or viscoelastic phases: General bounds for the moduli and solutions for special geometries. Rheologica Acta 12 (3), 404–411.

Rose, W., 1961. Fluid-fluid interfaces in steady motion. Nature 191 (4785), 242–243.

Russel, W. B., 1973. On the effective moduli of composite materials: Effect of fiber length and geometry at dilute concentrations. Zeitschrift für angewandte Mathematik und Physik 24 (4), 581–600.

Scheuer, A., Abisset-Chavanne, E., Chinesta, F., Keunings, R., 2016. Second-gradient modelling of orientation development and rheology of dilute confined suspensions. Journal of Non-Newtonian Fluid Mechanics 237, 54–64.

Scheuer, A., Grégoire, G., Abisset-Chavanne, E., Chinesta, F., Keunings, R., 2020. Modelling the effect of particle inertia on the orientation kinematics of fibres and spheroids immersed in a simple shear flow. Computers & Mathematics with Applications 79 (3), 539–554.

Scheufler, H., Roenby, J., 2019. Accurate and efficient surface reconstruction from volume fraction data on general meshes. Journal of Computational Physics 383, 1–23.

Schneider, M., 2016. On the effective viscosity of a periodic suspension - Analysis of primal and dual formulations for Newtonian and non-Newtonian solvents. Mathematical Methods in the Applied Sciences 39 (12), 3309–3327.

Schürmann, H., 2007. Konstruieren mit Faser-Kunststoff-Verbunden, 2nd Edition. Springer, Berlin, Heidelberg.

Seng, S., Monroy, C., Malenica, S., 2017. On the use of Euler and Crank-Nicolson time-stepping schemes for seakeeping simulations in OpenFOAM®. In: Proceedings of the VII International Conference on Computational Methods in Marine Engineering (May 15–17, 2017, Nantes, France), 905–920.

Shaqfeh, E. S. G., Fredrickson, G. H., 1990. The hydrodynamic stress in a suspension of rods. Physics of Fluids A: Fluid Dynamics 2 (1), 7–24.

Sillem, A., 2010. Fundamental Theory and Implementation of the Wang-O'Gara-Tucker Model for the Modeling of Fiber Orientation in Fiber Filled Injection Molded Thermoplastics. Master's thesis, Faculty of Mechanical, Maritime and Materials Engineering, Delft University of Technology.

Sommer, D. E., Favaloro, A. J., Pipes, R. B., 2018. Coupling anisotropic viscosity and fiber orientation in applications to squeeze flow. Journal of Rheology 62 (3), 669–679.

Spurk, J. H., Aksel, N., 2020. Fluid Mechanics, 3rd Edition. Springer, Cham.

Sterr, B., Hrymak, A., Schneider, M., Böhlke, T., 2025. Machine learning assisted discovery of effective viscous material laws for shear-thinning fiber suspensions. Computational Mechanics 75 (1), 51–69.

Sterr, B., Wicht, D., Hrymak, A., Schneider, M., Böhlke, T., 2023. Homogenizing the viscosity of shear-thinning fiber suspensions with an FFT-based computational method. Journal of Non-Newtonian Fluid Mechanics 321, Article 105101.

Stroud, A. H., 1971. Approximate Calculation of Multiple Integrals. Prentice-Hall, Englewood Cliffs.

Suquet, P. M., 1987. Part IV, Chapter 2: Averages, Boundary Conditions. In: Homogenization Techniques for Composite Media: Lectures Delivered at the CISM International Center for Mechanical Sciences (July 1–5, 1985, Udine, Italy). Vol. 272 of Lecture Notes in Physics, 199–208. Springer, Berlin, Heidelberg.

Talbot, D. R. S., Willis, J. R., 1992. Some simple explicit bounds for the overall behaviour of nonlinear composites. International Journal of Solids and Structures 29 (14–15), 1981–1987.

Tandon, G. P., Weng, G. J., 1984. The effect of aspect ratio of inclusions on the elastic properties of unidirectionally aligned composites. Polymer Composites 5 (4), 327–333.

Tang, L., Altan, M. C., 1995. Entry flow of fiber suspensions in a straight channel. Journal of Non-Newtonian Fluid Mechanics 56 (2), 183–216.

Thevenin, P., Perreux, D., 1996. The use of homogenization methods for estimating anisotropic viscosities of composite melts. Composites Science and Technology 56 (5), 595–603.

Torquato, S., 2002. Random Heterogeneous Materials: Microstructure and Macroscopic Properties. Vol. 16 of Interdisciplinary Applied Mathematics. Springer, New York.

Traxl, R., Pichler, C., Lackner, R., 2020. Micromechanics-based assessment of the effective viscosity of suspensions of generalized-Newtonian fluids embedding noncolloidal angular/spheroidal pores and particles. Journal of Rheology 64 (4), 899–913.

Truesdell, C., Noll, W., 1965. The Non-Linear Field Theories of Mechanics. Vol. III/3 of Encyclopedia of Physics. Springer, Berlin [a.o.].

Tseng, H.-C., 2024. The effect of fiber content and aspect ratio on anisotropic flow front and fiber orientation for injection-molded fiber composites. International Polymer Processing 39 (1), 47–58.

Tseng, H.-C., Chang, R.-Y., Hsu, C.-H., 2013. Phenomenological improvements to predictive models of fiber orientation in concentrated suspensions. Journal of Rheology 57 (6), 1597–1631.

Tseng, H.-C., Chang, R.-Y., Hsu, C.-H., 2016. An objective tensor to predict anisotropic fiber orientation in concentrated suspensions. Journal of Rheology 60 (2), 215–224.

Tseng, H.-C., Chang, R.-Y., Hsu, C.-H., 2018. The use of principal spatial tensor to predict anisotropic fiber orientation in concentrated fiber suspensions. Journal of Rheology 62 (1), 313–320.

Tseng, H.-C., Favaloro, A. J., 2019. The use of informed isotropic constitutive equation to simulate anisotropic rheological behaviors in fiber suspensions. Journal of Rheology 63 (2), 263–274.

Tucker III, C. L., 1991. Flow regimes for fiber suspensions in narrow gaps. Journal of Non-Newtonian Fluid Mechanics 39 (3), 239–268.

Tucker III, C. L., 2021. Fiber Orientation Tools (v1.0.0). Retrieved on February 10, 2023. `https://github.com/charlestucker3/Fiber-Orientation-Tools`.

Tucker III, C. L., 2022a. Fundamentals of Fiber Orientation: Description, Measurement and Prediction. Hanser, München.

Tucker III, C. L., 2022b. Planar fiber orientation: Jeffery, non-orthotropic closures, and reconstructing distribution functions. Journal of Non-Newtonian Fluid Mechanics 310, Article 104939.

Tucker III, C. L., Liang, E., 1999. Stiffness predictions for unidirectional short-fiber composites: Review and evaluation. Composites Science and Technology 59 (5), 655–671.

Tyler, D. E., 1987. Statistical analysis for the angular central Gaussian distribution on the sphere. Biometrika 74 (3), 579–589.

ul Qadir, N., Jack, D. A., 2009. Modeling fibre orientation in short fibre suspensions using the neural network-based orthotropic closure. Composites Part A: Applied Science and Manufacturing 40 (10), 1524–1533.

van Gurp, M., 1998. Letter to the Editor: On the use of spherical tensors and the maximum entropy method to obtain closure for anisotropic liquids. Journal of Rheology 42 (5), 1269–1271.

Verleye, V., Dupret, F., 1993. Prediction of fiber orientation in complex injection molded parts. In: Proceedings of the 1993 ASME Winter Annual Meeting (November 28 – December 3, 1993, New Orleans, Louisiana, USA). Vol. 175 of Applied Mechanics Division (AMD), Developments in non-Newtonian Flows, 139–163. American Society of Mechanical Engineers (ASME), New York.

VerWeyst, B. E., 1998. Numerical Predictions of Flow-Induced Fiber Orientation in Three-Dimensional Geometries. PhD thesis, University of Illinois at Urbana-Champaign.

VerWeyst, B. E., Tucker III, C. L., 2002. Fiber suspensions in complex geometries: Flow/orientation coupling. The Canadian Journal of Chemical Engineering 80 (6), 1093–1106.

Voigt, W., 1889. Ueber die Beziehung zwischen den beiden Elasticitätsconstanten isotroper Körper. Annalen der Physik 274 (12), 573–587.

Voigt, W., 1910. Lehrbuch der Kristallphysik (mit Ausschluß der Kristalloptik). Teubner, Leipzig, Reproduktion des 1928 [...] erschienenen Nachdrucks der ersten Auflage von 1910. Johnson Reprint, New York; Teubner, Stuttgart, 1966.

Voinov, O. V., 1976. Hydrodynamics of wetting. Fluid Dynamics 11 (5), 714–721.

Walpole, L. J., 1966a. On bounds for the overall elastic moduli of inhomogeneous systems - I. Journal of the Mechanics and Physics of Solids 14 (3), 151–162.

Walpole, L. J., 1966b. On bounds for the overall elastic moduli of inhomogeneous systems - II. Journal of the Mechanics and Physics of Solids 14 (5), 289–301.

Walpole, L. J., 1969. On the overall elastic moduli of composite materials. Journal of the Mechanics and Physics of Solids 17 (4), 235–251.

Walpole, L. J., 1981. Elastic behavior of composite materials: Theoretical foundations. Advances in Applied Mechanics 21, 169–242.

Wang, J., Mao, Q., Jiang, N., Chen, J., 2022. Effects of injection molding parameters on properties of insert-injection molded polypropylene single-polymer composites. Polymers 14 (1), Article 23.

Wang, J., O'Gara, J. F., Tucker III, C. L., 2008. An objective model for slow orientation kinetics in concentrated fiber suspensions: Theory and rheological evidence. Journal of Rheology 52 (5), 1179–1200.

Wang, Z., 2022. Exploring the applicability of a simplified fully coupled flow/orientation algorithm developed for polymer composites extrusion deposition additive manufacturing. International Polymer Processing 37 (1), 106–119.

Wang, Z., Smith, D. E., 2019. Simulation of mutually dependent polymer flow and fiber filled in polymer composite deposition additive manufacturing. In: Proceedings of the 30th Annual International Solid Freeform Fabrication Symposium - An Additive Manufacturing Conference (August 12–14, 2019, Austin, Texas, USA), 1297–1309.

Wang, Z., Smith, D. E., 2021a. Finite element modelling of fully-coupled flow/fiber-orientation effects in polymer composite deposition additive manufacturing nozzle-extrudate flow. Composites Part B: Engineering 219, Article 108811.

Wang, Z., Smith, D. E., 2021b. A fully coupled simulation of planar deposition flow and fiber orientation in polymer composites additive manufacturing. Materials 14 (10), Article 2596.

Wetzel, E. D., 1999. Modeling Flow-Induced Microstructure of Inhomogeneous Liquid-Liquid Mixtures. PhD thesis, University of Illinois at Urbana-Champaign.

Wetzel, E. D., Tucker III, C. L., 2001. Droplet deformation in dispersions with unequal viscosities and zero interfacial tension. Journal of Fluid Mechanics 426, 199–228.

Williams, M. L., Landel, R. F., Ferry, J. D., 1955. The temperature dependence of relaxation mechanisms in amorphous polymers and other glass-forming liquids. Journal of the American Chemical Society 77 (14), 3701–3707.

Willis, J. R., 1977. Bounds and self-consistent estimates for the overall properties of anisotropic composites. Journal of the Mechanics and Physics of Solids 25 (3), 185–202.

Willis, J. R., 1981. Variational and related methods for the overall properties of composites. Advances in Applied Mechanics 21, 1–78.

Wittemann, F., Kärger, L., Henning, F., 2021. Theoretical approximation of hydrodynamic and fiber-fiber interaction forces for macroscopic simulations of polymer flow process with fiber orientation tensors. Composites Part C: Open Access 5, Article 100152.

Wittemann, F., Kärger, L., Henning, F., 2022. Influence of fiber breakage on flow behavior in fiber length- and orientation-dependent injection molding simulations. Journal of Non-Newtonian Fluid Mechanics 310, Article 104950.

Wittemann, F., Maertens, R., Kärger, L., Henning, F., 2019. Injection molding simulation of short fiber reinforced thermosets with anisotropic and non-Newtonian flow behavior. Composites Part A: Applied Science and Manufacturing 124, Article 105476.

Wörner, M., Cai, X., Alla, H., Yue, P., 2018. A semi-analytical method to estimate the effective slip length of spreading spherical-cap shaped droplets using Cox theory. Fluid Dynamics Research 50 (3), Article 035501.

Zaidani, M., Omar, M. A., Kumar, S., 2015. Coupling of injection molding process to mechanical properties of short fiber composites: A through process modeling approach. Journal of Reinforced Plastics and Composites 34 (23), 1963–1978.

Zaremba, M. S., 1903. Sur une forme perfectionée de la théorie de la relaxation. Bulletin International de l'Académie des Sciences de Cracovie Classe des Sciences Mathématiques et Naturelles 8, 594–614.

Zheng, Q.-S., Du, D.-X., 2001. An explicit and universally applicable estimate for the effective properties of multiphase composites which accounts for inclusion distribution. Journal of the Mechanics and Physics of Solids 49 (11), 2765–2788.

Zheng, R., Tanner, R. I., Fan, X.-J., 2011. Injection Molding: Integration of Theory and Modeling Methods. Springer, Berlin, Heidelberg.

Own publications

Peer-reviewed journal articles

2021 Karl, T., Gatti, D., Böhlke, T., Frohnapfel, B., 2021a. Coupled simulation of flow-induced viscous and elastic anisotropy of short-fiber reinforced composites. Acta Mechanica 232 (6), 2249–2268.

Karl, T., Gatti, D., Frohnapfel, B., Böhlke, T., 2021b. Asymptotic fiber orientation states of the quadratically closed Folgar-Tucker equation and a subsequent closure improvement. Journal of Rheology 65 (5), 999–1022.

2022 Karl, T., Böhlke, T., 2022. Unified mean-field modeling of viscous short-fiber suspensions and solid short-fiber reinforced composites. Archive of Applied Mechanics 92 (12), 3695–3727.

2023 Karl, T., Schneider, M., Böhlke, T., 2023a. On fully symmetric implicit closure approximations for fiber orientation tensors. Journal of Non-Newtonian Fluid Mechanics 318, Article 105049.

Karl, T., Zartmann, J., Dalpke, S., Gatti, D., Frohnapfel, B., Böhlke, T., 2023b. Influence of flow-fiber coupling during mold-filling on the stress field in short-fiber reinforced composites. Computational Mechanics 71 (5), 991–1013.

2024 Karl, T., Böhlke, T., 2024. Generalized micromechanical formulation of fiber orientation tensor evolution equations. International Journal of Mechanical Sciences 263, Article 108771.

Research data

2020 Karl, T., Gatti, D., 2020. Research data of the journal article „Coupled simulation of flow-induced viscous and elastic anisotropy of short-fiber reinforced composites“. Latest version published online at https://doi.org/10.5445/IR/1000126534 (Repository KITopen), retrieved on January 31, 2025. Outdated versions: DOI: 10.5445/IR/1000119139 and DOI: 10.5445/IR/1000123343.

Schriftenreihe Kontinuumsmechanik im Maschinenbau
Karlsruher Institut für Technologie (KIT)
(ISSN 2192-693X)

Band 1 Felix Fritzen
Microstructural modeling and computational homogenization of the physically linear and nonlinear constitutive behavior of micro-heterogeneous materials.
ISBN 978-3-86644-699-1

Band 2 Rumena Tsotsova
Texturbasierte Modellierung anisotroper Fließpotentiale.
ISBN 978-3-86644-764-6

Band 3 Johannes Wippler
Micromechanical finite element simulations of crack propagation in silicon nitride.
ISBN 978-3-86644-818-6

Band 4 Katja Jöchen
Homogenization of the linear and non-linear mechanical behavior of polycrystals.
ISBN 978-3-86644-971-8

Band 5 Stephan Wulfinghoff
Numerically Efficient Gradient Crystal Plasticity with a Grain Boundary Yield Criterion and Dislocation-based Work-Hardening.
ISBN 978-3-7315-0245-6

Band 6 Viktor Müller
Micromechanical modeling of short-fiber reinforced composites.
ISBN 978-3-7315-0454-2

Die Bände sind unter www.ksp.kit.edu als PDF frei verfügbar oder als Druckausgabe bestellbar.

Band 7 Florian Rieger
Work-hardening of dual-phase steel.
ISBN 978-3-7315-0513-6

Band 8 Vedran Glavas
Micromechanical Modeling and Simulation of Forming Processes.
ISBN 978-3-7315-0602-7

Band 9 Eric Bayerschen
Single-crystal gradient plasticity with an accumulated plastic slip: Theory and applications.
ISBN 978-3-7315-0606-5

Band 10 Bartholomäus Brylka
Charakterisierung und Modellierung der Steifigkeit von langfaserverstärktem Polypropylen.
ISBN 978-3-7315-0680-5

Band 11 Rudolf Neumann
Two-Scale Thermomechanical Simulation of Hot Stamping.
ISBN 978-3-7315-0714-7

Band 12 Mauricio Lobos Fernández
Homogenization and materials design of mechanical properties of textured materials based on zeroth-, first- and second-order bounds of linear behavior.
ISBN 978-3-7315-0770-3

Band 13 Malte Schemmann
Biaxial Characterization and Mean-field Based Damage Modeling of Sheet Molding Compound Composites.
ISBN 978-3-7315-0818-2

Band 14 Jürgen Albiez
Finite element simulation of dislocation based plasticity and diffusion in multiphase materials at high temperature.
ISBN 978-3-7315-0918-9

Band 15 Maria Loredana Kehrer
Thermomechanical Mean-Field Modeling and Experimental Characterization of Long Fiber-Reinforced Sheet Molding Compound Composites.
ISBN 978-3-7315-0924-0

Band 16 Peter Hölz
A dynamic and statistical analysis of the temperature- and fatigue behavior of a race power unit – The effect of different thermodynamic states.
ISBN 978-3-7315-0988-2

Band 17 Andreas Prahs
A Gradient Crystal Plasticity Theory Based on an Extended Energy Balance.
ISBN 978-3-7315-1025-3

Band 18 Johannes Ruck
Modeling martensitic phase transformation in dual phase steels based on a sharp interface theory.
ISBN 978-3-7315-1072-7

Band 19 Hannes Erdle
Modeling of Dislocation - Grain Boundary Interactions in Gradient Crystal Plasticity Theories.
ISBN 978-3-7315-1196-0

Band 20 Johannes Görthofer
Microstructure generation and micromechanical modeling of sheet molding compound composites.
ISBN 978-3-7315-1205-9

Band 21 Daniel Wicht
Efficient fast Fourier transform-based solvers for computing the thermomechanical behavior of applied materials.
ISBN 978-3-7315-1220-2

Band 22 Juliane Lang
Thermomechanical Modeling and Experimental Characterization of Sheet Molding Compound Composites.
ISBN 978-3-7315-1232-5

Die Bände sind unter www.ksp.kit.edu als PDF frei verfügbar oder als Druckausgabe bestellbar.

Band 23 Julian Karl Bauer
Fiber Orientation Tensors and Mean Field Homogenization: Application to Sheet Molding Compound.
ISBN 978-3-7315-1262-2

Band 24 Sebastian Gajek
Deep material networks for efficient scale-bridging in thermomechanical simulations of solids.
ISBN 978-3-7315-1278-3

Band 25 Jannick Kuhn
Microstructure modeling and crystal plasticity parameter identification for predicting the cyclic mechanical behavior of polycrystalline metals.
ISBN 978-3-7315-1272-1

Band 26 Felix Ernesti
A computational multi-scale approach for brittle materials.
ISBN 978-3-7315-1285-1

Band 27 Patrick Arthur Hessman
On multi-scale modeling of fatigue in short glass fiber reinforced thermoplastics.
ISBN 978-3-7315-1398-8

Band 28 Benedikt Sterr
Machine learning aided multiscale mechanics of fiber suspensions.
ISBN 978-3-7315-11421-3

Band 29 Maximilian Krause
Local Stresses and Strains in Polycrystals.
ISBN 978-3-7315-1411-4

Band 30 Johannes Keursten
Thermoviscoelastic Modeling of Thermoplastic Polymers.
ISBN 978-3-7315-1422-0

Band 31 Alexander Dyck
Chemo-Mechanically Coupled Models in Continuum Thermodynamics.
ISBN 978-3-7315-1425-1

Band 32 Tobias Karl
Micromechanical Modeling of Short-Fiber Orientation Dynamics.
ISBN 978-3-7315-1431-2

Accurate prediction of the microstructure of short-fiber reinforced polymers and the associated effective mechanical properties is of great industrial importance. This work deals with the micromechanical modeling of the fiber orientation evolution during mold-filling of short-fiber suspensions. In the first part, the orientation evolution is studied taking into account the anisotropic viscosity of the suspension with emphasis on the stress field in the solid composite under load. The use of orientation tensors requires closures, which form the second part and are studied in particular in a micromechanical context for the estimation of effective mechanical properties. The common quadratic closure is transformed by symmetrization into a new form consisting of two variants, and the novel concept of implicit closures is introduced and investigated. The micromechanical formulation of the short-fiber orientation evolution is addressed in the third part. Based on mean-field homogenization, the evolution equation of the orientation tensor of arbitrary order is formulated. This generalized formulation allows the use of any mean-field model by inserting the respective localization relation. Thus, the anisotropic microstructure of the fiber suspension can be considered in the orientation evolution equation.

ISSN 2192-693X
ISBN 978-3-7315-1431-2

Gedruckt auf FSC-zertifiziertem Papier